CZECH TECHNICAL UNIVERSITY IN PRAGUE
FACULTY OF NUCLEAR SCIENCES AND PHYSICAL ENGINEERING

DOCTORAL THESIS

Mathematical modeling of fluid flow using lattice Boltzmann method

Prague 2023

Pavel Eichler

This thesis is submitted to the Faculty of Nuclear Sciences and Physical Engineering, Czech Technical University in Prague, in partial fulfilment of the requirements for the degree of Doctor of Philosophy (Ph.D.) in Mathematical Engineering.

Bibliografický záznam

Bibliographic Entry

Author	Ing. Pavel Eichler
	Czech Technical University in Prague, Faculty of Nuclear Sciences and Physical Engineering, Department of Mathematics
Title of thesis	Mathematical modeling of fluid flow using lattice Boltzmann method
Degree programme	Application of Natural Sciences
Field of study	Mathematical Engineering
Supervisor	doc. Ing. Radek Fučík, Ph.D.
	Czech Technical University in Prague, Faculty of Nuclear Sciences and Physical Engineering, Department of Mathematics
Academic year	2023
Number of pages	192
Keywords	Fluid flow numerical simulations, lattice Boltzmann method, laminar flow, turbulent flow, direct numerical simulations, boundary layer, validation, numerical analysis, mesh refinement

Abstrakt

Tato práce se věnuje matematickému modelování nestlačitelné tekutiny v izotermálním systému pomocí mřížkové Boltzmannovy metody (LBM). Hlavním cílem je zkoumání použití této numerické metody pro simulace volného proudění a implementace v rámci kódu vyvíjeného na KM, FJFI, ČVUT v Praze.

Nejprve je formulován matematický model popisující nestlačitelné vazké proudění. Dále je uveden popis nenewtonovských kapalin, teorie mezní vrstvy a úvod do kinetické teorie látek. Pro numerické řešení uvedených problémů je použita LBM, která je detailně popsána včetně různých typů kolizních operátorů a okrajových podmínek.

S použitím numerických testů a asymptotických metod je LBM analyzována. Výsledky asymptotické analýzy ukazují, že dané numerické řešení aproximuje nestlačitelné Navierovy-Stokesovy rovnice. Dále jsou odvozeny lokální vztahy pro výpočet parciálních derivací rychlosti, které jsou použity pro interpolaci s druhým řádem přesnosti. V rámci numerické analýzy jsou otestovány mezoskopické okrajové podmínky a ukazuje se, že námi navržené okrajové podmínky produkují řešení s nejmenší chybou.

Cílem druhé části je validace LBM pomocí řešení třech reálných problémů. Nejprve je testováno její použití na problému turbulentního proudění v mezní vrstvě nad hrubým povrchem. Získané výsledky ukazují, že tato metoda poskytuje dobré výsledky ve srovnání s experimentem či numerickou metodou konečných diferencí. V rámci druhého problému je zkoumáno numerické řešení tlakového pole ve fluidním kotli. Dobrá shoda je opět pozorována mezi výsledky LBM, experimentem a metodou konečných objemů. Poslední úloha zkoumá použitelnost LBM pro simulace nenewtonovského proudění v oblasti okolo stenotického zúžení cév. LBM výsledky jsou srovnány s experimentálními daty měřenými pomocí magnetické rezonance. Výsledky simulací ukazují dobrou shodu s většinou experimentálních dat a dále poukazují na nedostatky měření pomocí magnetické rezonance, tj. převážně na podhodnocení zpětného toku v oblastech turbulentního proudění.

Abstract

This thesis deals with the mathematical modeling of an incompressible fluid in an isothermal system using the lattice Boltzmann method (LBM). The main objective is to investigate the applicability of this numerical method to free-flow simulations and its implementation within the code developed at the Department of Mathematics, FNSPE, CTU in Prague.

First, a mathematical model is formulated that describes the incompressible viscous flow. Then, a description of non-Newtonian fluids models, boundary layer theory, and an introduction to kinetic theory are given. The LBM is used for the numerical solution of these problems and is extensively described including various types of collision operators and boundary conditions.

The LBM is analyzed using numerical tests and asymptotic methods. The results of the asymptotic analysis show that the given numerical solution approximates the incompressible Navier-Stokes equations. Furthermore, local relations are derived to calculate the partial derivatives of the velocity, which are used for the interpolation with the second-order accuracy. Mesoscopic boundary conditions are tested by the numerical analysis and it is shown that our proposed boundary conditions produce a numerical solution with the smallest error.

The aim of the second part is to validate the LBM in the context of three real-world problems. First, its application to the problem of a turbulent boundary layer flow above a rough surface is tested. The results obtained show that this method gives good results compared to the experimental data or numerical finite difference method. In the second problem, the numerical solution of the pressure field in a fluidized bed boiler is investigated. Good agreement is again observed between the results of the LBM, experiment, and finite volume method. The last problem investigates the applicability of the LBM for simulations of a non-Newtonian flow in the vicinity of stenotic valves. LBM results are compared with experimental data measured using magnetic resonance imaging. The simulation results show a good agreement with most of the experimental data and further highlight the imperfections of the MRI measurements, that is, mainly the underestimation of the backflow in regions of turbulent flow.

Acknowledgements

I would like to thank everyone who gave me any kind of support in any of my activities during the time when I was a Ph.D. student. I would like to express my thanks to my supportive supervisor, doc. Ing. Radek Fučík, Ph.D., who has supported me throughout this research project. Second, I would like to express my gratitude to my friends and family. Without their tremendous understanding and encouragement in the past few years, it would be impossible for me to complete my studies.

Author's declaration

I confirm having prepared the thesis on my own and having listed all used sources of information in the bibliography.

Prague, January 19, 2023   Pavel Eichler

Contents

Nomenclature

Acronyms

$\mathrm{Grid_{id}}$ Grid label, page 70

BC   Boundary Condition, page 1

CFD   Computational Fluid Dynamics, page 1

CFL   Courant–Friedrichs–Lewy number, page 86

CLBM   Lattice Boltzmann method with central moment based collision operator, page 31

CUDA   Compute Unified Device Architecture, page 59

CuLBM   Lattice Boltzmann method with cumulant collision operator, page 34

CuLBM2   Lattice Boltzmann method with improved cumulant collision operator, page 37

DDF   Discrete Density Function, page 27

ELMM   Extended Large-eddy Microscale Model, page 83

FAC2   Fraction of predictions within a factor of two, page 142

FB   Fractional Bias metric, page 141

FDM   Finite Difference Method, page 1

FEM   Finite Element Method, page 1

FVM   Finite Volume Method, page 1

GPU   Graphics Processing Unit, page 59

GX   Glycerol water solution with xanthan gum, page 112

GX   Sucrose water solution with xanthan gum, page 112

HWA   CTA(Constant Temperature Anemometer) hot wire anemometry measurement technique, page 92

LBM   Lattice Boltzmann Method, page 1

MiS   Mild stenosis, page 112

MoS   Moderate stenosis, page 112

MPI   Message Passing Interface, page 59

MRI   Magnetic Resonance Imaging, page 2

MRT   Lattice Boltzmann method with multiple relaxation time collision operator, page 30

NMSE   Normalized Mean Square Error, page 141

PC-MRI   Phase-Contrast Magnetic Resonance Imaging technique, page 111

PDE   Partial Differential Equation, page 1

PIV   Particle Image Velocimetry measurement technique, page 92

SeS   Severe stenosis, page 112

SRT   Lattice Boltzmann method with single relaxation time collision operator, page 29

TRT   Lattice Boltzmann method with two relaxation time collision operator, page 30

Greek letters

$\delta\rho$ Non-dimensional temporal fluctuations of ρ around ρ_0, page 57 $[-]$

$\delta f_{\boldsymbol{i}}$ Non-dimensional fluctuation of DDF around $f_{\boldsymbol{i}}^{(0)}$, page 59 $[-]$

Δt Non-dimensional time step, page 27 $[-]$

Δx Non-dimensional space step, page 27 $[-]$

δ Boundary layer height, page 18 $[\mathrm{m}]$

δ_ν Height of viscous sublayer, page 20 $[\mathrm{m}]$

δ_t Time step, page 26 $[\mathrm{s}]$

δ_t^ℓ Time step on grid with level ℓ, page 54 $[\mathrm{s}]$

$\delta_t^{(FVM)}$ Time step used by ANSYS Fluent, page 103 $[\mathrm{m}]$

δ_x Grid spacing parameter, page 25 $[\mathrm{m}]$

δ_x^ℓ Grid spacing parameter of grid with level ℓ, page 54 $[\mathrm{m}]$

$\delta_x^{(FVM)}$ Grid spacing parameter used by ANSYS Fluent, page 103 $[\mathrm{m}]$

δ_{99} Height above the wall, where fluid velocity reaches 99% of U_∞, page 19 $[\mathrm{m}]$

$\dot{\gamma}_0$ Reference shear rate, page 17 $[\mathrm{s}^{-1}]$

$\dot{\gamma}$ Shear rate, page 16 $[\mathrm{s}^{-1}]$

ϵ Asymptotic parameter, page 62 $[\mathrm{m}]$

ϵ_n Member of sequence of asymptotic parameters, page 62 $[\mathrm{m}]$

$\hat{\Omega}$	Discrete grid, page 25	
$\hat{\overline{\Omega}}$	Discretization of $\overline{\Omega}$, page 25	
$\kappa_{\boldsymbol{j}}$	Non-dimensional central moment, page 31	$[-]$
λ	Second viscous coefficient, page 12	$[\mathrm{kg\,m^{-1}\,s^{-1}}]$
$\lambda_3, \lambda_4, \lambda_5$	Non-dimensional parameters in CuLBM2, page 37	$[-]$
$\langle \varphi \rangle$	Space averaged quantity φ, page 84	
μ	Dynamic viscosity, page 10	$[\mathrm{kg\,m^{-1}\,s^{-1}}]$
μ_0	Dynamic viscosity at zero shear rate, page 17	$[\mathrm{kg\,m^{-1}\,s^{-1}}]$
μ_∞	Dynamic viscosity at infinite shear rate, page 17	$[\mathrm{kg\,m^{-1}\,s^{-1}}]$
μ_{CA}	Casson model of dynamic viscosity, page 17	$[\mathrm{kg\,m^{-1}\,s^{-1}}]$
μ_{CR}	Cross model of dynamic viscosity, page 17	$[\mathrm{kg\,m^{-1}\,s^{-1}}]$
μ_{CY}	Carreau-Yasuda model of dynamic viscosity, page 17	$[\mathrm{kg\,m^{-1}\,s^{-1}}]$
μ_{PL}	Power law model of dynamic viscosity, page 17	$[\mathrm{kg\,m^{-1}\,s^{-1}}]$
μ_{SP}	Spriggs model of dynamic viscosity, page 17	$[\mathrm{kg\,m^{-1}\,s^{-1}}]$
ν	Kinematic viscosity, page 10	$[\mathrm{m^2\,s^{-1}}]$
Ω	Computational domain, page 11	
ω	Non-dimensional relaxation frequency, page 30	$[-]$
ω^ℓ	Non-dimensional relaxation frequency on grid with level ℓ, page 55	$[-]$
Ω_2	Computational domain, page 92	
ω_i	Non-dimensional relaxation frequencies, page 31	$[-]$
ω_t	Integration frequency, page 116	$[\mathrm{s^{-1}}]$
$\omega_{120+102}, \omega_{120-102}, \omega_{111}$	Non-dimensional relaxation frequencies in CuLBM2, page 37	$[-]$
Ω_{1a}, Ω_{1b}	Computational domain, page 84	
$\overline{\Omega}$	Closure of Ω, page 25	
$\overline{\tau}_w$	Time-averaged wall shear stress, page 22	$[\mathrm{kg\,m^{-1}\,s^{-2}}]$
$\overline{\varphi}$	Time average of arbitrary function φ, page 20	
$\partial\hat{\Omega}$	Discretization of $\partial\Omega$, page 25	
$\partial\Omega$	Boundary of Ω, page 13	
$\partial\Omega_2$	Boundary of Ω_2, page 92	
$\partial\Omega_{\mathrm{in}}$	Inflow boundary, page 14	

$\partial\Omega_{\text{out}}$ Outflow boundary, page 14

$\partial\Omega_{\text{wall}}$ Wall, page 13

Ψ Ordering of $\mathcal{Q}$, page 31 $[-]$

ρ Fluid density, page 12 $[\text{kg}\,\text{m}^{-3}]$

$\rho^{(k)}$ Non-dimensional member of asymptotic expansion of ρ, page 64 $[-]$

ρ_0 Reference density, page 26 $[\text{kg}\,\text{m}^{-3}]$

ρ_a Non-dimensional density calculated from DDFs right after performing interpolated outflow BC, page 42 $[-]$

σ_X Standard deviation of $\boldsymbol{X}$, page 141

τ Non-dimensional relaxation time, page 30 $[-]$

τ_j Non-dimensional relaxation time, page 30 $[-]$

τ_w Wall shear stress, page 19 $[\text{kg}\,\text{m}^{-1}\,\text{s}^{-1}]$

τ_{BGK} Relaxation time in BGK collision operator, page 24 $[\text{s}]$

τ_{FP} Relaxation time in Fokker-Planck collision operator, page 24 $[\text{s}]$

Θ Thermodynamic temperature, page 12 $[\text{K}]$

$\tilde{\mathcal{E}}$ Turbulent dissipation, page 21 $[\text{m}^2\,\text{s}^{-3}]$

ε Non-dimensional asymptotic parameter, page 62 $[-]$

ε_1 Non-dimensional asymptotic parameter, page 64 $[-]$

ε_2 Non-dimensional asymptotic parameter, page 64 $[-]$

φ Arbitrary function, page 20

φ' Fluctuation from the time average $\overline{\varphi}$ of arbitrary function, page 21

$\varrho_{X,Y}$ Correlation between data $\boldsymbol{X}$ and $\boldsymbol{Y}$, page 141

ς_X Mean absolute deviation of $\boldsymbol{X}$, page 141

ϑ Parameter of Carreau-Yasuda model, page 17 $[\text{s}]$

$\boldsymbol{\xi}$ Microscopic velocity, page 22 $[\text{m}\,\text{s}^{-1}]$

$\boldsymbol{\xi_i}$ Non-dimensional discrete microscopic velocity, page 27 $[-]$

$\tilde{\nu}^\ell$ Non-dimensional kinematic viscosity on grid with level ℓ, page 54 $[-]$

$\widetilde{\Omega}$ Discrete lattice, page 26

$\widetilde{\phi}$ Non-dimensional quantity ϕ, page 26

$\widetilde{\boldsymbol{\kappa}}$ Vector of combinations of non-dimensional central moments, page 31 $[-]$

$\widetilde{\boldsymbol{\kappa}}^{(eq)}$	Non-dimensional attractro of $\widetilde{\boldsymbol{\kappa}}$, page 31	$[-]$

Latin letters

ℓ_K	Kolmogorov length, page 21	$[\mathrm{m}]$
ℓ_m	Mean free path, page 11	$[\mathrm{m}]$
Kn	Knudsen number, page 11	$[-]$
Ma	Mach number, page 10	$[-]$
$\mathbb{A}_f$, $\mathbb{A}_m$	Matrices for expressing unknown DDFs using known DDFs and raw moments, page 45	$[-]$
$\mathbb{D}$	Deformation-rate tensor, page 12	$[\mathrm{s}^{-1}]$
$\mathbb{F}$	Diagonal matrix with relaxation frequencies, page 31	$[-]$
$\mathbb{K}$	Transformation matrix to central moments, page 31	$[-]$
$\mathbb{M}$	Transformation matrix to raw moments, page 31	$[-]$
$\mathbb{S}$	Strain-rate tensor, page 12	$[\mathrm{s}^{-1}]$
$\mathbb{T}$	Stress tensor, page 12	$[\mathrm{kg\,m^{-1}\,s^{-2}}]$
$\mathbb{T}'$	Stress tensor of the turbulent apparent friction, page 21	$[\mathrm{kg\,m^{-1}\,s^{-2}}]$
$\mathbb{T}^\nu$	Viscous stress tensor, page 12	$[\mathrm{kg\,m^{-1}\,s^{-2}}]$
$\mathcal{A}$	Subset of $\mathbb{R}^3 \times \mathbb{R}^3$, page 139	
$\mathcal{C}$	Collision operator, page 24	$[\mathrm{kg\,m^{-6}\,s^2}]$
$\mathcal{C}_{\boldsymbol{i}}$	Non-dimensional discrete collision operator, page 27	$[-]$
$\mathcal{C}_{\mathrm{BGK}}$	BGK approximation of collision operator, page 24	$[\mathrm{kg\,m^{-6}\,s^2}]$
$\mathcal{C}_{\mathrm{FP}}$	Fokker-Planck approximation of collision operator, page 24	$[\mathrm{kg\,m^{-6}\,s^2}]$
$\mathcal{D}$	Diffusion tensor in Fokker-Planck collision operator, page 24	$[\mathrm{m^2\,s^{-2}}]$
$\mathcal{P}$	Probability, page 139	$[-]$
$\mathcal{Q}$	Discrete set of microscopic velocities, page 27	
$\mathcal{T}$	Time interval, page 12	
$\mathcal{V}$	Volume in $\mathbb{R}^3$, page 22	
$\mathbf{q}$	Hit rate metric, page 142	
$\overline{\boldsymbol{u}}$	Time average of velocity vector, page 21	$[\mathrm{m\,s^{-1}}]$
$\overline{p}$	Time average of pressure, page 21	$[\mathrm{kg\,m^{-1}\,s^{-2}}]$
Pr	Prandtl number, page 10	$[-]$

Re	Reynolds number, page 10	$[-]$
$\text{Re}_c^{(k)}$	Critical Reynolds number, $k \in \mathbb{N}$, page 10	$[-]$
Re_x	Reynolds number of flat plate, page 20	$[-]$
$\mathrm{d}p$	Pressure drop, page 15	$[\text{kg}\,\text{m}^{-1}\,\text{s}^{-2}]$
$\boldsymbol{G}$	Source term with non-Newtonian effects, page 114	$[\text{kg}\,\text{m}^{-2}\,\text{s}^{-2}]$
$\boldsymbol{g}$	Volume force acceleration, page 12	$[\text{m}\,\text{s}^{-2}]$
$\boldsymbol{i}$	Multi-index, page 27	
$\boldsymbol{n}$	Normal vector, page 13	
$\boldsymbol{P}$	Offset vector, page 25	$[\text{m}]$
$\boldsymbol{q}$	Heat flux, page 24	$[\text{kg}\,\text{s}^{-3}]$
$\boldsymbol{S_c}$	Center of cylinder, page 113	$[\text{m}]$
$\boldsymbol{u}$	Fluid velocity, page 12	$[\text{m}\,\text{s}^{-1}]$
$\boldsymbol{u}'$	Fluctuation from the time average $\overline{\boldsymbol{u}}$ of velocity vector, page 21	$[\text{m}\,\text{s}^{-1}]$
$\boldsymbol{u}^{(k)}$	Non-dimensional member of asymptotic expansion of $\boldsymbol{u}$, page 64	$[-]$
$\boldsymbol{u}_a$	Non-dimensional velocity calculated from DDFs right after performing interpolated outflow BC, page 42	$[-]$
$\boldsymbol{u}_{\text{an}}$	Analytical velocity solution, page 15	$[\text{m}\,\text{s}^{-1}]$
$\boldsymbol{u}_{\text{ini}}$	Initial velocity value, page 14	$[\text{m}\,\text{s}^{-1}]$
$\boldsymbol{u}_{\text{in}}$	Inflow velocity value, page 14	$[\text{m}\,\text{s}^{-1}]$
$\boldsymbol{X}, \boldsymbol{Y}$	Data sets, page 140	
$\boldsymbol{Z}_{\text{avg}}$	Average of data $\boldsymbol{X}$ and $\boldsymbol{Y}$, page 142	
$\boldsymbol{Z}_{\text{diff}}$	Difference between experimental and simulated data, page 117	
$\widetilde{\frac{\partial u_i}{\partial x_j}}$	Approximation of non-dimensional $\frac{\partial u_i}{\partial x_j}$ used in CuLBM2, page 35	$[-]$
$\widetilde{\boldsymbol{m}}$	Vector of combinations of non-dimensional raw moments, page 31	$[-]$
$\widetilde{\boldsymbol{m}}^{(eq)}$	Non-dimensional attractor of $\widetilde{\boldsymbol{m}}$, page 31	$[-]$
$\widetilde{\mathcal{T}}$	Discretization of time interval $\mathcal{T}$, page 26	
$\widetilde{M}$	Central moment generating function, page 140	
c	Non-dimensional lattice velocity, page 27	$[-]$
$C_{\boldsymbol{j}}^{\star}$	Non-dimensional post collision cumulant, page 34	$[-]$
$C_{(\alpha,\beta,\gamma)}^{(k)}$	Non-dimensional coefficient of asymptotic expansion of $C_{(\alpha,\beta,\gamma)}$, page 67	$[-]$

C_ϵ Constant of proportionality, page 62 $[\mathrm{m^2\,s^{-1}}]$

$C_{\boldsymbol{j}}$ Non-dimensional cumulant, page 32 $[-]$

$c_{\boldsymbol{j}}$ Non-dimensional cumulant, page 31 $[-]$

C_P Heat capacity at constant pressure, page 10 $[\mathrm{J\,kg^{-1}\,K^{-1}}]$

C_p Empirical coefficient of power law model, page 17 $[\mathrm{kg\,m^{-1}\,s^{-1}}]$

c_p Specific heat at constant pressure, page 12 $[\mathrm{m^2\,s^{-2}\,K^{-1}}]$

c_s Speed of sound, page 10 $[\mathrm{m\,s^{-1}}]$

c_v Specific heat at constant volume, page 12 $[\mathrm{m^2\,s^{-2}\,K^{-1}}]$

C_{99} Non-dimensional constant parameter, page 19 $[-]$

D Continuous Dirac delta function, page 32

e Specific energy, page 24 $[\mathrm{m^2\,s^{-2}}]$

f Density function, page 22 $[\mathrm{kg\,m^{-6}\,s^3}]$

$f_{\boldsymbol{i}}^{(0)}$ Non-dimensional constant part of DDF, page 59 $[-]$

$f^{(eq)}$ Equilibrium density function, page 24 $[\mathrm{kg\,m^{-6}\,s^3}]$

$f_{\boldsymbol{i}}^{(eq)}$ Non-dimensional discrete equilibrium density function, page 29 $[-]$

$f_{\boldsymbol{i}}^{(neq),\ell}$ Non-equilibrium part of DDF on grid with level ℓ, page 57 $[-]$

$F_{\boldsymbol{i}}$ Non-dimensional forcing term, page 37 $[-]$

$f_{\boldsymbol{i}}$ Non-dimensional discrete density function, page 27 $[-]$

$f_{\boldsymbol{i}}^{\star}$ Non-dimensional post-collision discrete density function, page 28 $[-]$

$f_{\boldsymbol{i}}^{(neq)}$ Non-equilibrium part of non-dimensional discrete density function, page 38 $[-]$

f_p Probability density function, page 139 $[-]$

G_N Number of grid levels, page 55 $[-]$

$h(t)$ Non-dimensional time-dependent scaling function, page 115 $[-]$

I_i Time interval, page 117

K Cumulant generating function, page 140

k Turbulent kinetic energy, page 21 $[\mathrm{m^2\,s^{-2}}]$

k_0 Parameter of Casson model, page 17 $[\mathrm{kg^2\,m^{-2}}]$

k_1 Parameter of Casson model, page 17 $[\mathrm{kg^2\,m^{-2}}]$

k_c Thermal conductivity, page 10 $[\mathrm{J\,m^{-1}\,s^{-1}\,K^{-1}}]$

L Characteristic length, page 10 $[\mathrm{m}]$

l	Length of plate, page 19	[m]
L_i	Dimension of Ω in x_i direction, $i \in \{1, 2, 3\}$, page 14	[m]
M	Raw moment generating function, page 139	
$m_{\boldsymbol{j}}^{(eq)}$	Non-dimensional equilibrium raw moment of discrete density function, page 30	[−]
$m_{(\alpha,\beta,\gamma)}^{(k)\,(eq)}$	Non-dimensional member of asymptotic expansion of $m_{(\alpha,\beta,\gamma)}^{(eq)}$, page 64	[−]
$m_{(\alpha,\beta,\gamma)}^{(k)}$	Non-dimensional member of asymptotic expansion of $m_{(\alpha,\beta,\gamma)}$, page 63	[−]
$m_{(\alpha,\beta,\gamma)}^{\star\,(k)}$	Non-dimensional member of asymptotic expansion of $m_{(\alpha,\beta,\gamma)}^{\star}$, page 63	[−]
$m_{\star}$	Selected non-dimensional raw moment in moment-based BC, page 44	[−]
$m_{\boldsymbol{j}}$	Non-dimensional raw moment of discrete density function, page 30	[−]
N_1, N_2, N_3	Number of grid nodes, page 25	[−]
N_t	Number of time steps, page 26	[−]
N_{ti}	Number of time steps used for time integration, page 116	[−]
P	Rescaled pressure, page 18	$[\mathrm{m^2\,s^{-2}}]$
p	Fluid pressure, page 12	$[\mathrm{kg\,m^{-1}\,s^{-2}}]$
p'	Fluctuation from the time average $\overline{p}$ of pressure, page 21	$[\mathrm{kg\,m^{-1}\,s^{-2}}]$
p_0	Non-dimensional reference pressure, page 28	[−]
p_{an}	Analytical pressure solution, page 15	$[\mathrm{kg\,m^{-1}\,s^{-2}}]$
p_{ini}	Initial pressure value, page 14	$[\mathrm{kg\,m^{-1}\,s^{-2}}]$
p_{out}	Outflow pressure value, page 14	$[\mathrm{kg\,m^{-1}\,s^{-2}}]$
q^+	Positive flux, page 116	$[\mathrm{m^3\,s^{-1}}]$
q^-	Negative flux, page 116	$[\mathrm{m^3\,s^{-1}}]$
R_s	Specific gas constant, page 12	$[\mathrm{m^2\,s^{-2}\,K^{-1}}]$
r_{in}	Radius of cylinder at inflow, page 113	[m]
r_{out}	Radius of cylinder at outflow, page 113	[m]
$S(x_1)$	Cross section of Ω at x_1, page 70	
T	Final time, page 12	[s]
t	Time, page 12	[s]
t_I	Time unit, page 17	[s]
t_K	Kolmogorov time, page 21	[s]

System of Notation

This chapter summarizes the used notation in this thesis. All vector quantities are printed using bold symbols. Matrices and tensors are printed using the **blackboard bold** style in math mode in LaTeX. Let $\varphi \subset \mathbb{R}$, $\boldsymbol{v} \subset \mathbb{R}^3$ and $\mathbb{C} \subset \mathbb{R}^3 \times \mathbb{R}^3$ be an arbitrary scalar, vector, and tensor quantity, respectively. The i-th component of vector $\boldsymbol{v}$ is labeled by v_i, $i \in \{1, 2, 3\}$. Similarly, the i, j-th component of tensor $\mathbb{C}$ is labeled by $\mathbb{C}_{i,j}$, $i, j \in \{1, 2, 3\}$. The differential operator ∇ is represented by a vector of spatial partial derivatives $\left(\frac{\partial}{\partial x_1}, \frac{\partial}{\partial x_2}, \frac{\partial}{\partial x_3} \right)^T$.

In this thesis, the following notation for scalar, vector, and tensor quantities is used:

- **Gradient of scalar:**
$$(\nabla \varphi)_i = \frac{\partial \varphi}{\partial x_i}, \ i \in \{1, 2, 3\},$$

- **Laplacian of scalar:**
$$\Delta \varphi = \sum_{i=1}^{3} \frac{\partial^2 \varphi}{\partial x_i^2},$$

- **Vector norm:**
$$\|\boldsymbol{v}\| = \sqrt{\sum_{i=1}^{3} (v_i)^2},$$

- **Scalar product between vectors:**
$$\boldsymbol{v} \cdot \boldsymbol{w} = \prod_{i=1}^{3} v_i w_i, \ \boldsymbol{w} \subset \mathbb{R}^3,$$

- **Gradient of vector:**
$$(\nabla \boldsymbol{v})_{i,j} = \frac{\partial v_i}{\partial x_j} \ i, j \in \{1, 2, 3\},$$

- **Divergence of vector:**
$$\nabla \cdot \boldsymbol{v} = \sum_{i=1}^{3} \frac{\partial v_i}{\partial x_i},$$

- **Laplacian of vector:**
$$(\Delta \boldsymbol{v})_i = \sum_{j=1}^{3} \frac{\partial^2 v_i}{\partial x_j^2}, \ i \in \{1, 2, 3\},$$

- **Outer product:**
$$(\boldsymbol{v} \otimes \boldsymbol{w})_{i,j} = v_i w_j, \ \boldsymbol{w} \subset \mathbb{R}^3, \ i,j \in \{1,2,3\}$$

- **Divergence of tensor:**
$$(\nabla \cdot \mathbb{C})_i = \sum_{j=1}^{3} \frac{\partial \mathbb{C}_{j,i}}{\partial x_j}, \ i \in \{1,2,3\},$$

- **Double-dot product:**
$$\mathbb{C} : \mathbb{D} = \sum_{i,j=1}^{3} \mathbb{C}_{i,j} \mathbb{D}_{i,j}, \ \mathbb{D} \subset \mathbb{R}^3 \times \mathbb{R}^3.$$

Next, the following operators are used in this thesis:

- **Derivative with respect to vector $\boldsymbol{v}$:**
$$\frac{\partial}{\partial \boldsymbol{v}} = \boldsymbol{v} \cdot \nabla,$$

- **Material derivative:**
$$\frac{D}{Dt} = \frac{\partial}{\partial t} + \boldsymbol{u} \cdot \nabla,$$

where $\boldsymbol{u}$ is the fluid velocity.

Finally, several types of norms are used in this thesis. Let $\varphi = \varphi(x)$ and $\boldsymbol{v} = \boldsymbol{v}(x)$ are scalar and vector fields, respectively, defined in a discrete set $\widehat{\Omega}$ and let $\Gamma \subset \mathbb{R}^3$. Then, the following norms are used:

- **L_1 norm over $\widehat{\Omega}$:**
$$\|\varphi\|_{\mathrm{L}_1} = \sum_{\boldsymbol{x} \in \widehat{\Omega}} |\varphi(\boldsymbol{x})|, \quad \|\boldsymbol{v}\|_{\mathrm{L}_1} = \sum_{\boldsymbol{x} \in \widehat{\Omega}} \left(\sum_{i=1}^{3} |v_i(\boldsymbol{x})| \right).$$

- **L_1 norm over $\Gamma \subset \mathbb{R}^3$:**
$$\|\varphi\|_{\mathrm{L}_1,\Gamma} = \sum_{\boldsymbol{x} \in \Gamma \cap \widehat{\Omega}} |\varphi(\boldsymbol{x})|, \quad \|\boldsymbol{v}\|_{\mathrm{L}_1,\Gamma} = \sum_{\boldsymbol{x} \in \Gamma \cap \widehat{\Omega}} \left(\sum_{i=1}^{3} |v_i(\boldsymbol{x})| \right),$$

- **L_2 norm over $\widehat{\Omega}$:**
$$\|\varphi\|_{\mathrm{L}_2} = \left(\sum_{\boldsymbol{x} \in \widehat{\Omega}} (\varphi(\boldsymbol{x}))^2 \right)^{\frac{1}{2}}, \quad \|\boldsymbol{v}\|_{\mathrm{L}_2} = \left(\sum_{\boldsymbol{x} \in \widehat{\Omega}} \left(\sum_{i=1}^{3} (v_i(\boldsymbol{x}))^2 \right) \right)^{\frac{1}{2}},$$

- **L_2 norm over $\Gamma \subset \mathbb{R}^3$:**
$$\|\varphi\|_{\mathrm{L}_2,\Gamma} = \left(\sum_{\boldsymbol{x} \in \Gamma \cap \widehat{\Omega}} (\varphi(\boldsymbol{x}))^2 \right)^{\frac{1}{2}}, \quad \|\boldsymbol{v}\|_{\mathrm{L}_2,\Gamma} = \left(\sum_{\boldsymbol{x} \in \Gamma \cap \widehat{\Omega}} \left(\sum_{i=1}^{3} (v_i(\boldsymbol{x}))^2 \right) \right)^{\frac{1}{2}}.$$

Introduction 1

The main topic of this thesis are the numerical simulations of fluid dynamics (referred to as computational fluid dynamics (CFD)), which are one of the most intensively investigated problems of numerical mathematics. Problems of fluid dynamics are often encountered in practice, for example, in the automotive or aerospace industry when determining aerodynamics, in the energy industry, in medicine when investigating the hemodynamics in vessels, and in many other fields. The advantages of numerical simulations include lower financial costs compared to physical experiments, time savings, and adaptability to particular problems. CFD includes several numerical methods to simulate fluid dynamics. To the conventional CFD methods belong, for example, the finite difference method (FDM) [128], the finite volume method (FVM) [182], and the finite element method (FEM) [21].

The FDM approximates continuous partial differential equation (PDE) using finite differences on a discrete grid. The advantage of the FDM is its simplicity. The main drawbacks include the additional numerical diffusion caused by the approximation of the advection term [118]. Contrary to the FDM, the FVM is based on the volume approach. It divides the investigated domain into volumes of different shapes and sizes. The structure of the final discrete PDEs is often similar to the structure of discretized equations of the FDM. However, the FVM is easily adapted to irregular grids. In contrast to the FDM and FVM, the FEM method works with the weak form of the given PDEs. The whole investigated domain is discretized using small parts that are called finite elements. The main advantage of the FEM is the developed mathematical theory of existence and uniqueness of discrete solutions. Next, it is suitable for unstructured grids, which discretize complex geometries. The main disadvantage of the FEM is its complexity and computational demands.

Contrary to these numerical methods, the CFD includes additional methods such as boundary-element method [151], spectral methods [24], or particle based mesoscopic methods [118]. The main objective of this work is the numerical lattice Boltzmann method (LBM) that uses mesoscopic description of the fluid. In contrast to the FDM, FVM, and FEM, the LBM usually uses a uniform grid for numerical simulations and the discrete scheme is usually constructed in a "down-to-top" manner. That is, a discrete scheme is designed first and the target PDEs with numerical errors are found using a backward analysis.

In this thesis, the LBM is studied using two approaches. First, the theoretical analysis of the LBM is performed. Using the asymptotic analysis, the LBM is investigated and the associated PDEs are recovered. Moreover, the asymptotic analysis allows to express useful approximations of velocity derivatives that can be calculated locally, that is, unlike the FDM, no information from neighboring lattice sites is needed. Furthermore, numerical experiments are performed to investigate the quality of the numerical solution obtained by the LBM. In these experiments, the effect of boundary condition (BC) approximations on the numerical solution is investigated and

two novel BCs are proposed.

Three real-world application problems are used for the validation of the LBM. The first problem studies a turbulent air flow in the boundary layer above a rough surface and is motivated by the collaboration with the Institute of Thermomechanics of the Czech Academy of Sciences. The second problem is inspired by the research project investigating biomass combustion in a fluidized bed boiler. Within this problem, the air flow through a perforated plate in the combustion chamber is studied and the numerical solution of the pressure drop across the plate is compared with the experimental data measured at the Faculty of Mechanical Engineering, CTU in Prague. For the last problem, the inspiration comes from the collaboration with the Institute for Clinical and Experimental Medicine in Prague and the problem deals with the non-Newtonian fluid flow through arterial valves with different degree of stenosis . The fluid flow simulations are compared with experimental data acquired using magnetic resonance imaging (MRI). The experimental data are used for the validation of several viscosity models and the simulations are then used to point out the imperfections of MRI.

1.1   State of the art

In this thesis, we focus on the numerical simulations of an incompressible, viscous fluid flow in an isothermal domain using the LBM. The LBM was proposed for numerical simulations of fluid dynamics in 1988 by McNamara and Zanetti in [137]. Since the first approach in 1988, the LBM has evolved rapidly, as illustrated in Figure 1.1. In the last five years, more than 5000 articles were published with the keyword "lattice Boltzmann method". The reason for this development is its ability to simulate various fluid flow problems and still huge amount of open problems. Up to now, the LBM has been used, for example, for the numerical solution of the Navier-Stokes equations [88, 118], heat transport equation [162, 189], advection-diffusion equation [72, 101], phase-field equation [39, 56, 73], shallow water equation [38, 133, 180], multiphase flow equations [27, 100, 183, 192], Poisson equation [28, 138], etc.
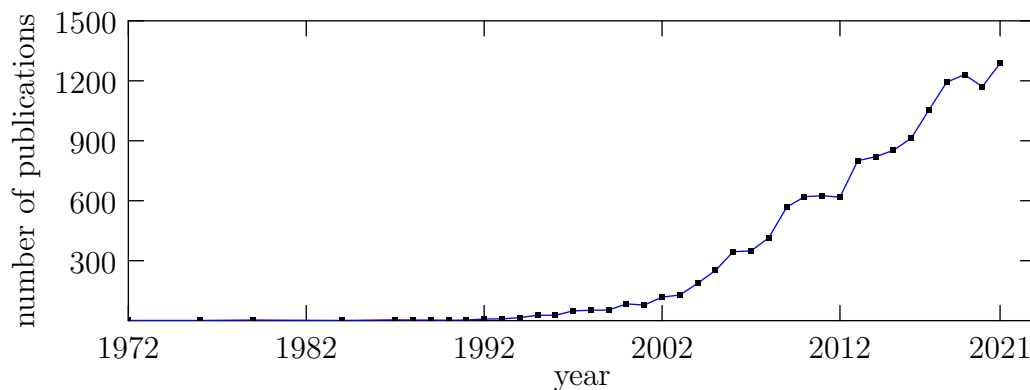
Figure 1.1: Number of publications with the keyword "lattice Boltzmann method" based on the Scopus database [160].

The LBM is well suited for the parallel implementation, especially on GPUs [145], and therefore, the interest in the LBM has increased with the development of hardware performance. So far, several LBM-based software for fluid flow simulations enabling parallel run emerged [57, 97, 116, 126]. In this work, we use a custom, in-house LBM implementation that is being developed at the Department of Mathematics, FNSPE CTU in Prague, which enables parallel execution on distributed systems equipped with GPUs. The author of this thesis is one of the founders and main developers of the in-house code.

1.2 Research goals

The main objective of this work is to investigate the capabilities of the LBM for fluid flow simulations. Due to the extensiveness of the investigation, this main topic is divided into several tasks comprising various aspects of the problem. The following objectives of this work are pursued:

- To formulate the mathematical model describing the evolution of the incompressible, single-phase, viscous fluid in an isothermal domain.

- To propose a variant of the LBM suitable for particular CFD problems.

- To suggest and implement mesoscopic BCs. The newly derived BCs can be assessed using a comparison with commonly used mesoscopic BCs.

- To investigate the ability of the LBM to directly numerically simulate the turbulent fluid flow in the boundary layer above rough surface.

- To improve and implement a parallel variant of the LBM with a grid refinement technique. The LBM with a grid refinement can be tested on the turbulent boundary layer problem.

- To choose and implement an appropriate non-Newtonian model of viscosity to the existing numerical LBM code and validate it using a comparison with experimental data acquired by MRI measurement.

1.3 Content of this thesis

The thesis is organized as follows.

- In Chapter 1, an introduction to the theory and the state of the art are summarized.

- In Chapter 2, the theoretical background is presented. It comprises a formulation of the mathematical model of incompressible, viscous fluid flow, a summary of viscosity models for non-Newtonian fluids, and an introduction to the kinetic and boundary layer theory.

- In Chapter 3, the LBM is described. It consists of basics of the LBM and the overview of collision operators, BCs, and grid refinement techniques used in this thesis.

- In Chapter 4, asymptotic analysis of the LBM with cumulant collision operator is performed. The output of the analysis is the incompressible Navier-Stokes equations actually solved by the LBM and formulas for the local approximation of the velocity derivatives.

- In Chapter 5, the mesoscopic BCs are assessed within the laminar fluid flow problem.

- In Chapter 6, the ability of the LBM to numerically solve the turbulent boundary layer flow is investigated. First, the LBM and FDM numerical solutions are compared. Next, the grid refinement technique for the LBM is tested. Finally, the LBM solution of a turbulent street canyon flow is compared with the experimental measurement and results of the FDM.

- In Chapter 7, the turbulent fluid flow in the combustion chamber of the fluidized bed boiler is numerically solved using the LBM. The LBM solution is compared with experimental data and numerical results obtained by the FVM.

- In Chapter 8, the non-Newtonian fluid flow simulations in an aortic vessel are presented. The LBM results are compared with experimental MRI measurements and the necessity of using a non-Newtonian model for sufficiently accurate numerical simulations is assessed.

- In Chapter 9, the thesis is concluded, achieved results are summarized, and the future work is devised.

1.4   Achieved results

- We derived moment-based BCs for the D3Q27 velocity model used in the LBM. Next, we modified the interpolated BCs to achieve better numerical accuracy of the pressure at the outflow boundary. These newly derived BCs were tested by comparison with other commonly used BCs. We found that the suggested BCs provided the smallest numerical error compared to the other BCs tested. These findings are summarized in [51].

- We validated the LBM for direct numerical simulations of turbulent boundary layer flow above a rough surface. The computed results were in a good agreement with the experimental data and the numerical simulations using the FDM. This validation is summarized in [50].

- We investigated possible techniques for the interpolation of discrete density functions between numerical grids with different resolutions. A simplified model of the LBM with a grid refinement technique has been implemented in parallel using MPI and CUDA and tested on the problem of turbulent boundary layer flow above rough surface. The results show a good agreement with the LBM results using a uniform grid.

- On the basis of the experimental pressure measurement in the combustion chamber, we compared the numerical LBM pressure solution with experimental data. Moreover, the LBM was compared with the FVM implemented in the ANSYS Fluent software package [3]. We found that the LBM produces results comparable to the experimental data. Furthermore, LBM simulations are less computationally expensive than FVM simulations. These findings are collected in [9].

- Motivated by the collaboration with the Institute of Clinical and Experimental Medicine in Prague, we implemented a model for non-Newtonian fluids into the code developed at the Department of Mathematics, FNSPE CTU in Prague. Next, a series of numerical simulations were performed in the approximate geometry of the arterial vessel with stenotic valve. Numerical results were compared with experimental data and the influence of the non-Newtonian model used was assessed. The results of Newtonian models with constant kinematic viscosity are comparable to experiments and can be regarded as suitable for further use. These findings are summarized in [52].

1.5   Author's contribution in journal papers

The author's contribution to the aforementioned publications in impacted journals and books related to this thesis is listed below:

Related to doctoral thesis

- Eichler, P., Fuka, V., and Fučík, R. (2021). Cumulant lattice Boltzmann simulations of turbulent flow above rough surfaces. *Computers & Mathematics with Applications (IF 3.218)*, 92:37-47, [50].

  ▷ Pavel Eichler was the leading author, he prepared and performed all LBM simulations. He wrote the main body of the paper and processed the results.

- Beneš, M., Eichler, P., Fučík, R., Hrdlička, J., Klinkovský, J., Kolář, M., Smejkal, T., Skopec, P., Solovský, J., Strachota, P., Straka, R., Žák, A. (2022). Experimental and numerical investigation of air flow through the distributor plate in a laboratory-scale model of a bubbling fluidized bed boiler. *Japan Journal of Industrial and Applied Mathematics (IF 0.681)*, 1-16, [9].

  ▷ Pavel Eichler was the co-author, he prepared and performed all LBM and FVM simulations. He processed the results and collaborated on the preparation of the main body of the paper.

- Fučík, R., Galabov, R., Pauš, P., Eichler, P., Klinkovský, J., Straka, R., Tintěra, J., Chabiniok, R. (2020). Investigation of phase-contrast magnetic resonance imaging underestimation of turbulent flow through the aortic valve phantom: Experimental and computational study using lattice Boltzmann method. *Magnetic Resonance Materials in Physics, Biology and Medicine (IF 2.671)*. 33.5: 649-662, [71].

  ▷ Pavel Eichler was the co-author. He contributed to the preparation of the article by running simulations on a local HPC cluster and collaborated on the preparation of the main body of the paper.

- Eichler, P., Fučík, R., Straka, R. (2021). Computational study of immersed boundary - lattice Boltzmann method for fluid-structure interaction. *Discrete & Continuous Dynamical Systems-S (IF 1.622)*, 14.3: 819, [49].

  ▷ Pavel Eichler was the leading author, he prepared and performed all simulations. He wrote the main body of the paper and processed the results.

- Fučík, R., Eichler, P., Straka, R., Pauš, P., Klinkovský, J., Oberhuber, T. (2019). On optimal node spacing for immersed boundary–lattice Boltzmann method in 2D and 3D. *Computers & Mathematics with Applications (IF 3.218)*, 77.4: 1144-1162, [68].

  ▷ Pavel Eichler was the co-author. He contributed to the preparation of the article by running simulations and collaborated on the preparation of the main body of the paper.

- Fučík, R., Eichler, P., Klinkovský, J., Straka, R., Oberhuber, T. (2022). Lattice Boltzmann Method Analysis Tool (LBMAT). *Numerical algorithms (IF 2.502)*, 1-17, [67]

  ▷ Pavel Eichler was the co-author. He contributed to the preparation of simulations and collaborated on the preparation of the main body of the paper.

- Eichler, P., Galabov, R., Fučík, R., Škardová, K., Oberhuber, T., Pauš, P., Tintěra, J., Chabiniok, R. Non-Newtonian turbulent flow through aortic phantom: Experimental and computational study using magnetic resonance imaging and lattice Boltzmann method. *Under review in Computers & Mathematics with Applications (IF 3.218)*, [52].

  ▷ Pavel Eichler was the leading author, he prepared and performed all LBM simulations.
    He wrote the main body of the paper and processed the results.

- Eichler, P., Fučík, R., Strachota, P. Investigation of mesoscopic boundary conditions
  for lattice Boltzmann method in laminar flow problems. *Under review in Computers &
  Mathematics with Applications (IF 3.218)*, [51].

  ▷ Pavel Eichler was the leading author, he prepared and performed all LBM simulations.
    He wrote the main body of the paper and processed the results.

- Chabiniok, R., Škardová, K., Galabov, R., Eichler, P., Gusseva, M., Janoušek, J., Fučík, R.,
  Tintěra, J., Oberhuber, T., Hussain, T. Translational Cardiovascular Modeling: Tetralogy
  of Fallot and Modeling of Diseases. In: Modeling Biomaterials. Birkhäuser, Cham, 2021.
  p. 241-276, [26].

  ▷ Pavel Eichler was the co-author. He wrote a part of this book chapter summarizing
    the large-vessel flow modeling.

Other papers

- Beneš, M., Eichler, P., Klinkovský, J., Kolář, M., Solovský, J., Strachota, P., Žák, A. (2021).
  Numerical simulation of fluidization for application in oxyfuel combustion. *Discrete and
  Continuous Dynamical Systems-S (IF 1.622)*, 14(3), 769-783, [10].

  ▷ Pavel Eichler was the co-author. He contributed to the preparation of the article by
    running simulations and collaborated on the preparation of the main body of the
    paper.

- Beneš, M., Eichler, P., Hrdlička, J., Klinkovský, J., Kolář, M., Smejkal, T., Skopec, P.,
  Solovský, J., Strachota, P., Žák, A. (2022). Experimental Validation of Multiphase Particle-
  in-Cell Simulations of Fluidization in a Bubbling Fluidized Bed Combustor. *Powder
  Technology (IF 5.165)*, 416, 118204, [9].

  ▷ Pavel Eichler was the co-author. He contributed to the preparation of the main body
    of the paper.

1.6   Future work

Beyond the presented thesis and the achieved results, there remain several challenging tasks that
need to be further explored. These include:

- To investigate the proposed moment-based BCs on the problems of the turbulent flow.
  Currently, the moments are defined by their equilibrium. Thus, a better, physically
  consistent interpretation of higher-order moments needs to be derived and analyzed.
  Furthermore, the current implementation of these BCs in the in-house code is not efficient.
  Thus, the efficiency of the implementation also needs to be improved.

- To further investigate the numerical errors of the LBM pressure solution by comparing
  it with the numerical solution of the Poisson's equation. For the comparison, real-world
  application problem, such as the fluid flow in a combustion chamber of a fluidized bed
  boiler, can be used. Next, the influence of the compressibility on the LBM solution should
  be analyzed.

- To improve the efficiency of the parallel code of the LBM with the grid refinement technique. Next, a more general configuration of the refinement will be implemented using a sophisticated grid structure and optimized for the parallel execution on GPUs.

Theoretical Background 2

This chapter summarizes basic concepts and phenomena studied in this thesis. First, the basic physical concepts are introduced and the Navier-Stokes equations are discussed. It is followed by an introduction to laminar and turbulent boundary layer theory. Finally, an introduction to the kinetic theory is presented.

2.1 Basic concepts

The main objective of this thesis is the fluid flow. *Fluid* can be characterized as a material that continuously deforms under applied shear stress. The deformation process is then called *flow*. Since the fluid flow is one of the most prominent physical phenomena in the world, it has always been studied intensively. The fluid flow can be seen at different scales. We can start with the atmospheric jet stream (airflow at an altitude of 9-16 km above the surface with a typical speed of 100 km/h) and end with the capillary flow in the subsurface.

The modern description of the fluid flow began in the 18th century in connection with the development of mathematics. Among the founders of modern descriptions of the fluid flow are Isaac Newton (1642–1727), Leonhard Euler (1707-1783), Gabriel Stokes (1819-1903), Jean-Baptiste Joseph Fourier (1768-1830), Claude-Louis Navier (1785-1836), Osborne Reynolds (1842-1912), Ludwig Prandtl (1875-1953), and others [157, 188].

L. Euler introduced the theory of inviscid fluids, which is now called the Euler theory after him. This theory is applicable to an *ideal fluid*, i.e., inviscid, incompressible fluid (labeled as the Euler fluid). The advantage of such Euler fluid is that the theory was mathematically highly developed and the agreement with experimental results was observed for low viscosity fluids such as air or water. On the other hand, this theory has several weaknesses. One of them is called the *d'Alembert's paradox* stating that the drag force acting on the body moving with constant velocity in the Euler fluid is zero. This is contrary to actual observations and is consistent with the fact that Euler's equations assume only normal forces acting on the body [157].

To improve this disagreement, the concept of a real fluid was introduced, which adds the effect of tangential forces, i.e. shear stress, to the governing equations. The shear stress is proportional to the change in velocity components parallel to the surface in the normal direction (Newton's law of friction). The constant of proportionality is called the fluid viscosity. Thus, these fluids are called viscous fluids. On the basis of viscosity, fluids are called Newtonian, i.e., the viscosity is constant in space and time, and non-Newtonian, i.e., the relationship between shear stress and change in velocity is nonlinear.

Next, the concept of mechanical similarity was introduced to classify the fluid flow. The fluid flow is called *mechanically similar*, if and only if the obstacles have geometrically similar boundaries and the flow has similar streamline portraits [157]. Two fluids will be mechanically

similar if the forces acting on the body are in a similar ratio. These forces are the *friction forces* and *inertial forces*, and their ratio $^{\text{inertial forces}}/_{\text{friction forces}}$ is proportional to the Reynolds number.

Definition 2.1 (Reynolds number)
Reynolds number Re $[-]$ expresses the mechanical similarity and is defined by

$$\text{Re} = \frac{VL}{\nu}, \tag{2.1}$$

where V $[\text{m s}^{-1}]$ is the characteristic velocity, L $[\text{m}]$ is the characteristic length, and ν $[\text{m}^2\,\text{s}^{-1}]$ is the kinematic viscosity of the fluid [188].

The flow field can be further characterized, for example, by the following numbers:

Definition 2.2 (Mach number)
Mach number Ma $[-]$ expresses the velocity flow regime (subsonic vs. supersonic flow) and is defined by

$$\text{Ma} = \frac{V}{c_s}, \tag{2.2}$$

where c_s $[\text{m s}^{-1}]$ is the speed of sound [188].

Definition 2.3 (Prandtl number)
Prandtl number Pr $[-]$ expresses the relation between momentum and thermal diffusion and is defined by

$$\text{Pr} = \frac{C_P\,\mu}{k_c}, \tag{2.3}$$

where C_P $[\text{J kg}^{-1}\,\text{K}^{-1}]$ is the heat capacity at constant pressure, μ $[\text{kg m}^{-1}\,\text{s}^{-1}]$ is the dynamic viscosity, and k_c $[\text{J m}^{-1}\,\text{s}^{-1}\,\text{K}^{-1}]$ is the thermal conductivity [188].

Based on the value of Re, the flow can be categorized into three groups: laminar flow, transitional flow, and turbulent flow. The laminar flow occurs at small Re. The laminar flow can be characterized as a layered flow, that is, a flow perpendicular to the flow direction is negligible. A typical example of a laminar flow can be the slow flow of water from a tap. As Re increases, more complicated flow structures emerge. This can be illustrated using the problem of the fluid flow around a circular cylinder, see Figure 2.1. Figure 2.1a represents the laminar flow around the circular cylinder. The streamlines are represented by straight lines without vortices. Then, Figures 2.1b, 2.1c represent two regimes of the transition flow. Finally, Figure 2.1d represents a fully developed turbulent flow consisting of a chaotic fluctuating motion [157].

The turbulent flow occurs for high Re. Such flow consists of a highly irregular random fluctuating motion and can often be found in complex devices, such as combustion chambers or engines. Next, the air flow behind vehicles is also often highly turbulent. Since the turbulent flow is more complex than the laminar flow, its description remains a big challenge in the science dealing with the fluid flow.

The transition from a simple laminar flow to a more complex flow is characterized by critical Reynolds numbers $\text{Re}_c^{(k)}$, $k \in \mathbb{N}$. Values can be found by experimental investigation or using the mathematical method called *stability analysis*, which adds perturbation to the laminar solution. The solution is called *unstable*, if and only if the added perturbations disappear in time. The results of stability theory are illustrated in Figure 2.2, where the black line represents the stable solution (stable in the sense of time evolution) and the red lines represent the "disappearing perturbations" [157].

(a) Creeping flow, i.e., laminar flow around cylinder, Re ≈ 0.

(b) Onset of Kármán vortex flow. Flow field is laminar, small vortexes occur, Re < 100.

(c) Full Kármán vortex flow. The velocity and pressure field creates Kármán vortex street, Re < 300.

(d) Supercritical regime. Full turbulent flow, Re > 10^6.
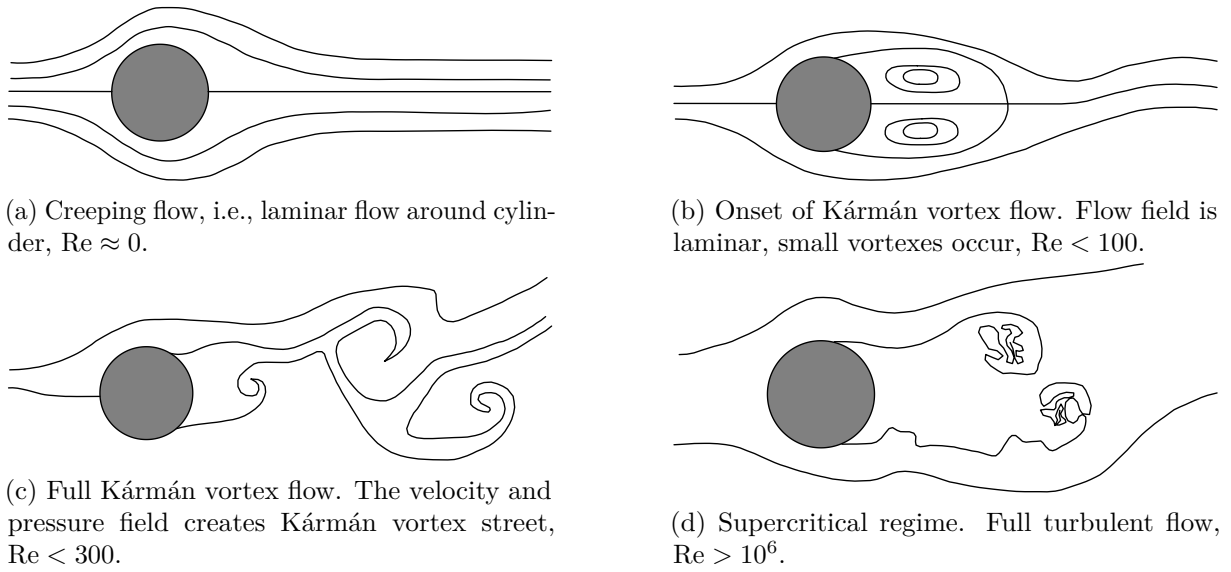
Figure 2.1: Streamlines of the fluid flow around cylinder for different values of Re.
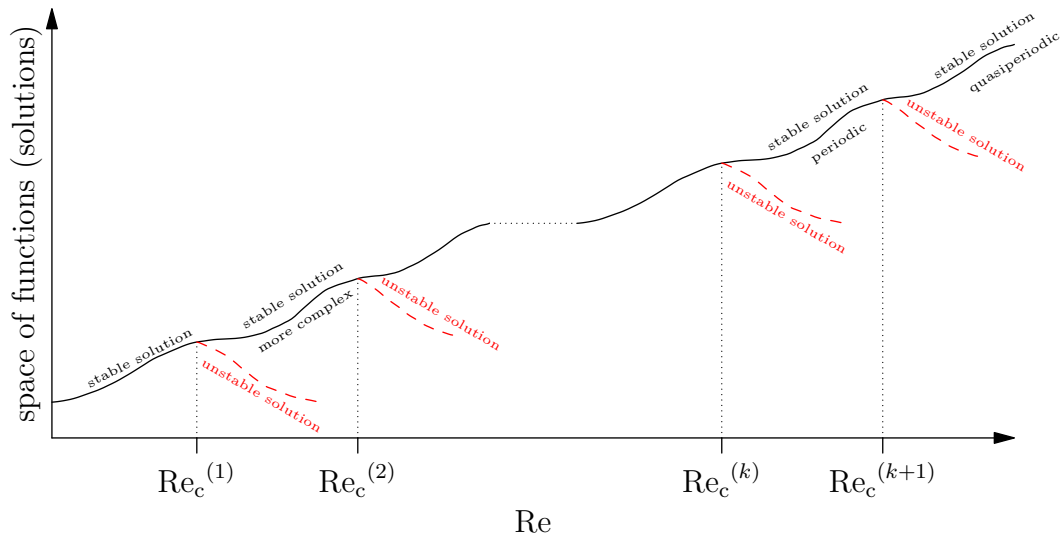
Figure 2.2: Schematic illustration of the fluid flow solution based on the value of Re. Critical Reynolds numbers $\text{Re}_c^{(\cdot)}$ characterize changes in the complexity of the solution. On the basis of experimental observations, the real fluid flow follows the black line. The red lines represent the results of the stability theory, where the perturbations do not occur in the time evolution.

2.2 Navier-Stokes equations

The fluid flow is considered in the isothermal domain $\Omega \subset \mathbb{R}^3$ without heat sources. To describe the evolution of the fluid by macroscopic equations, the fluid is treated as a continuum, that is, there are no gaps in Ω without fluid. However, not all fluids satisfy this assumption. Restrictions on fluids can be expressed using the Knudsen number Kn [−].

Definition 2.4 (Knudsen number)
Knudsen number Kn expresses the ratio between the mean free path ℓ_m [m] (of molecules or

atoms that make up the fluid) and the representative physical length scale L by

$$\text{Kn} = \frac{\ell_m}{L}. \tag{2.4}$$

If $\text{Kn} \ll 1$, the system can be considered as a continuum [118].

The evolution of fluids with $\text{Kn} \ll 1$ in Ω and within time interval $\mathcal{T} = (0, T)$, T [s], can be described by the Navier-Stokes equations as

$$\frac{\partial \rho}{\partial t} + \nabla \cdot (\rho \, \boldsymbol{u}) = 0, \tag{2.5a}$$

$$\frac{\partial (\rho \, \boldsymbol{u})}{\partial t} + \nabla \cdot (\rho \, \boldsymbol{u} \otimes \boldsymbol{u}) = \nabla \cdot \mathbb{T} + \rho \, \boldsymbol{g}, \tag{2.5b}$$

where t [s] is time, ρ [kg m^{-3}] is the fluid density, $\boldsymbol{u}$ [m s^{-1}] is the macroscopic velocity (with components u_i, $i \in \{1, 2, 3\}$), $\mathbb{T}$ [kg m^{-1} s^{-2}] is the stress tensor (with components $\mathbb{T}_{i,j}$, $i, j \in \{1, 2, 3\}$), $\boldsymbol{g}$ [m s^{-2}] is the volume force acceleration vector (with components g_i, $i \in \{1, 2, 3\}$). The stress tensor satisfies

$$\mathbb{T} = -p\mathbb{I} + \mathbb{T}^{\nu}, \tag{2.6}$$

where $\mathbb{I}$ is the unit tensor, p [kg m^{-1} s^{-2}] is the fluid pressure, and, under the assumption of Newtonian fluid, the entries of viscous stress tensor $\mathbb{T}^{\nu}$ reads

$$\mathbb{T}_{i,i}^{\nu} = \lambda \, \nabla \cdot \boldsymbol{u} + 2\mu \, \frac{\partial u_i}{\partial x_i}, \quad i \in \{1, 2, 3\}, \tag{2.7a}$$

$$\mathbb{T}_{i,j}^{\nu} = \mathbb{T}_{j,i}^{\nu} = \mu \left(\frac{\partial u_i}{\partial x_j} + \frac{\partial u_j}{\partial x_i} \right), \quad i \neq j, \ i, j \in \{1, 2, 3\}, \tag{2.7b}$$

where μ [kg m^{-1} s^{-1}] is the dynamic viscosity and λ [kg m^{-1} s^{-1}] is the second viscous coefficient [118]. The viscous stress tensor can be equivalently formulated as

$$\mathbb{T}^{\nu} = 2\mu \mathbb{S} + \lambda (\nabla \cdot \boldsymbol{u}) \mathbb{I} = 2\mu \mathbb{D} + \left(\lambda + \frac{2}{3}\mu \right) (\nabla \cdot \boldsymbol{u}) \mathbb{I}, \tag{2.8}$$

where $\mathbb{S}$ is the strain-rate tensor and $\mathbb{D}$ (called the *deformation-rate tensor*) is $\mathbb{S}$ without its diagonal, i.e.,

$$\mathbb{D} = \frac{1}{2} \left[\nabla \boldsymbol{u} + (\nabla \boldsymbol{u})^T \right]. \tag{2.9}$$

The system of Eqs. (2.5) is closed by an equation of state [118]. For the ideal gas, the equation of state is considered in the form

$$p = R_s \Theta \rho, \tag{2.10}$$

where Θ [K] is the thermodynamic temperature, R_s [m^2 s^{-2} K^{-1}] is the specific gas constant, and

$$R_s = c_p - c_v, \tag{2.11}$$

where c_p [m^2 s^{-2} K^{-1}] is the specific heat at constant pressure and c_v [m^2 s^{-2} K^{-1}] is the specific heat at constant volume [118]. It should be noted that Eqs. (2.5) hold under the following assumptions:

1. The fluid is a continuum.

2. The stress tensor is symmetric.

3. The fluid is isotropic.

4. The fluid can be described by the equation of state for ideal gases.

Next, Eqs. (2.5) must be supplemented by proper initial and boundary conditions (BCs).

The aforementioned equations are further simplified using the assumption of fluid incompressibility, that is, the material derivative of the fluid density ρ is zero [157]

$$\frac{D\rho}{Dt} = \frac{\partial \rho}{\partial t} + \boldsymbol{u} \cdot \nabla \rho = 0. \tag{2.12}$$

Using Eq. (2.5a), the assumption of incompressibility in Eq. (2.12) can be expressed as

$$\nabla \cdot \boldsymbol{u} = 0, \tag{2.13}$$

i.e., the fluid is divergence-free (also called *solenoidal*). Using condition (2.13), Eq. (2.5b) can be written as

$$\rho \frac{D\boldsymbol{u}}{Dt} = -\nabla p + \mu \Delta \boldsymbol{u} + \rho \boldsymbol{g}, \tag{2.14}$$

where

$$\frac{D\boldsymbol{u}}{Dt} = \frac{\partial \boldsymbol{u}}{\partial t} + \boldsymbol{u} \cdot \nabla \boldsymbol{u}.$$

Finally, the equation of state for the incompressible, Newtonian fluid in the isothermal domain Ω is considered in the form of

$$p = c_s^2 \rho, \tag{2.15}$$

[118].

2.2.1   Boundary and initial conditions

The equations for the incompressible fluid hold in Ω. Thus, the conditions on the boundary $\partial \Omega$ must be specified based on the physical type of the boundary.

Wall:
The walls represent the interface between the fluid domain and the solid object. In this thesis, only solid objects with impermeable boundaries are considered. The solid boundary is labeled by $\partial \Omega_{\text{wall}}$. The BC considered for the wall is the "no-slip" BC, which prescribes zero velocity at $\partial \Omega_{\text{wall}}$. The BC for pressure p can be derived as follows. Let us assume the normal vector of the wall $\boldsymbol{n} = (0, 1, 0)^T$. Eq.(2.14) multiplied by the normal vector $\boldsymbol{n}$ is

$$\frac{\partial u_2}{\partial t} + (\boldsymbol{u} \cdot \nabla) u_2 = -\frac{1}{\rho} \frac{\partial p}{\partial x_2} + \nu \Delta u_2.$$

Since $\boldsymbol{u} = \boldsymbol{0}$, the left-hand side is zero, thus

$$\frac{1}{\rho} \frac{\partial p}{\partial x_2} = \nu \frac{\partial^2 u_2}{\partial x_2^2}.$$

Because the fluid flow in the normal direction to the wall is often negligible, the pressure condition is usually considered as [157]

$$\frac{\partial p}{\partial \boldsymbol{n}} \approx 0, \tag{2.16}$$

where $\frac{\partial}{\partial \boldsymbol{n}} = \boldsymbol{n} \cdot \nabla$.

Inlet:
The inlet condition is prescribed at the boundary where the fluid enters Ω. The boundary with the prescribed inlet condition is labeled by $\partial\Omega_{\text{in}}$. It is common to specify the inlet velocity $\boldsymbol{u}_{\text{in}}$. The BC for the pressure can be derived as above, i.e., Eq. (2.14) is multiplied by the normal vector to the boundary and the particular values of $\boldsymbol{u}_{\text{in}}$ are used to derive the pressure BC.

Outlet:
The outlet condition is prescribed at the boundary where the fluid leaves Ω and is labeled by $\partial\Omega_{\text{out}}$. Contrary to the inlet condition, the Dirichlet BC for pressure p_{out} is used. There are several ways of solving the velocity at the outlet. One possible option is the *transparent boundary condition* that, for the boundary $\partial\Omega_{\text{out}}$ with inward normal vector $\boldsymbol{n} = (1, 0, 0)^T$, is given by [130]

$$\frac{\partial u_1}{\partial t} + u_1 \frac{\partial u_1}{\partial x_1} = 0, \ u_2 = u_3 = 0. \tag{2.17}$$

Initial condition:
At the initial time $t = 0$ s, the initial velocity $\boldsymbol{u}_{\text{ini}}$ [m s^{-1}] and pressure p_{ini} [kg m^{-1} s^{-2}] are prescribed in Ω.

2.2.2 Summary

The equations describing the evolution of Newtonian, incompressible fluid in isothermal domain Ω can be summarized as:

$$\nabla \cdot \boldsymbol{u} = 0 \qquad\qquad\qquad \text{in } \Omega \times \mathcal{T}, \tag{2.18a}$$

$$\rho \frac{D\boldsymbol{u}}{Dt} = -\nabla p + \mu \Delta \boldsymbol{u} + \rho \boldsymbol{g} \qquad \text{in } \Omega \times \mathcal{T}, \tag{2.18b}$$

$$\boldsymbol{u} = \boldsymbol{u}_{\text{ini}}, \ p = p_{\text{ini}} \qquad\qquad \text{in } \Omega \times \{0\}, \tag{2.18c}$$

$$\boldsymbol{u} = \boldsymbol{u}_{\text{in}}, \ \frac{\partial p}{\partial \boldsymbol{n}} = \nu \Delta (\boldsymbol{n} \cdot \boldsymbol{u}) \qquad \text{on } \partial\Omega_{in} \times \mathcal{T}, \tag{2.18d}$$

$$\boldsymbol{u} = \boldsymbol{0}, \ \frac{\partial p}{\partial \boldsymbol{n}} = 0 \qquad\qquad \text{on } \partial\Omega_{\text{wall}} \times \mathcal{T}, \tag{2.18e}$$

$$\frac{\partial u_1}{\partial t} + u_1 \frac{\partial u_1}{\partial x_1} = 0, \ u_2 = u_3 = 0, \ p = p_{\text{out}} \ \text{ on } \partial\Omega_{out} \times \mathcal{T}. \tag{2.18f}$$

2.2.3 Analytical solution of Navier-Stokes equations

For some particular formulations, Eqs. (2.18) have analytical solution. In this thesis, the following two problems with analytical solution in a cuboidal domain $\Omega = (0, L_1) \times (0, L_2) \times (0, L_3)$ are considered, where L_i [m], $i = 1, 2, 3$ are the dimensions of Ω.

Hagen-Poiseuille flow

The Hagen-Poiseuille flow problem [6] solves the laminar fluid flow between two parallel plates as illustrated in Figure 2.3. In the x_3-direction, the periodic boundary conditions are prescribed.

The flow is induced by the constant pressure drop across the domain in the x_1-direction and the analytical solution of velocity is in the form $\boldsymbol{u}_{\mathrm{an}} = (u_{1,\mathrm{an}}, 0, 0)^T$, where

$$u_{1,\mathrm{an}}(\boldsymbol{x}) = U_{\max}\left(1 - \left(\frac{2x_2 - L_2}{L_2}\right)^2\right), \tag{2.19}$$

where $U_{\max}$ [m s^{-1}] is the maximal velocity. The inflow velocity condition $\boldsymbol{u}_{\mathrm{in}} = \boldsymbol{u}_{\mathrm{an}}$.

Accordingly, the analytical solution for pressure p_{an} [kg m^{-1} s^{-2}] is a linear function in the x_1-direction (and constant in the x_2- and x_3-directions) in the form

$$p_{\mathrm{an}}(\boldsymbol{x}) = p_{\mathrm{out}} - \rho\nu U_{\max}\frac{8}{L_2^2}(x_1 - L_1), \tag{2.20}$$

where p_{out} is the pressure value set at the outflow.
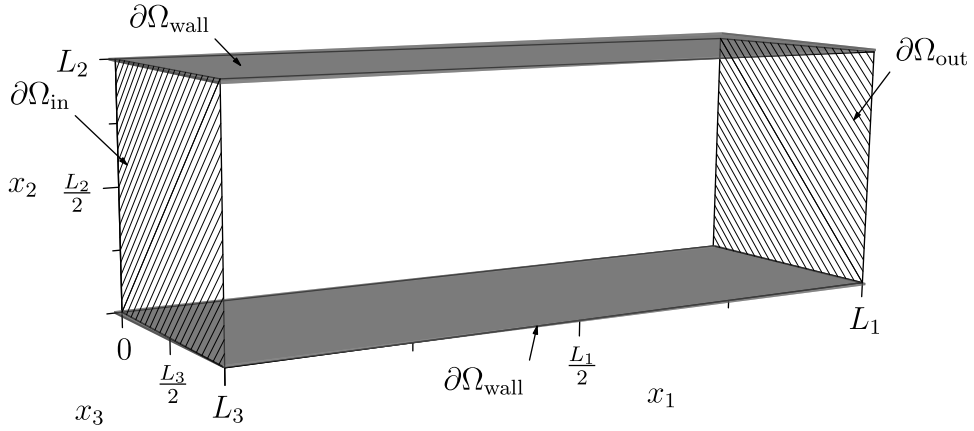
Figure 2.3: Computational domain Ω of the Hagen-Poiseuille flow. The gray planes represent impermeable walls.

Rectangular duct flow

Another fluid flow problem with the analytical solution is the rectangular duct flow. The flow is assumed in the domain Ω illustrated in Figure 2.4 and is induced by the pressure drop dp [kg m^{-1} s^{-2}] across the domain in the x_1-direction. Based on [191], the analytical solution $\boldsymbol{u}_{\mathrm{an}}$ of Eqs.(2.18) is in the form $\boldsymbol{u}_{\mathrm{an}} = (u_{1,\mathrm{an}}, 0, 0)^T$, where

$$u_{1,\mathrm{an}}(\boldsymbol{x}) = -\frac{1}{\rho\nu}\mathrm{d}p\frac{16L_2^2}{4\pi^3}\sum_{i=0}^{+\infty}\frac{(-1)^i}{(2i+1)^3}\left(1 - \frac{\cosh\left[\frac{(2i+1)\pi}{L_2}\left(x_3 - \frac{L_3}{2}\right)\right]}{\cosh\left[(2i+1)\pi\frac{L_3}{2L_2}\right]}\right)\cos\left(\frac{(2i+1)\pi\left(x_2 - \frac{L_2}{2}\right)}{L_2}\right). \tag{2.21}$$

The maximal velocity, attained for $x_2 = \frac{L_2}{2}$ and $x_3 = \frac{L_3}{2}$, is given by

$$U_{\max} = -\frac{1}{\rho\nu}\mathrm{d}p\frac{16L_2^2}{4\pi^3}\sum_{i=0}^{+\infty}\frac{(-1)^i}{(2i+1)^3}\left(1 - \frac{1}{\cosh\left[(2i+1)\pi\frac{L_3}{2L_2}\right]}\right). \tag{2.22}$$

At the inflow $\partial\Omega_{\mathrm{in}}$, the velocity boundary condition satisfies $\boldsymbol{u}_{\mathrm{in}} = \boldsymbol{u}_{\mathrm{an}}$.

The analytical solution for pressure p_{an} is a linear function in the x_1-direction (and constant in the x_2- and x_3-directions) in the form

$$p_{\mathrm{an}}(\boldsymbol{x}) = p_{\mathrm{out}} - \mathrm{d}p(x_1 - L_1), \tag{2.23}$$

where p_{out} is the pressure value set at the outflow.
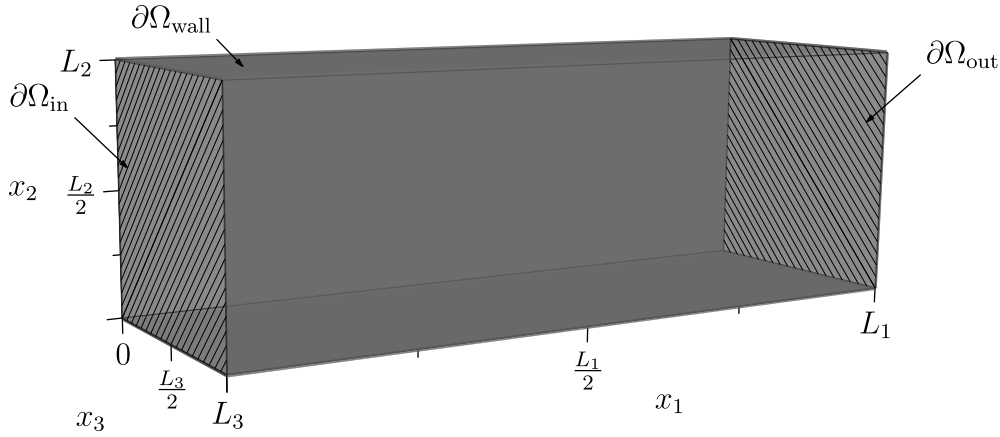
Figure 2.4: Computational domain Ω of the rectangular duct flow. The gray planes represent impermeable walls.

2.3 Non-Newtonian fluids

In the previous section, Newtonian fluids were considered, that is, fluids with a linear relation between the shear stress and the velocity gradient. Fluids with a non-linear relation between shear stress and the velocity gradient are called non-Newtonian fluids. The non-Newtonian fluids can be classified according to several properties, for example, as follows:

Classification

- **Generalized Newtonian Fluid:**
  The fluid dynamic viscosity depends on the shear rate $\dot{\gamma}$ [s^{-1}] defined by [113]

$$\dot{\gamma} = \sqrt{2\mathbb{D} : \mathbb{D}}. \tag{2.24}$$

  These fluids have neither memory nor elasticity. On the basis of the relation between shear rate and viscosity, generalized Newtonian fluids can be further classified as

  - *Pseudoplastic fluid*:
    The dynamic viscosity decreases as the shear rate increases.
  - *Dilatant fluid*:
    The dynamic viscosity increases with applied shear stress.

  Typical examples are drilling fluids, sand in water, granular materials, margarine, toothpaste, some paints, some polymer melts, or fresh concrete.

- **Viscoelastic Fluid:**
  The stress in the fluid depends on both the strain and strain rate. It is typical that stress depends on the history of deformation [102]. A typical example of such fluid is, for instance, vulcanized rubber.

- **Time dependent viscosity:**
  The shear stress depends on temperature and shear rate $\dot{\gamma}$. Based on the dependence of shear stress on time, these fluids are further classified as

  - *Thixotropic fluid:*
    The shear stress decreases at constant shear rate. Typical examples are grease, printing ink, margarine, etc.

      – *Rheopectic fluid:*
        The shear stress increases at a constant shear rate. These fluids are also called antithixotropic fluids. A typical example is gypsum paste.

Hemodynamics

In this thesis, the motivation for the non-Newtonian fluid flow modeling is the blood dynamics in vessels. Since blood behaves as a generalized Newtonian fluid [175], only models for these fluids are introduced. The most commonly used constitutive models for fluid viscosity are as follows.

1. Power Law Model: [113]

$$\mu_{\mathrm{PL}}\left(\dot{\gamma}\right) = C_p \left(t_I \dot{\gamma}\right)^{n-1}, \tag{2.25a}$$

    where C_p [kg m^{-1} s^{-1}] $\in \mathbb{R}$ and n [$-$] $\in \mathbb{R}$ are empirical parameters and $t_I = 1$ s is the time unit.

2. Spriggs Model: [164]

$$\mu_{\mathrm{SP}}\left(\dot{\gamma}\right) = \mu_0 \ \text{ for } \ \dot{\gamma} \leq \dot{\gamma}_0, \ \text{ else } \ \mu\left(\dot{\gamma}\right) = \mu_0 \left(\frac{\dot{\gamma}}{\dot{\gamma}_0}\right)^{n-1}, \tag{2.25b}$$

    where μ_0 [kg m^{-1} s^{-1}] is the dynamic viscosity at the reference shear rate $\dot{\gamma}_0$ [s^{-1}].

3. Carreau-Yasuda Model: [20]

$$\mu_{\mathrm{CY}}\left(\dot{\gamma}\right) = \mu_\infty + \left(\mu_0 - \mu_\infty\right)\left[1 - \left(\vartheta\,\dot{\gamma}\right)^a\right]^{\frac{n-1}{a}}, \tag{2.25c}$$

    where μ_0 [kg m^{-1} s^{-1}] is the dynamic viscosity at zero shear rate, μ_∞ [kg m^{-1} s^{-1}] is the dynamic viscosity at infinite shear rate, and ϑ [s] $\in \mathbb{R}$, a [$-$] $\in \mathbb{R}$, n [$-$] $\in \mathbb{R}$ are empirical parameters.

4. Cross Model: [91]

$$\mu_{\mathrm{CR}}\left(\dot{\gamma}\right) = \frac{\mu_0 - \mu_\infty}{1 + \left(k\dot{\gamma}\right)^n} + \mu_\infty, \tag{2.25d}$$

    where μ_0 [kg m^{-1} s^{-1}] is the dynamic viscosity at zero shear rate, μ_∞ [kg m^{-1} s^{-1}] is the dynamic viscosity at infinite shear rate, and n [$-$] $\in \mathbb{R}$ and k [s] are empirical parameters.

5. Casson Model: [20]

$$\mu_{\mathrm{CA}}\left(\dot{\gamma}\right) = \frac{1}{\dot{\gamma}}\left[k_0 + k_1 \sqrt{t_I \dot{\gamma}}\right]^2, \tag{2.25e}$$

    where k_0 [kg^2 m^{-2}] and k_1 [kg^2 m^{-2}] are empirical parameters. $t_I = 1$ s is the time unit.

    All models listed in this section have several applicability restrictions and are often valid only for finite intervals of $\dot{\gamma}$. The usage of these non-Newtonian models will be further discussed in Chapter 8.

2.4 Boundary layer theory

In this section, the concept of the Boundary layer theory is introduced. Eq. (2.18b) can be rewritten as

$$\frac{D\boldsymbol{u}}{Dt} = -\nabla P + \nu \Delta \boldsymbol{u} + \boldsymbol{g}, \tag{2.26}$$

where $P = p/\rho$ [$\mathrm{m^2\,s^{-2}}$] is the rescaled pressure. Scaling by the characteristic length L and characteristic velocity V, Eq. (2.26) is given in a non-dimensional form as

$$\frac{L}{V^2}\frac{D\boldsymbol{u}}{Dt} = -\frac{L}{V^2}\nabla P + \frac{1}{\mathrm{Re}}\frac{L^2}{V}\Delta \boldsymbol{u} + \frac{L}{V^2}\boldsymbol{g}. \tag{2.27}$$

In Eq. (2.27), the term before $\frac{L^2}{V}\Delta \boldsymbol{u}$ is $1/\mathrm{Re}$. As Re increases, the influence of the term $\frac{L^2}{V}\Delta \boldsymbol{u}$ decreases and, therefore, it is common to neglect this term for high Reynolds number flows. Thus, Eq. (2.27) can be reduced to

$$\frac{D\boldsymbol{u}}{Dt} = -\nabla P + \boldsymbol{g}. \tag{2.28}$$

Eqs. (2.18a) and (2.28) are called the Euler equations for an incompressible fluid.

Due to the absence of $\Delta \boldsymbol{u}$, the mathematical theory of Euler equations has a firm background contrary to the incompressible Navier-Stokes equations [157]. In many situations, the solution of the Euler equations agrees well with experimental observations, since ideal fluids such as air or water have very small kinematic viscosity (on the order of 10^{-5} $\mathrm{m^2\,s^{-1}}$). However, since no tangential forces exist in the Euler equations (only normal forces are included), the no-slip BC cannot be satisfied at the wall. This causes a problem in many engineering applications, such as those investigating the applied drag force on the body by the fluid.

The fluid flow near the solid body is investigated by the Boundary layer theory introduced in 1904 by L. Prandtl. It is an asymptotic method and investigates situations when $\mathrm{Re} \to +\infty$, that is, when the friction forces can be neglected. The main concept of the Boundary layer theory is that the fluid domain can be distinguished into two unequally large regions:

- **Bulk flow**:
  A region far from solid boundaries where the friction forces (viscosity of the fluid) can be neglected. The fluid can be described by the Euler equations.

- **Boundary layer**:
  A region close to the wall where the friction forces play a dominant role. This region is characterized by its height δ [m], which describes the distance from the wall.

Next, based on Re, the Boundary layer theory can be divided into laminar and turbulent boundary layer theory.

2.4.1 Laminar boundary layer

The laminar boundary layer investigates the near-wall fluid flow for a low Reynolds number flow. A typical example of laminar boundary layer is the fluid flow around the plate at zero incidence illustrated in Figure 2.5. Figure 2.5 shows that with an increasing distance x [m] from the plate edge, the height of the boundary layer δ also increases. The value of δ can be approximated as [157]

$$\delta \approx \sqrt{\frac{\nu x}{U_\infty}}, \tag{2.29}$$

where U_∞ [m s^{-1}] is the maximal velocity in the bulk flow region. Since the transition between the boundary layer and the outer flow region is not sharp, the parameter δ_{99} is used to characterize the height of the boundary layer. δ_{99} is defined by the height above the wall, where the fluid velocity reaches 99% of U_∞ and can estimated by

$$\delta_{99} = C_{99}\sqrt{\frac{\nu x}{U_\infty}}, \tag{2.30}$$

where C_{99} [$-$] is the constant determined experimentally. For the flat plate at zero incidence $C_{99} = 5$ [157].
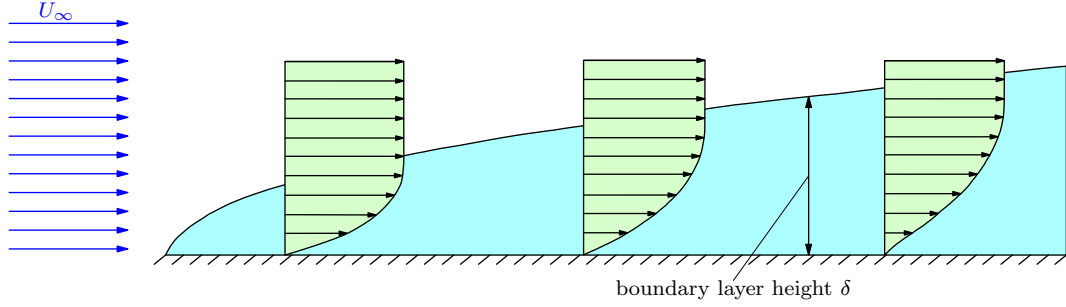
Figure 2.5: Illustration of the laminar boundary layer structure above plate.

Let us now define the Reynolds number for the flat plate by

$$\mathrm{Re} = \frac{U_\infty l}{\nu},$$

where l [m] is the length of the flat plate. The definition of δ_{99} in Eq. (2.30) can be written as

$$\delta_{99} = \frac{C_{99}}{\sqrt{\mathrm{Re}}}\sqrt{x\,l}. \tag{2.31}$$

Thus, as Re increases, δ decreases, that is, the region, where the solution of the Euler equations is applicable, increases.

For a flat plate with normal vector $(0, 1, 0)^T$, the wall shear stress τ_w [kg m^{-1} s^{-1}] is given by [157]

$$\tau_w = \mu\frac{\partial u_1}{\partial x_2}. \tag{2.32}$$

Thus, τ_w can be approximated using the FDM as

$$\tau_w \approx \mu\frac{U_\infty}{\delta} \tag{2.33}$$

and as δ increases, τ_w (and the drag coefficient of the body) decreases. An interesting point at the flat plate is the point, where the wall shear stress vanishes, that is, where $\tau_w = 0$. This point is called the *separation point*. Beyond this point, backflow occurs, and the boundary layer disconnects from the surface boundary [157].

2.4.2   Turbulent boundary layer

In the turbulent fluid flow, more complex flow structures are created in contrast to the laminar flow. Pressure and velocity are not constant in space and time due to irregular fluctuations.

The evolution of the turbulent boundary layer is illustrated in Figure 2.6 on the problem of the fluid flow over a flat plate at zero incidence. At the beginning, a laminar boundary layer

starts to evolve. The flow between the laminar and turbulent regions consists of transition phenomena.

Contrary to the laminar boundary layer, the turbulent boundary layer has a four-layer character as illustrated in Figure 2.6. The outer layer, called the *turbulent layer*, covers the flow where the *apparent friction* caused by the turbulence dominates the friction forces. The region close to the wall is called the *viscous sublayer*, where the viscous forces play a dominant role and the velocity profile of the mean velocity is almost laminar. The last two layers are called the *buffer layer* and the *overlap layer*, where the viscous forces still play a significant role. The difference between these two layers is mainly in the logarithmic profile of the averaged velocity.
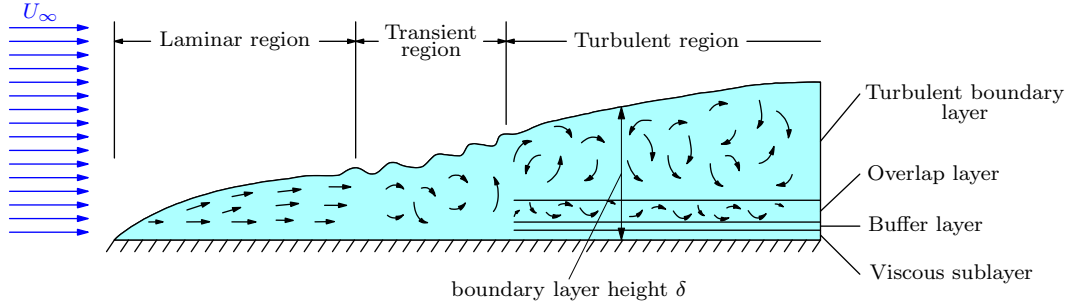
Figure 2.6: Illustration of the turbulent boundary layer structure above the plate.

In contrast to the laminar boundary layer, the height δ_ν [m] of the viscous sublayer is also investigated in the turbulent boundary layer. If we denote the plate Reynolds number by

$$\mathrm{Re}_x = \frac{x U_\infty}{\nu}, \tag{2.34}$$

then the relation between δ and δ_ν can be approximated as

$$\frac{\delta_\nu}{\delta} \approx 680 \frac{\ln^2 \mathrm{Re}_x}{\mathrm{Re}_x}, \tag{2.35}$$

which implies that $\delta_\nu \ll \delta$ for $\mathrm{Re}_x > 10^5$. This behaviour is crucial for numerical simulations because a very fine computational mesh is needed to capture the processes in the viscous sublayer for highly turbulent flow regimes.

2.5   Reynolds decomposition and turbulent scales

The turbulent fluid flow is composed of unsteady motion and vortex structures called *eddies*. Since there is no steady-state in the velocity and pressure fields, Reynolds decomposition is introduced to study the flow.

Denoting the time average over the time interval (t_1, t_2) for the quantity φ by

$$\overline{\varphi}\left(\boldsymbol{x}\right) = \frac{1}{t_2 - t_1} \int_{t_1}^{t_2} \varphi\left(\boldsymbol{x}, t\right) \mathrm{d}t, \tag{2.36}$$

the Reynolds decomposition is introduced as

$$\varphi = \overline{\varphi} + \varphi', \tag{2.37}$$

where φ' represents the fluctuation from the time average $\overline{\varphi}$. In the case of the incompressible fluid flow, the aforementioned decomposition is used for all velocity components and pressure, i.e.,

$$u_i = \overline{u_i} + u_i', \quad i \in \{1, 2, 3\}, \tag{2.38a}$$

$$p = \overline{p} + p'. \tag{2.38b}$$

Substituting Eqs. (2.38) into the governing equations for the incompressible fluid flow (2.18), we obtain [157]

$$\nabla \cdot \overline{\boldsymbol{u}} = 0, \tag{2.39a}$$

$$\nabla \cdot \boldsymbol{u}' = 0, \tag{2.39b}$$

$$\rho \sum_{j=1}^{3} \overline{u}_j \frac{\partial \overline{u}_i}{\partial x_j} = -\frac{\partial \overline{p}}{\partial x_i} + \mu \Delta \overline{u}_i - \rho \sum_{j=1}^{3} \frac{\partial \overline{u_i' u_j'}}{\partial x_j} + \rho g_i, \quad i \in \{1, 2, 3\}. \tag{2.39c}$$

Thus, Eqs. (2.39) are in a similar form as the incompressible equations in (2.18). However, an extra term emerges in the right-hand-side of Eq. (2.39c). This term represents partial derivatives of components of $\mathbb{T}'$ $[\text{kg}\,\text{m}^{-1}\,\text{s}^{-2}]$ called the *stress tensor of the turbulent apparent friction*. From the boundary layer theory, the viscosity plays a role in the viscous sublayer only. As a result, apparent stresses $-\rho\overline{u_i' u_j'}$ dominate above the viscous stresses, and represents another characteristic quantity in the turbulent boundary layer flow.

To further quantify the turbulent fluid flow, the *turbulent kinetic energy k* $[\text{m}^2\,\text{s}^{-2}]$ [157] is introduced by

$$k = \frac{1}{2}\overline{\left((u_1')^2 + (u_2')^2 + (u_3')^2\right)}. \tag{2.40}$$

From the balance equation for the turbulent kinetic energy k, the *turbulent dissipation $\tilde{\mathcal{E}}$* $[\text{m}^2\,\text{s}^{-3}]$ [157] is introduced by

$$\tilde{\mathcal{E}} = \nu \sum_{i=1}^{3} \sum_{j=1}^{3} \overline{\left(\frac{\partial u_i'}{\partial x_j} + \frac{\partial u_j'}{\partial x_i}\right)^2} \tag{2.41}$$

and represents the energy loss due to turbulent motion.

According to [114], the locally isotropic turbulence is determined by the kinematic viscosity ν and turbulent dissipation $\tilde{\mathcal{E}}$. Based on the these parameters, *Kolmogorov length scale ℓ_K* [m] and *Kolmogorov time scale t_K* [s] are defined by

$$\ell_K = \left(\frac{\nu^3}{\tilde{\mathcal{E}}}\right)^{\frac{1}{4}}, \tag{2.42a}$$

$$t_K = \left(\frac{\nu}{\tilde{\mathcal{E}}}\right)^{\frac{1}{2}}. \tag{2.42b}$$

These scales (2.42) represent the smallest scales of the fine turbulent structures in the flow [157].

The solution of the fluid flow in the boundary layer is often based on the boundary layer equations. These equations are a simplified version of the Navier-Stokes equations (2.18) under special assumptions. For the turbulent fluid flow, the system of the boundary layer equations is often not closed and some turbulence models must be added, such as the k-ϵ or k-ω turbulence model [157]. In this thesis, the flow field in the boundary layer is solved without any simplification used, i.e., the original Navier-Stokes equations given by Eqs. (2.18) are solved directly.

To solve the Navier-Stokes equations directly, however, the computational resolution of the mesh must be below the Kolmogorov length scale ℓ_K. These simulations are called direct

numerical simulations (DNS). Since $\ell_K \ll 1$, DNS are very memory- and time-consuming numerical methods. Thus, there are several methods that can reduce the restriction on the mesh dimension. One of such methods is the *large-eddy simulation method* (LES) which is based on the spatial filtering of the governing equations [157].

Remark 2.5 (Steady and unsteady turbulent flow)
The introduced Reynolds decomposition is based on the assumption that the time average does not depend on the time, that is, there exists a sufficiently large time interval (t_1, t_2) over which the time average is constant in time. Then, the flow is called the *steady turbulent flow*. The flow for which the time average is not constant for any time interval is called *unsteady turbulent flow*. For this flow, a similar decomposition can be introduced as described in [157]. In this thesis, only steady turbulent flow is considered.

Remark 2.6 (Wall friction velocity)
Another quantity used for the characterization of the turbulent flow is the wall friction velocity u_τ $[\mathrm{m\,s^{-1}}]$ defined by

$$u_\tau = \sqrt{\frac{\overline{\tau_w}}{\rho}}, \tag{2.43}$$

where $\overline{\tau}_w$ $[\mathrm{kg\,m^{-1}\,s^{-2}}]$ is the time-averaged wall shear stress [157].

2.6   Kinetic theory of fluids

The fluid description can be based on several scales. The Navier-Stokes equations mentioned in Section 2.2 are based on the macroscopic scale. On this scale, the fluid is described as a continuum, and macroscopic quantities, such as the fluid density, fluid velocity, pressure, etc., are used for the description of the current state.

Another possible description of the fluid is based on the microscopic scale [172], where the dynamics of individual atoms or molecules is based on Newton's law of motion. The advantage of this description is the simplicity of the motion law. On the other hand, the biggest disadvantage lies in the number of particles for which the dynamics must be solved. Since the number of particles forming the fluid is proportional to the Avogadro's constant (approx. 10^{23}), it is beyond the current computational abilities to simulate the entire dynamics of 10^{23} atoms.

Between macroscopic and microscopic, there is an intermediate scale called the *mesoscopic scale* illustrated in Figure 2.7. This scale is based on the Kinetic theory [8] developed by Ludwig Eduard Boltzmann (1844-1906). The fluid is described by an one-particle density function (PDF) f $[\mathrm{kg\,m^{-6}\,s^3}]$, which describes the system in the phase space, i.e., the space of the positions $\boldsymbol{x}$ and microscopic velocities $\boldsymbol{\xi}$ of individual particles. PDF gives us the density of particles with position $(\boldsymbol{x}, \boldsymbol{\xi})$ in the phase space at time t. Next, if we take the volume $\mathcal{V} \subset \mathbb{R}^3$ as illustrated in Figure 2.8, then the integral

$$\int_{\mathcal{V}} \mathrm{d}\boldsymbol{x} \int_{\mathbb{R}^3} \mathrm{d}\boldsymbol{\xi}\, f(\boldsymbol{x}, \boldsymbol{\xi}, t) \tag{2.44}$$

gives us the total mass at time t of all particles contained in volume $\mathcal{V}$ with all possible velocities [131].

One of the advantages of the mesoscopic description is that it works with microscopic velocity $\boldsymbol{\xi}$ that does not depend on position $\boldsymbol{x}$ and time t, contrary to macroscopic velocity $\boldsymbol{u}$. Thus, the particle with the position $(\boldsymbol{x}, \boldsymbol{\xi})$ in the phase space moves to position $\boldsymbol{x} + dt\,\boldsymbol{\xi}$ over time dt. On the other hand, the material point in the macroscopic description with position $\boldsymbol{x}$ and velocity $\boldsymbol{u}(\boldsymbol{x}, t)$ moves to position $\boldsymbol{x} + dt\,\boldsymbol{u}(\boldsymbol{x}, t)$. Thus, the advection on the mesoscopic scale is linear,
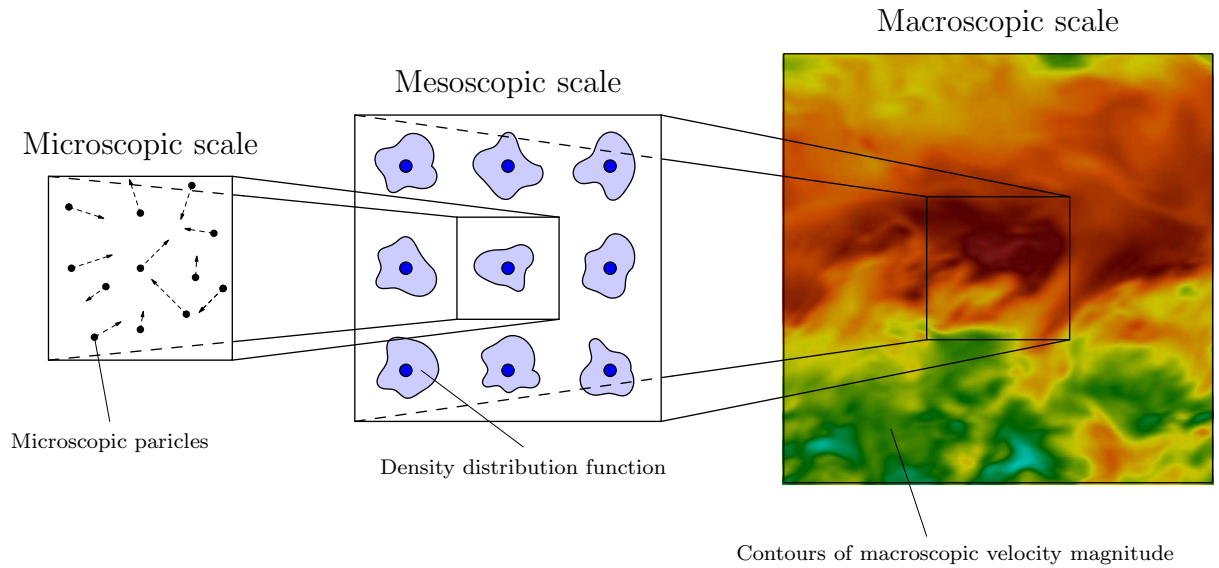
Figure 2.7: Illustration of the fluid description with respect to different scales.
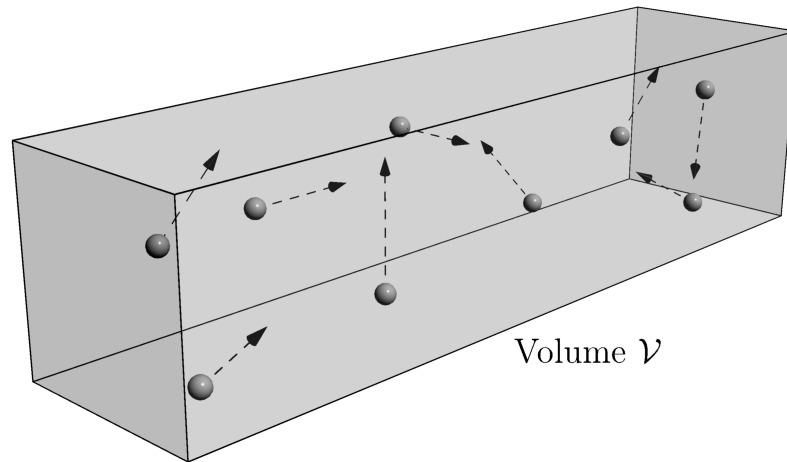
Figure 2.8: Schematic illustration of the volume with particles in the phase space. The dashed vectors represent the velocities of the particles.

but on the macroscopic scale, it is generally nonlinear as the velocity $\boldsymbol{u}\left(\boldsymbol{x}, t\right)$ can be a highly non-linear function, especially in the turbulent flow regime.

Next, in the macroscopic description, the diffusion is represented by the term $\nu \Delta \boldsymbol{u}$ that is obviously non-local. On the mesoscale, the diffusion is the result of particle collisions. Particle collisions are processes that shift the particles to the local equilibrium defined by the equilibrium PDF. Since the interactions between particles occur within short distances of colliding particles, it is possible to consider this process as a local process. Macroscopic diffusion appears to be caused by particle collisions [167]. Thus, the "diffusion" on the mesoscopic scale (collision) is a local process. These two observations represent the biggest advantages of the mesoscopic approach.

The changes of the PDF f in the phase space can be described by the Boltzmann transport equation

$$\frac{\partial f}{\partial t} + \sum_{i=1}^{3} \xi_i \frac{\partial f}{\partial x_i} + \sum_{i=1}^{3} g_i \frac{\partial f}{\partial \xi_i} = \mathcal{C}\left(f\right), \tag{2.45}$$

where $\boldsymbol{\xi} = \left(\xi_1, \xi_2, \xi_3\right)^T$ is the microscopic velocity, $\boldsymbol{g} = \left(g_1, g_2, g_3\right)^T$ is the acceleration of the

volume forces, and $\mathcal{C}$ [kg m^{-6} s^2] is the collision operator. Eq. (2.45) is an integro-differential equation, since the collision operator $\mathcal{C}$ is given in an integral form [117].

Based on PDF, some macroscopic quantities can be calculated as statistical moments:

$$\rho(\boldsymbol{x}, t) = \int\limits_{\mathbb{R}^3} \mathrm{d}\boldsymbol{\xi}\, f(\boldsymbol{x}, \boldsymbol{\xi}, t)\,, \tag{2.46}$$

$$\rho(\boldsymbol{x}, t)\boldsymbol{u}(\boldsymbol{x}, t) = \int\limits_{\mathbb{R}^3} \mathrm{d}\boldsymbol{\xi}\, \boldsymbol{\xi}\, f(\boldsymbol{x}, \boldsymbol{\xi}, t)\,, \tag{2.47}$$

$$\rho(\boldsymbol{x}, t)\, e(\boldsymbol{x}, t) = \frac{1}{2} \int\limits_{\mathbb{R}^3} \mathrm{d}\boldsymbol{\xi}\, \|\boldsymbol{\xi} - \boldsymbol{u}(\boldsymbol{x}, t)\|^2\, f(\boldsymbol{x}, \boldsymbol{\xi}, t), \tag{2.48}$$

$$\mathbb{T}_{i,j}^{\nu}(\boldsymbol{x}, t) = \int\limits_{\mathbb{R}^3} \mathrm{d}\boldsymbol{\xi}\, (\boldsymbol{\xi} - \boldsymbol{u}(\boldsymbol{x}, t))_i\, (\boldsymbol{\xi} - \boldsymbol{u}(\boldsymbol{x}, t))_j\, f(\boldsymbol{x}, \boldsymbol{\xi}, t), \tag{2.49}$$

$$\mathbb{T}_{i,j}(\boldsymbol{x}, t) = \int\limits_{\mathbb{R}^3} \mathrm{d}\boldsymbol{\xi}\, \xi_i\, \xi_j\, f(\boldsymbol{x}, \boldsymbol{\xi}, t) = \rho(\boldsymbol{x}, t)\, u_i(\boldsymbol{x}, t)\, u_j(\boldsymbol{x}, t) + \mathbb{T}_{i,j}^{\nu}(\boldsymbol{x}, t), \tag{2.50}$$

$$\boldsymbol{q}(\boldsymbol{x}, t) = \frac{1}{2} \int\limits_{\mathbb{R}^3} \mathrm{d}\boldsymbol{\xi}\, \|\boldsymbol{\xi} - \boldsymbol{u}(\boldsymbol{x}, t)\|^2\, (\boldsymbol{\xi} - \boldsymbol{u}(\boldsymbol{x}, t))\, f(\boldsymbol{x}, \boldsymbol{\xi}, t), \tag{2.51}$$

where $i, j \in \{1, 2, 3\}$, e [m^2 s^{-2}] is the specific energy, and $\boldsymbol{q}$ [kg s^{-3}] is the heat flux [88]. These formulas have their analogical form in the discrete description as shown later in Chapter 3.

Next, the collisions of particles shift the mesoscopic system towards the local equilibrium given by the equilibrium PDF. This function can be derived from the PDF using the *H-theorem* [131]. The Maxwell-Boltzmann equilibrium PDF reads

$$\begin{aligned} f^{(eq)}(\rho, \boldsymbol{u}, \Theta, \boldsymbol{\xi}) &= \frac{\rho}{(2\pi R_s\, \Theta)^{\frac{3}{2}}} \exp\left(-\frac{\|\boldsymbol{\xi} - \boldsymbol{u}\|^2}{2R_s\, \Theta}\right), \\ &= \frac{\rho}{(2\pi c_s^2)^{\frac{3}{2}}} \exp\left(-\frac{\|\boldsymbol{\xi} - \boldsymbol{u}\|^2}{2c_s^2}\right), \end{aligned} \tag{2.52}$$

where $R_s\, \Theta = c_s^2$ [131].

Since the collision operator is in general a non-trivial expression, some approximations have been suggested. The simplest approximation is $\mathcal{C} = 0$, that is, there are no collisions considered between particles. Another possible approximation is the Bhatnagar-Gross-Krook (BGK) approximation $\mathcal{C}_{\mathrm{BGK}}$ suggested in [14]. The BGK collision operator can be expressed as

$$\mathcal{C}_{\mathrm{BGK}} = -\frac{1}{\tau_{\mathrm{BGK}}} \left(f - f^{(eq)}\right) \tag{2.53}$$

and can be interpreted as the change in PDF due to the collision during time τ_{BGK}, where τ_{BGK} [s] is called the BGK collision time.

A more sophisticated approximation is the Fokker-Planck (FP) approximation $\mathcal{C}_{\mathrm{FP}}$ proposed in [127] as

$$\mathcal{C}_{\mathrm{FP}} = \frac{1}{\tau_{\mathrm{FP}}} \sum_{i=1}^{3} \left[\frac{\partial}{\partial \xi_i} (\xi_i - u_i)\, f + \sum_{j=1}^{3} \mathcal{D}_{i,j} \frac{\partial^2 f}{\partial \xi_i \partial \xi_j} \right], \tag{2.54}$$

where τ_{FP} [s] is the FP collision time and $\mathcal{D}$ [m^2 s^{-2}] is the FP diffusion tensor (with entries $\mathcal{D}_{i,j}$, $i, j \in \{1, 2, 3\}$).

Lattice Boltzmann Method 3

The lattice Boltzmann method (LBM) is a relatively new numerical method that was originally developed for fluid flow simulations in the late 1980s and early 1990s from cellular automata [88]. In later years, this method was derived from kinetic theory, more precisely from the Boltzmann transport equation, showing its independence of cellular automata theory. Although the LBM is commonly used in practical applications and is now part of many commercial software, it is still a rapidly developing numerical method. The biggest advantage of the LBM is that it is a time explicit method and no large system of linear algebraic equations needs to be solved, which is a typical FDM or FVM problem where one needs to iteratively solve a large system of equations for the numerical solution of the Navier-Stokes equations. On the other hand, the drawback of the LBM is its mesoscopic nature, that is, a complicated backward analysis usually needs to be performed to find the PDEs that are actually solved.

This chapter describes the concept of the LBM. First, the discretizations of space and time are defined. This is followed by a summary of the basics of the LBM. Next, the collision operators, forcing terms, initial conditions, and mesoscopic boundary conditions (BCs) used in this thesis are introduced. The last two sections of this chapter are composed of the description of the grid refinement technique and implementation remarks.

3.1 Discretization of space and time

Finding analytical solutions to the continuous macroscopic equations introduced in Chapter 2 is often complicated or even impossible. Thus, the continuous solution is approximated by a discrete solution defined on a discrete grid that covers the investigated domain Ω. With the increasing number of discrete grid nodes, the approximation provides more detailed pieces of information about the continuous solution.

In all considered cases in this thesis, the computational domain Ω is a cuboid with dimensions L_1, L_2, L_3 [m], i.e., $\Omega = (0, L_1) \times (0, L_2) \times (0, L_3)$. The domain is discretized using a uniform grid

$$\hat{\Omega} = \left\{ \boldsymbol{x}_{ijk} \in \Omega \,|\, i \in \{1, 2, \cdots, N_1 - 2\}, j \in \{1, 2, \cdots, N_2 - 2\}, k \in \{1, 2, \cdots, N_3 - 2\} \right\}, \quad (3.1)$$

where N_1, N_2, N_3 $[-]$ determine the number of grid nodes in the x_1-, x_2-, and x_3-direction, respectively. The discretization of Ω is illustrated in Figure 3.1. The nodes are defined by $\boldsymbol{x}_{ijk} = (i\delta_x + P_1, j\delta_x + P_2, k\delta_x + P_3)^T$, where δ_x [m] is the grid spacing parameter and $\boldsymbol{P} = (P_1, P_2, P_3)^T$ is the offset vector, P_i [m], $i \in \{1, 2, 3\}$. The definitions of $\boldsymbol{P}$ and δ_x depend on the particular problem studied.

The closure $\overline{\Omega}$ is discretized by the set $\hat{\overline{\Omega}} = \hat{\Omega} \cup \partial\hat{\Omega}$, where $\partial\hat{\Omega}$ discretizes the boundary $\partial\Omega$. Contrary to the discretization of Ω, nodes of $\partial\hat{\Omega}$ do not have to be from $\partial\Omega$. This is a consequence
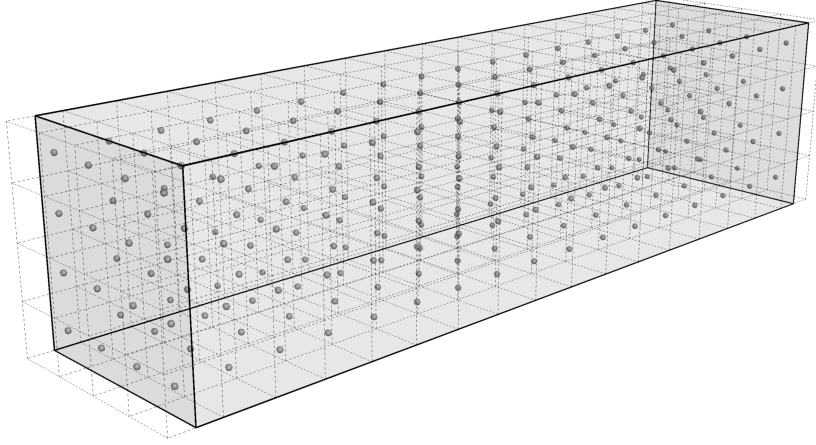
Figure 3.1: Discretization of Ω using uniform grid $\hat{\Omega}$. The discrete points (marked as gray circles) discretize the continuous domain. The points are not drawn at the boundary since the exact location of boundary points depends on the particular choice of the mesoscopic BC used.

of the specific implementation of some mesoscopic BCs (later discussed in Section 3.7). Boundary nodes $\boldsymbol{x}_{ijk} \in \partial\hat{\Omega}$ that exactly belong to the boundary $\partial\hat{\Omega}$ are called *wet-nodes*. The other nodes $\boldsymbol{x}_{ijk} \in \partial\hat{\Omega}$ on which the BCs are applied can be in $\partial\Omega$ (for example, the equilibrium BC uses this type of nodes defined in Section 3.7.3) or can be from the exterior of $\overline{\Omega}$ (for example, the full-way bounce-back BC uses this type of nodes defined in Section 3.7.4).

In the LBM, the uniform grid $\hat{\Omega}$ is replaced by the discrete lattice $\widetilde{\Omega}$ defined by

$$\widetilde{\Omega} = \{\widetilde{\boldsymbol{x}}_{ijk} \,|\, i \in \{1, 2, \cdots, N_1 - 2\}, j \in \{1, 2, \cdots, N_2 - 2\}, k \in \{1, 2, \cdots, N_3 - 2\}\}. \tag{3.2}$$

Each lattice site $\widetilde{\boldsymbol{x}}_{ijk} = (i, j, k)^T$ corresponds to the grid point $\boldsymbol{x}_{ijk} = (i\delta_x, j\delta_x, k\delta_x)^T + \boldsymbol{P}$. Similarly, the boundary discretization $\partial\hat{\Omega}$ is replaced by the set of lattice sites $\partial\widetilde{\Omega}$.

The time interval $\mathcal{T} = (0, T)$ is discretized uniformly by the set

$$\widetilde{\mathcal{T}} = \{\ell \,|\, \ell\delta_t \in (0, T), \ell \in \{1, 2, \cdots, N_t - 1\}\}, \tag{3.3}$$

where N_t [$-$] defines the number of discrete time steps and δ_t [s] is the time step that satisfies $\delta_t = \frac{T}{N_t}$.

It is common to work with non-dimensional quantities instead of the original ones. There are several reasons discussed in [118]. One of them is that the computer only stores numbers without their units and, therefore, it is more convenient to transform all variables into a non-dimensional form defined by the user. To perform the non-dimensionalization, scaling factors are needed for all physical units used in the problem. Usually, the scaling parameters for the length and time scales are the grid spacing parameter δ_x and time step δ_t, respectively. The scaling parameter for the mass is $\rho_0\delta_x^3$, where ρ_0 [kg m^{-3}] is the reference density. Thus, to transfer the quantity ϕ with dimensions [kg^i m^j s^k], $i, j, k \in \mathbb{Z}$ to its non-dimensional form, the scaling factor $\rho_0^i \delta_x^{3i+j} \delta_t^k$ is used. If the dimensional and non-dimensional quantities are used together, the non-dimensional quantity of ϕ is labeled by $\widetilde{\phi}$.

The parameters δ_x and δ_t are not used arbitrarily, but a certain relationship is used between them. This relation influences the resulting PDEs numerically solved by the LBM [118]. In this thesis, the following two relations are used:

- **Acoustic scaling**: $\frac{\delta_x}{\delta_t} = \text{const.}$
  Using this scaling, the velocities have the same magnitude for different discretizations of

space and time.

- **Diffusive scaling**: $\frac{\delta_x^2}{\delta_t} = \text{const.}$
  Using this scaling, the diffusion (kinematic viscosity) has the same magnitude for different discretizations of space and time.

For most problems in this work, the diffusive scaling is used. The acoustic scaling is used only in problems in Chapter 6 that use the grid refinement technique to discretize Ω.

3.2   Basics of LBM

In this section, the basic concepts of the LBM are summarized. All quantities are assumed to be in the non-dimensional form. Since the LBM is based on the mesoscopic description, the velocity space of the microscopic particle velocity is discretized by a set $\{\boldsymbol{\xi_i}\}_{i\in\mathcal{Q}}$. In this thesis, we use the D3Q27 velocity model illustrated in Figure 3.2. Thus, $\mathcal{Q} = \overset{3}{\underset{i=1}{\times}} \{-1, 0, 1\}$, where $\boldsymbol{\xi_i} = c(i_1, i_2, i_d)^T$ is the discrete microscopic velocity defined by the multi-index $\boldsymbol{i} = (i_1, i_2, i_3)$, $c = \Delta x/\Delta t$ is the non-dimensional lattice velocity, and Δx and Δt are the non-dimensional space and time steps, respectively. For simplicity, $\Delta x = \Delta t = 1$ are used, and thus $c = 1$.
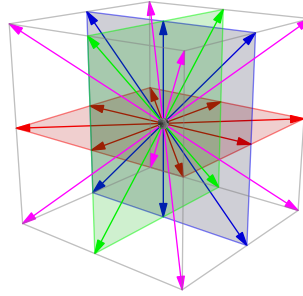
Figure 3.2: Illustration of 27 discrete directions in which the information is propagated within the lattice.

Based on the discretization of the velocity space, the discrete one-particle density function (DDF) can be defined by

$$f_i(\boldsymbol{x}, t) = \Lambda_i f(\boldsymbol{x}, \boldsymbol{\xi_i}, t), \tag{3.4}$$

where $\boldsymbol{x} \in \hat{\Omega}$, $t \in \hat{\mathcal{T}}$, Λ_i is the scaling factor [118], and multi-index $\boldsymbol{i} \in \mathcal{Q}$. The evolution of discrete density functions f_i is described by the discrete Boltzmann transport equation

$$f_i(\boldsymbol{x} + \Delta t \boldsymbol{\xi_i}, t + \Delta t) - f_i(\boldsymbol{x}, t) = \Delta t \, \mathcal{C}_i(\boldsymbol{x}, t), \tag{3.5}$$

where $\boldsymbol{x} \in \widetilde{\Omega}$, $t \in \widetilde{\mathcal{T}}$, and $\mathcal{C}_i$ is the discrete collision operator. Eq. (3.5) can be derived from the Boltzmann transport equation (2.45) using the method of characteristics, Hermite series expansion, and Gauss-Hermite quadrature.

Remark 3.1
It should be noted that during the discretization of Eq. (2.45), the DDF f_i are redefined by [118]

$$f_i := \Lambda_i \left(f_i - \frac{\Delta}{2} \mathcal{C}_i \right), \forall \boldsymbol{i} \in \mathcal{Q}. \tag{3.6}$$

Since the former DDFs are not used in this thesis, the newly defined DDFs are referred to as the former.

On the basis of the set of discrete microscopic velocities, some statistical moments can be calculated from DDFs. The approximation is based on the quadrature rules [118] and, for example, the discrete form of Eqs. (2.47) and (2.48) in the case of the velocity model D3Q27 is

$$\rho = \sum_{i \in \mathcal{Q}} f_i, \tag{3.7a}$$

$$\rho \boldsymbol{u} = \sum_{i \in \mathcal{Q}} f_i \boldsymbol{\xi_i} + \rho \frac{\Delta t}{2} \boldsymbol{g}, \tag{3.7b}$$

respectively. Finally, the pressure p is related to the density trough the equation of state as

$$p = p_0 + c_s^2 (\rho - \rho_0), \tag{3.8}$$

where p_0 $[-]$ is the non-dimensional reference pressure and $\rho_0 = 1$ is the non-dimensional reference density [118].

3.3 Algorithm

In this part, a single time step of the LBM algorithm is described. First, Eq. (3.5) can be decomposed into its local part

$$f_i^\star(\boldsymbol{x}, t) = f_i(\boldsymbol{x}, t) + \Delta t \mathcal{C}_i(\boldsymbol{x}, t), \ \forall \boldsymbol{i} \in \mathcal{Q}, \tag{3.9a}$$

and streaming part

$$f_i(\boldsymbol{x} + \Delta t \boldsymbol{\xi_i}, t + \Delta t) = f_i^\star(\boldsymbol{x}, t), \ \forall \boldsymbol{i} \in \mathcal{Q}, \tag{3.9b}$$

where $f_i^\star$ is the post-collision DDF. Eq. (3.9a) is called the *collision step* and Eq. (3.9b) is called the *streaming step*.

A scheme in which post-collision DDFs are computed before the streaming step defined by Eq. (3.9b) is called the *push-scheme*. The reason why this scheme is called a push-scheme is that the post-collision DDFs are streamed to neighboring lattice sites in the direction of discrete velocities $\boldsymbol{\xi_i}$.

Another option is to write Eq.(3.9b) as

$$f_i(\boldsymbol{x}, t) = f_i^\star(\boldsymbol{x} - \Delta t \boldsymbol{\xi_i}, t - \Delta t), \ \forall \boldsymbol{i} \in \mathcal{Q}. \tag{3.10}$$

A scheme in which post-collision DDFs are computed after the streaming step defined by Eq. (3.10) is called the *pull-scheme*, since the DDFs are pulled from the neighboring lattice sites. In this thesis, the pull-scheme is used.

The algorithm of a single time step can be decomposed into several steps:

1. Streaming of density functions from the neighboring lattice sites according to Eq.(3.10)

2. Treatment of boundary sites

3. Computation of macroscopic quantities (Eqs. (3.7a), (3.7b))

4. Collision step according to Eq.(3.9a)

These steps are repeated until the end criterion is satisfied. The entire algorithm, including initialization, is illustrated in Figure 3.3.
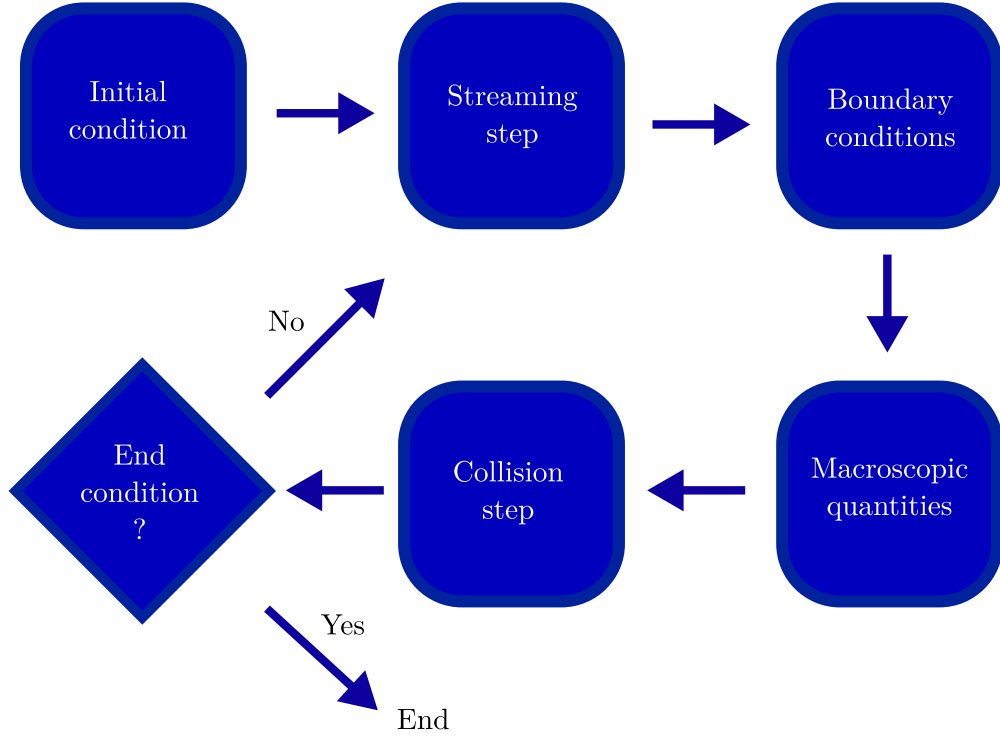
Figure 3.3: Illustration of the algorithm for a one-time step in the lattice Boltzmann method.

3.4   Collision operators

The right-hand side of Eq. (3.5) contains the discrete collision operator $\mathcal{C}_i$. The discrete collision operator takes current DDFs and relaxes them to the attractor. The form of the attractor depends on the current problem studied. In the case of fluid flow simulations, the attractor is considered to be defined by the Maxwell-Boltzmann density function. To adapt the LBM to a particular problem, the attractor is usually one of the modified parts. Thus, the discrete collision operator is one of the most investigated parts of the LBM.

3.4.1   Single relaxation time

A straightforward way of designing a discrete collision operator is based directly on the BGK approximation (2.53) and is referred to as the *Single Relaxation Time* (SRT) collision operator [88]. The form of the collision operator for all $\boldsymbol{i} \in \mathcal{Q}$ is

$$\mathcal{C}_{\boldsymbol{i}} = -\frac{1}{\tau}\left(f_{\boldsymbol{i}} - f_{\boldsymbol{i}}^{(eq)}\right),\tag{3.11}$$

where $f_{\boldsymbol{i}}^{(eq)}$ is the discrete equilibrium density function (i.e., the attractor), τ is the non-dimensional relaxation time. In the case of the Navier-Stokes equations, the discrete attractor has the form [118]

$$f_{\boldsymbol{i}}^{(eq)} = w_{\boldsymbol{i}}\rho\left(1 + \frac{\boldsymbol{u} \cdot \boldsymbol{\xi_i}}{c_s^2} + \frac{(\boldsymbol{u} \cdot \boldsymbol{\xi_i})^2}{2c_s^4} - \frac{\boldsymbol{u} \cdot \boldsymbol{u}}{2c_s^2}\right),\tag{3.12}$$

where $w_{\boldsymbol{i}}$ are the weights defined for $D3Q27$ by

$$
w_{\boldsymbol{i}} =
\begin{cases}
\frac{8}{27} & \text{for } |\boldsymbol{i}| = 0, \\[4pt]
\frac{2}{27} & \text{for } |\boldsymbol{i}| = 1, \\[4pt]
\frac{1}{54} & \text{for } |\boldsymbol{i}| = 2, \\[4pt]
\frac{1}{216} & \text{for } |\boldsymbol{i}| = 3,
\end{cases}
\tag{3.13}
$$

where $|\boldsymbol{i}| = \sum\limits_{k=1}^{3} |i_k|$.

The relaxation time τ defines the attraction rate and is connected to the non-dimensional kinematic viscosity as [88]

$$
\nu = c_s^2 \left(\tau - \frac{\Delta t}{2} \right) = c_s^2 \left(\frac{1}{\omega} - \frac{\Delta t}{2} \right),
\tag{3.14}
$$

where c_s is the non-dimensional sound speed for isothermal fluid and $\omega = \tau^{-1}$ is the relaxation frequency. For D3Q27, $c_s = \frac{1}{\sqrt{3}}$ [118]. Since the kinematic viscosity is a non-negative quantity, the relaxation time must satisfy $\tau \geq \frac{1}{2}$, see Eq. (3.14). If $\tau < 1$ or $\tau > 1$, the collision is called *over-relaxation* or *under-relaxation*, respectively, and these choices lead to different relaxation to the given attractor [118]. A special choice of the relaxation time is $\tau = 1$, where the DDFs are set directly to their attractor.

3.4.2 Multiple relaxation time

Despite its simplicity, the SRT collision operator has several, mainly numerical drawbacks [118]. One of them is the relaxation of all DDFs at a single rate. Thus, more relaxation times (frequencies) were introduced. Based on the number of relaxation times, the collision operators are called *Two Relaxation Time* (TRT) [84] or *Multiple Relaxation Time* (MRT) [41, 42]. Since the relaxation times for particular DDFs cannot be changed, raw moments of DDFs are relaxed to their attractors. The raw moments are defined by

$$
m_{\boldsymbol{j}} = \sum_{\boldsymbol{i} \in \mathcal{Q}} f_{\boldsymbol{i}} \boldsymbol{\xi}_{\boldsymbol{i}}^{\boldsymbol{j}},
\tag{3.15}
$$

where $\boldsymbol{\xi}_{\boldsymbol{i}}^{\boldsymbol{j}} = \prod\limits_{k=1}^{3} i_k^{j_k}$, $\boldsymbol{i} = (i_1, i_2, i_3) \in \mathcal{Q}$ and $\boldsymbol{j} = (j_1, j_2, j_3)$, $j_1, j_2, j_3 \in \{0, 1, 2\}$, are the multi-indexes. Definitions of continuous raw moments are given in Appendix A. Next, $m_{\boldsymbol{j}}$ is called a raw moment of order r, if and only if $\sum\limits_{k=1}^{d} |j_k| = r$.

During the collision, the moments are relaxed to their equilibriums $m_{\boldsymbol{j}}^{(eq)}$. For D3Q27, the DDFs have 27 independent raw moments, respectively. The first moments that are related to the investigated quantities (density and momentum in the case of the Navier-Stokes equations) are the so-called collision invariants, i.e., they are not changed during the collision since $m_{\boldsymbol{j}} = m_{\boldsymbol{j}}^{(eq)}$. The rest of the moments are relaxed to their equilibriums as

$$
-\frac{1}{\tau_{\boldsymbol{j}}} \left(m_{\boldsymbol{j}} - m_{\boldsymbol{j}}^{(eq)} \right),
\tag{3.16}
$$

where $\tau_{\boldsymbol{j}}$ is the relaxation time of the particular moment $m_{\boldsymbol{j}}$.

Instead of relaxing moments independently, moments are grouped together. For example, moments that have hydrodynamic sense are relaxed together with the same relaxation rate. After

the collision, the moments are transformed back to the DDFs. Particularly, the collision operator can be written as

$$\mathcal{C} = -\mathbb{M}^{-1}\mathbb{F}\left(\widetilde{\boldsymbol{m}} - \widetilde{\boldsymbol{m}}^{(eq)}\right), \tag{3.17}$$

where $\mathcal{C}$ is the vector with components $\mathcal{C}_{\Psi(i)}$, $i \in \{1, 2, \cdots, 27\}$, where the mapping $\Psi : \{1, 2, \cdots, 27\} \to \mathcal{Q}$ introduces the ordering of $\mathcal{Q}$ and is defined in Appendix B. $\mathbb{F} = \mathrm{diag}(\omega_1, \omega_2, \cdots, \omega_{27})$ is the diagonal matrix of relaxation frequencies, $\widetilde{\boldsymbol{m}}^{(eq)}$ is the vector of discrete attractors, and $\widetilde{\boldsymbol{m}}$ is the vector of combined raw moments defined by the transformation matrix $\mathbb{M}$ as $\widetilde{\boldsymbol{m}} = \mathbb{M}\boldsymbol{f}$, where $\boldsymbol{f}$ is the vector of DDFs with components $f_{\Psi(i)}$, $i \in \{1, 2, \cdots, 27\}$. The particular form of the transformation matrix $\mathbb{M}$ and attractors $\widetilde{\boldsymbol{m}}^{(eq)}$ can be found, for instance, in [67, 80].

3.4.3   Central moment-based collision operator

Another possible option is to transform DDFs to the space of central moments and carry out the collision there. For the definition of continuous central moments, see Appendix A. The discrete central moments are defined by

$$\kappa_{\boldsymbol{j}} = \sum_{i \in \mathcal{Q}} f_{\boldsymbol{i}}(\boldsymbol{\xi_i} - \boldsymbol{u})^{\boldsymbol{j}}. \tag{3.18}$$

The central moment is of order $r \in \mathbb{N}$, if and only if $\sum\limits_{k=1}^{d} |j_k| = r$. Obviously, the zeroth-order central moment is identical to the zeroth-order raw moment. Next, thanks to Eq. (3.7b), the first-order central moments satisfies

$$\kappa_{(1,0,0)} = -\rho\frac{\Delta t}{2}g_1, \tag{3.19a}$$

$$\kappa_{(0,1,0)} = -\rho\frac{\Delta t}{2}g_2, \tag{3.19b}$$

$$\kappa_{(0,0,1)} = -\rho\frac{\Delta t}{2}g_3. \tag{3.19c}$$

Thus, contrary to the first-order moments, they are velocity-independent.

The LBM with the collision operator that performs the collision in the space of the central moments is called the *Central Moment-based LBM* (CLBM). Similar to the MRT collision operator, it is numerically advantageous to relax a particular combination of central moments. For the D3Q27 velocity model, the CLBM collision operator can be expressed as

$$\mathcal{C} = -\mathbb{K}^{-1}\mathbb{F}\left(\widetilde{\boldsymbol{\kappa}} - \widetilde{\boldsymbol{\kappa}}^{(eq)}\right), \tag{3.20}$$

where $\mathbb{K}$ is the transformation matrix, $\widetilde{\boldsymbol{\kappa}}$ is the vector of combined central moments defined by $\widetilde{\boldsymbol{\kappa}} = \mathbb{K}\boldsymbol{f}$, and $\widetilde{\boldsymbol{\kappa}}^{(eq)}$ is the vector of discrete attractors. Particular form of transformation matrix $\mathbb{K}$ and discrete attractors $\widetilde{\boldsymbol{\kappa}}^{(eq)}$ can be found, for instance, in [67, 80].

3.4.4   Cumulant collision operator

Cumulants are alternative statistical quantities to statistical moments. For the continuous density distribution function, the cumulant $c_{\boldsymbol{j}}$, $\boldsymbol{j} = (j_1, j_2, j_3)$, $j_1, j_2, j_3 \in \{0, 1, 2\}$, is defined using the cumulant generating function as summarized in Appendix A. For the definition in the discrete space, the DDFs need to be made continuous, for example, as [80]

$$f(\boldsymbol{\xi}) = \sum_{\boldsymbol{i} \in \mathcal{Q}} f_{\boldsymbol{i}} \prod_{k=1}^{3} D(i_k c - \xi_k), \tag{3.21}$$

where $\boldsymbol{\xi} = (\xi_1, \xi_2, \xi_3)^T$ and D is the Dirac delta function [184]. Then, the raw moment generating function defined in Appendix A satisfies

$$M(\boldsymbol{\Xi}) = \int_{\mathbb{R}^3} \exp\left(\boldsymbol{\Xi} \cdot \boldsymbol{\xi}\right) f(\boldsymbol{\xi}) \mathrm{d}\boldsymbol{\xi} = \sum_{i \in \mathcal{Q}} f_i \exp\left(\boldsymbol{\Xi} \cdot \boldsymbol{\xi_i}\right), \tag{3.22}$$

where $\boldsymbol{\Xi} = (\Xi_1, \Xi_2, \Xi_3)^T \subset \mathbb{R}^3$. Next, the cumulant generating function is defined by

$$K(\boldsymbol{\Xi}) = \ln\left(M(\boldsymbol{\Xi})\right) \tag{3.23}$$

and the discrete cumulant $c_{\boldsymbol{j}}$ is defined (see Appendix A) by

$$c_{\boldsymbol{j}} = \frac{\partial^{|\boldsymbol{j}|}}{\partial \Xi_1^{j_1} \partial \Xi_2^{j_2} \partial \Xi_3^{j_3}} K(\boldsymbol{\Xi}) \Bigg|_{\boldsymbol{\Xi}=\boldsymbol{0}}, \tag{3.24}$$

where $|\boldsymbol{j}| = \sum\limits_{k=1}^{3} |j_k|$ is the order of the cumulant $c_{\boldsymbol{j}}$. The zeroth-order cumulant satisfies $c_{(0,0,0)} = \ln\left(\rho\right)$. Additionally, the first- and second-order cumulants are proportional to the first- and second-order central moments, respectively. Contrary to the raw and central moments, the transformation between DDFs and cumulants is non-linear. Hence, it cannot be written in a matrix form.

The advantage of cumulants is their attractor. Let the attractor be the Maxwell-Boltzmann density function in the form of Eq. (2.52)

$$f^{(eq)}(\boldsymbol{\xi}) = \frac{\rho}{(2\pi c_s^2)^{\frac{3}{2}}} \exp\left(\frac{-\|\boldsymbol{\xi} - \boldsymbol{u}\|^2}{2c_s^2}\right). \tag{3.25}$$

Then the raw moment-generating function is

$$M(\boldsymbol{\Xi}) = \rho \exp\left(\boldsymbol{\Xi} \cdot \boldsymbol{u} + \frac{1}{2} c_s^2 \boldsymbol{\Xi} \cdot \boldsymbol{\Xi}\right). \tag{3.26}$$

Based on Eq. (3.23), the cumulant generating function is

$$K(\boldsymbol{\Xi}) = \ln\left(M(\boldsymbol{\Xi})\right) = \ln\left(\rho\right) + \boldsymbol{\Xi} \cdot \boldsymbol{u} + \frac{1}{2} c_s^2 \boldsymbol{\Xi} \cdot \boldsymbol{\Xi}. \tag{3.27}$$

Consequently, the third- and higher-order cumulant attractors are zero since $K(\boldsymbol{\Xi})$ is the second-order polynomial in $\boldsymbol{\Xi}$.

As in [80], $C_{\boldsymbol{j}} = \rho c_{\boldsymbol{j}}$ (called also cumulant) is used in the collision because $C_{\boldsymbol{j}}$ can be easily calculated from the central moments. Moreover, as in the case of the MRT and CLBM, it is convenient to relax the cumulants in some linear combination. In this thesis, the LBM with cumulant collision operator introduced in [80] is used. $C_{\boldsymbol{j}}$ can be constructed using the central

moments as:

$$\rho = \kappa_{(0,0,0)}, \tag{3.28a}$$

$$C_{\boldsymbol{j}} = \kappa_{\boldsymbol{j}}, \ \forall 1 \le |\boldsymbol{j}| \le 3, \tag{3.28b}$$

$$C_{(2,1,1)} = \kappa_{(2,1,1)} - \Big(\kappa_{(2,0,0)}\kappa_{(0,1,1)} + 2\kappa_{(1,1,0)}\kappa_{(1,0,1)}\Big)/\rho, \tag{3.28c}$$

$$C_{(2,2,0)} = \kappa_{(2,2,0)} - \Big(\kappa_{(2,0,0)}\kappa_{(0,2,0)} + 2\kappa_{(1,1,0)}^2\Big)/\rho, \tag{3.28d}$$

$$C_{(1,2,2)} = \kappa_{(1,2,2)} - \Big(\kappa_{(0,0,2)}\kappa_{(1,2,0)} + \kappa_{(0,2,0)}\kappa_{(1,0,2)} + 4\kappa_{(0,1,1)}\kappa_{(1,1,1)} + 2\Big(\kappa_{(1,0,1)}\kappa_{(0,2,1)} \tag{3.28e}$$

$$+ \kappa_{(1,1,0)}\kappa_{(0,1,2)}\Big)\Big)/\rho, \tag{3.28f}$$

$$C_{(2,2,2)} = \kappa_{(2,2,2)} - \Big(4\kappa_{(1,1,1)}^2 + \kappa_{(2,0,0)}\kappa_{(0,2,2)} + \kappa_{(0,2,0)}\kappa_{(2,0,2)} + \kappa_{(0,0,2)}\kappa_{(2,2,0)} \tag{3.28g}$$

$$+ 4\Big(\kappa_{(0,1,1)}\kappa_{(2,1,1)} + \kappa_{(1,0,1)}\kappa_{(1,2,1)} + \kappa_{(1,1,0)}\kappa_{(1,1,2)}\Big) + 2\Big(\kappa_{(1,2,0)}\kappa_{(1,0,2)} \tag{3.28h}$$

$$+ \kappa_{(2,1,0)}\kappa_{(0,1,2)} + \kappa_{(2,0,1)}\kappa_{(0,2,1)}\Big)\Big)/\rho + \Big(16\kappa_{(1,1,0)}\kappa_{(1,0,1)}\kappa_{(0,1,1)} \tag{3.28i}$$

$$+ 4\Big(\kappa_{(1,0,1)}^2\kappa_{(0,2,0)} + \kappa_{(0,1,1)}^2\kappa_{(2,0,0)} + \kappa_{(1,1,0)}^2\kappa_{(0,0,2)}\Big) + 2\kappa_{(2,0,0)}\kappa_{(0,2,0)}\kappa_{(0,0,2)}\Big)/\rho^2. \tag{3.28j}$$

The rest of the cumulants are obtained by the index permutations [80]. Similarly, the transformation from cumulants to central moments is performed using

$$\kappa_{(0,0,0)} = \rho, \tag{3.29a}$$

$$\kappa_{\boldsymbol{j}} = C_{\boldsymbol{j}}, \ \forall 1 \le |\boldsymbol{j}| \le 3, \tag{3.29b}$$

$$\kappa_{(2,1,1)} = C_{(2,1,1)} - \Big(C_{(2,0,0)}C_{(0,1,1)} + 2C_{(1,1,0)}C_{(1,0,1)}\Big)/\rho, \tag{3.29c}$$

$$\kappa_{(2,2,0)} = C_{(2,2,0)} - \Big(C_{(2,0,0)}C_{(0,2,0)} + 2C_{(1,1,0)}^2\Big)/\rho, \tag{3.29d}$$

$$\kappa_{(1,2,2)} = C_{(1,2,2)} - \Big(C_{(0,0,2)}C_{(1,2,0)} + C_{(0,2,0)}C_{(1,0,2)} + 4C_{(0,1,1)}C_{(1,1,1)} \tag{3.29e}$$

$$+ 2\Big(C_{(1,0,1)}C_{(0,2,1)} + C_{(1,1,0)}C_{(0,1,2)}\Big)\Big)/\rho, \tag{3.29f}$$

$$\kappa_{(2,2,2)} = C_{(2,2,2)} - \Big(4C_{(1,1,1)}^2 + C_{(2,0,0)}C_{(0,2,2)} + C_{(0,2,0)}C_{(2,0,2)} + C_{(0,0,2)}C_{(2,2,0)} \tag{3.29g}$$

$$+ 4\Big(C_{(0,1,1)}C_{(2,1,1)} + C_{(1,0,1)}C_{(1,2,1)} + C_{(1,1,0)}C_{(1,1,2)}\Big) + 2\Big(C_{(1,2,0)}C_{(1,0,2)} \tag{3.29h}$$

$$+ C_{(2,1,0)}C_{(0,1,2)} + C_{(2,0,1)}C_{(0,2,1)}\Big)\Big)/\rho + \Big(16C_{(1,1,0)}C_{(1,0,1)}C_{(0,1,1)} \tag{3.29i}$$

$$+ 4\Big(C_{(1,0,1)}^2C_{(0,2,0)} + C_{(0,1,1)}^2C_{(2,0,0)} + C_{(1,1,0)}^2C_{(0,0,2)}\Big) \tag{3.29j}$$

$$+ 2C_{(2,0,0)}C_{(0,2,0)}C_{(0,0,2)}\Big)/\rho^2, \tag{3.29k}$$

and again the rest of the central moments are obtained by the index permutations analogously.

Finally, the collision of cumulants is performed as [80]

$$C^\star_{(1,1,0)} = (1 - \omega_1)C_{(1,1,0)}, \tag{3.30a}$$

$$C^\star_{(1,0,1)} = (1 - \omega_1)C_{(1,0,1)}, \tag{3.30b}$$

$$C^\star_{(0,1,1)} = (1 - \omega_1)C_{(0,1,1)}, \tag{3.30c}$$

$$C^\star_{(2,0,0)} - C^\star_{(0,2,0)} = (1 - \omega_1)\big(C_{(2,0,0)} - C_{(0,2,0)}\big), \tag{3.30d}$$

$$C^\star_{(2,0,0)} - C^\star_{(0,0,2)} = (1 - \omega_1)\big(C_{(2,0,0)} - C_{(0,0,2)}\big), \tag{3.30e}$$

$$C^\star_{(2,0,0)} + C^\star_{(0,2,0)} + C^\star_{(0,0,2)} = \omega_2\kappa_{(0,0,0)} + (1 - \omega_2)\big(C_{(2,0,0)} + C_{(0,2,0)} + C_{(0,0,2)}\big), \tag{3.30f}$$

$$C^\star_{(1,2,0)} + C^\star_{(1,0,2)} = (1 - \omega_3)\big(C_{(1,2,0)} + C_{(1,0,2)}\big), \tag{3.30g}$$

$$C^\star_{(2,1,0)} + C^\star_{(0,1,2)} = (1 - \omega_3)\big(C_{(2,1,0)} + C_{(0,1,2)}\big), \tag{3.30h}$$

$$C^\star_{(2,0,1)} + C^\star_{(0,2,1)} = (1 - \omega_3)\big(C_{(2,0,1)} + C_{(0,2,1)}\big), \tag{3.30i}$$

$$C^\star_{(1,2,0)} - C^\star_{(1,0,2)} = (1 - \omega_4)\big(C_{(1,2,0)} - C_{(1,0,2)}\big), \tag{3.30j}$$

$$C^\star_{(2,1,0)} - C^\star_{(0,1,2)} = (1 - \omega_4)\big(C_{(2,1,0)} - C_{(0,1,2)}\big), \tag{3.30k}$$

$$C^\star_{(2,0,1)} - C^\star_{(0,2,1)} = (1 - \omega_4)\big(C_{(2,0,1)} - C_{(0,2,1)}\big), \tag{3.30l}$$

$$C^\star_{(1,1,1)} = (1 - \omega_5)C_{(1,1,1)}, \tag{3.30m}$$

$$C^\star_{(2,2,0)} - 2C^\star_{(2,0,2)} + C^\star_{(0,2,2)} = (1 - \omega_6)\big(C_{(2,2,0)} - 2C_{(2,0,2)} + C_{(0,2,2)}\big), \tag{3.30n}$$

$$C^\star_{(2,2,0)} + C^\star_{(2,0,2)} - 2C^\star_{(0,2,2)} = (1 - \omega_6)\big(C_{(2,2,0)} + C_{(2,0,2)} - 2C_{(0,2,2)}\big), \tag{3.30o}$$

$$C^\star_{(2,2,0)} + C^\star_{(2,0,2)} + C^\star_{(0,2,2)} = (1 - \omega_7)\big(C_{(2,2,0)} + C_{(2,0,2)} + C_{(0,2,2)}\big), \tag{3.30p}$$

$$C^\star_{(2,1,1)} = (1 - \omega_8)C_{(2,1,1)}, \tag{3.30q}$$

$$C^\star_{(1,2,1)} = (1 - \omega_8)C_{(1,2,1)}, \tag{3.30r}$$

$$C^\star_{(1,1,2)} = (1 - \omega_8)C_{(1,1,2)}, \tag{3.30s}$$

$$C^\star_{(2,2,1)} = (1 - \omega_9)C_{(2,2,1)}, \tag{3.30t}$$

$$C^\star_{(2,1,2)} = (1 - \omega_9)C_{(2,1,2)}, \tag{3.30u}$$

$$C^\star_{(1,2,2)} = (1 - \omega_9)C_{(1,2,2)}, \tag{3.30v}$$

$$C^\star_{(2,2,2)} = (1 - \omega_{10})C_{(2,2,2)}, \tag{3.30w}$$

where $C^\star_j$ is the post-collision cumulant.

The post-collision DDFs $f^\star_i$ are reconstructed from the post-collision cumulants $C^\star_i$ using Eq. (3.29) and the transformation from the central moments [80]. The relaxation frequency ω_1 is related to the kinematic viscosity as

$$\nu = c_s^2\left(\frac{1}{\omega_1} - \frac{\Delta t}{2}\right). \tag{3.31}$$

Other relaxation frequencies can be set, for example, to 1. The LBM with the collision operator described using Eq. (3.30) is referred to as CuLBM.

To minimize the artifacts originating from the absence of higher order cumulants, the

modification of the collision in Eqs. (3.30d), (3.30e), (3.30f) is suggested in [80] as

$$
C^{\star}_{(2,0,0)} - C^{\star}_{(0,2,0)} = (1 - \omega_1)\Big(C_{(2,0,0)} - C_{(0,2,0)}\Big)
$$
$$
- 3\rho\Big(1 - \frac{\omega_1}{2}\Big)\Big(u_1^2 \frac{\widetilde{\partial u_1}}{\partial x_1} - u_2^2 \frac{\widetilde{\partial u_2}}{\partial x_2}\Big), \tag{3.32a}
$$
$$
C^{\star}_{(2,0,0)} - C^{\star}_{(0,0,2)} = (1 - \omega_1)\Big(C_{(2,0,0)} - C_{(0,0,2)}\Big)
$$
$$
- 3\rho\Big(1 - \frac{\omega_1}{2}\Big)\Big(u_1^2 \frac{\widetilde{\partial u_1}}{\partial x_1} - u_3^2 \frac{\widetilde{\partial u_3}}{\partial x_3}\Big), \tag{3.32b}
$$
$$
C^{\star}_{(2,0,0)} + C^{\star}_{(0,2,0)} + C^{\star}_{(0,0,2)} = \omega_2 \kappa_{(0,0,0)} + (1 - \omega_2)\Big(C_{(2,0,0)} + C_{(0,2,0)} + C_{(0,0,2)}\Big)
$$
$$
- 3\rho\Big(1 - \frac{\omega_1}{2}\Big)\Big(u_1^2 \frac{\widetilde{\partial u_1}}{\partial x_1} + u_2^2 \frac{\widetilde{\partial u_2}}{\partial x_2} + u_3^2 \frac{\widetilde{\partial u_3}}{\partial x_3}\Big), \tag{3.32c}
$$
$$
\tag{3.32d}
$$

where

$$
\frac{\widetilde{\partial u_1}}{\partial x_1} = -\frac{\omega_1}{2\rho}\Big(2C_{(2,0,0)} - C_{(0,2,0)} - C_{(0,0,2)}\Big) - \frac{\omega_2}{2\rho}\Big(C_{(2,0,0)} + C_{(0,2,0)} + C_{(0,0,2)} - \kappa_{(0,0,0)}\Big), \tag{3.33a}
$$
$$
\frac{\widetilde{\partial u_2}}{\partial x_2} = \frac{\widetilde{\partial u_1}}{\partial x_1} + \frac{3\omega_1}{2\rho}\Big(C_{(2,0,0)} - C_{(0,2,0)}\Big), \tag{3.33b}
$$
$$
\frac{\widetilde{\partial u_3}}{\partial x_3} = \frac{\widetilde{\partial u_1}}{\partial x_1} + \frac{3\omega_1}{2\rho}\Big(C_{(2,0,0)} - C_{(0,0,2)}\Big), \tag{3.33c}
$$
$$
\frac{\widetilde{\partial u_1}}{\partial x_2} + \frac{\widetilde{\partial u_2}}{\partial x_1} = -\frac{3\omega_1}{\rho}C_{(1,1,0)}, \tag{3.33d}
$$
$$
\frac{\widetilde{\partial u_1}}{\partial x_3} + \frac{\widetilde{\partial u_3}}{\partial x_1} = -\frac{3\omega_1}{\rho}C_{(1,0,1)}, \tag{3.33e}
$$
$$
\frac{\widetilde{\partial u_3}}{\partial x_2} + \frac{\widetilde{\partial u_2}}{\partial x_3} = -\frac{3\omega_1}{\rho}C_{(0,1,1)}, \tag{3.33f}
$$

are the approximations of the partial derivatives using cumulants.

The choice of relaxation frequencies ω_k, $k \in \{2, 3, \cdots, 10\}$ can be further improved. To increase the numerical accuracy of the CuLBM, the collisions of the four-order cumulants are

proposed in the form [78]

$$C_{(2,2,0)}^\star - 2C_{(2,0,2)}^\star + C_{(0,2,2)}^\star = (1 - \omega_6)\Big(C_{(2,2,0)} - 2C_{(2,0,2)} + C_{(0,2,2)}\Big)$$
$$+ \frac{2}{3}\left(\frac{1}{\omega_1} - \frac{1}{2}\right)\omega_6 A\rho\left(\widetilde{\frac{\partial u_1}{\partial x_1}} - 2\widetilde{\frac{\partial u_2}{\partial x_2}} + \widetilde{\frac{\partial u_3}{\partial x_3}}\right), \qquad (3.34a)$$

$$C_{(2,2,0)}^\star + C_{(2,0,2)}^\star - 2C_{(0,2,2)}^\star = (1 - \omega_6)\Big(C_{(2,2,0)} + C_{(2,0,2)} - 2C_{(0,2,2)}\Big)$$
$$+ \frac{2}{3}\left(\frac{1}{\omega_1} - \frac{1}{2}\right)\omega_6 A\rho\left(\widetilde{\frac{\partial u_1}{\partial x_1}} + \widetilde{\frac{\partial u_2}{\partial x_2}} - 2\widetilde{\frac{\partial u_3}{\partial x_3}}\right), \qquad (3.34b)$$

$$C_{(2,2,0)}^\star + C_{(2,0,2)}^\star + C_{(0,2,2)}^\star = (1 - \omega_7)\Big(C_{(2,2,0)} + C_{(2,0,2)} + C_{(0,2,2)}\Big)$$
$$- \frac{4}{3}\left(\frac{1}{\omega_1} - \frac{1}{2}\right)\omega_7 A\rho\left(\widetilde{\frac{\partial u_1}{\partial x_1}} + \widetilde{\frac{\partial u_2}{\partial x_2}} + \widetilde{\frac{\partial u_3}{\partial x_3}}\right), \qquad (3.34c)$$

$$C_{(2,1,1)}^\star = (1 - \omega_8)C_{(2,1,1)}$$
$$- \frac{1}{3}\left(\frac{1}{\omega_1} - \frac{1}{2}\right)\omega_8 B\rho\left(\widetilde{\frac{\partial u_3}{\partial x_2}} + \widetilde{\frac{\partial u_2}{\partial x_3}}\right), \qquad (3.34d)$$

$$C_{(1,2,1)}^\star = (1 - \omega_8)C_{(1,2,1)}$$
$$- \frac{1}{3}\left(\frac{1}{\omega_1} - \frac{1}{2}\right)\omega_8 B\rho\left(\widetilde{\frac{\partial u_3}{\partial x_1}} + \widetilde{\frac{\partial u_1}{\partial x_3}}\right), \qquad (3.34e)$$

$$C_{(1,1,2)}^\star = (1 - \omega_8)C_{(1,1,2)}$$
$$- \frac{1}{3}\left(\frac{1}{\omega_1} - \frac{1}{2}\right)\omega_8 B\rho\left(\widetilde{\frac{\partial u_2}{\partial x_1}} + \widetilde{\frac{\partial u_1}{\partial x_2}}\right), \qquad (3.34f)$$

$$(3.34g)$$

where parameters A, B are defined by

$$A = \frac{4\omega_1^2 + 2\omega_1\omega_2(\omega_1 - 6) + \omega_2^2(\omega_1(10 - 3\omega_1) - 4)}{(\omega_1 - \omega_2)(\omega_2(2 + 3\omega_1) - 8\omega_1)}, \qquad (3.35a)$$

$$B = \frac{4\omega_1\omega_2(9\omega_1 - 16) - 4\omega_1^2 - 2\omega_2^2(2 + 9\omega_1(\omega_1 - 2))}{3(\omega_1 - \omega_2)(\omega_2(2 + 3\omega_1) - 8\omega_1)}. \qquad (3.35b)$$

In Eqs.(3.35), however, A and B are undefined for $\omega_1 = \omega_2$ and $\omega_1 = \frac{2\omega_2}{8-3\omega_2}$. In this thesis $\omega_2 = 1$, thus $\omega_1 \neq 1$ and $\omega_1 \neq \frac{2}{5}$. Since $\omega_1 = \frac{2}{6\nu+1}$ and $\nu \ll 1$, the problematic point is not attained. Next, based on [78], the relaxation frequencies for the third-order moments are modified as follows

$$\omega_3 = \frac{8(\omega_1 - 2)(\omega_2(3\omega_1 - 1) - 5\omega_1)}{8(5 - 2\omega_1)\omega_1 + \omega_2(8 + \omega_1(9\omega_1 - 26))}, \qquad (3.36a)$$

$$\omega_4 = \frac{8(\omega_1 - 2)(\omega_1 + \omega_2(3\omega_1 - 7))}{\omega_2(56 - 42\omega_1 + 9\omega_1^2) - 8\omega_1}, \qquad (3.36b)$$

$$\omega_5 = \frac{24(\omega_1 - 2)\big(4\omega_1^2 + \omega_1\omega_2(18 - 13\omega_1) + \omega_2^2(2 + \omega_1(6\omega_1 - 11))\big)}{16\omega_1^2(\omega_1 - 6) - 2\omega_1\omega_2(216 + 5\omega_1(9\omega_1 - 46)) + \omega_2^2(\omega_1(3\omega_1 - 10)(15\omega_1 - 28) - 48)}. \qquad (3.36c)$$

If $\omega_2 = 1$ and $\omega_1 < \frac{7}{4}$, then the frequency ω_4 defined by Eq. (3.36b) is negative and thus not acceptable. Since Eqs. (3.36a) and (3.36c) have no requirements for ω_1 selection within the

interval $(0, 2)$, $\omega_1 \in \left(\frac{7}{4}, 2\right)$. Thus, the non-dimensional kinematic viscosity can be chosen in $\left(0, \frac{1}{42}\right)$.

If ω_2 tends to 2, the relaxation frequencies ω_3, ω_4, and ω_5 defined in Eq. (3.36) tend to 0. Thus, the relaxation is slow. To improve this behavior, a limiter for the relaxation frequencies of particular cumulants was proposed in [78] as

$$\omega_{120+102} = \omega_3 + \frac{(1-\omega_3)\left|C_{(1,2,0)} + C_{(1,0,2)}\right|}{\rho\lambda_3 + \left|C_{(1,2,0)} + C_{(1,0,2)}\right|}, \tag{3.37a}$$

$$\omega_{120-102} = \omega_3 + \frac{(1-\omega_4)\left|C_{(1,2,0)} - C_{(1,0,2)}\right|}{\rho\lambda_4 + \left|C_{(1,2,0)} - C_{(1,0,2)}\right|}, \tag{3.37b}$$

$$\omega_{111} = \omega_3 + \frac{(1-\omega_5)\left|C_{(1,1,1)}\right|}{\rho\lambda_5 + \left|C_{(1,1,1)}\right|}, \tag{3.37c}$$

where λ_3, λ_4, and λ_5 are constants set, for instance, to 0.01 [78]. The relaxation frequencies $\omega_{120+102}$, $\omega_{120-102}$, and ω_{111} with the permutations of the subscripts are used in Eqs.(3.30g)-(3.30m) as

$$C^{\star}_{(1,2,0)} + C^{\star}_{(1,0,2)} = (1-\omega_{120+102})\Big(C_{(1,2,0)} + C_{(1,0,2)}\Big), \tag{3.38a}$$

$$C^{\star}_{(2,1,0)} + C^{\star}_{(0,1,2)} = (1-\omega_{210+012})\Big(C_{(2,1,0)} + C_{(0,1,2)}\Big), \tag{3.38b}$$

$$C^{\star}_{(2,0,1)} + C^{\star}_{(0,2,1)} = (1-\omega_{201+021})\Big(C_{(2,0,1)} + C_{(0,2,1)}\Big), \tag{3.38c}$$

$$C^{\star}_{(1,2,0)} - C^{\star}_{(1,0,2)} = (1-\omega_{120-102})\Big(C_{(1,2,0)} - C_{(1,0,2)}\Big), \tag{3.38d}$$

$$C^{\star}_{(2,1,0)} - C^{\star}_{(0,1,2)} = (1-\omega_{210-012})\Big(C_{(2,1,0)} - C_{(0,1,2)}\Big), \tag{3.38e}$$

$$C^{\star}_{(2,0,1)} - C^{\star}_{(0,2,1)} = (1-\omega_{201-021})\Big(C_{(2,0,1)} - C_{(0,2,1)}\Big), \tag{3.38f}$$

$$C^{\star}_{(1,1,1)} = (1-\omega_{111})C_{(1,1,1)}. \tag{3.38g}$$

The LBM with such improved collision operator is further referred to as CuLBM2.

In addition to the collision operators mentioned above, there are other collision operators in literature. For example, the cascaded collision operator [76], the factorized central moment collision operator [74], the entropic multi-relaxation time collision operator [111], the central moment collision operator based on Fokker-Plank approximation [159], the hybrid recursive regularized collision operator [59], etc.

3.5 Forcing term

The commonly used strategy in the derivation of the LBM is to first set the action of volume forces to zero. After the derivation, the discrete forcing term is derived separately. Thus, for each collision operator, the incorporation of the forcing term can be different. To incorporate the force, the term $F_{\boldsymbol{i}}$ is added to the right-hand side of Eq. (3.5). The forms of forcing terms for particular collision operators can be found in [92, 118, 153]. In this thesis, we follow [80]. Hence, $F_{\boldsymbol{i}} = 0$ and the volume force is added to Eq. (3.7b) only. However, first-order cumulants are multiplied by -1 within the transformation to DDFs to include the effect of volume forces.

3.6   Initial conditions

The initialization of unknown variables is fundamental for simulating proper time evolution from the very beginning. In the case of real-world application problems, such as problems based on the observation of physical experiments, the initial condition is given in the form of macroscopic variables, such as the pressure and velocity. This initial condition is suitable for numerical methods that directly solve the macroscopic governing equations, such as the FEM, FVM, or FDM. However, the LBM works with DDFs. Thus, to initialize the unknown DDFs, additional information are needed. In general, to initialize unknown DDFs properly, all macroscopic moments need to be known. Since all macroscopic moments are usually not known, some approximations of unknown DDFs need to be employed at the initial step.

One of the commonly used approximations is based on setting unknown DDFs to their equilibrium (attractor) based on the initial value of pressure (density) and momentum [118]. Schematically, the initial condition can be written as

$$f_{\boldsymbol{i}}(\boldsymbol{x}, 0) = f_{\boldsymbol{i}}^{(eq)}(\rho_{\mathrm{ini}}(\boldsymbol{x}), \boldsymbol{u}_{\mathrm{ini}}(\boldsymbol{x})), \ \forall \boldsymbol{x} \in \widetilde{\Omega}, \ \forall \boldsymbol{i} \in \mathcal{Q}, \qquad (3.39)$$

where ρ_{ini} and $\boldsymbol{u}_{\mathrm{ini}}$ are the initial macroscopic conditions. This initial approximation suggests that the non-equilibrium part of the DDF can be neglected, that is, $f_i - f_i^{(eq)} = f_i^{(neq)} \approx 0$. Since the non-equilibrium part is related to the partial derivatives of $\boldsymbol{u}$, it works well for a constant initial velocity field [118].

A more sophisticated initial condition is the iterative initial condition proposed in [138]. It is based on the solution of the Poisson's equation for the initial velocity field using the LBM. The initial velocity field is fixed in the algorithm, and therefore only the zeroth-order moment is the collision invariant. There are two outputs of the algorithm. First, it produces a pressure field that satisfies the Poisson's equation. The second output of the algorithm are the DDFs from the final step of the iterative algorithm. These DDFs approximate the solution of the Poisson's equation and can be used as the initial approximation for the DDFs in the LBM algorithm for the main problem solved.

In this thesis, the first strategy described by Eq. (3.39) is used for simplicity since the iterative initial condition can prolong the simulation. Furthermore, in all cases, the simulation results are collected after several thousand iterations to minimize the effect of initial errors.

3.7   Boundary conditions

In Chapter 2, macroscopic BCs for the Navier-Stokes equations were introduced. In the mesoscopic description, BCs are a challenging problem and can not be generally classified into groups, such as the Dirichlet BC, Neumann BC, etc. Thus, we describe some macroscopic BC approximations suitable for the LBM that are used in this work. Without loss of generality, most BCs are described for the boundary face with the outward normal vector $\boldsymbol{n} = (1, 0, 0)^T$.

3.7.1   Periodic boundary condition

The periodic BCs are often chosen to approximate a large (infinite) domain by using only a small part of it.

A simple case of this type of BCs for a discrete domain in 2D is illustrated in Figure 3.4. In 3D, the topological interpretation is analogous.

In the LBM, the periodic BC is the condition for the streaming step, i.e., it extends the neighborhood for the boundary nodes according to the periodic rules. Thanks to the interpretation of this BC in the sense of DDFs, it causes no additional errors.
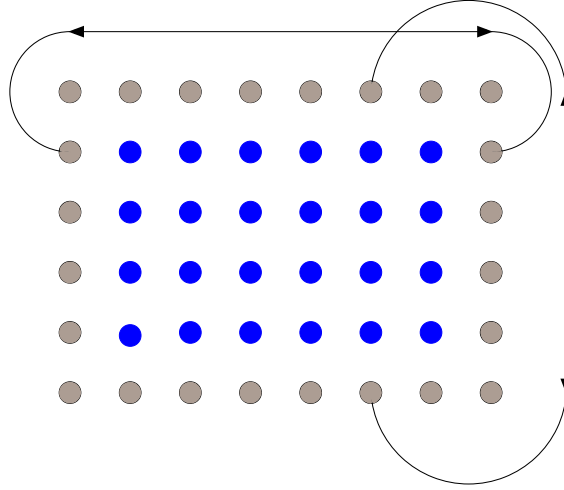
Figure 3.4: Schematic representation of periodic BCs in 2D.

3.7.2   Symmetric boundary condition

This BC assumes that the domain is symmetric with respect to a given mirror plane. In DDFs, the condition can be expressed as

$$f_{\boldsymbol{i}}(\boldsymbol{x}, t) = f_{\widetilde{\boldsymbol{i}}}^{\star}(\boldsymbol{x}, t - \Delta t), \tag{3.40}$$

where $\boldsymbol{x} \in \partial\widetilde{\Omega}$, $\widetilde{\boldsymbol{i}}$ is the mirrored direction with respect to the plane of the symmetry. In the case illustrated in Figure 3.5, the mirrored direction satisfies $\widetilde{\boldsymbol{i}} = \widetilde{(1, i_2, i_3)} = (-1, i_2, i_3)$ for $i_2, i_3 \in \{-1, 0, 1\}$. For the remaining boundary faces of $\partial\Omega$, the mirrored direction can be calculated analogously.
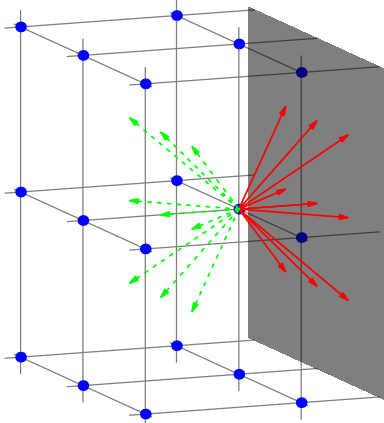
(a) The DDFs in fluid sites before the plane of symmetry. DDFs labeled by green dotted arrows are unknown.
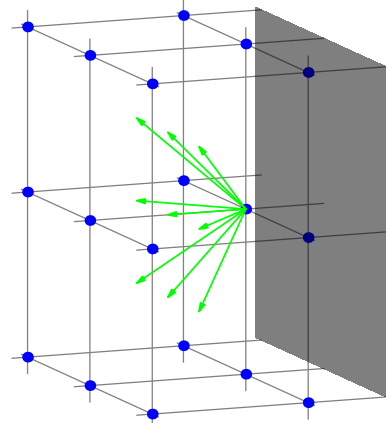
(b) The known DDFs were mirrored to obtain unknown green DDFs.

Figure 3.5: Schematic representation of the symmetric BC in 3D for D3Q27 velocity model. Blue points represent fluid sites. Gray plane represents the plane of symmetry. The unknown DDFs (green dotted arrows) in Figure (a) are obtained by the mirroring of known DDFs (solid red arrows) according to Eq. (3.40).

This BC modifies the streaming step only, i.e., other steps of the LBM algorithm are performed in the usual way.

3.7.3   Equilibrium boundary condition

One possibility is to approximate the unknown DDFs at the boundary nodes by equilibrium DDFs evaluated from the macroscopic density and velocity. Density ρ and velocity $\boldsymbol{u}$ are obtained from the prescribed macroscopic BC at the boundary sites $\boldsymbol{x} \in \partial\widetilde{\Omega}$ and all DDFs are set as [118]

$$f_{\boldsymbol{i}}(\boldsymbol{x}, t) = f_{\boldsymbol{i}}^{(eq)}(\rho(\boldsymbol{x}, t), \boldsymbol{u}(\boldsymbol{x}, t)), \forall \boldsymbol{i} \in \mathcal{Q}, \forall t \in \widetilde{\mathcal{T}}. \tag{3.41}$$

This type of BC is called the *wet-node* approach, since the site $\boldsymbol{x} \in \partial\widetilde{\Omega}$ is located at the boundary $\partial\Omega$. The disadvantage of this BC is that it neglects the non-equilibrium part.

3.7.4   Fullway bounce-back boundary condition

The fullway bounce-back BC reflects mesoscopic particle interaction with solid wall [168]. The particle with velocity $\boldsymbol{\xi}_{\boldsymbol{i}}$ bounces off the wall with velocity $\boldsymbol{\xi}_{\bar{\boldsymbol{i}}} = -\boldsymbol{\xi}_{\boldsymbol{i}}$. It implies that there is no flux through the boundary. Next, because of the final reverse motion of the particle, the fluid does not slip on the wall. As illustrated in Figure 3.6, two time steps are needed for the reflection. First, the known densities are streamed to the *ghost* sites in Figure 3.6b. Then, the DDFs in the *ghost* sites are reflected, and no collision is performed in these *ghost* sites. Finally, the reflected densities are streamed back to the domain $\widetilde{\Omega}$.

The boundary (wall) is located in the middle between the fluid site and the *ghost* site (blue and black points in Figure 3.6, respectively). Thus, the part of the boundary $\partial\widetilde{\Omega}$ represented by the fullway bounce-back BC is not a subset of $\partial\Omega$.

The time step from $t - \Delta t$ to t is illustrated by Figures 3.6a and 3.6b. The step at time t of the fullway bounce-back BC in a ghost site $\boldsymbol{x} \in \partial\widetilde{\Omega}$ can be written as

$$f_{\bar{\boldsymbol{i}}}(\boldsymbol{x}, t) = f_{\boldsymbol{i}}(\boldsymbol{x}, t), \forall \boldsymbol{i} \in \mathcal{Q}, \tag{3.42}$$

where $\bar{\boldsymbol{i}} = (-i_1, -i_2, -i_3)$, see Figures. 3.6b, 3.6c. Finally, the step from t to $t + \Delta t$ is illustrated by Figures 3.6c and 3.6d.

The advantages of the fullway bounce-back BC are its mass conservation and simple implementation, because no information about the wall location needs to be stored. The disadvantages are the accuracy (only second-order accurate in space [118]) and the *staircase* shape of the boundary. Thus, the curved boundaries are not resolved accurately [118].

Remark 3.2

An alternative to the fullway bounce-back BC is the halfway bounce-back BC. The halfway bounce-back BC reflects only the unknown DDFs and needs only one time step for the reflection. The disadvantage of the halfway bounce-back BC is that it is necessary to store information about which functions should be reflected [118].

3.7.5   Free outflow boundary condition

This BC is inspired by the outflow Neumann BC for the velocity. If the outward normal outflow boundary vector is $\boldsymbol{n} = (1, 0, 0)^T$, then the free outflow BC can be expressed as

$$f_{(-1, i_2, i_3)}(\boldsymbol{x}, t) = f_{(-1, i_2, i_3)}^{\star}(\boldsymbol{x} - \Delta x \boldsymbol{n}, t - \Delta t), \tag{3.43}$$

$\forall i_2, i_3 \in \{-1, 0, 1\}$ and for all $\boldsymbol{x}$ from the outflow part of $\partial\widetilde{\Omega}$. The drawback of this BC is the unphysical behavior of the velocity and pressure field near the outflow, which is investigated later in Chapter 5. The advantage of this BC is its good numerical stability.

The free outflow BC modifies the streaming step only, i.e., the other steps of the LBM algorithm are performed in the usual way.

(a) Step before the streaming at time $t - \Delta t$.

(b) Step after streaming at time t. The known DDFs were shifted to the sites behind the wall.

(c) Step of bounce-back. The red DDFs in the Fig 3.6b were reversed.

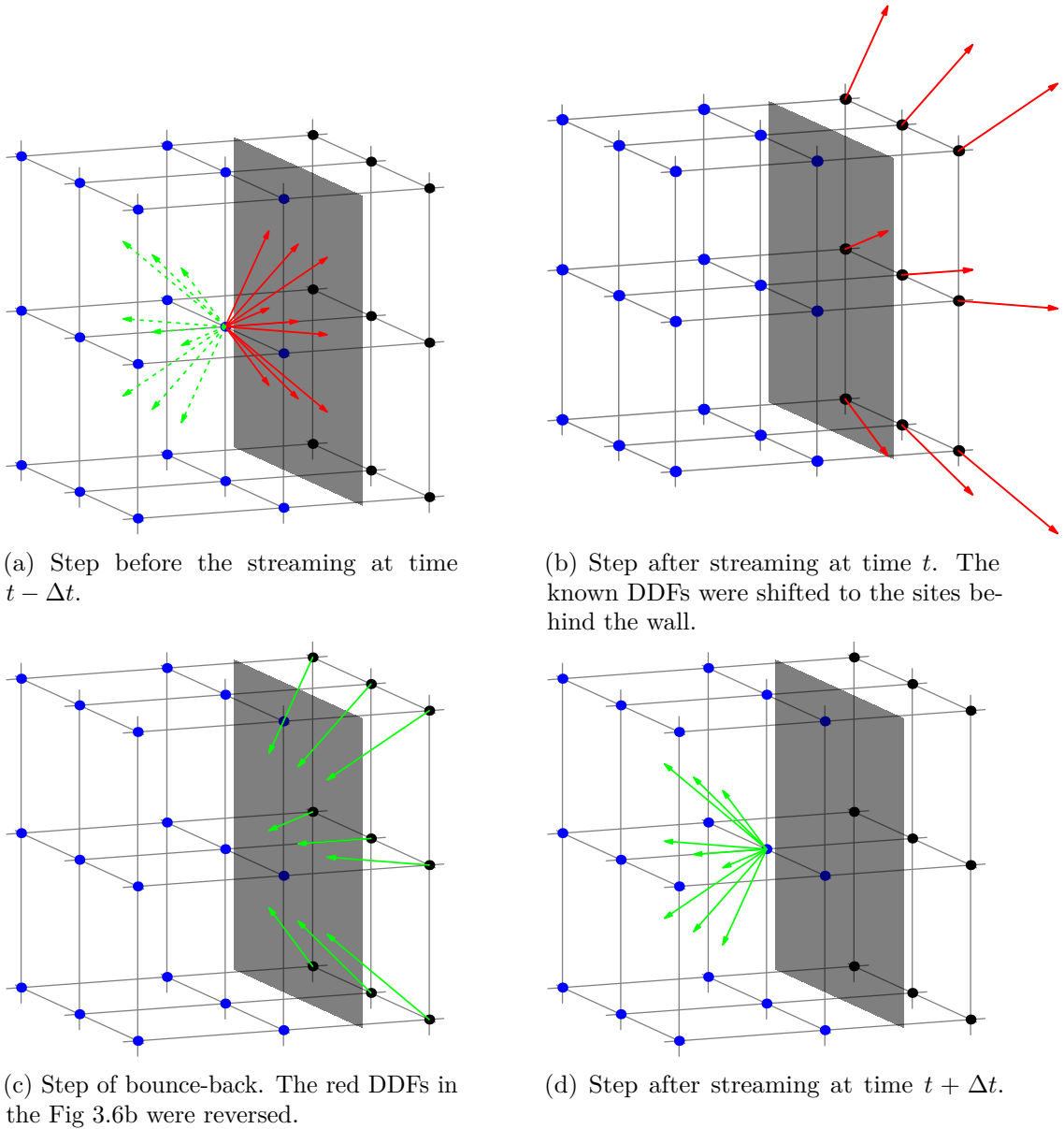(d) Step after streaming at time $t + \Delta t$.

Figure 3.6: Schematic representation of the fullway bounce-back BC in 3D for the velocity model D3Q27. Blue points represent fluid sites. Black points represent *ghost* sites behind the wall presented as a grey plane. The unknown and known DDFs are labeled by dashed and solid arrows, respectively.

3.7.6   Interpolated outflow boundary condition

Application of the free outflow BC (Section 3.7.5) or the equilibrium BC (Section 3.7.3) based on the macroscopic outflow BC often causes inconsistency between the prescribed macroscopic values and the obtained values at the outflow. Next, these outflow BCs often cause a reflection of acoustic waves in the pressure field. To improve these drawbacks, the BC with a reduced acoustic reflection was introduced in [80] as

$$f_{(-1,i_2,i_3)}(\boldsymbol{x},t) = (c_s - u_1)\frac{\Delta t}{\Delta x}f^{\star}_{(-1,i_2,i_3)}(\boldsymbol{x} - \Delta x\boldsymbol{n}, t - \Delta t)$$
$$+ \left(1 - (c_s - u_1)\frac{\Delta t}{\Delta x}\right)f^{\star}_{(-1,i_2,i_3)}(\boldsymbol{x},t - \Delta t), \tag{3.44}$$

where $i_2, i_3 \in \{-1,0,1\}$ and $\boldsymbol{x} \in \partial\widetilde{\Omega}$ is the outflow boundary with the outward normal vector $\boldsymbol{n} = (1,0,0)^T$ node, and $\boldsymbol{u} = (u_1, u_2, u_3)^T$. If $u_1 \ll c_s$, then Eq. (3.44) can be simplified into

$$f_{(-1,i_2,i_3)}(\boldsymbol{x},t) = f^{\star}_{(-1,i_2,i_3)}(\boldsymbol{x} - \Delta x\boldsymbol{n}, t - \Delta t)c_s\frac{\Delta t}{\Delta x} + \left(1 - c_s\frac{\Delta t}{\Delta x}\right)f^{\star}_{(-1,i_2,i_3)}(\boldsymbol{x},t - \Delta t). \tag{3.45}$$

Such BC is referred to as the *interpolated outflow BC without decomposition.*

Using the described interpolation, the outflow density (pressure) often does not correspond to the prescribed macroscopic value. To improve this drawback, we propose a modification of densities after the interpolation as

$$f_{\boldsymbol{i}} = \left(f_{\boldsymbol{i}} - f^{(eq)}_{\boldsymbol{i}}(\rho_a, \boldsymbol{u}_a)\right) + f^{(eq)}_{\boldsymbol{i}}(\rho_{\text{out}}, \boldsymbol{u}_a), \tag{3.46}$$

where ρ_{out} is the prescribed outflow density and ρ_a and $\boldsymbol{u}_a$ are the density and velocity, respectively, calculated from the DDFs right after the interpolation. The resulting BC is further referred to as the *interpolated outflow BC with decomposition.*

The interpolated outflow BC modifies the streaming step only, i.e., the other steps of the LBM algorithm are performed in the usual way.

3.7.7   Anti-bounce-back boundary condition

This BC is used for open boundaries with prescribed pressure. It is similar to the halfway bounce-back BC and the derivation can be found in [83, 84]. For the boundary with the outward normal vector $\boldsymbol{n} = (1,0,0)^T$, the anti-bounce-back BC can be expressed as

$$f_{(-1,i_2,i_3)}(\boldsymbol{x}, t + \Delta t) = -f^{\star}_{(1,i_2,i_3)}(\boldsymbol{x},t) + 2w_{(-1,i_2,i_3)}\rho_{\text{out}}\left(1 + \frac{\left(\boldsymbol{\xi}_{(-1,i_2,i_3)} \cdot \boldsymbol{u}_{\text{out}}\right)^2}{2c_s^4} - \frac{\boldsymbol{u}_{\text{out}} \cdot \boldsymbol{u}_{\text{out}}}{2c_s^2}\right), \tag{3.47}$$

where $i_2, i_3 \in \{-1,0,1\}$, ρ_{out} is the specified boundary value of density (pressure), $\boldsymbol{u}_{\text{out}}$ is the outflow condition for velocity, and $\boldsymbol{x}$ is the boundary site. Regarding the bounce-back method, the boundary is placed at $\frac{\Delta x}{2}$ away in the normal direction $\boldsymbol{n}$ from the boundary site $\boldsymbol{x}$. Since the value of $\boldsymbol{u}_{\text{out}}$ is often not known, there are two options for its approximation. First, the corresponding macroscopic BC can be used or the value can be extrapolated as in [103] as

$$\boldsymbol{u}_{\text{out}}\left(\boldsymbol{x} + \frac{1}{2}\boldsymbol{n}, t\right) \approx \boldsymbol{u}(\boldsymbol{x},t) + \frac{1}{2}\left[\boldsymbol{u}(\boldsymbol{x},t) - \boldsymbol{u}(\boldsymbol{x} - \boldsymbol{n}, t)\right]. \tag{3.48}$$

The anti-bounce-back BC modifies the streaming step only, i.e., the other steps of the LBM algorithm are performed in the usual way.

3.7.8   Moment-based boundary condition

An alternative approach to the previous BCs is the moment-based BC, which reconstructs the unknown DDFs from the known DDFs and known macroscopic moments. This BC was introduced for the D3Q19 velocity model in [115]. In this thesis, the moment-based BCs are extended for the velocity model D3Q27 [51].

The moment-based BCs are not as general as the fullway bounce-back BC. For every specific set of unknown DDFs, the moment-based BC must be separately derived. In this thesis, the moment-based BCs are applied only for parts of the boundary of the cuboidal domain.

The assumption of moment-based BCs is that all discrete macroscopic moments m_j defined by Eq. (3.15) are known. Since the transformation matrix between DDFs and raw moments is non-singular, arbitrary number of unknown DDFs can be expressed using raw moments and known DDFs. As will be illustrated later, in some cases, different combinations of raw moments can be used in the expression of unknown DDFs. It is recommended to use the raw moments with the lowest possible order since these moments usually have a better physical interpretation. If the velocity is given, the density is expressed using the velocity and the known DDFs, and vice versa.

The boundary of the cuboidal domain Ω is composed of 6 faces, 12 edges, and 8 corners, see Figure 3.7. For each of these parts, the moment-based BC has a different form. For brevity, moment-based BCs are derived for one representative of a face, edge, and corner.
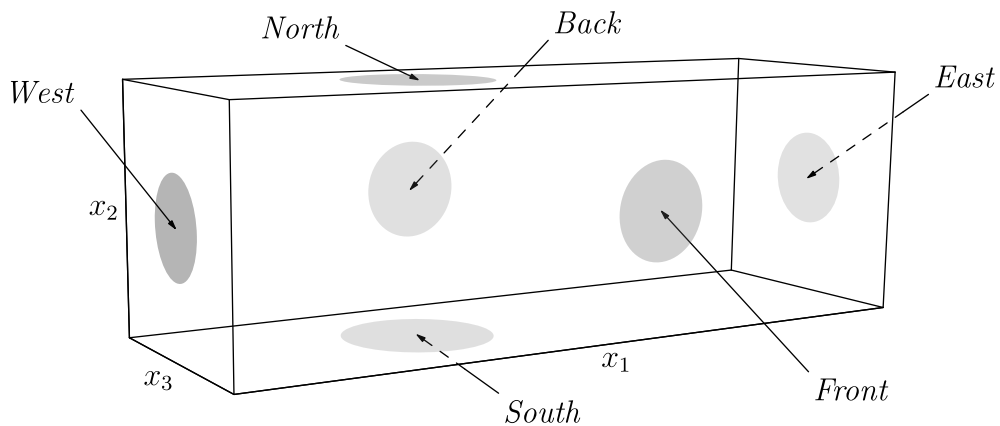

Figure 3.7: Illustration of the computational domain Ω with labels of faces.

Face

Here we explore the derivation of the moment-based BC for the face labeled as *West-boundary* with the inner normal vector $\boldsymbol{n} = (1, 0, 0)^T$.

Using combinations of Eqs. (3.7a) and (3.7b), the known DDFs can be expressed as

$$
\begin{aligned}
\rho(1 - u_1) = \Big(& f_{(0,1,-1)} + 2f_{(-1,1,-1)} + f_{(0,-1,0)} + f_{(0,1,0)} + 2f_{(-1,0,-1)} + f_{(0,-1,1)} \\
& + 2f_{(-1,-1,1)} + f_{(0,0,-1)} + f_{(0,0,1)} + f_{(0,0,0)} + 2f_{(-1,1,0)} + f_{(0,-1,-1)} + 2f_{(-1,-1,-1)} \\
& + f_{(0,1,1)} + 2f_{(-1,1,1)} + 2f_{(-1,0,0)} + 2f_{(-1,0,1)} + 2f_{(-1,-1,0)} \Big).
\end{aligned}
\tag{3.49}
$$

In all considered cases, the low Mach number condition is assumed, thus $u_1 \ll c_s = \frac{1}{\sqrt{3}}$, Eq. (3.49) can be used to express the unknown density ρ or velocity u_1.

The nine unknown DDFs are $f_{(1,0,-1)}$, $f_{(1,1,-1)}$, $f_{(1,0,0)}$, $f_{(1,1,0)}$, $f_{(1,-1,1)}$, $f_{(1,-1,0)}$, $f_{(1,0,1)}$, $f_{(1,-1,-1)}$, and $f_{(1,1,1)}$. In Table 3.1, the raw moments are categorized into groups according to the combination of unknown DDFs. In each group, a moment is selected for the expression of unknown DDFs. The selection of the moment $m_\star$ in the first group depends on the boundary type. We set $m_\star = m_{(0,0,0)}$ or $m_\star = m_{(1,0,0)}$, if the Dirichlet BC is specified for pressure or velocity, respectively.

#	Moments	Unknown f_i combinations	Selected
1	$m_{(0,0,0)}, m_{(1,0,0)}, m_{(2,0,0)}$	$f_{(1,-1,1)} + f_{(1,-1,0)} + f_{(1,0,1)} + f_{(1,-1,-1)} + f_{(1,1,1)} + f_{(1,0,-1)}$ $+f_{(1,1,-1)} + f_{(1,0,0)} + f_{(1,1,0)}$	$m_\star$
2	$m_{(0,1,0)}, m_{(1,1,0)}, m_{(2,1,0)}$	$-f_{(1,-1,1)} - f_{(1,-1,0)} - f_{(1,-1,-1)} + f_{(1,1,1)} + f_{(1,1,-1)} + f_{(1,1,0)}$	$m_{(0,1,0)}$
3	$m_{(0,0,1)}, m_{(1,0,1)}, m_{(2,0,1)}$	$f_{(1,-1,1)} + f_{(1,0,1)} - f_{(1,-1,-1)} + f_{(1,1,1)} - f_{(1,0,-1)} - f_{(1,1,-1)}$	$m_{(0,0,1)}$
4	$m_{(0,1,1)}$	$-f_{(1,-1,1)} + f_{(1,-1,-1)} + f_{(1,1,1)} - f_{(1,1,-1)}$	$m_{(0,1,1)}$
5	$m_{(0,2,0)}, m_{(1,2,0)}, m_{(2,2,0)}$	$f_{(1,-1,1)} + f_{(1,-1,0)} + f_{(1,-1,-1)} + f_{(1,1,1)} + f_{(1,1,-1)} + f_{(1,1,0)}$	$m_{(0,2,0)}$
6	$m_{(0,0,2)}, m_{(1,0,2)}, m_{(2,0,2)}$	$f_{(1,-1,1)} + f_{(1,0,1)} + f_{(1,-1,-1)} + f_{(1,1,1)} + f_{(1,0,-1)} + f_{(1,1,-1)}$	$m_{(0,0,2)}$
7	$m_{(0,2,1)}$	$f_{(1,-1,1)} - f_{(1,-1,-1)} + f_{(1,1,1)} - f_{(1,1,-1)}$	$m_{(0,2,1)}$
8	$m_{(0,1,2)}$	$-f_{(1,-1,1)} - f_{(1,-1,-1)} + f_{(1,1,1)} + f_{(1,1,-1)}$	$m_{(0,1,2)}$
9	$m_{(0,2,2)}$	$f_{(1,-1,1)} + f_{(1,-1,-1)} + f_{(1,1,1)} + f_{(1,1,-1)}$	$m_{(0,2,2)}$

Table 3.1: Raw moment categorization based on the combination of unknown DDFs. The selected moments are used for the expression of unknown DDFs with $m_\star = m_{(0,0,0)}$ or $m_\star = m_{(1,0,0)}$ for unknown velocity or pressure, respectively.

Based on the selection in Table 3.1, the unknown density functions are expressed as

$$
\begin{pmatrix}
f_{(1,0,0)} \\
f_{(1,1,0)} \\
f_{(1,-1,0)} \\
f_{(1,0,1)} \\
f_{(1,0,-1)} \\
f_{(1,1,1)} \\
f_{(1,1,-1)} \\
f_{(1,-1,1)} \\
f_{(1,-1,-1)}
\end{pmatrix}
= \mathbb{A}_f
\begin{pmatrix}
f_{(0,0,0)} \\
f_{(0,1,0)} \\
f_{(0,0,1)} \\
f_{(-1,0,0)} \\
f_{(0,-1,0)} \\
f_{(0,0,-1)} \\
f_{(0,1,1)} \\
f_{(0,1,-1)} \\
f_{(0,-1,1)} \\
f_{(0,-1,-1)} \\
f_{(-1,1,0)} \\
f_{(-1,-1,0)} \\
f_{(-1,0,1)} \\
f_{(-1,0,-1)} \\
f_{(-1,1,1)} \\
f_{(-1,1,-1)} \\
f_{(-1,-1,1)} \\
f_{(-1,-1,-1)}
\end{pmatrix}
+ \mathbb{A}_m
\begin{pmatrix}
m_{(1,0,0)} \\
m_{(0,1,0)} \\
m_{(0,0,1)} \\
m_{(0,1,1)} \\
m_{(0,2,0)} \\
m_{(0,0,2)} \\
m_{(0,2,1)} \\
m_{(0,1,2)} \\
m_{(0,2,2)}
\end{pmatrix},
\tag{3.50a}
$$

where

$$
\mathbb{A}_f =
\begin{pmatrix}
0 & 1 & 1 & 1 & 1 & 1 & 1 & 1 & 1 & 1 & 2 & 2 & 2 & 2 & 2 & 2 & 2 & 2 \\
0 & -1 & 0 & 0 & 0 & 0 & 0 & 0 & 0 & 0 & -1 & 0 & 0 & 0 & 0 & 0 & 0 & 0 \\
0 & 0 & 0 & 0 & -1 & 0 & 0 & 0 & 0 & 0 & 0 & -1 & 0 & 0 & 0 & 0 & 0 & 0 \\
0 & 0 & -1 & 0 & 0 & 0 & 0 & 0 & 0 & 0 & 0 & 0 & -1 & 0 & 0 & 0 & 0 & 0 \\
0 & 0 & 0 & 0 & 0 & -1 & 0 & 0 & 0 & 0 & 0 & 0 & 0 & -1 & 0 & 0 & 0 & 0 \\
0 & 0 & 0 & 0 & 0 & 0 & -1 & 0 & 0 & 0 & 0 & 0 & 0 & 0 & -1 & 0 & 0 & 0 \\
0 & 0 & 0 & 0 & 0 & 0 & 0 & -1 & 0 & 0 & 0 & 0 & 0 & 0 & 0 & -1 & 0 & 0 \\
0 & 0 & 0 & 0 & 0 & 0 & 0 & 0 & -1 & 0 & 0 & 0 & 0 & 0 & 0 & 0 & -1 & 0 \\
0 & 0 & 0 & 0 & 0 & 0 & 0 & 0 & 0 & -1 & 0 & 0 & 0 & 0 & 0 & 0 & 0 & -1
\end{pmatrix},
\tag{3.50b}
$$

and

$$
\mathbb{A}_m =
\begin{pmatrix}
1 & 0 & 0 & 0 & -1 & -1 & 0 & 0 & 1 \\
0 & \frac{1}{2} & 0 & 0 & \frac{1}{2} & 0 & 0 & -\frac{1}{2} & -\frac{1}{2} \\
0 & -\frac{1}{2} & 0 & 0 & \frac{1}{2} & 0 & 0 & \frac{1}{2} & -\frac{1}{2} \\
0 & 0 & \frac{1}{2} & 0 & 0 & \frac{1}{2} & -\frac{1}{2} & 0 & -\frac{1}{2} \\
0 & 0 & -\frac{1}{2} & 0 & 0 & \frac{1}{2} & \frac{1}{2} & 0 & -\frac{1}{2} \\
0 & 0 & 0 & \frac{1}{4} & 0 & 0 & \frac{1}{4} & \frac{1}{4} & \frac{1}{4} \\
0 & 0 & 0 & -\frac{1}{4} & 0 & 0 & -\frac{1}{4} & \frac{1}{4} & \frac{1}{4} \\
0 & 0 & 0 & -\frac{1}{4} & 0 & 0 & \frac{1}{4} & -\frac{1}{4} & \frac{1}{4} \\
0 & 0 & 0 & \frac{1}{4} & 0 & 0 & -\frac{1}{4} & -\frac{1}{4} & \frac{1}{4}
\end{pmatrix}.
\tag{3.50c}
$$

The selected raw moments in Table 3.1 are set as

$$
\begin{aligned}
m_{(1,0,0)} &= \rho u_1, \\
m_{(0,1,0)} &= \rho u_2, \\
m_{(0,0,1)} &= \rho u_3, \\
m_{(0,1,1)} &= \rho u_2 u_3, \\
m_{(0,2,0)} &= \frac{1}{3}\rho + \rho u_2 u_2, \\
m_{(0,0,2)} &= \frac{1}{3}\rho + \rho u_3 u_3, \\
m_{(0,2,1)} &= \frac{1}{3}\rho u_3 + \rho u_2 u_2 u_3, \\
m_{(0,1,2)} &= \frac{1}{3}\rho u_2 + \rho u_2 u_3 u_3, \\
m_{(0,2,2)} &= \frac{1}{9}\rho + \frac{1}{3}\rho u_2 u_2 + \frac{1}{3}\rho u_3 u_3 + \rho u_2 u_2 u_3 u_3.
\end{aligned}
\tag{3.50d}
$$

The moments are set to their Maxwell-Boltzmann equilibrium. The first order moments are set accurately. Nevertheless, the higher-order moments are only approximated since the non-equilibrium part is neglected.

Next, the moment-based BCs for an edge and a corner are derived for boundary with the Dirichlet BC for velocity only. The moment-based BCs for specified pressure Dirichlet BC can be derived analogously.

Edge

The edge between faces with inner normal vectors $\boldsymbol{n} = (1,0,0)^T$ and $\boldsymbol{n} = (0,-1,0)^T$ is labeled as *West-North* edge, see Figure 3.7. For this part of the boundary, fifteen DDFs are unknown. If the velocity is given, the unknown density can be computed as

$$
\begin{aligned}
\rho = -\frac{1}{-1 + u_1(1+u_2) - u_2} \Big(&2f_{(-1,0,1)} + 2f_{(0,1,-1)} + 4f_{(-1,1,-1)} + 2f_{(0,1,0)} + 2f_{(-1,0,-1)} \\
&+ f_{(0,0,-1)} + f_{(0,0,1)} + f_{(0,0,0)} + 4f_{(-1,1,0)} + 2f_{(0,1,1)} \\
&+ 4f_{(-1,1,1)} + 2f_{(-1,0,0)} \Big).
\end{aligned}
\tag{3.51}
$$

The raw moments are classified into groups given in Table 3.2. The moments in Table 3.2 are selected of the lowest order to maintaining non-singularity of the linear system for unknown

#	Moments	Unknown f_i combinations	Selected
1	$m_{(0,0,0)}$	$f_{(1,1,-1)} + f_{(1,0,0)} + f_{(1,1,0)} + f_{(-1,-1,0)} + f_{(0,-1,0)} + f_{(1,-1,1)} + f_{(1,-1,0)} + f_{(1,0,1)} + f_{(0,-1,1)}$ $+f_{(-1,-1,1)} + f_{(1,-1,-1)} + f_{(1,1,1)} + f_{(1,0,-1)} + f_{(0,-1,-1)} + f_{(-1,-1,-1)}$	–
2	$m_{(1,0,0)}$	$f_{(1,1,-1)} + f_{(1,0,0)} + f_{(1,1,0)} - f_{(-1,-1,0)} + f_{(1,-1,1)} + f_{(1,-1,0)} + f_{(1,0,1)} - f_{(-1,-1,1)} + f_{(1,-1,-1)}$ $+f_{(1,1,1)} + f_{(1,0,-1)} - f_{(-1,-1,-1)}$	$m_{(1,0,0)}$
3	$m_{(0,1,0)}$	$f_{(1,1,-1)} + f_{(1,1,0)} - f_{(-1,-1,0)} - f_{(0,-1,0)} - f_{(1,-1,1)} - f_{(1,-1,0)} - f_{(0,-1,1)} - f_{(-1,-1,1)} - f_{(1,-1,-1)}$ $+f_{(1,1,1)} - f_{(0,-1,-1)} - f_{(-1,-1,-1)}$	$m_{(0,1,0)}$
4	$m_{(0,0,1)}$	$-f_{(1,1,-1)} + f_{(1,-1,1)} + f_{(1,0,1)} + f_{(0,-1,1)} + f_{(-1,-1,1)} - f_{(1,-1,-1)} + f_{(1,1,1)} - f_{(1,0,-1)} - f_{(0,-1,-1)}$ $-f_{(-1,-1,-1)}$	$m_{(0,0,1)}$
5	$m_{(1,1,0)}$	$f_{(1,1,-1)} + f_{(1,1,0)} + f_{(-1,-1,0)} - f_{(1,-1,1)} - f_{(1,-1,0)} + f_{(-1,-1,1)} - f_{(1,-1,-1)} + f_{(1,1,1)} + f_{(-1,-1,-1)}$	$m_{(1,1,0)}$
6	$m_{(1,0,1)}$	$-f_{(1,1,-1)} + f_{(1,-1,1)} + f_{(1,0,1)} - f_{(-1,-1,1)} - f_{(1,-1,-1)} + f_{(1,1,1)} - f_{(1,0,-1)} + f_{(-1,-1,-1)}$	$m_{(1,0,1)}$
7	$m_{(0,1,1)}$	$-f_{(1,1,-1)} - f_{(1,-1,1)} - f_{(0,-1,1)} - f_{(-1,-1,1)} + f_{(1,-1,-1)} + f_{(1,1,1)} + f_{(0,-1,-1)} + f_{(-1,-1,-1)}$	$m_{(0,1,1)}$
8	$m_{(2,0,0)}$	$f_{(1,1,-1)} + f_{(1,0,0)} + f_{(1,1,0)} + f_{(-1,-1,0)} + f_{(1,-1,1)} + f_{(1,-1,0)} + f_{(1,0,1)} + f_{(-1,-1,1)} + f_{(1,-1,-1)}$ $+f_{(1,1,1)} + f_{(1,0,-1)} + f_{(-1,-1,-1)}$	$m_{(2,0,0)}$
9	$m_{(0,2,0)}$	$f_{(1,1,-1)} + f_{(1,1,0)} + f_{(-1,-1,0)} + f_{(0,-1,0)} + f_{(1,-1,1)} + f_{(1,-1,0)} + f_{(0,-1,1)} + f_{(-1,-1,1)} + f_{(1,-1,-1)}$ $+f_{(1,1,1)} + f_{(0,-1,-1)} + f_{(-1,-1,-1)}$	$m_{(0,2,0)}$
10	$m_{(0,0,2)}$	$f_{(1,1,-1)} + f_{(1,-1,1)} + f_{(1,0,1)} + f_{(0,-1,1)} + f_{(-1,-1,1)} + f_{(1,-1,-1)} + f_{(1,1,1)} + f_{(1,0,-1)} + f_{(0,-1,-1)}$ $+f_{(-1,-1,-1)}$	$m_{(0,0,2)}$
11	$m_{(2,1,0)}$	$f_{(1,1,-1)} + f_{(1,1,0)} - f_{(-1,-1,0)} - f_{(1,-1,1)} - f_{(1,-1,0)} - f_{(-1,-1,1)} - f_{(1,-1,-1)} + f_{(1,1,1)} - f_{(-1,-1,-1)}$	–
12	$m_{(2,0,1)}$	$-f_{(1,1,-1)} + f_{(1,-1,1)} + f_{(1,0,1)} + f_{(-1,-1,1)} - f_{(1,-1,-1)} + f_{(1,1,1)} - f_{(1,0,-1)} - f_{(-1,-1,-1)}$	$m_{(2,0,1)}$
13	$m_{(1,2,0)}$	$f_{(1,1,-1)} + f_{(1,1,0)} - f_{(-1,-1,0)} + f_{(1,-1,1)} + f_{(1,-1,0)} - f_{(-1,-1,1)} + f_{(1,-1,-1)} + f_{(1,1,1)} - f_{(-1,-1,-1)}$	–
14	$m_{(0,2,1)}$	$-f_{(1,1,-1)} + f_{(1,-1,1)} + f_{(0,-1,1)} + f_{(-1,-1,1)} - f_{(1,-1,-1)} + f_{(1,1,1)} - f_{(0,-1,-1)} - f_{(-1,-1,-1)}$	$m_{(0,2,1)}$
15	$m_{(1,0,2)}$	$f_{(1,1,-1)} + f_{(1,-1,1)} + f_{(1,0,1)} - f_{(-1,-1,1)} + f_{(1,-1,-1)} + f_{(1,1,1)} + f_{(1,0,-1)} - f_{(-1,-1,-1)}$	$m_{(1,0,2)}$
16	$m_{(0,1,2)}$	$f_{(1,1,-1)} - f_{(1,-1,1)} - f_{(0,-1,1)} - f_{(-1,-1,1)} - f_{(1,-1,-1)} + f_{(1,1,1)} - f_{(0,-1,-1)} - f_{(-1,-1,-1)}$	$m_{(0,1,2)}$
17	$m_{(2,2,0)}$	$f_{(1,1,-1)} + f_{(1,1,0)} + f_{(-1,-1,0)} + f_{(1,-1,1)} + f_{(1,-1,0)} + f_{(-1,-1,1)} + f_{(1,-1,-1)} + f_{(1,1,1)} + f_{(-1,-1,-1)}$	–
18	$m_{(2,0,2)}$	$f_{(1,1,-1)} + f_{(1,-1,1)} + f_{(1,0,1)} + f_{(-1,-1,1)} + f_{(1,-1,-1)} + f_{(1,1,1)} + f_{(1,0,-1)} + f_{(-1,-1,-1)}$	$m_{(2,0,2)}$
19	$m_{(0,2,2)}$	$f_{(1,1,-1)} + f_{(1,-1,1)} + f_{(0,-1,1)} + f_{(-1,-1,1)} + f_{(1,-1,-1)} + f_{(1,1,1)} + f_{(0,-1,-1)} + f_{(-1,-1,-1)}$	$m_{(0,2,2)}$

Table 3.2: Raw moment categorization based on the combination of unknown DDFs for edge *West-North*. The selected moments are used for the expression of the unknown DDFs. Since the Dirichlet BC for velocity is considered, the first moment is not chosen.

DDFs. Based on the selection of raw moments in Table 3.2, the unknown DDFs are expressed as

$$
\begin{pmatrix}
f_{(1,0,0)} \\
f_{(0,-1,0)} \\
f_{(0,-1,1)} \\
f_{(0,-1,-1)} \\
f_{(1,1,0)} \\
f_{(1,-1,0)} \\
f_{(-1,-1,0)} \\
f_{(1,0,1)} \\
f_{(1,0,-1)} \\
f_{(1,1,1)} \\
f_{(1,1,-1)} \\
f_{(1,-1,1)} \\
f_{(1,-1,-1)} \\
f_{(-1,-1,1)} \\
f_{(-1,-1,-1)}
\end{pmatrix}
= \mathbb{A}_f
\begin{pmatrix}
f_{(0,0,0)} \\
f_{(0,1,0)} \\
f_{(0,0,1)} \\
f_{(-1,0,0)} \\
f_{(0,0,-1)} \\
f_{(0,1,1)} \\
f_{(0,1,-1)} \\
f_{(-1,1,0)} \\
f_{(-1,0,1)} \\
f_{(-1,0,-1)} \\
f_{(-1,1,1)} \\
f_{(-1,1,-1)}
\end{pmatrix}
+ \mathbb{A}_m
\begin{pmatrix}
m_{(1,0,0)} \\
m_{(0,1,0)} \\
m_{(0,0,1)} \\
m_{(1,1,0)} \\
m_{(1,0,1)} \\
m_{(0,1,1)} \\
m_{(2,0,0)} \\
m_{(0,2,0)} \\
m_{(0,0,2)} \\
m_{(2,0,1)} \\
m_{(0,2,1)} \\
m_{(1,0,2)} \\
m_{(0,1,2)} \\
m_{(2,0,2)} \\
m_{(0,2,2)}
\end{pmatrix},
\tag{3.52a}
$$

where

$$
\mathbb{A}_f =
\begin{pmatrix}
0 & 2 & 1 & 1 & 1 & 2 & 2 & 4 & 2 & 2 & 4 & 4 \\
0 & 1 & 1 & 2 & 1 & 2 & 2 & 4 & 2 & 2 & 4 & 4 \\
0 & 0 & -1 & 0 & 0 & -1 & 0 & 0 & 0 & 0 & 0 & 0 \\
0 & 0 & 0 & 0 & -1 & 0 & -1 & 0 & 0 & 0 & 0 & 0 \\
0 & -1 & 0 & 0 & 0 & 0 & 0 & -1 & 0 & 0 & 0 & 0 \\
0 & -1 & -1 & -1 & -1 & -2 & -2 & -3 & -2 & -2 & -4 & -4 \\
0 & 0 & 0 & -1 & 0 & 0 & 0 & -1 & 0 & 0 & 0 & 0 \\
0 & 0 & -1 & 0 & 0 & 0 & 0 & 0 & -1 & 0 & 0 & 0 \\
0 & 0 & 0 & 0 & -1 & 0 & 0 & 0 & 0 & -1 & 0 & 0 \\
0 & 0 & 0 & 0 & 0 & -1 & 0 & 0 & 0 & 0 & -1 & 0 \\
0 & 0 & 0 & 0 & 0 & 0 & -1 & 0 & 0 & 0 & 0 & -1 \\
0 & 0 & 1 & 0 & 0 & 1 & 0 & 0 & 1 & 0 & 1 & 0 \\
0 & 0 & 0 & 0 & 1 & 0 & 1 & 0 & 0 & 1 & 0 & 1 \\
0 & 0 & 0 & 0 & 0 & 0 & 0 & 0 & -1 & 0 & -1 & 0 \\
0 & 0 & 0 & 0 & 0 & 0 & 0 & 0 & 0 & -1 & 0 & -1
\end{pmatrix},
\tag{3.52b}
$$

and

$$
\mathbb{A}_m =
\begin{pmatrix}
1 & -1 & 0 & 1 & 0 & 0 & 0 & -1 & -1 & 0 & 0 & 0 & 0 & 0 & 1 \\
1 & -1 & 0 & 1 & 0 & 0 & -1 & 0 & -1 & 0 & 0 & 0 & 0 & 1 & 0 \\
0 & 0 & \tfrac{1}{2} & 0 & 0 & 0 & 0 & 0 & \tfrac{1}{2} & -\tfrac{1}{2} & 0 & 0 & 0 & -\tfrac{1}{2} & 0 \\
0 & 0 & -\tfrac{1}{2} & 0 & 0 & 0 & 0 & 0 & \tfrac{1}{2} & \tfrac{1}{2} & 0 & 0 & 0 & -\tfrac{1}{2} & 0 \\
0 & \tfrac{1}{2} & 0 & 0 & 0 & 0 & 0 & \tfrac{1}{2} & 0 & 0 & 0 & 0 & -\tfrac{1}{2} & 0 & -\tfrac{1}{2} \\
-\tfrac{1}{2} & \tfrac{1}{2} & 0 & -1 & 0 & 0 & \tfrac{1}{2} & \tfrac{1}{2} & 1 & 0 & 0 & -\tfrac{1}{2} & \tfrac{1}{2} & -\tfrac{1}{2} & -\tfrac{1}{2} \\
-\tfrac{1}{2} & 0 & 0 & 0 & 0 & 0 & \tfrac{1}{2} & 0 & 0 & 0 & 0 & \tfrac{1}{2} & 0 & -\tfrac{1}{2} & 0 \\
0 & 0 & \tfrac{1}{2} & 0 & 0 & 0 & 0 & 0 & \tfrac{1}{2} & 0 & -\tfrac{1}{2} & 0 & 0 & 0 & -\tfrac{1}{2} \\
0 & 0 & -\tfrac{1}{2} & 0 & 0 & 0 & 0 & 0 & \tfrac{1}{2} & 0 & \tfrac{1}{2} & 0 & 0 & 0 & -\tfrac{1}{2} \\
0 & 0 & 0 & 0 & 0 & \tfrac{1}{4} & 0 & 0 & 0 & 0 & \tfrac{1}{4} & 0 & \tfrac{1}{4} & 0 & \tfrac{1}{4} \\
0 & 0 & 0 & 0 & 0 & -\tfrac{1}{4} & 0 & 0 & 0 & 0 & -\tfrac{1}{4} & 0 & \tfrac{1}{4} & 0 & \tfrac{1}{4} \\
0 & 0 & -\tfrac{1}{2} & 0 & \tfrac{1}{4} & -\tfrac{1}{4} & 0 & 0 & -\tfrac{1}{2} & \tfrac{1}{4} & \tfrac{1}{4} & \tfrac{1}{4} & -\tfrac{1}{4} & \tfrac{1}{4} & \tfrac{1}{4} \\
0 & 0 & \tfrac{1}{2} & 0 & -\tfrac{1}{4} & \tfrac{1}{4} & 0 & 0 & -\tfrac{1}{2} & -\tfrac{1}{4} & -\tfrac{1}{4} & \tfrac{1}{4} & -\tfrac{1}{4} & \tfrac{1}{4} & \tfrac{1}{4} \\
0 & 0 & 0 & 0 & -\tfrac{1}{4} & 0 & 0 & 0 & 0 & \tfrac{1}{4} & 0 & -\tfrac{1}{4} & 0 & \tfrac{1}{4} & 0 \\
0 & 0 & 0 & 0 & \tfrac{1}{4} & 0 & 0 & 0 & 0 & -\tfrac{1}{4} & 0 & -\tfrac{1}{4} & 0 & \tfrac{1}{4} & 0
\end{pmatrix}.
\tag{3.52c}
$$

The selected raw moments in Table 3.2 are set as

$$
\begin{aligned}
m_{(1,0,0)} &= \rho u_1, \\
m_{(0,1,0)} &= \rho u_2, \\
m_{(0,0,1)} &= \rho u_3, \\
m_{(1,1,0)} &= \rho u_1 u_2, \\
m_{(1,0,1)} &= \rho u_1 u_3, \\
m_{(0,1,1)} &= \rho u_2 u_3, \\
m_{(2,0,0)} &= \frac{1}{3}\rho + \rho u_1 u_1, \\
m_{(0,2,0)} &= \frac{1}{3}\rho + \rho u_2 u_2, \\
m_{(0,0,2)} &= \frac{1}{3}\rho + \rho u_3 u_3, \\
m_{(2,0,1)} &= \frac{1}{3}\rho u_3 + \rho u_1 u_1 u_3, \\
m_{(0,2,1)} &= \frac{1}{3}\rho u_3 + \rho u_2 u_2 u_3, \\
m_{(1,0,2)} &= \frac{1}{3}\rho u_1 + \rho u_1 u_3 u_3, \\
m_{(0,1,2)} &= \frac{1}{3}\rho u_2 + \rho u_2 u_3 u_3, \\
m_{(2,0,2)} &= \frac{1}{9}\rho + \frac{1}{3}\rho u_1 u_1 + \frac{1}{3}\rho u_3 u_3 + \rho u_1 u_1 u_3 u_3, \\
m_{(0,2,2)} &= \frac{1}{9}\rho + \frac{1}{3}\rho u_2 u_2 + \frac{1}{3}\rho u_3 u_3 + \rho u_2 u_2 u_3 u_3.
\end{aligned} \tag{3.52d}
$$

Corner

The moment-based BC with the given velocity vector for the corner between faces with inner normal vectors $\boldsymbol{n} = (1,0,0)^T$, $\boldsymbol{n} = (0,-1,0)^T$, and $\boldsymbol{n} = (0,0,1)^T$, labeled as *West-North-Front* edge, see Figure 3.7, can be derived similarly. The unknown density can be computed as

$$
\rho = -\frac{1}{-1 + u_3 + (-1 + u_3)u_2 - (-1 + u_3 - u_2)u_1 - u_3 u_1 u_2}\Big(2f_{(0,1,0)} + 4f_{(-1,0,-1)}
$$
$$
+ 2f_{(0,0,-1)} + f_{(0,0,0)} + 4f_{(-1,1,0)} + 2f_{(-1,0,0)} + 4f_{(0,1,-1)} + 8f_{(-1,1,-1)}\Big) \tag{3.53}
$$

The raw moments are divided into groups as shown in the Table 3.3.

#	Moments	Unknown f_i combinations	Selected
1	$m_{(0,0,0)}$	$f_{(1,-1,1)} + f_{(1,-1,0)} + f_{(1,0,1)} + f_{(0,-1,1)} + f_{(-1,-1,1)} + f_{(1,-1,-1)} + f_{(0,0,1)} + f_{(1,1,1)} + f_{(1,0,-1)} + f_{(0,-1,-1)}$ $+ f_{(-1,-1,-1)} + f_{(0,1,1)} + f_{(-1,1,1)} + f_{(1,1,-1)} + f_{(1,0,0)} + f_{(-1,0,1)} + f_{(1,1,0)} + f_{(-1,-1,0)} + f_{(0,-1,0)}$	–
2	$m_{(1,0,0)}$	$f_{(1,-1,1)} + f_{(1,-1,0)} + f_{(1,0,1)} - f_{(-1,-1,1)} + f_{(1,-1,-1)} + f_{(1,1,1)} + f_{(1,0,-1)} - f_{(-1,-1,-1)} - f_{(-1,1,1)}$ $+ f_{(1,1,-1)} + f_{(1,0,0)} - f_{(-1,0,1)} + f_{(1,1,0)} - f_{(-1,-1,0)}$	$m_{(1,0,0)}$
3	$m_{(0,1,0)}$	$-f_{(1,-1,1)} - f_{(1,-1,0)} - f_{(0,-1,1)} - f_{(-1,1,1)} - f_{(1,-1,-1)} + f_{(1,1,1)} - f_{(0,-1,-1)} - f_{(-1,-1,-1)} + f_{(0,1,1)}$ $+ f_{(-1,1,1)} + f_{(1,1,-1)} + f_{(1,1,0)} - f_{(-1,-1,0)} - f_{(0,-1,0)}$	$m_{(0,1,0)}$
4	$m_{(0,0,1)}$	$f_{(1,-1,1)} + f_{(1,0,1)} + f_{(0,-1,1)} + f_{(-1,-1,1)} - f_{(1,-1,-1)} + f_{(0,0,1)} + f_{(1,1,1)} - f_{(1,0,-1)} - f_{(0,-1,-1)}$ $- f_{(-1,-1,-1)} + f_{(0,1,1)} + f_{(-1,1,1)} - f_{(1,1,-1)} + f_{(-1,0,1)}$	$m_{(0,0,1)}$
5	$m_{(1,1,0)}$	$-f_{(1,-1,1)} - f_{(1,-1,0)} + f_{(-1,1,1)} - f_{(1,-1,-1)} + f_{(1,1,1)} + f_{(-1,-1,-1)} - f_{(-1,1,1)} + f_{(1,1,-1)} + f_{(1,1,0)} + f_{(-1,-1,0)}$	$m_{(1,1,0)}$
6	$m_{(1,0,1)}$	$f_{(1,-1,1)} + f_{(1,0,1)} - f_{(-1,-1,1)} - f_{(1,-1,-1)} + f_{(1,1,1)} - f_{(1,0,-1)} + f_{(-1,-1,-1)} - f_{(-1,1,1)} - f_{(1,1,-1)} - f_{(-1,0,1)}$	$m_{(1,0,1)}$
7	$m_{(0,1,1)}$	$-f_{(1,-1,1)} - f_{(0,-1,1)} - f_{(-1,-1,1)} + f_{(1,-1,-1)} + f_{(1,1,1)} + f_{(0,-1,-1)} + f_{(-1,-1,-1)} + f_{(0,1,1)} + f_{(-1,1,1)} - f_{(1,1,-1)}$	$m_{(0,1,1)}$
8	$m_{(2,0,0)}$	$f_{(1,-1,1)} + f_{(1,-1,0)} + f_{(1,0,1)} + f_{(-1,-1,1)} + f_{(1,-1,-1)} + f_{(1,1,1)} + f_{(1,0,-1)} + f_{(-1,-1,-1)} + f_{(-1,1,1)}$ $+ f_{(1,1,-1)} + f_{(1,0,0)} + f_{(-1,0,1)} + f_{(1,1,0)} + f_{(-1,-1,0)}$	$m_{(2,0,0)}$
9	$m_{(0,2,0)}$	$f_{(1,-1,1)} + f_{(1,-1,0)} + f_{(0,-1,1)} + f_{(-1,-1,1)} + f_{(1,-1,-1)} + f_{(1,1,1)} + f_{(0,-1,-1)} + f_{(-1,-1,-1)} + f_{(0,1,1)}$ $+ f_{(-1,1,1)} + f_{(1,1,-1)} + f_{(1,1,0)} + f_{(-1,-1,0)} + f_{(0,-1,0)}$	$m_{(0,2,0)}$
10	$m_{(0,0,2)}$	$f_{(1,-1,1)} + f_{(1,0,1)} + f_{(0,-1,1)} + f_{(-1,-1,1)} + f_{(1,-1,-1)} + f_{(0,0,1)} + f_{(1,1,1)} + f_{(1,0,-1)} + f_{(0,-1,-1)}$ $+ f_{(-1,-1,-1)} + f_{(0,1,1)} + f_{(-1,1,1)} + f_{(1,1,-1)} + f_{(-1,0,1)}$	$m_{(0,0,2)}$
11	$m_{(2,1,0)}$	$-f_{(1,-1,1)} - f_{(1,-1,0)} - f_{(-1,-1,1)} - f_{(1,-1,-1)} + f_{(1,1,1)} - f_{(-1,-1,-1)} + f_{(-1,1,1)} + f_{(1,1,-1)} + f_{(1,1,0)} - f_{(-1,-1,0)}$	$m_{(2,1,0)}$
12	$m_{(2,0,1)}$	$f_{(1,-1,1)} + f_{(1,0,1)} + f_{(-1,-1,1)} - f_{(1,-1,-1)} + f_{(1,1,1)} - f_{(1,0,-1)} - f_{(-1,-1,-1)} + f_{(-1,1,1)} - f_{(1,1,-1)} + f_{(-1,0,1)}$	$m_{(2,0,1)}$
13	$m_{(1,2,0)}$	$f_{(1,-1,1)} + f_{(1,-1,0)} - f_{(-1,-1,1)} + f_{(1,-1,-1)} + f_{(1,1,1)} - f_{(-1,-1,-1)} - f_{(-1,1,1)} + f_{(1,1,-1)} + f_{(1,1,0)} - f_{(-1,-1,0)}$	$m_{(1,2,0)}$
14	$m_{(0,2,1)}$	$f_{(1,-1,1)} + f_{(0,-1,1)} + f_{(-1,-1,1)} - f_{(1,-1,-1)} + f_{(1,1,1)} - f_{(0,-1,-1)} - f_{(-1,-1,-1)} + f_{(0,1,1)} + f_{(-1,1,1)} - f_{(1,1,-1)}$	$m_{(0,2,1)}$
15	$m_{(1,0,2)}$	$f_{(1,-1,1)} + f_{(1,0,1)} - f_{(-1,-1,1)} + f_{(1,-1,-1)} + f_{(1,1,1)} + f_{(1,0,-1)} - f_{(-1,-1,-1)} - f_{(-1,1,1)} + f_{(1,1,-1)} - f_{(-1,0,1)}$	$m_{(1,0,2)}$
16	$m_{(0,1,2)}$	$-f_{(1,-1,1)} - f_{(0,-1,1)} - f_{(-1,-1,1)} - f_{(1,-1,-1)} + f_{(1,1,1)} - f_{(0,-1,-1)} - f_{(-1,-1,-1)} + f_{(0,1,1)} + f_{(-1,1,1)} + f_{(1,1,-1)}$	$m_{(0,1,2)}$
17	$m_{(1,1,1)}$	$-f_{(1,-1,1)} + f_{(-1,-1,1)} + f_{(1,-1,-1)} + f_{(1,1,1)} - f_{(-1,-1,-1)} - f_{(-1,1,1)} - f_{(1,1,-1)}$	$m_{(1,1,1)}$
18	$m_{(2,2,0)}$	$f_{(1,-1,1)} + f_{(1,-1,0)} + f_{(-1,-1,1)} + f_{(1,-1,-1)} + f_{(1,1,1)} + f_{(-1,-1,-1)} + f_{(-1,1,1)} + f_{(1,1,-1)} + f_{(1,1,0)} + f_{(-1,-1,0)}$	$m_{(2,2,0)}$
19	$m_{(2,0,2)}$	$f_{(1,-1,1)} + f_{(1,0,1)} + f_{(-1,-1,1)} + f_{(1,-1,-1)} + f_{(1,1,1)} + f_{(1,0,-1)} + f_{(-1,-1,-1)} + f_{(-1,1,1)} + f_{(1,1,-1)} + f_{(-1,0,1)}$	$m_{(2,0,2)}$
20	$m_{(0,2,2)}$	$f_{(1,-1,1)} + f_{(0,-1,1)} + f_{(-1,-1,1)} + f_{(1,-1,-1)} + f_{(1,1,1)} + f_{(0,-1,-1)} + f_{(-1,-1,-1)} + f_{(0,1,1)} + f_{(-1,1,1)} + f_{(1,1,-1)}$	$m_{(0,2,2)}$
21	$m_{(2,1,1)}$	$-f_{(1,-1,1)} - f_{(-1,-1,1)} + f_{(1,-1,-1)} + f_{(1,1,1)} + f_{(-1,-1,-1)} + f_{(-1,1,1)} - f_{(1,1,-1)}$	–
22	$m_{(1,2,1)}$	$f_{(1,-1,1)} - f_{(-1,-1,1)} - f_{(1,-1,-1)} + f_{(1,1,1)} + f_{(-1,-1,-1)} - f_{(-1,1,1)} - f_{(1,1,-1)}$	–
23	$m_{(1,1,2)}$	$-f_{(1,-1,1)} + f_{(-1,-1,1)} - f_{(1,-1,-1)} + f_{(1,1,1)} + f_{(-1,-1,-1)} - f_{(-1,1,1)} + f_{(1,1,-1)}$	–
24	$m_{(2,2,1)}$	$f_{(1,-1,1)} + f_{(-1,-1,1)} - f_{(1,-1,-1)} + f_{(1,1,1)} - f_{(-1,-1,-1)} + f_{(-1,1,1)} - f_{(1,1,-1)}$	–
25	$m_{(2,1,2)}$	$-f_{(1,-1,1)} - f_{(-1,-1,1)} - f_{(1,-1,-1)} + f_{(1,1,1)} - f_{(-1,-1,-1)} + f_{(-1,1,1)} + f_{(1,1,-1)}$	–
26	$m_{(1,2,2)}$	$f_{(1,-1,1)} - f_{(-1,-1,1)} + f_{(1,-1,-1)} + f_{(1,1,1)} - f_{(-1,-1,-1)} - f_{(-1,1,1)} + f_{(1,1,-1)}$	–
27	$m_{(2,2,2)}$	$f_{(1,-1,1)} + f_{(-1,-1,1)} + f_{(1,-1,-1)} + f_{(1,1,1)} + f_{(-1,-1,-1)} + f_{(-1,1,1)} + f_{(1,1,-1)}$	–

Table 3.3: Raw moment categorization based on the combination of unknown density functions for corner *West-North-Front*. The selected moments are used for the expression of the unknown density functions. Since the Dirichlet BC for velocity is considered, the first moment is not chosen.

Based on the selection of raw moments in Table 3.3, the unknown density functions are expressed as

$$
\begin{pmatrix}
f_{(1,0,0)} \\
f_{(0,0,1)} \\
f_{(0,-1,0)} \\
f_{(0,1,1)} \\
f_{(0,-1,1)} \\
f_{(0,-1,-1)} \\
f_{(1,1,0)} \\
f_{(1,-1,0)} \\
f_{(-1,-1,0)} \\
f_{(1,0,1)} \\
f_{(1,0,-1)} \\
f_{(-1,0,1)} \\
f_{(1,1,1)} \\
f_{(1,1,-1)} \\
f_{(1,-1,1)} \\
f_{(1,-1,-1)} \\
f_{(-1,1,1)} \\
f_{(-1,-1,1)} \\
f_{(-1,-1,-1)}
\end{pmatrix}
= \mathbb{A}_f
\begin{pmatrix}
f_{(0,0,0)} \\
f_{(0,1,0)} \\
f_{(-1,0,0)} \\
f_{(0,0,-1)} \\
f_{(0,1,-1)} \\
f_{(-1,1,0)} \\
f_{(-1,0,-1)} \\
f_{(-1,1,-1)}
\end{pmatrix}
+ \mathbb{A}_m
\begin{pmatrix}
m_{(1,0,0)} \\
m_{(0,1,0)} \\
m_{(0,0,1)} \\
m_{(1,1,0)} \\
m_{(1,0,1)} \\
m_{(0,1,1)} \\
m_{(2,0,0)} \\
m_{(0,2,0)} \\
m_{(0,0,2)} \\
m_{(2,1,0)} \\
m_{(2,0,1)} \\
m_{(1,2,0)} \\
m_{(0,2,1)} \\
m_{(1,0,2)} \\
m_{(0,1,2)} \\
m_{(1,1,1)} \\
m_{(2,2,0)} \\
m_{(2,0,2)} \\
m_{(0,2,2)}
\end{pmatrix},
\tag{3.54a}
$$

where

$$\mathbb{A}_f = \begin{pmatrix}
0 & 2 & 1 & 2 & 4 & 4 & 4 & 8 \\
0 & 2 & 2 & 1 & 4 & 4 & 4 & 8 \\
0 & 1 & 2 & 2 & 4 & 4 & 4 & 8 \\
0 & -1 & 0 & 0 & -1 & 0 & 0 & 0 \\
0 & -1 & -2 & -1 & -3 & -4 & -4 & -8 \\
0 & 0 & 0 & -1 & -1 & 0 & 0 & 0 \\
0 & -1 & 0 & 0 & 0 & -1 & 0 & 0 \\
0 & -1 & -1 & -2 & -4 & -3 & -4 & -8 \\
0 & 0 & -1 & 0 & 0 & -1 & 0 & 0 \\
0 & -2 & -1 & -1 & -4 & -4 & -3 & -8 \\
0 & 0 & 0 & -1 & 0 & 0 & -1 & 0 \\
0 & 0 & -1 & 0 & 0 & 0 & -1 & 0 \\
0 & 1 & 0 & 0 & 1 & 1 & 0 & 1 \\
0 & 0 & 0 & 0 & -1 & 0 & 0 & -1 \\
0 & 1 & 1 & 1 & 3 & 3 & 3 & 7 \\
0 & 0 & 0 & 1 & 1 & 0 & 1 & 1 \\
0 & 0 & 0 & 0 & 0 & -1 & 0 & -1 \\
0 & 0 & 1 & 0 & 0 & 1 & 1 & 1 \\
0 & 0 & 0 & 0 & 0 & 0 & -1 & -1
\end{pmatrix}, \tag{3.54b}$$

and

$$\mathbb{A}_m = \begin{pmatrix}
1 & -1 & 1 & 1 & -1 & 1 & 0 & -1 & -1 & 0 & 0 & 0 & 0 & 0 & 0 & -1 & 0 & 0 & 1 \\
1 & -1 & 1 & 1 & -1 & 1 & -1 & -1 & 0 & 0 & 0 & 0 & 0 & 0 & 0 & -1 & 1 & 0 & 0 \\
1 & -1 & 1 & 1 & -1 & 1 & -1 & 0 & -1 & 0 & 0 & 0 & 0 & 0 & 0 & -1 & 0 & 1 & 0 \\
0 & \frac{1}{2} & 0 & 0 & 0 & 0 & 0 & \frac{1}{2} & 0 & -\frac{1}{2} & 0 & 0 & 0 & 0 & 0 & 0 & -\frac{1}{2} & 0 & 0 \\
-1 & \frac{1}{2} & -\frac{1}{2} & -1 & 1 & -1 & 1 & \frac{1}{2} & \frac{1}{2} & \frac{1}{2} & -\frac{1}{2} & 0 & 0 & 0 & 0 & 1 & -\frac{1}{2} & -\frac{1}{2} & 0 \\
0 & 0 & -\frac{1}{2} & 0 & 0 & 0 & 0 & 0 & \frac{1}{2} & 0 & \frac{1}{2} & 0 & 0 & 0 & 0 & 0 & 0 & -\frac{1}{2} & 0 \\
0 & \frac{1}{2} & 0 & 0 & 0 & 0 & 0 & \frac{1}{2} & 0 & 0 & 0 & 0 & 0 & 0 & -\frac{1}{2} & 0 & 0 & 0 & -\frac{1}{2} \\
-\frac{1}{2} & \frac{1}{2} & -1 & -1 & 1 & -1 & \frac{1}{2} & \frac{1}{2} & 1 & 0 & 0 & 0 & 0 & -\frac{1}{2} & \frac{1}{2} & 1 & 0 & -\frac{1}{2} & -\frac{1}{2} \\
-\frac{1}{2} & 0 & 0 & 0 & 0 & 0 & \frac{1}{2} & 0 & 0 & 0 & 0 & 0 & 0 & \frac{1}{2} & 0 & 0 & 0 & -\frac{1}{2} & 0 \\
-\frac{1}{2} & 1 & -\frac{1}{2} & -1 & 1 & -1 & \frac{1}{2} & 1 & \frac{1}{2} & 0 & 0 & -\frac{1}{2} & -\frac{1}{2} & 0 & 0 & 1 & -\frac{1}{2} & 0 & -\frac{1}{2} \\
0 & 0 & -\frac{1}{2} & 0 & 0 & 0 & 0 & 0 & \frac{1}{2} & 0 & 0 & 0 & \frac{1}{2} & 0 & 0 & 0 & 0 & 0 & -\frac{1}{2} \\
-\frac{1}{2} & 0 & 0 & 0 & 0 & 0 & \frac{1}{2} & 0 & 0 & 0 & 0 & \frac{1}{2} & 0 & 0 & 0 & 0 & -\frac{1}{2} & 0 & 0 \\
0 & -\frac{1}{2} & 0 & \frac{1}{4} & 0 & \frac{1}{4} & 0 & -\frac{1}{2} & 0 & \frac{1}{4} & 0 & \frac{1}{4} & \frac{1}{4} & 0 & \frac{1}{4} & 0 & \frac{1}{4} & 0 & \frac{1}{4} \\
0 & 0 & 0 & 0 & 0 & -\frac{1}{4} & 0 & 0 & 0 & 0 & 0 & 0 & -\frac{1}{4} & 0 & \frac{1}{4} & 0 & 0 & 0 & \frac{1}{4} \\
\frac{1}{2} & -\frac{1}{2} & \frac{1}{2} & \frac{3}{4} & -\frac{3}{4} & \frac{3}{4} & -\frac{1}{2} & -\frac{1}{2} & -\frac{1}{2} & -\frac{1}{4} & \frac{1}{4} & \frac{1}{4} & \frac{1}{4} & \frac{1}{4} & -\frac{1}{4} & -1 & \frac{1}{4} & \frac{1}{4} & \frac{1}{4} \\
0 & 0 & \frac{1}{2} & 0 & -\frac{1}{4} & \frac{1}{4} & 0 & 0 & -\frac{1}{2} & 0 & -\frac{1}{4} & 0 & -\frac{1}{4} & \frac{1}{4} & -\frac{1}{4} & 0 & 0 & \frac{1}{4} & \frac{1}{4} \\
0 & 0 & 0 & -\frac{1}{4} & 0 & 0 & 0 & 0 & 0 & \frac{1}{4} & 0 & -\frac{1}{4} & 0 & 0 & 0 & 0 & \frac{1}{4} & 0 & 0 \\
\frac{1}{2} & 0 & 0 & \frac{1}{4} & -\frac{1}{4} & 0 & -\frac{1}{2} & 0 & 0 & -\frac{1}{4} & \frac{1}{4} & -\frac{1}{4} & 0 & -\frac{1}{4} & 0 & 0 & \frac{1}{4} & \frac{1}{4} & 0 \\
0 & 0 & 0 & 0 & \frac{1}{4} & 0 & 0 & 0 & 0 & 0 & -\frac{1}{4} & 0 & 0 & -\frac{1}{4} & 0 & 0 & 0 & \frac{1}{4} & 0
\end{pmatrix}. \tag{3.54c}$$

The selected raw moments in Table 3.3 are set as

$$m_{(1,0,0)} = \rho u_1,$$
$$m_{(0,1,0)} = \rho u_2,$$
$$m_{(0,0,1)} = \rho u_3,$$
$$m_{(1,1,0)} = \rho u_1 u_2,$$
$$m_{(1,0,1)} = \rho u_1 u_3,$$
$$m_{(0,1,1)} = \rho u_2 u_3,$$
$$m_{(2,0,0)} = \frac{1}{3}\rho + \rho u_1 u_1,$$
$$m_{(0,2,0)} = \frac{1}{3}\rho + \rho u_2 u_2,$$
$$m_{(0,0,2)} = \frac{1}{3}\rho + \rho u_3 u_3,$$
$$m_{(2,1,0)} = \frac{1}{3}\rho u_2 + \rho u_1 u_1 u_2,$$
$$m_{(2,0,1)} = \frac{1}{3}\rho u_3 + \rho u_1 u_1 u_3,$$
$$m_{(1,2,0)} = \frac{1}{3}\rho u_1 + \rho u_1 u_2 u_2,$$
$$m_{(0,2,1)} = \frac{1}{3}\rho u_3 + \rho u_2 u_2 u_3,$$
$$m_{(1,0,2)} = \frac{1}{3}\rho u_1 + \rho u_1 u_3 u_3,$$
$$m_{(0,1,2)} = \frac{1}{3}\rho u_2 + \rho u_2 u_3 u_3,$$
$$m_{(1,1,1)} = \rho u_1 u_2 u_3,$$
$$m_{(2,2,0)} = \frac{1}{9}\rho + \frac{1}{3}\rho u_1 u_1 + \frac{1}{3}\rho u_2 u_2 + \rho u_1 u_1 u_2 u_2,$$
$$m_{(2,0,2)} = \frac{1}{9}\rho + \frac{1}{3}\rho u_1 u_1 + \frac{1}{3}\rho u_3 u_3 + \rho u_1 u_1 u_3 u_3,$$
$$m_{(0,2,2)} = \frac{1}{9}\rho + \frac{1}{3}\rho u_2 u_2 + \frac{1}{3}\rho u_3 u_3 + \rho u_2 u_2 u_3 u_3. \tag{3.54d}$$

For the remaining faces, edges, and corners with the prescribed velocity or pressure Dirichlet BC, the moment-based BCs are given in [51].

Automatic generation of moment-based BC

Manual derivation of moment BCs is a tedious procedure, thus we have implemented a generator of these BCs in C++ using GiNaC, which allows symbolic operations. The code is available upon request on the web site `https://mmg-gitlab.fjfi.cvut.cz/gitlab/eichler/moment-based-bc-for-lbm`.

3.8 Grid refinement

The LBM uses a lattice (corresponding to the regular grid) to discretize the computational domain. Thus, the lattice does not need to be stored in the computer memory. However, this causes many drawbacks. First, the discretization of complex domains can contain many lattice

sites outside the domain, which causes unnecessary allocation of computer memory. Next, since the Kolmogorov scale is not constant in the whole flow field, the requirements on the grid resolution depend on the position in the computational domain. Typically, the grid needs to be finer near body surfaces or in turbulent flow field regions. In this section, the topic of grid refinement technique is addressed.

There are several options for the grid refinement in the LBM. One of the strategies is based on the *mesh-less* approach, where the discrete points discretizing the computational domain are not arranged in a lattice [132, 166]. The basic problem of this mesh-less approach is the necessity of storing coordinates of each discrete point in the computer memory. Next, the streaming step is not accurate, and some interpolation is needed. Finally, in the mesh-less approach, the space step for the unit conversion must be chosen carefully.
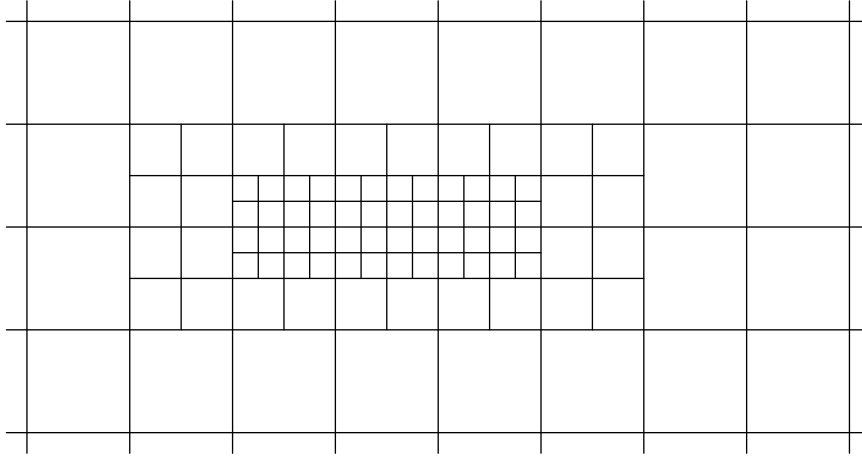

Figure 3.8: Illustration of the octree mesh structure.

3.8.1   Grid structure and scaling

Another approach uses a grid composed of blocks with uniform parts. The ratio of grid spacing parameters between adjacent blocks can be an arbitrary natural number [194]. A special approach, with the ration 2 [89], used in this thesis, is based on the octree grid structure [55, 89, 196], illustrated in Figure 3.8. The octree grid is composed of blocks with a different grid spacing parameter δ_x^ℓ [m] , where the upper index $\ell \in \mathbb{N}_0$ defines the level of the block. The block with the coarsest grid has the level $\ell = 0$. The grid spacing parameters of other blocks satisfy $\delta_x^\ell = \frac{1}{2}\delta_x^{\ell-1}$ for $\ell \in \mathbb{N}$.

The ratio between grid spacing parameter δ_x^ℓ and time step δ_t^ℓ [t] is commonly set in two ways. The first option is to use the diffusive scaling, that is, $\delta_t^\ell \sim \left(\delta_x^\ell\right)^2$ [189]. The main disadvantage of this approach is the reflection of pressure waves at the mesh interfaces, as a consequence of the Snell-Descartes law [19]. The second option uses the acoustic scaling, that is, $\delta_t^\ell \sim \delta_x^\ell$. Therefore, the time step at level ℓ satisfies $\delta_t^{\ell+1} = \frac{1}{2}\delta_t^\ell$ and 2^ℓ iterations of the LBM algorithm must be performed in a block on level ℓ to update the state at time $t + \delta_t^0$.

In the case of the acoustic scaling, the relaxation parameters related to kinematic viscosity are not constant. If we denote the non-dimensional kinematic viscosity in the block on level ℓ as $\widetilde{\nu}^\ell$ [−], then with the acoustic scaling, the non-dimensional viscosity $\widetilde{\nu}^{\ell+1}$ satisfies

$$\widetilde{\nu}^{\ell+1}\frac{\left(\delta_x^{\ell+1}\right)^2}{\delta_t^{\ell+1}} = \widetilde{\nu}^\ell\frac{\left(\delta_x^\ell\right)^2}{\delta_t^\ell} \implies \widetilde{\nu}^{\ell+1} = 2\widetilde{\nu}^\ell. \tag{3.55}$$

Thanks to Eq. (3.14), the relaxation frequencies ω^ℓ [$-$] and $\omega^{\ell+1}$ related to kinematic viscosity $\widetilde{\nu}^\ell$ and $\widetilde{\nu}^{\ell+1}$, respectively, satisfy

$$\omega^{\ell+1} = \frac{2\omega^\ell}{4 - \omega^\ell}. \tag{3.56}$$

Since the applicability of the acoustic scaling was successfully tested in [122, 158], it is also used in this thesis.

Next, the distribution of grid blocks can be static or dynamic [53, 190]. The dynamic distribution is mainly used for problems with moving obstacles or for problems such as Kármán vortex street, where the blocks follow the vortexes. In this thesis, the static distribution is considered, since the dynamic distribution requires additional computational cost.

3.8.2   LBM algorithm with grid refinement

The algorithm of the grid refinement depends on the data layout on the grid. Data can be vertex-centered or cell-centered, see Figure 3.9. The advantage of the vertex-centered layout is the overlap of the fine and coarse grid nodes. Thus, no interpolation is needed in these nodes. However, the interpolation between other vertices can disrupt mass conservation [30]. The vertex-centered approach in the LBM was used, for example, in [44, 61]. On the other hand, the cell-centered approach ensures mass conservation [30] and was applied in the context of the LBM in [54, 158]. In this thesis, the cell-centered approach is used, since this approach is more appropriate for some BCs, such as the bounce-back BC.

(a) Cell-centered.   (b) Vertex-centered.
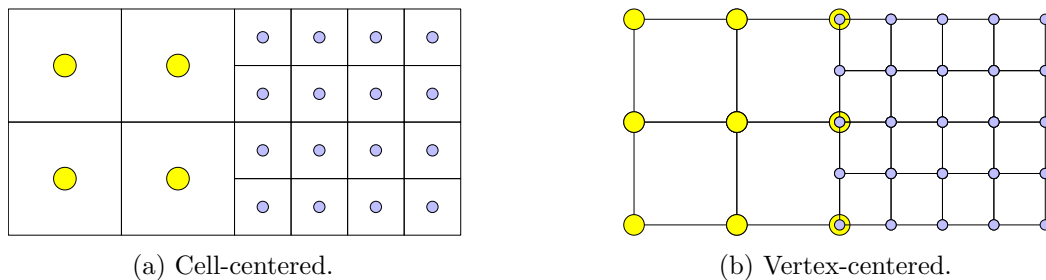
Figure 3.9: Illustration of the representation of the data in the numerical grid with a cell-centered and a vertex-centered representation. The data in coarse and fine grids are represented by the yellow and blue circles, respectively.

The generation of the grid blocks can be performed by coarsening the initial fine mesh. After generation, the blocks are disjoint and extrapolation is needed for the communication between neighboring blocks, see Figure 3.9a. To improve this drawback, the overlap region is additionally generated on each blocks interface as illustrated in Figure 3.10a. The interpolation from fine cells to coarse cells is performed first (light blue arrows in Figure 3.10b), since the overlap cells of the coarse block are needed for the interpolation from coarse cells to fine cells, see Figure 3.10b. Next, the interpolation from the block with level ℓ to the block with level $\ell + 1$ is performed twice, since the LBM algorithm is performed twice on the block with level $\ell + 1$ to reach the time level $t + \delta_t^\ell$. To minimize such extra communication, an extra layer of overlap cells is added to the block with level $\ell + 1$ at the block interface with level ℓ, see Figure 3.10c. Finally, to communicate between neighboring blocks simultaneously, the fine block is immersed in the coarse block with one level of grid nodes, as illustrated by the colored regions in Figure 3.10d.

The LBM algorithm for one time step of the block with level 0 is modified. Let the number of different grid levels be $G_N \in \mathbb{N}$. The LBM algorithm with grid refinement is described in Algorithm 1.
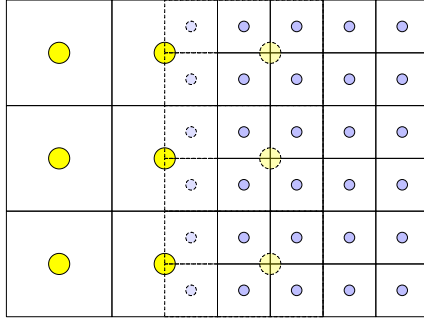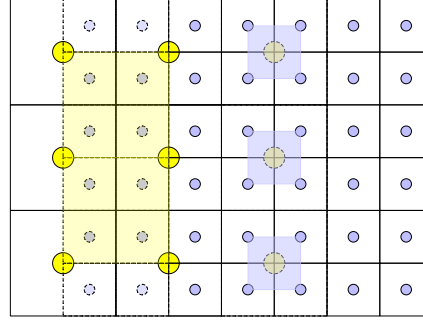
(a) Grid blocks with additionally generated overlap region for the interpolation.
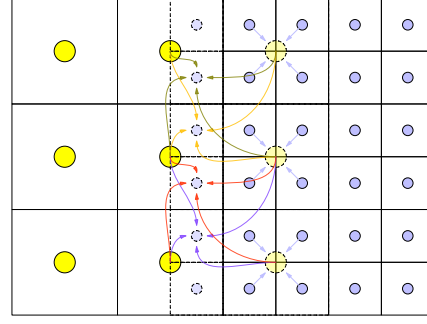
(b) Illustration of the interpolation between grid blocks with one-layer overlap on each side. The direction of the interpolation is depicted by arrows.
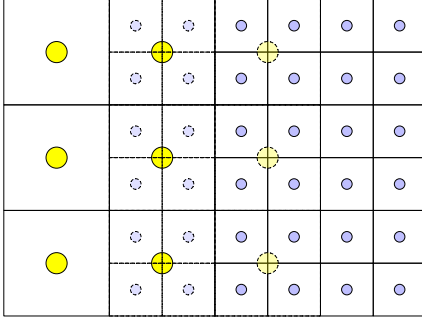
(c) Grid blocks with an additional overlap layer on the fine block side.

(d) Grid blocks with illustrated regions of interpolation.

Figure 3.10: Illustration of different strategies for the overlap construction between blocks of different levels. The overlap region is drawn with the dashed lines. Coarse and fine cells are represented by yellow and light blue points, respectively.

Algorithm 1: Algorithm for LBM with grid refinement

$\ell \leftarrow G_N - 1$;
while $\ell \geq 0$ **do**
    label all grid blocks with level $\geq \ell$ as **active**;
    perform one time step of classical LBM algorithm for all **active** blocks;
    communication for **active** blocks
    (*active blocks update their overlap regions*);
    $\ell \leftarrow \ell - 1$;
end

3.8.3   Interpolation of DDFs

With the cell-centered approach, the interpolation from fine cells to coarse cells and vice versa is performed inside a cell with known values in its vertices, see Figure 3.10d. To perform the interpolation inside a cell, different interpolations are used. The basic interpolation technique is based on the trilinear interpolation [37] of DDFs f_i. An arbitrary variable ϕ can be linearly

interpolated in the unit cube as

$$\phi(x_1, x_2, x_3) = \left(\frac{1}{2} - x_1\right)\left(\frac{1}{2} - x_2\right)\left(\frac{1}{2} - x_3\right)\phi\left(-\frac{1}{2}, -\frac{1}{2}, -\frac{1}{2}\right) + \left(\frac{1}{2} + x_1\right)\left(\frac{1}{2} - x_2\right)\left(\frac{1}{2} - x_3\right)\phi\left(\frac{1}{2}, -\frac{1}{2}, -\frac{1}{2}\right)$$
$$+ \left(\frac{1}{2} - x_1\right)\left(\frac{1}{2} + x_2\right)\left(\frac{1}{2} - x_3\right)\phi\left(-\frac{1}{2}, \frac{1}{2}, -\frac{1}{2}\right) + \left(\frac{1}{2} - x_1\right)\left(\frac{1}{2} - x_2\right)\left(\frac{1}{2} + x_3\right)\phi\left(-\frac{1}{2}, -\frac{1}{2}, \frac{1}{2}\right)$$
$$+ \left(\frac{1}{2} + x_1\right)\left(\frac{1}{2} - x_2\right)\left(\frac{1}{2} + x_3\right)\phi\left(\frac{1}{2}, -\frac{1}{2}, \frac{1}{2}\right) + \left(\frac{1}{2} + x_1\right)\left(\frac{1}{2} + x_2\right)\left(\frac{1}{2} - x_3\right)\phi\left(\frac{1}{2}, \frac{1}{2}, -\frac{1}{2}\right)$$
$$+ \left(\frac{1}{2} - x_1\right)\left(\frac{1}{2} + x_2\right)\left(\frac{1}{2} + x_3\right)\phi\left(-\frac{1}{2}, \frac{1}{2}, \frac{1}{2}\right) + \left(\frac{1}{2} + x_1\right)\left(\frac{1}{2}x_2\right)\left(\frac{1}{2} + x_3\right)\phi\left(\frac{1}{2}, \frac{1}{2}, \frac{1}{2}\right), \tag{3.57}$$

where $\phi(x_1, x_2, x_3)$, $x_i \in \{-\frac{1}{2}, \frac{1}{2}\}$, $i \in \{1, 2, 3\}$ are values at the vertices of the unit cube with the origin $(0, 0, 0)^T$ in its center.

Direct linear interpolation of f_i causes oscillations at the block interface. To improve this drawback, the DDF is decomposed into the equilibrium part and the non-equilibrium part as

$$f_i = f_i^{(eq)} + f_i^{(neq)}. \tag{3.58}$$

The equilibrium part $f_i^{(eq)}$ is proportional to the velocity and thus is not scaled within the interpolation. The non-equilibrium part $f_i^{(neq)}$ is proportional to the spatial velocity derivatives [122] and, therefore, it should be scaled as

$$f_i^{(neq),\ell} = \frac{2\omega^{\ell+1}}{\omega^\ell} f_i^{(neq),\ell+1}, \tag{3.59}$$

where $f_i^{(neq),\ell}$ [−] is the non-equilibrium part in block nodes with level ℓ and ω^ℓ is the relaxation frequency related to the kinematic viscosity of the block with level ℓ. Next, instead of the equilibrium part $f_i^{(eq)}$, the density and the velocity are interpolated. To obtain an interpolated DDFs f_i, the equilibrium parts are reconstructed from the interpolated density and velocity and added to the interpolated non-equilibrium parts. The interpolation of density and velocity is performed according to Eq. (3.57).

The interpolation of density ρ can be further improved. The density can be written as $\rho = \rho_0 + \delta\rho$, where $\rho_0 = 1$ is the non-dimensional initial reference density (see page 26) and $\delta\rho$ are temporal fluctuations of ρ around ρ_0. Thus, the numerical precision of the interpolation can be improved by interpolating $\delta\rho$ instead of ρ.

If the linear velocity interpolation is used, the second derivative of the interpolated velocity is zero. It means that in the context of the Navier-Stokes equations, the viscous forces are neglected. This inconsistency can cause errors in the solution. To improve it, a second-order interpolation of velocity is used. However, for the second-order interpolation, more information is needed. In order to use only the information from the vertices of the unit cube, the second derivatives of the velocity are used in the interpolation [75, 121]. The second-order interpolation used in this thesis is inspired by [121] and can be written as

$$u_1(\boldsymbol{x}) = a_0 + a_1 x_1 + a_2 x_2 + a_3 x_3 + a_{12} x_1 x_2 + a_{13} x_1 x_3 + a_{23} x_2 x_3 + a_{11} x_1^2 + a_{22} x_2^2$$
$$+ a_{33} x_3^2 + a_{123} x_1 x_2 x_3, \tag{3.60a}$$

$$u_2(\boldsymbol{x}) = b_0 + b_1 x_1 + b_2 x_2 + b_3 x_3 + b_{12} x_1 x_2 + b_{13} x_1 x_3 + b_{23} x_2 x_3 + b_{11} x_1^2 + b_{22} x_2^2$$
$$+ b_{33} x_3^2 + b_{123} x_1 x_2 x_3, \tag{3.60b}$$

$$u_3(\boldsymbol{x}) = c_0 + c_1 x_1 + c_2 x_2 + c_3 x_3 + c_{12} x_1 x_2 + c_{13} x_1 x_3 + c_{23} x_2 x_3 + c_{11} x_1^2 + c_{22} x_2^2$$
$$+ c_{33} x_3^2 + c_{123} x_1 x_2 x_3, \tag{3.60c}$$

where $\boldsymbol{x} = (x_1, x_2, x_3)^T$, $x_1, x_2, x_3 \in \left[-\frac{1}{2}, \frac{1}{2}\right]$. To find 33 unknown coefficients $a_{\{.\}}, b_{\{.\}}, c_{\{.\}}$, $3 \times 8 = 24$ vertex values of velocity are used. As in [121], the rest of equations for the unknown coefficients are obtained from the spatial second-order velocity derivatives in the cube center (i.e. $\boldsymbol{x} = \boldsymbol{0}$)

$$\frac{\partial}{\partial x_1}\left(\frac{\partial}{\partial x_1}u_2 + \frac{\partial}{\partial x_2}u_1\right) = 2b_{11} + a_{12}, \tag{3.61a}$$

$$\frac{\partial}{\partial x_1}\left(\frac{\partial}{\partial x_1}u_3 + \frac{\partial}{\partial x_3}u_1\right) = 2c_{11} + a_{13}, \tag{3.61b}$$

$$\frac{\partial^2}{\partial x_1^2}(u_1) = 2a_{11}, \tag{3.61c}$$

$$\frac{\partial}{\partial x_2}\left(\frac{\partial}{\partial x_2}u_1 + \frac{\partial}{\partial x_1}u_2\right) = 2a_{22} + b_{12}, \tag{3.61d}$$

$$\frac{\partial}{\partial x_2}\left(\frac{\partial}{\partial x_2}u_3 + \frac{\partial}{\partial x_3}u_2\right) = 2c_{22} + b_{23}, \tag{3.61e}$$

$$\frac{\partial^2}{\partial x_2^2}(u_2) = 2b_{22}, \tag{3.61f}$$

$$\frac{\partial}{\partial x_3}\left(\frac{\partial}{\partial x_3}u_1 + \frac{\partial}{\partial x_1}u_3\right) = 2a_{33} + c_{13}, \tag{3.61g}$$

$$\frac{\partial}{\partial x_3}\left(\frac{\partial}{\partial x_3}u_2 + \frac{\partial}{\partial x_2}u_3\right) = 2b_{33} + c_{23}, \tag{3.61h}$$

$$\frac{\partial^2}{\partial x_3^2}(u_3) = 2c_{33}. \tag{3.61i}$$

To obtain the second-order derivatives, the first order derivatives at cube vertices are used. The first-order derivatives can be locally obtained from the cumulants, see Chapter 4. To obtain the second order derivative $\frac{\partial}{\partial x_1}\left(\frac{\partial}{\partial x_1}u_2 + \frac{\partial}{\partial x_2}u_1\right)$, the values $\frac{\partial}{\partial x_1}u_2 + \frac{\partial}{\partial x_2}u_1$ in the cube vertices are averaged within faces perpendicular to the x_1 axis and, then, the central second-order differences are used, that is,

$$\frac{\partial}{\partial x_1}\left(\frac{\partial}{\partial x_1}u_2 + \frac{\partial}{\partial x_2}u_1\right)(\boldsymbol{0}) \approx \frac{1}{4}\sum_{j,k=0}^{1}\left[\left(\frac{\partial}{\partial x_1}u_2 + \frac{\partial}{\partial x_2}u_1\right)\left(\left(\frac{1}{2}, j - \frac{1}{2}, k - \frac{1}{2}\right)^T\right)\right.$$
$$\left. - \left(\frac{\partial}{\partial x_1}u_2 + \frac{\partial}{\partial x_2}u_1\right)\left(\left(-\frac{1}{2}, j - \frac{1}{2}, k - \frac{1}{2}\right)^T\right)\right]. \tag{3.62}$$

The remaining second-order derivatives are computed similarly. The list of interpolation coefficients can be found in Appendix C.

Finally, the following two interpolation strategies are used:

S.I Linear interpolation

- DDFs are decomposed as in Eq. (3.58).

- The linear interpolation defined by Eq. (3.57) is used for the velocity, density, and non-equilibrium parts of DDFs.

- The interpolated non-equilibrium parts of DDFs is scaled as in Eq. (3.59).

- The equilibrium parts of interpolated DDFs are computed from the interpolated density and velocity and added to the scaled non-equilibrium parts.

S.II Quadratic interpolation

- DDFs are decomposed as in Eq. (3.58).
- The quadratic interpolation defined by Eq. (3.60) is used for the velocity, the linear interpolation defined by Eq. (3.57) is used for the density, and the non-equilibrium parts of DDFs.
- The interpolated non-equilibrium parts of DDFs are scaled as in Eq. (3.59).
- The equilibrium parts of interpolated DDFs are computed from the interpolated density and velocity and added to the scaled non-equilibrium parts.

3.9 Implementation remarks

Remark 3.3
For all numerical simulations, a in-house LBM software developed at the Department of Mathematics, FNSPE CTU in Prague since 2015 is used. This software is implemented in C++ and enables parallel executions on clusters with distributed nodes equipped with GPUs (Graphics Processing Unit) using libraries MPI (Message Passing Interface) and CUDA (Compute Unified Device Architecture). The author of this thesis is one of the main developers of this in-house code.

Remark 3.4
The LBM algorithm introduced in Section 3.3 stores two sets of DDFs in the computer memory. One set for the previous and one for the current time level. Some techniques [79, 120, 142], however, allow to store only one set of DDFs by modifying the LBM algorithm.

3.9.1 Well conditioning

In the computer code, the variables are stored using different computer data formats. The most commonly used representations for real numbers in C++ are floats (single-precision arithmetic) and doubles (double-precision arithmetic). The limitation of these computer data formats is their finite precision.

In the LBM, the DDFs can be written as

$$f_{\boldsymbol{i}} = f_{\boldsymbol{i}}^{(0)} + \delta f_{\boldsymbol{i}}, \ \boldsymbol{i} \in \mathcal{Q}, \tag{3.63}$$

where $f_{\boldsymbol{i}}^{(0)} = f_{\boldsymbol{i}}^{eq}(\rho_0, \mathbf{0})$ with the reference density $\rho_0 = 1$. From the equilibrium DDF $f_{\boldsymbol{i}}^{(eq)}$ defined by Eq. (3.12), the constant part satisfies

$$f_{\boldsymbol{i}}^{(0)} = \rho_0 w_{\boldsymbol{i}}, \ \boldsymbol{i} \in \mathcal{Q}, \tag{3.64}$$

where $w_{\boldsymbol{i}}$ are the weights defined by Eq. (3.13). Thus, it is convenient to store $\delta f_{\boldsymbol{i}}$ in the computer memory instead of $f_{\boldsymbol{i}}$ and modify the LBM algorithm accordingly. This technique is referred to as the *well conditioning* in the LBM community [80]. With the decomposition introduced by Eq. (3.63), the density ρ is computed as

$$\rho = \sum_{\boldsymbol{i} \in \mathcal{Q}} f_{\boldsymbol{i}} = \sum_{\boldsymbol{i} \in \mathcal{Q}} \rho_0 w_{\boldsymbol{i}} + \sum_{\boldsymbol{i} \in \mathcal{Q}} \delta f_{\boldsymbol{i}} = \rho_0 + \delta\rho, \tag{3.65}$$

where $\sum_{\boldsymbol{i} \in \mathcal{Q}} w_{\boldsymbol{i}} = 1$ is used. It should be noted that it is recommended to store the fluctuations $\delta\rho$ in the computer memory instead of ρ since $\delta\rho \ll \rho_0$. Next, there is no difference in the first-order

moment computation using $f_{\boldsymbol{i}}$ and $\delta f_{\boldsymbol{i}}$ since

$$\rho\boldsymbol{u} = \sum_{i\in\mathcal{Q}} f_{\boldsymbol{i}}\boldsymbol{\xi_i} = \sum_{i\in\mathcal{Q}} w_i\boldsymbol{\xi_i} + \sum_{i\in\mathcal{Q}} \delta f_{\boldsymbol{i}}\boldsymbol{\xi_i} = 0 + \sum_{i\in\mathcal{Q}} \delta f_{\boldsymbol{i}}\boldsymbol{\xi_i} = \sum_{i\in\mathcal{Q}} \delta f_{\boldsymbol{i}}\boldsymbol{\xi_i}, \tag{3.66}$$

where $\sum\limits_{i\in\mathcal{Q}} w_i\boldsymbol{\xi} = 0$ follows from the symmetric definition of $\mathcal{Q}$ and weights $w_{\boldsymbol{i}}$. Thus, the formula for the velocity can be written as

$$\boldsymbol{u} = \frac{1}{1 + \delta\rho} \sum_{i\in\mathcal{Q}} \delta f_{\boldsymbol{i}}\boldsymbol{\xi_i}. \tag{3.67}$$

The collision step is not affected by the well conditioning approach. Only the transformations from DDFs to raw moments, central moments, and cumulants are affected. The details can be found in [80]. In this thesis, the well conditioning technique is used only in connection with the grid refinement technique in Chapter 6.

Analysis of Lattice Boltzmann Method

4

In general, numerical methods produce an approximate solution of a given PDE with some error. Quantification of the error is essential, since it provides pieces of information about the numerical scheme. The analysis of the error can be theoretical or based on numerical experiments.

The error is often proportional to the space and the time step δ_x and δ_t, respectively. The numerical method is called convergent, if the error decreases as the space and time step decrease. The rate of convergence can be expressed using the order of convergence. Let the solution of PDE be function $\Phi : \Omega \to \mathbb{R}$ and let the numerical solution of an arbitrary numerical scheme be denoted by $\widetilde{\Phi} : \widehat{\Omega} \to \mathbb{R}$. Then, the error term can be written as

$$\widetilde{\Phi}(\boldsymbol{x}) = \Phi(\boldsymbol{x}) + \mathcal{O}(\delta_x^\alpha)\mathcal{O}\left(\delta_t^\beta\right), \ \forall \boldsymbol{x} \in \widehat{\Omega}, \tag{4.1}$$

where $\alpha, \beta \in \mathbb{R}$ and $\mathcal{O}$ is the Bachmann–Landau notation [140]. Then, the order of convergence of the numerical method is α in space and β in time.

To investigate the order of convergence of the numerical method, numerical experiments or a backward analysis [36] need to be performed. The order of convergence determined based on the numerical simulations is called the *experimental order of convergence (EOC)*. The EOC provides only approximation of the exact convergence order and does not provide explicit knowledge about the error. On the other hand, the backward analysis produces both the convergence orders and the explicit form of the error. Furthermore, the backward analysis is crucial for numerical methods, since it provides information about the PDEs that are numerically solved.

There are several techniques of backward analysis for the LBM. The commonly used techniques are the Chapman-Enskog asymptotic expansion [29, 31], analysis based on Maxwell iterations [197], equivalent partial differential equation analysis [43, 69, 96], recurrence equation analysis [82], Taylor expansion method [67], and asymptotic expansion analysis [106]. The Chapman-Enskog expansion is widely used for the analysis of the LBM [88, 118, 129, 141, 152, 156] and was originally derived for the analysis of the continuous Boltzmann equations, where the kinetic scale (i.e., the mean free path) and the hydrodynamic scale (given by the Knudsen number) are independent. However, in numerical simulations of the fluid flow, no such independence exists [123]. Thus, the use of the Chapman-Enskog analysis is omitted in this thesis.

Here, the asymptotic expansion described in [108] is used to investigate the equivalent partial differential equations of the CuLBM collision operator. Next, some relations are derived for the approximations of the spatial velocity derivatives.

4.1   Asymptotic expansion

The backward analysis based on the asymptotic expansion of unknown functions is a well established method in the analysis of ordinary differential equations and partial differential equations [17, 90]. Contrary to the Taylor expansion method, the asymptotic expansion method can provide more information about the error terms which can be used to improve the numerical method [108].

As in [108], the asymptotic analysis is performed only formally. The asymptotic expansion method works with a regular expansion with a "small" parameter $\epsilon \in \mathbb{R} \setminus \{0\}$. The parameter ϵ is proportional to the space step δ_x and the time step δ_t. In this thesis, the diffusive scaling is mainly used, thus, it is considered that $\epsilon = \delta_x$ and $\epsilon^2 = C_\epsilon \delta_t$, $C_\epsilon \in \mathbb{R}^+$ is a constant of proportionality.

The position of point $\boldsymbol{x}_{ijk}(\epsilon) \in \hat{\Omega}$ for given indexes i, j, k depends on the parameter ϵ. The asymptotic expansion for a function $\widetilde{\Phi}$ is assumed to take the form of a regular expansion as follows:

$$\widetilde{\Phi}(\boldsymbol{x}_{ijk}(\epsilon)) = \sum_{\ell=0}^{\infty} \epsilon^\ell \Phi^{(\ell)}(\boldsymbol{x}_{ijk}(\epsilon)), \tag{4.2}$$

where $\Phi^{(k)}(\boldsymbol{x}_{ijk}(\epsilon))$ are smooth coefficients of the expansion that do not explicitly depend on ϵ. The asymptotic analysis investigates the case where $\epsilon \to 0$. For a given point $\boldsymbol{x} \in \Omega$, we will find a sequence of points $\boldsymbol{x}_{i_n j_n k_n}(\epsilon_n)$ for a sequence $\{\epsilon_n\}_{n=1}^{\infty}$ such that $\lim_{n\to\infty} \epsilon_n = 0$ and $\lim_{n\to\infty} \boldsymbol{x}_{i_n j_n k_n}(\epsilon_n) = \boldsymbol{x}$. Thus, after substituting the regular expansion (4.2) into a given numerical scheme, the limiting case $\lim_{n\to\infty} \epsilon_n = 0$ is investigated.

The output of the analysis is a set of equations that are solved by the first non-zero coefficient $\Phi^{(\ell_1)}$, $\ell_1 \in \mathbb{N}_0$. If the coefficient $\Phi^{(\ell_1+\ell_2)} \neq 0$ is the second non-zero coefficient, then the numerical solution $\widetilde{\Phi}$ is the approximation of $\Phi^{(\ell_1)}$ of order $\ell_2 \in \mathbb{N}$.

In the context of the LBM, the asymptotic analysis can be performed for the DDFs [106] or for the macroscopic moments [80]. In this thesis, the second option is explored. The analysis assumes $\Omega = \mathbb{R}^3$, so no boundary treatment is investigated.

4.2   Analysis of cumulant LBM

In this section, an asymptotic analysis of the CuLBM is performed. It follows the steps of the asymptotic analysis in [80]. The reason for the analysis being presented here is to verify the correctness of the formulas derived in [80] that are used for the second-order interpolation of the velocity in Section 3.8.

In the LBM, non-dimensional quantities are used instead of dimensional quantities. Thus the regular expansion (4.2) is assumed in the non-dimensional form. Since $\epsilon = \delta_x$, its non-dimensional form satisfies $\widetilde{\epsilon} = \frac{1}{\delta_x}\epsilon = 1$. The non-dimensionalization causes that the coefficients of the regular expansion in the non-dimensional form $\widetilde{\Phi^{(k)}}$ depend on ϵ. Thus, with decreasing ϵ, coefficients $\widetilde{\Phi^{(k)}}$ behave as ϵ^k, $k \in \mathbb{N}_0$. This allows to separate the coefficients of the same power of ϵ in each equation. In the following, all quantities are assumed to be non-dimensional, the tilde is omitted above all non-dimensional quantities for better readability, and the non-dimensional parameter $\widetilde{\epsilon}$ is labeled by ε.

For the purpose of the analysis, Eq. (3.9b) is rewritten as

$$f_i(\boldsymbol{x}, t + \Delta t) = f_i^\star(\boldsymbol{x} - \Delta t \boldsymbol{\xi}_i, t). \tag{4.3}$$

Next, the Taylor expansion of Eq. (4.3) is used. The left-hand side is expanded in time, and the right-hand side is expanded in space. This results in the equation

$$\sum_{r=0}^{\infty} \frac{(\Delta t)^r}{r!} \partial_{t^r} f_i(\boldsymbol{x}, t) = \sum_{m,n,l=0}^{\infty} \frac{i_1^m \, i_2^n \, i_3^l (-c\Delta t)^{m+n+l}}{m!n!l!} \partial_{x_1^m} \partial_{x_2^n} \partial_{x_3^l} f_{\boldsymbol{i}}^{\star}(\boldsymbol{x}, t), \tag{4.4}$$

where $c = \Delta x / \Delta t$ is the lattice velocity, $\partial_{t^k} = \frac{\partial^k}{\partial t^k}, \partial_{x_i^k} = \frac{\partial^k}{\partial x_i^k}$, $i = 1, 2, 3$, $k \in \mathbb{N}$. Since position $\boldsymbol{x}$ and time t are constant in this procedure, the dependence on them will be omitted in the following steps.

For all $\alpha, \beta, \gamma \in \{0, 1, 2\}$, the post-collision raw moment $m^{\star}_{(\alpha,\beta,\gamma)}$ is defined by

$$m^{\star}_{(\alpha,\beta,\gamma)} = \sum_{\boldsymbol{i} \in \mathcal{Q}} i_1^{\alpha} \, i_2^{\beta} \, i_3^{\gamma} \, f_{\boldsymbol{i}}^{\star}. \tag{4.5}$$

If Eq. (4.4) is multiplied by i_1^{α}, i_2^{β}, i_3^{γ}, where $\alpha, \beta, \gamma \in \{0, 1, 2\}$, and summed over the indices $i_1, i_2, i_3 \in \{-1, 0, 1\}$, we get

$$\sum_{r=0}^{\infty} \frac{(\Delta t)^r}{r!} \partial_{t^r} m_{(\alpha,\beta,\gamma)} = \sum_{m,n,l=0}^{\infty} \frac{(-c\Delta t)^{m+n+l}}{m!n!l!} \partial_{x^m} \partial_{y^n} \partial_{z^l} m^{\star}_{(\alpha+m,\beta+n,\gamma+l)}. \tag{4.6}$$

Next, the diffusive scaling is chosen such that $\Delta x = \varepsilon$, $\Delta t = \varepsilon^2$. Then, Eq. (4.6) becomes

$$\sum_{r=0}^{\infty} \frac{(\varepsilon)^{2r}}{r!} \partial_{t^r} m_{(\alpha,\beta,\gamma)} = \sum_{m,n,l=0}^{\infty} \frac{(-\varepsilon)^{m+n+l}}{m!n!l!} \partial_{x^m} \partial_{y^n} \partial_{z^l} m^{\star}_{(\alpha+m,\beta+n,\gamma+l)}. \tag{4.7}$$

Now, we have Eq. (4.7) with the perturbation parameter ε and the unknowns $m_{(\alpha,\beta,\gamma)}$ and $m^{\star}_{(\alpha,\beta,\gamma)}$. Using the regular perturbation expansion of $m_{\alpha,\beta,\gamma}$ and $m^{\star}_{\alpha,\beta,\gamma}$ with respect to ε, we obtain [80] $\forall \alpha, \beta, \gamma \in \{0, 1, 2\}$

$$m_{(\alpha,\beta,\gamma)} = \sum_{k=0}^{\infty} \varepsilon^k m^{(k)}_{(\alpha,\beta,\gamma)}, \tag{4.8a}$$

$$m^{\star}_{(\alpha,\beta,\gamma)} = \sum_{k=0}^{\infty} \varepsilon^k m^{\star (k)}_{(\alpha,\beta,\gamma)}, \tag{4.8b}$$

where $m^{(k)}_{(\alpha,\beta,\gamma)}$ and $m^{\star (k)}_{(\alpha,\beta,\gamma)}$ are coefficients of the proposed regular expansions. Combining the expansions (4.8) together with Eq. (4.7), we can write

$$\sum_{r=0}^{\infty} \frac{(\varepsilon)^{2r}}{r!} \partial_{t^r} \sum_{k=0}^{\infty} \varepsilon^k m^{(k)}_{(\alpha,\beta,\gamma)} = \sum_{m,n,l=0}^{\infty} \frac{(-\varepsilon)^{m+n+l}}{m!n!l!} \partial_{x^m} \partial_{y^n} \partial_{z^l} \sum_{k=0}^{\infty} \varepsilon^k m^{\star (k)}_{(\alpha+m,\beta+n,\gamma+l)}. \tag{4.9}$$

Since $\epsilon = \delta_x$ is arbitrary, Eq. (4.9) implies that the coefficients on the left- and right-hand side corresponding to the same power of ε must be equal [140].

As the raw moments, the fundamental unknowns, such as the density and velocity for the incompressible fluid, are expanded too, i.e.,

$$\rho = \sum_{k=0}^{\infty} \varepsilon^k \rho^{(k)}, \tag{4.10a}$$

$$\boldsymbol{u} = \sum_{k=0}^{\infty} \varepsilon^k \boldsymbol{u}^{(k)}. \tag{4.10b}$$

The regular expansion of the vector quantity (4.10b) is defined as the regular expansion of individual components. Within the asymptotic analysis, the coefficients $m_{(\alpha,\beta,\gamma)}^{(k)\,(eq)}$ must be expressed using the density and velocity. For example, the raw moment $m_{(1,0,0)}^{(eq)} = m_{(1,0,0)} = \rho u_1$ is expanded as

$$\rho u_1 = m_{(1,0,0)},$$
$$\sum_{k=0}^{\infty} \varepsilon^k \rho^{(k)} \sum_{k=0}^{\infty} \varepsilon^k u_1^{(k)} = \sum_{k=0}^{\infty} \varepsilon^k m_{(1,0,0)}^{(k)}. \tag{4.11}$$

Based on the coefficients comparison in Eq. (4.11), the following relation is satisfied:

$$m_{(1,0,0)}^{(k)} = \sum_{i=0}^{k} \rho^{(i)} u_1^{(k-i)}. \tag{4.12}$$

The density is not scaled by Δx and Δt, thus the first non-zero coefficient is $\rho^{(0)}$. On the other hand, the velocity vector is scaled as $\frac{\Delta x}{\Delta t}\widetilde{\boldsymbol{u}} = \varepsilon\widetilde{\boldsymbol{u}}$ and, thus, the zeroth-order coefficient in the velocity expansion is zero. Next, due to the assumption $\Omega = \mathbb{R}^3$, the discrete domain $\hat{\Omega}$ does not change if we multiply δ_x by the factor -1, that is, if the orientation of the axes is changed [80]. It influences only the regular expansion, since the new "small" parameter has the opposite sign. We denote the original parameter ε by ε_1 and the negative parameter by ε_2. Thus, it holds $\varepsilon_1 = -\varepsilon_2$. The scalar quantities, such as the density, do not depend on the orientation of the axes. Thus

$$\sum_{k=0}^{\infty} \varepsilon_1^k \rho^{(k)} = \rho = \sum_{k=0}^{\infty} \varepsilon_2^k \rho^{(k)} = \sum_{k=0}^{\infty} (-\varepsilon_1)^k \rho^{(k)}. \tag{4.13}$$

Since $\epsilon_1 = \varepsilon_1 \delta_x$ is arbitrary, the odd coefficients must be zero, that is, $\rho^{(2k+1)} = 0, k \in \mathbb{N}$. Thus, the regular expansion of the density can be written as

$$\rho = \sum_{k=0}^{\infty} \varepsilon^{2k} \rho^{(2k)}. \tag{4.14}$$

In contrast to scalar quantities, vector quantities, such as $\boldsymbol{u}$, depend on the orientation of the axes. Thus, if we compare the regular expansions for parameters ε_1 and $\varepsilon_2 = -\varepsilon_1$, we get the following

$$\sum_{k=0}^{\infty} \varepsilon_1^k \boldsymbol{u}^{(k)} = \boldsymbol{u} = -\sum_{k=0}^{\infty} \varepsilon_2^k \boldsymbol{u}^{(k)} = -\sum_{k=0}^{\infty} (-\varepsilon_1)^k \boldsymbol{u}^{(k)}. \tag{4.15}$$

Thus, the even-order coefficients must be zero, i.e., $\boldsymbol{u}^{(2k)} = 0, k \in \mathbb{N}$. Finally, since ρ and $\boldsymbol{u}$ are collision invariants, we have $\forall \alpha, \beta, \gamma \in \{0, 1, 2\}, \alpha + \beta + \gamma \leq 1$

$$m_{(\alpha,\beta,\gamma)} = m_{(\alpha,\beta,\gamma)}^{\star}. \tag{4.16}$$

In the following, the coefficients of the same order of ε in Eq. (4.9) are compared.

Zeroth-order

$$m_{(\alpha,\beta,\gamma)}^{(0)} = m_{(\alpha,\beta,\gamma)}^{\star\,(0)}, \ \forall \alpha, \beta, \gamma \in \{0, 1, 2\}. \tag{4.17}$$

It follows from Eq. (4.17) that all zero orders of $m_{(\alpha,\beta,\gamma)}$ are collision invariants. From the properties of the LBM collision operators results

$$m_{\alpha,\beta,\gamma}^{(0)} = m_{\alpha,\beta,\gamma}^{\star\,(0)} = m_{\alpha,\beta,\gamma}^{(0)\,(eq)}, \ \forall \alpha, \beta, \gamma \in \{0, 1, 2\}. \tag{4.18}$$

Thanks to Eq. (4.18), the explicit form of the zeroth-order moment is known, since all equilibrium raw moments are equal to the combination of density and velocity. Since the zeroth-order coefficient of $\boldsymbol{u}$ is zero, the zeroth-order coefficients of raw moments are proportional to the zeroth-order density coefficient. Since $\rho^{(0)} = \rho_0 = 1$, all coefficients $m^{(0)}_{\alpha,\beta,\gamma}$ are constant with respect to space and time.

First-order

$$m^{(1)}_{(\alpha,\beta,\gamma)} = m^{\star\,(1)}_{(\alpha,\beta,\gamma)} - \partial_{x_1} m^{(0)}_{(\alpha+1,\beta,\gamma)} - \partial_{x_2} m^{(0)}_{(\alpha,\beta+1,\gamma)} - \partial_{x_3} m^{(0)}_{(\alpha,\beta,\gamma+1)}. \tag{4.19}$$

Because all zeroth-order coefficients of raw moments are constant,

$$m^{(1)}_{\alpha,\beta,\gamma} = m^{\star\,(1)}_{\alpha,\beta,\gamma}, \ \forall \alpha, \beta, \gamma \in \{0,1,2\}. \tag{4.20}$$

Thus, coefficients $m^{(1)}_{\alpha,\beta,\gamma}$ are collision invariants, too. The properties of the LBM imply

$$m^{(1)}_{\alpha,\beta,\gamma} = m^{\star\,(1)}_{\alpha,\beta,\gamma} = m^{(1)\,(eq)}_{\alpha,\beta,\gamma}, \ \forall \alpha, \beta, \gamma \in \{0,1,2\}. \tag{4.21}$$

Second-order

$$m^{(2)}_{(\alpha,\beta,\gamma)} + \partial_t m^{(0)}_{(\alpha,\beta,\gamma)} = \frac{1}{2}\left(\partial_{x_1 x_1} m^{\star\,(0)}_{(\alpha+2,\beta,\gamma)} + \partial_{x_2 x_2} m^{\star\,(0)}_{(\alpha,\beta+2,\gamma)} + \partial_{x_3 x_3} m^{\star\,(0)}_{(\alpha,\beta,\gamma+2)}\right)$$
$$+ \partial_{x_1 x_2} m^{\star\,(0)}_{(\alpha+1,\beta+1,\gamma)} + \partial_{x_1 x_3} m^{\star\,(0)}_{(\alpha+1,\beta,\gamma+1)} + \partial_{x_2 x_3} m^{\star\,(0)}_{(\alpha,\beta+1,\gamma+1)} - \partial_{x_1} m^{\star\,(1)}_{(\alpha+1,\beta,\gamma)} - \partial_{x_2} m^{\star\,(1)}_{(\alpha,\beta+1,\gamma)}$$
$$- \partial_{x_3} m^{\star\,(1)}_{(\alpha,\beta,\gamma+1)} + m^{\star\,(2)}_{\alpha,\beta,\gamma}. \tag{4.22}$$

Since the zeroth-order coefficients are constant, we get

$$m^{(2)}_{(\alpha,\beta,\gamma)} - m^{\star\,(2)}_{\alpha,\beta,\gamma} = -\partial_{x_1} m^{\star\,(1)}_{(\alpha+1,\beta,\gamma)} - \partial_{x_2} m^{\star\,(1)}_{(\alpha,\beta+1,\gamma)} - \partial_{x_3} m^{\star\,(1)}_{(\alpha,\beta,\gamma+1)}. \tag{4.23}$$

With the choice of $\alpha = \beta = \gamma = 0$, we obtain

$$\partial_{x_1} m^{\star\,(1)}_{(1,0,0)} + \partial_{x_2} m^{\star\,(1)}_{(0,1,0)} + \partial_{x_3} m^{\star\,(1)}_{(0,0,1)} = m^{\star\,(2)}_{(0,0,0)} - m^{(2)}_{(0,0,0)} = 0, \tag{4.24}$$

since $m_{(0,0,0)} = \rho$ is the collision invariant. Eq. (4.24) can be written as

$$\nabla \cdot \left(\rho^{(0)} \boldsymbol{u}^{(1)}\right) = \rho^{(0)} \nabla \cdot \left(\boldsymbol{u}^{(1)}\right) = 0. \tag{4.25}$$

Thus the velocity vector $\boldsymbol{u}^{(1)}$ satisfies the incompressible condition (2.18a) since $\rho^{(0)} \neq 0$.

Third-order

$$m^{(3)}_{(\alpha,\beta,\gamma)} + \partial_t m^{(1)}_{(\alpha,\beta,\gamma)} = m^{\star\,(3)}_{(\alpha,\beta,\gamma)} + Q - \left(\partial_{x_1} m^{\star\,(2)}_{(\alpha+1,\beta,\gamma)} + \partial_{x_2} m^{\star\,(2)}_{(\alpha,\beta+1,\gamma)} + \partial_{x_3} m^{\star\,(2)}_{(\alpha,\beta,\gamma+1)}\right)$$
$$+ \frac{1}{2}\left(\partial_{x_1 x_1} m^{\star\,(1)}_{(\alpha+2,\beta,\gamma)} + \partial_{x_2 x_2} m^{\star\,(1)}_{(\alpha,\beta+2,\gamma)} + \partial_{x_3 x_3} m^{\star\,(1)}_{(\alpha,\beta,\gamma+2)}\right) + \partial_{x_1 x_2} m^{\star\,(1)}_{(\alpha+1,\beta+1,\gamma)}$$
$$+ \partial_{x_1 x_3} m^{\star\,(1)}_{(\alpha+1,\beta,\gamma+1)} + \partial_{x_2 x_3} m^{\star\,(1)}_{(\alpha,\beta+1,\gamma+1)}, \tag{4.26}$$

where Q comprises all partial derivatives with respect to spatial coordinates of the zeroth-order raw moments. Since all zeroth-order raw moments are constant, $Q = 0$. To derive the conservation

of the momentum for the incompressible fluid from Eq. (4.26), $\alpha = 1$, $\beta = 0$, and $\gamma = 0$ are substituted into Eq. (4.26), that is,

$$\partial_t m^{(1)}_{(1,0,0)} = m^{\star\,(3)}_{(1,0,0)} - m^{(3)}_{(1,0,0)} - \left(\partial_{x_1} m^{\star\,(2)}_{(2,0,0)} + \partial_{x_2} m^{\star\,(2)}_{(1,1,0)} + \partial_{x_3} m^{\star\,(2)}_{(1,0,1)}\right) - \frac{1}{2}\left(\partial_{x_1 x_1} m^{(1)}_{(3,0,0)}\right.$$
$$\left. + \partial_{x_2 x_2} m^{(1)}_{(1,2,0)} + \partial_{x_3 x_3} m^{(1)}_{(1,0,2)}\right) + \partial_{x_1 x_2} m^{(1)}_{(2,1,0)} + \partial_{x_1 x_3} m^{(1)}_{(2,0,1)} + \partial_{x_2 x_3} m^{(1)}_{(1,1,1)}, \quad (4.27)$$

where it takes advantage of the fact that the first-order moments are collision invariants and the zeroth-order moments are constant in space. Next, according to the definition of raw moments in Eq. (3.15), $m_{(3,0,0)} = m_{(1,0,0)}$, which follows from the finite dimension of the velocity space considered. Hence, Eq. (4.27) can be written as

$$\partial_t m^{(1)}_{(1,0,0)} = m^{\star\,(3)}_{(1,0,0)} - m^{(3)}_{(1,0,0)} - \left(\partial_{x_1} m^{\star\,(2)}_{(2,0,0)} + \partial_{x_2} m^{\star\,(2)}_{(1,1,0)} + \partial_{x_3} m^{\star\,(2)}_{(1,0,1)}\right) + \frac{1}{2}\left(\partial_{x_1 x_1} m^{(1)}_{(1,0,0)}\right.$$
$$\left. + \partial_{x_2 x_2} m^{(1)}_{(1,2,0)} + \partial_{x_3 x_3} m^{(1)}_{(1,0,2)}\right) + \partial_{x_1 x_2} m^{(1)}_{(2,1,0)} + \partial_{x_1 x_3} m^{(1)}_{(2,0,1)} + \partial_{x_2 x_3} m^{(1)}_{(1,1,1)}. \quad (4.28)$$

To derive the momentum conservation law from Eq. (4.28), the second-order coefficients need to be removed. The complete procedure is summarized in [46]. It uses the features of the collision operator and contains many technical steps. The final equation of this procedure is

$$\partial_t u^{(1)}_1 = F^{(3)}_1 - \partial_{x_1} c_s^2 \frac{\rho^{(2)}}{\rho^{(0)}} - \left(u^{(1)}_1 \partial_{x_1} u^{(1)}_1 + u^{(1)}_2 \partial_{x_2} u^{(1)}_{x_1} + u^{(1)}_{x_3} \partial_{x_3} u^{(1)}_{x_1}\right)$$
$$+ \nu\left(\partial^2_{x_1} u^{(1)}_1 + \partial^2_{x_2} u^{(1)}_1 + \partial^2_{x_3} u^{(1)}_1\right). \quad (4.29)$$

The term $F^{(3)}_1$ represents the volume forces and $c_s^2 \frac{\rho^{(2)}}{\rho^{(0)}}$ is the pressure. Hence, the pressure p in the LBM is approximated as

$$p = p_0 + c_s^2 \frac{\delta\rho}{\rho^{(0)}} = p_0 c_s^2 \frac{\rho - \rho^{(0)}}{\rho^{(0)}} = c_s^2 \frac{\rho^{(2)}}{\rho^{(0)}} + \mathcal{O}\left(\varepsilon^4\right), \quad (4.30)$$

where $\rho^{(0)} = 1$ and p_0 is the reference pressure [118]. It is consistent with Eq. (3.8).

4.2.1 Local computation of spatial partial derivatives of fluid velocity

In the grid refinement technique (see Section 3.8), the local computation of the partial derivatives of the fluid velocity is used. These formulae are derived using asymptotic analysis. The starting equation for the derivation is the second-order equation (4.23) with $\alpha = 2$, $\beta = 0$, $\gamma = 0$, and we obtain the following equation.

$$m^{(2)}_{(2,0,0)} = m^{\star\,(2)}_{(2,0,0)} - \left(\partial_{x_1} m^{(1)}_{(1,0,0)} + \partial_{x_2} m^{(1)}_{(2,1,0)} + \partial_{x_3} m^{(1)}_{(2,0,1)}\right), \quad (4.31)$$

and with $\alpha = 0$, $\beta = 2$, $\gamma = 0$

$$m^{(2)}_{(0,2,0)} = m^{\star\,(2)}_{(0,2,0)} - \left(\partial_{x_1} m^{(1)}_{(1,2,0)} + \partial_{x_2} m^{(1)}_{(0,1,0)} + \partial_{x_3} m^{(1)}_{(0,2,1)}\right). \quad (4.32)$$

Eqs. (4.31), (4.32) are modified according to several steps described in detail in the technical report [46]. The resulting equations are

$$\partial_{x_1} u^{(1)}_1 = \frac{\omega_1}{2\rho^{(0)}}\left(-2C^{(2)}_{(2,0,0)} + C^{(2)}_{(0,2,0)} + C^{(2)}_{(0,0,2)}\right) + \frac{\omega_2}{2\rho^{(0)}}\left(\rho^{(2)} - C^{(2)}_{(2,0,0)} - C^{(2)}_{(0,2,0)} - C^{(2)}_{(0,0,2)}\right),$$
$$(4.33a)$$

$$\partial_{x_2} u^{(1)}_2 = \partial_{x_1} u^{(1)}_1 + \frac{3\omega_1}{2\rho^{(0)}}\left(C^{(2)}_{(2,0,0)} - C^{(2)}_{(0,2,0)}\right), \quad (4.33b)$$

$$\partial_{x_3} u^{(1)}_3 = \partial_{x_1} u^{(1)}_1 + \frac{3\omega_1}{2\rho^{(0)}}\left(C^{(2)}_{(2,0,0)} - C^{(2)}_{(0,0,2)}\right), \quad (4.33c)$$

where $C^{(k)}_{(\alpha,\beta,\gamma)}$ is the coefficient of the asymptotic expansion of $C_{(\alpha,\beta,\gamma)}$, $k \in \mathbb{N}_0$, $\alpha, \beta, \gamma \in \{0, 1, 2\}$. The zeroth-order coefficient of the density can be replaced by $\rho^{(0)} = 1$ or by ρ with the error term proportional to $\mathcal{O}(\varepsilon^2)$. The velocity coefficient $u_1^{(1)}$ approximates the velocity component u_1 with the error proportional to $\mathcal{O}(\varepsilon^3)$. The zeroth-order cumulants satisfy $C^{(0)}_{(2,0,0)} = C^{(0)}_{(0,2,0)} = C^{(0)}_{(0,0,2)} = c_s^2 \rho^{(0)}$. Thus, the term $\left(\rho^{(2)} - C^{(2)}_{(2,0,0)} - C^{(2)}_{(0,2,0)} - C^{(2)}_{(0,0,2)}\right)$ can be replaced by the term $\left(\rho - C_{(2,0,0)} - C_{(0,2,0)} - C_{(0,0,2)}\right)$ with an error proportional $\mathcal{O}(\varepsilon^2)$. Thus, Eq. (4.33a) approximates the $\partial_{x_1} u_1$ with an error proportional to $\mathcal{O}(\varepsilon^2)$. Similarly, the terms $\left(C^{(2)}_{(2,0,0)} - C^{(2)}_{(0,2,0)}\right)$, $\left(C^{(2)}_{(2,0,0)} - C^{(2)}_{(0,0,2)}\right)$ can be replaced by $\left(C_{(2,0,0)} - C_{(0,2,0)}\right)$, $\left(C_{(2,0,0)} - C_{(0,0,2)}\right)$ with an error proportional to $\mathcal{O}(\varepsilon^2)$.

The remaining space partial derivatives of the velocity vector $\boldsymbol{u}$ can be approximated as

$$\partial_{x_2} u_1^{(1)} = -\frac{3\omega_1}{\rho^{(0)}} C^{(2)}_{(1,1,0)} - \partial_{x_1} u_2^{(1)}, \tag{4.34a}$$

$$\partial_{x_2} u_3^{(1)} = -\frac{3\omega_1}{\rho^{(0)}} C^{(2)}_{(0,1,1)} - \partial_{x_3} u_2^{(1)}, \tag{4.34b}$$

$$\partial_{x_1} u_3^{(1)} = -\frac{3\omega_1}{\rho^{(0)}} C^{(2)}_{(1,0,1)} - \partial_{x_3} u_1^{(1)}. \tag{4.34c}$$

Eqs. (4.34) produce only approximations for particular combinations of the partial derivatives of $\boldsymbol{u}$. Thus, to compute individual partial derivatives, the approximations (4.34) need to be combined with other methods such as the finite difference method. However, Eqs. (4.34) can be used for the approximation of the stress tensor components. The second-order coefficients of cumulants $C^{(2)}_{(1,1,0)}$, $C^{(2)}_{(0,1,1)}$, and $C^{(2)}_{(1,0,1)}$ can be approximated by cumulants $C_{(1,1,0)}$, $C_{(0,1,1)}$, and $C_{(1,0,1)}$ with an error proportional to $\mathcal{O}(\varepsilon^2)$, respectively. Finally, the complete derivation of the formulae (4.34) can be found in [46].

4.3   Chapter summary

In this chapter, the asymptotic analysis of the CuLBM was performed. We have found that the CuLBM numerical solution approximates the solution of the incompressible Navier-Stokes equations. Next, the local approximations of spatial partial velocity derivatives were derived, which coincide with approximations in [121]. These approximations are further used in the grid refinement technique in Chapter 6.

Investigation of Boundary Conditions

<div align="right">5</div>

Boundary conditions (BCs) are one of the most investigated problems related to the LBM. In real-world application problems, BCs specify the behavior at the boundary by prescribing pressure or velocity profiles. The accuracy of BCs treatment influences the accuracy of the whole numerical method, and therefore a correct treatment is desirable in various applications, such as simulations of processes in fluidized bed reactors, where the numerical solution is affected by small changes at the boundaries [9].

The accuracy of BCs in the LBM began to be investigated in the 90s of the twentieth century [32, 199]. Due to the lattice structure used by the LBM, BC modifications for curved geometries such as interpolated [181, 185] and extrapolated [198] BCs were introduced. Alternatively, the immersed boundary method was used in connection with the LBM [49, 68, 148]. Since improved BCs often disturb the locality of the LBM algorithm [198], locality-preserving BCs were suggested even for curved boundaries [93, 136, 171]. Furthermore, numerical stability has been improved by adjustment of BCs to particular collision operators [2, 60], flow regimes [33, 99, 125], compressible fluids [63], and non-Newtonian fluids [169]. Another problem of BCs is the reflection of acoustic waves at the boundaries, thus BCs with reduced reflection have been derived [103]. The investigation of BCs is usually conducted numerically [7, 58, 186] or by the use of asymptotic analysis [107, 109].

In this chapter, the BCs given in Chapter 3 are investigated numerically using two benchmark problems with analytical solution to demonstrate their accuracy and influence on the numerical solution.

5.1   Methods

The mesoscopic boundary conditions given in Section 3.7 are investigated in the time interval $\mathcal{T} = (0, T)$ and in the cuboidal domain $\Omega = (0, L_1) \times (0, L_2) \times (0, L_3)$ with dimensions $L_1 = 3$ m and $L_2 = L_3 = 1$ m. The final time is $T = 100$ s. The boundary $\partial\Omega$ consists of the inflow $\partial\Omega_{\text{in}}$, outflow $\partial\Omega_{\text{out}}$, and wall $\partial\Omega_{\text{wall}}$. The Dirichlet and Neumann BC for velocity and pressure are prescribed at $\partial\Omega_{\text{in}}$, respectively. At $\partial\Omega_{\text{wall}}$, the no-slip BC is assumed. Finally, zero Neumann and Dirichlet BC ($p_{\text{out}} = 0$ kg m^{-1} s^{-2}) are prescribed at $\partial\Omega_{\text{out}}$ for velocity and pressure, respectively. Initially, zero velocity and pressure are considered in Ω. For the purpose of the investigation, the Newtonian fluid with constant kinematic viscosity $\nu = 0.01$ m^2 s^{-1} and constant density $\rho_0 = 1$ kg m^{-3} is considered. The cumulant collision operator CuLBM with the non-dimensional kinematic viscosity $\widetilde{\nu} = 0.01$ is used for all simulations.

5.2   Benchmark problems

In Figures 5.1a, 5.1b, the configurations of the domain and BCs for two benchmark problems (BP1 and BP2) are illustrated. At $\partial\Omega_{\text{in}}$, the analytical velocity profile described in Section 2.2.3 is prescribed with the corresponding Neumann BC for pressure given by Eq. (2.18d). At Ω_{wall} (gray planes in Figures 5.1a, 5.1b), the no-slip boundary condition is prescribed. Finally, in BP1, the periodic boundary conditions are assumed in the x_3-direction.

To assess the boundary conditions used, the relative errors in terms of the L_1 and L_2 norms computed in the entire domain Ω are evaluated for both benchmark problems. Furthermore, to see the distribution of errors in the x_1-direction, the L_1 norms $\|\cdot\|_{\text{L}_1,S(x_1)}$ (for the definition see page xxvii) of numerical and analytical solutions are computed within the cross section

$$S(x_1) = \left\{ (x_1, x_2, x_3)^T \big| 0 < x_2 < L_2, 0 < x_3 < L_3 \right\}. \tag{5.1}$$

For the investigation, four grids with parameters in Table 5.2 and six BCs listed in Table 5.1 are used.

BC id.	BC at $\partial\Omega_{\text{out}}$	Section
I	Free outflow BC	3.7.5
II	Equilibrium BC	3.7.3
III	Anti-bounce-back	3.7.7
IV	Interpolated outflow BC without decomposition	3.7.6
V	Interpolated outflow BC with decomposition	3.7.6
VI	Moment-based outflow BC	3.7.8

Table 5.1: List of the used outflow boundary conditions (BCs) for the investigation of their influence on the numerical solution.

Grid$_{\text{id}}$	N_1	N_2	N_3	δ_x	δ_t
Grid$_1$	189	64	64	$1.59 \cdot 10^{-2}$	$2.52 \cdot 10^{-4}$
Grid$_2$	381	128	128	$7.87 \cdot 10^{-3}$	$6.20 \cdot 10^{-5}$
Grid$_3$	573	192	192	$5.23 \cdot 10^{-3}$	$2.74 \cdot 10^{-5}$
Grid$_4$	765	256	256	$3.92 \cdot 10^{-3}$	$1.54 \cdot 10^{-5}$

Table 5.2: Parameters of the numerical grid used for the investigation of the outflow boundary conditions.

(a) Computational domain Ω for BP1.   (b) Computational domain Ω for BP2.
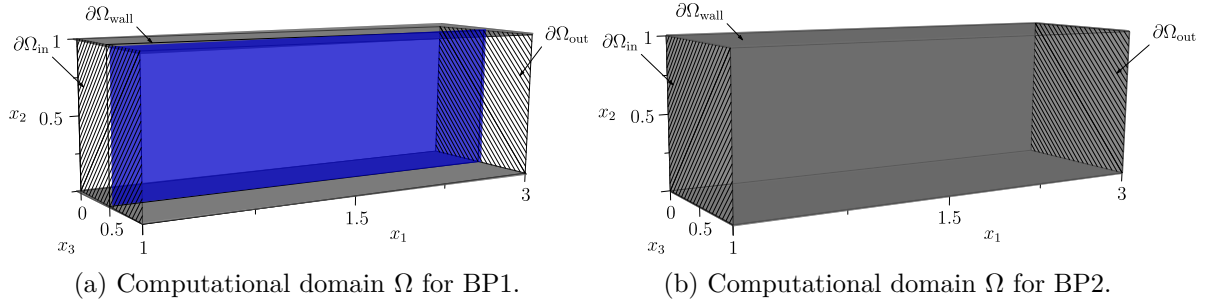
Figure 5.1: Computational domains for BP1 and BP2. The blue plane in Figure 5.1a represents a slice through Ω used for investigation and demonstration of the results in Section 5.3.1 . The gray planes represent the wall. Periodic boundary conditions are used in the x_3-direction in Figure 5.1a.

5.2.1   BP1: Hagen-Poiseuille flow

The first benchmark problem BP1 describes fluid flow between two parallel plates with the analytical solution given in Section 2.2.3. The maximal velocity in Ω is $U_{\max} = 0.6 \text{ m s}^{-1}$. The purpose of this benchmark problem is to investigate the effect of inflow and outflow BCs on the numerical solution. First, the influence of two inflow BCs given in Section 3.7 is investigated. Subsequently, the outflow BCs listed in Table 5.1 are assessed.

Setup for inflow boundary investigation

First, the equilibrium BC is used at $\partial\Omega_{\mathrm{in}}$ to prescribe the given velocity profile (2.19) and the Neumann BC for pressure. At $\partial\Omega_{\mathrm{out}}$ and $\partial\Omega_{\mathrm{wall}}$, equilibrium outflow BC and fullway bounce-back BC are used, respectively. Due to the fullway bounce-back BC applied at walls, the offset vector (defined in Section 3.1) is $\boldsymbol{P} = (0, {}^{\delta_x}\!/_2, 0)^T$, therefore, $\delta_x = {}^{L_2}\!/_{(N_2-2)}$ to correctly approximate the vertical dimension of Ω.

The second BC used at $\partial\Omega_{\mathrm{in}}$ is the moment-based BC. It is combined with moment-based BC and equilibrium BC applied at $\partial\Omega_{\mathrm{wall}}$ and $\partial\Omega_{\mathrm{out}}$, respectively. Due to BCs applied on the walls, the offset vector is $\boldsymbol{P} = \boldsymbol{0}$ and $\delta_x = {}^{L_2}\!/_{(N_2-1)}$.

The inflow BCs are investigated using one grid only. In the case of moment-based BC applied at $\partial\Omega_{\mathrm{in}}$, the grid with the Grid id.($k = 2$) in Table 5.2 is used. On the other hand, in the case of the fullway bounce-back BC applied at $\partial\Omega_{\mathrm{wall}}$, the grid needs to be adjusted in the horizontal direction to correctly preserve the vertical and horizontal dimensions of computational domain Ω, i.e., $N_1 = 378, N_2 = N_3 = 128$ points are used with the grid spacing parameter $\delta_x = 7.94 \cdot 10^{-3}$ m and the time step $\delta_t = 6.3 \cdot 10^{-5}$ s.

To demonstrate the behavior of the flow near the interface between different BC types, the results are plotted in the plane given by the (physical) point $(0, 0, 0.5)^T$ (in meters) and the normal unit vector $(0, 0, 1)^T$, as illustrated in Figure 5.1a.

Setup for outflow boundary investigation

The outflow BCs given in Table 5.1 are investigated with the moment-based BCs applied at $\partial\Omega_{\mathrm{in}}$ and $\partial\Omega_{\mathrm{wall}}$. Thus, the offset vector is $\boldsymbol{P} = \boldsymbol{0}$ and all the grids given in Table 5.2 are used.

5.2.2   BP2: Rectangular duct flow

In the second benchmark problem BP2, fluid flow in a rectangular duct is considered with the analytical solution given in Section 2.2.3. The infinite sums in Eqs. (2.21) and (2.22) are truncated at $i = 50$ terms. The (constant) pressure drop $\mathrm{d}p$ is set to obtain maximal velocity $U_{\max} = 0.6 \ \mathrm{m\,s}^{-1}$ (i.e., the same values are used as in BP1).

In contrast to BP1, only the outflow BCs given in Table 5.1 are investigated together with the moment-based BCs applied at $\partial\Omega_{\mathrm{in}}$ and $\partial\Omega_{\mathrm{wall}}$. Since periodic BCs in the x_3-direction were used in BP1, moment-based BCs were applied only for faces of $\partial\Omega$. To show the effect of moment-based BCs on the edges and corners of the boundary $\partial\widetilde{\Omega}$, no-slip BCs are applied in the x_3-direction. Based on the results of BP1, moment-based BCs are applied at the inflow and solid walls to minimize the error caused by the inflow BC and the offset vector is $\boldsymbol{P} = \boldsymbol{0}$.

5.3   Results and Discussion

5.3.1   BP1: Hagen-Poiseuille flow

The discrepancies between the numerical and analytical solutions are illustrated using Figures 5.2, 5.3, and 5.4 in the planar cut through Ω (see Figure 5.1a). The differences of $u_1 - u_{1,\mathrm{an}}$ and $u_2 - u_{2,\mathrm{an}}$ in Figure 5.2 show that the equilibrium BC causes spurious oscillations near the corners of the inflow boundary with a magnitude of $0.02 \ \mathrm{m\,s}^{-1}$. We hypothesize that the source of these oscillations is the interface between different types of BCs, i.e., between the equilibrium BC at the inflow and the fullway bounce-back BC at the walls. This hypothesis is supported by the results in Figure 5.3, where moment-based BCs were used both at the inflow and at the walls and nonphysical artifacts were significantly reduced. The degree of improvement is further illustrated in Figure 5.4, which shows that the differences are orders of magnitude smaller. Finally, in Figure 5.5, a profile of the velocity component u_1 along the vertical line $\left\{ \left(\frac{L_1}{2}, y, \frac{L_3}{2}\right)^T \middle| 0 < y < L_2 \right\}$ is given for both inflow boundary configurations.
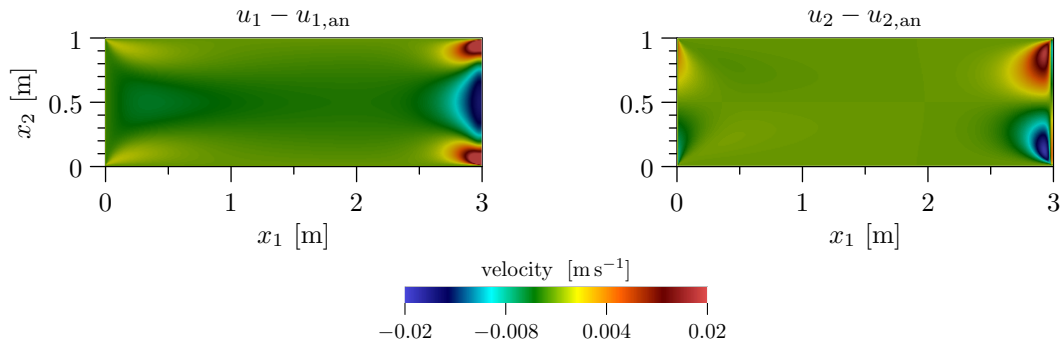

Figure 5.2: BP1: 2D profile of velocity differences for the problem with the equilibrium BC at the inflow and at the outflow, and the bounce-back BC at the walls.

The persisting oscillations at the outflow shown in Figure 5.3 are the starting point for the following investigation of the outflow BCs. The outflow BCs are further evaluated using the plots of relative errors in terms of $\| \cdot \|_{\mathrm{L}_1, S(x_1)}$ along the x_1 coordinate shown in Figures 5.6 and 5.7, respectively. The largest discrepancy between numerical and analytical solutions is observed for outflow BCs I and IV. For the remaining BCs considered, more significant differences are observed in the pressure error plots and our proposed outflow conditions V (Interpolated boundary condition with decomposition) and VI (Moment-based outflow) produce the best results.
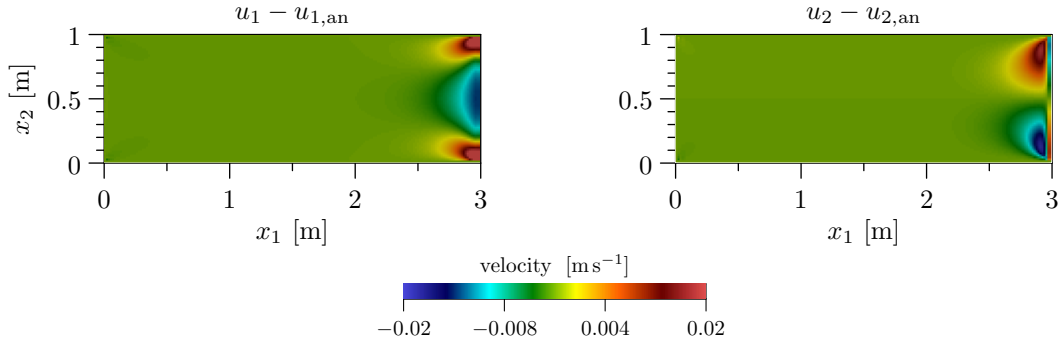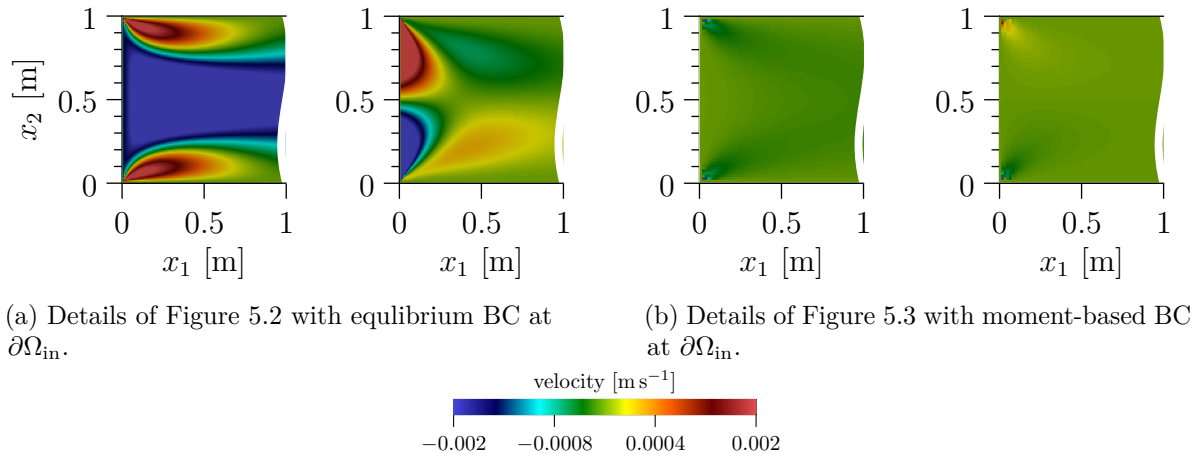
Figure 5.3: BP1: 2D profile of velocity differences for the problem with the moment-based BC at the inflow and at walls, and the equilibrium BC at the outflow.

(a) Details of Figure 5.2 with equilibrium BC at $\partial\Omega_{\mathrm{in}}$.

(b) Details of Figure 5.3 with moment-based BC at $\partial\Omega_{\mathrm{in}}$.

Figure 5.4: BP1: Details of the velocity fields near the inflow boundary for different BCs at the inflow and walls. Note that the scale of the differences is an order of magnitude smaller compared to Figures 5.2 and 5.3.
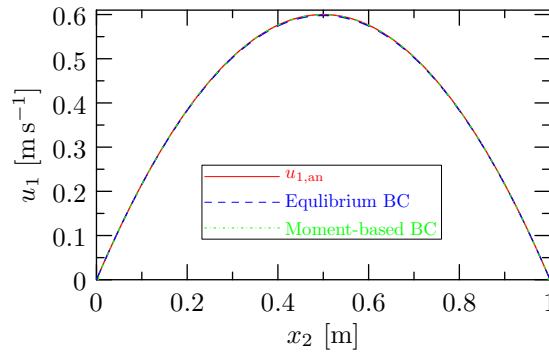

Figure 5.5: BP1: 1D plot of the velocity component $u_1\left(\frac{L_1}{2}, x_2, \frac{L_3}{2}\right)$, $x_2 \in (0, L_2)$.

Table 5.3 lists the relative errors L_1 and L_2 of the pressure and velocity calculated in the entire domain Ω. In agreement with the graphs in Figure 5.7, the boundary configurations I and IV produced large pressure errors. The remaining errors for the boundary conditions were within units of percent, except for configuration II. For both pressure and velocity, the lowest L_1 and L_2 errors are achieved with boundary configuration VI. The second-lowest error corresponds to the boundary configuration V.
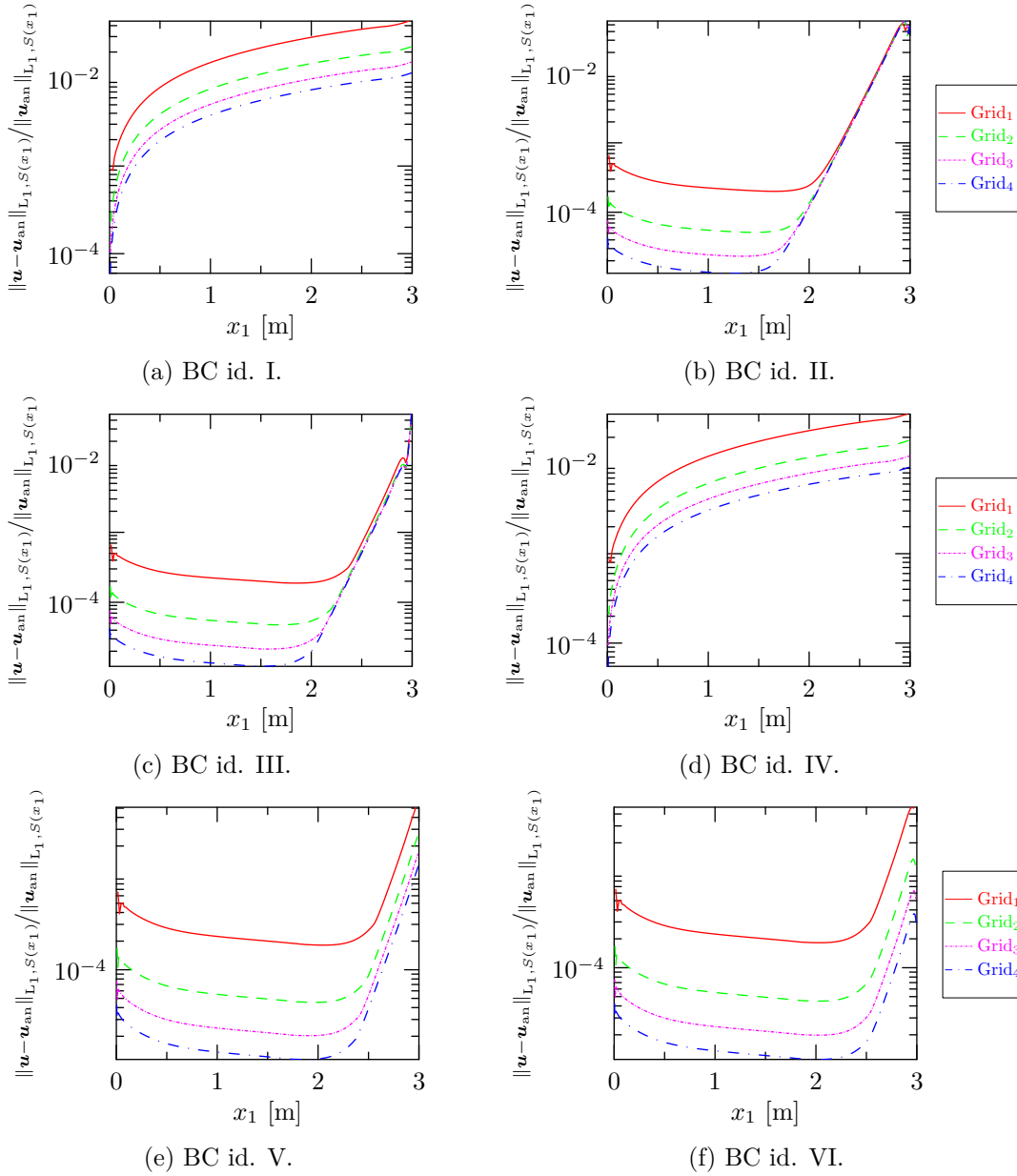
(a) BC id. I.

(b) BC id. II.

(c) BC id. III.

(d) BC id. IV.

(e) BC id. V.

(f) BC id. VI.

Figure 5.6: BP1: L_1 realtive error plots $\|\boldsymbol{u}-\boldsymbol{u}_{\mathrm{an}}\|_{\mathrm{L}_1,S(x_1)}/\|\boldsymbol{u}_{\mathrm{an}}\|_{\mathrm{L}_1,S(x_1)}$ $[-]$ for different BC configurations defined in Table 5.1.

Finally, the 2D plots of $u_1 - u_{1,\mathrm{an}}$ and $u_2 - u_{2,\mathrm{an}}$ are given for boundary configuration VI in Figure 5.8. Although oscillations at the corners of the outflow boundary still persist, their magnitude does not exceed $0.002\ \mathrm{m\,s^{-1}}$ which is an order of magnitude less than in the original case shown in Figure 5.3.
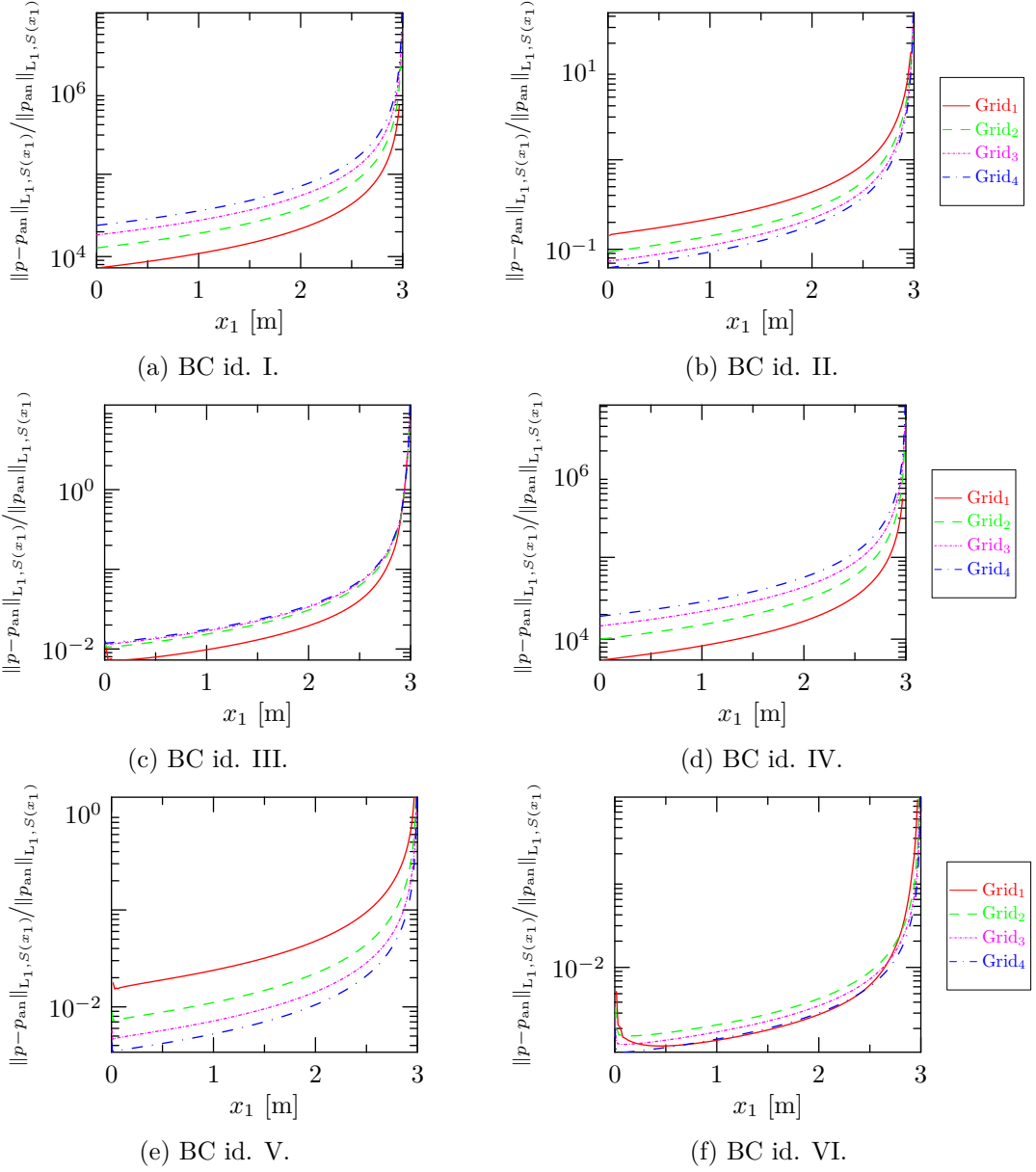
Figure 5.7: BP1: L_1 relative error plots $\|p-p_{\mathrm{an}}\|_{L_1,S(x_1)}/\|p_{\mathrm{an}}\|_{L_1,S(x_1)}$ $[-]$ for different BC configurations defined in Table 5.1.

BC id:	I	II	III	IV	V	VI
$\|p - p_{\mathrm{an}}\|_{\mathrm{L}_1} / \|p_{\mathrm{an}}\|_{\mathrm{L}_1}$						
Grid_1	$1.45 \cdot 10^4$	$2.93 \cdot 10^{-1}$	$1.43 \cdot 10^{-2}$	$1.10 \cdot 10^4$	$3.14 \cdot 10^{-2}$	$\mathbf{2.44 \cdot 10^{-3}}$
Grid_2	$2.54 \cdot 10^4$	$1.90 \cdot 10^{-1}$	$2.14 \cdot 10^{-2}$	$1.99 \cdot 10^4$	$1.47 \cdot 10^{-2}$	$\mathbf{3.05 \cdot 10^{-3}}$
Grid_3	$3.66 \cdot 10^4$	$1.50 \cdot 10^{-1}$	$2.34 \cdot 10^{-2}$	$2.90 \cdot 10^4$	$9.47 \cdot 10^{-3}$	$\mathbf{2.48 \cdot 10^{-3}}$
Grid_4	$4.78 \cdot 10^4$	$1.28 \cdot 10^{-1}$	$2.43 \cdot 10^{-2}$	$3.80 \cdot 10^4$	$6.96 \cdot 10^{-3}$	$\mathbf{2.04 \cdot 10^{-3}}$
$\|p - p_{\mathrm{an}}\|_{\mathrm{L}_2} / \|p_{\mathrm{an}}\|_{\mathrm{L}_2}$						
Grid_1	$1.26 \cdot 10^4$	$2.55 \cdot 10^{-1}$	$1.46 \cdot 10^{-2}$	$9.56 \cdot 10^3$	$2.74 \cdot 10^{-2}$	$\mathbf{3.93 \cdot 10^{-3}}$
Grid_2	$2.21 \cdot 10^4$	$1.66 \cdot 10^{-1}$	$1.98 \cdot 10^{-2}$	$1.73 \cdot 10^4$	$1.28 \cdot 10^{-2}$	$\mathbf{3.08 \cdot 10^{-3}}$
Grid_3	$3.17 \cdot 10^4$	$1.32 \cdot 10^{-1}$	$2.14 \cdot 10^{-2}$	$2.51 \cdot 10^4$	$8.26 \cdot 10^{-3}$	$\mathbf{2.40 \cdot 10^{-3}}$
Grid_4	$4.14 \cdot 10^4$	$1.12 \cdot 10^{-1}$	$2.21 \cdot 10^{-2}$	$3.30 \cdot 10^4$	$6.07 \cdot 10^{-3}$	$\mathbf{1.94 \cdot 10^{-3}}$
$\|\boldsymbol{u} - \boldsymbol{u}_{\mathrm{an}}\|_{\mathrm{L}_1} / \|\boldsymbol{u}_{\mathrm{an}}\|_{\mathrm{L}_1}$						
Grid_1	$2.21 \cdot 10^{-2}$	$3.89 \cdot 10^{-3}$	$1.09 \cdot 10^{-3}$	$1.79 \cdot 10^{-2}$	$\mathbf{4.45 \cdot 10^{-4}}$	$4.72 \cdot 10^{-4}$
Grid_2	$1.11 \cdot 10^{-2}$	$3.82 \cdot 10^{-3}$	$9.21 \cdot 10^{-4}$	$8.96 \cdot 10^{-3}$	$1.65 \cdot 10^{-4}$	$\mathbf{1.25 \cdot 10^{-4}}$
Grid_3	$7.42 \cdot 10^{-3}$	$3.86 \cdot 10^{-3}$	$9.11 \cdot 10^{-4}$	$5.98 \cdot 10^{-3}$	$9.76 \cdot 10^{-5}$	$\mathbf{5.67 \cdot 10^{-5}}$
Grid_4	$5.57 \cdot 10^{-3}$	$3.89 \cdot 10^{-3}$	$9.16 \cdot 10^{-4}$	$4.49 \cdot 10^{-3}$	$6.84 \cdot 10^{-5}$	$\mathbf{3.22 \cdot 10^{-5}}$
$\|\boldsymbol{u} - \boldsymbol{u}_{\mathrm{an}}\|_{\mathrm{L}_2} / \|\boldsymbol{u}_{\mathrm{an}}\|_{\mathrm{L}_2}$						
Grid_1	$2.38 \cdot 10^{-2}$	$8.36 \cdot 10^{-3}$	$2.46 \cdot 10^{-3}$	$1.92 \cdot 10^{-2}$	$\mathbf{6.61 \cdot 10^{-4}}$	$7.96 \cdot 10^{-4}$
Grid_2	$1.20 \cdot 10^{-2}$	$8.60 \cdot 10^{-3}$	$3.05 \cdot 10^{-3}$	$9.66 \cdot 10^{-3}$	$2.95 \cdot 10^{-4}$	$\mathbf{2.33 \cdot 10^{-4}}$
Grid_3	$8.01 \cdot 10^{-3}$	$8.75 \cdot 10^{-3}$	$3.43 \cdot 10^{-3}$	$6.45 \cdot 10^{-3}$	$1.90 \cdot 10^{-4}$	$\mathbf{1.11 \cdot 10^{-4}}$
Grid_4	$6.01 \cdot 10^{-3}$	$8.85 \cdot 10^{-3}$	$3.66 \cdot 10^{-3}$	$4.84 \cdot 10^{-3}$	$1.40 \cdot 10^{-4}$	$\mathbf{6.52 \cdot 10^{-5}}$

Table 5.3: BP1: L_1 and L_2 relative errors of pressure and velocity for different BC configurations (Table 5.1) and grid resolutions (Table 5.2). The values typeset in bold highlight the lowest error for the given grid resolution.
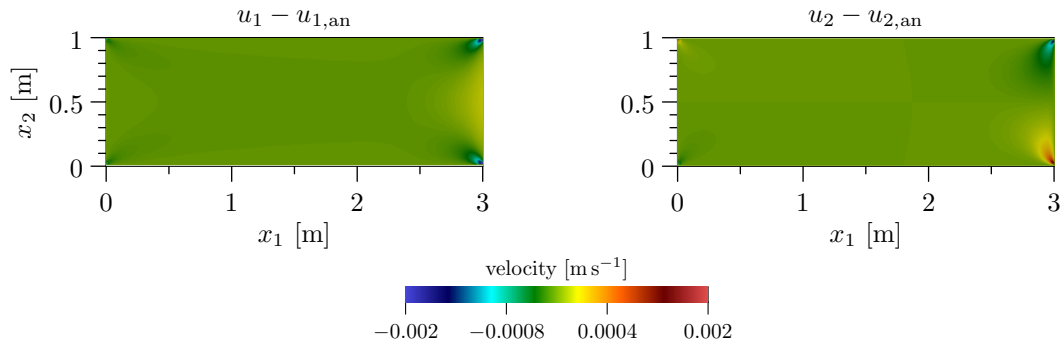
Figure 5.8: BP1: 2D plots of the difference between numerical and analytical velocity components for the problem with boundary configuration VI, see Table 5.1.

5.3.2   BP2: Rectangular duct flow

Similar to BP1, BP2 studies the numerical solution with the particular outflow BC. First, the graphs consisting of relative L_1 errors in the cross section $S(x_1)$ are presented for four grids given in Table 5.2 and six outflow BCs given in Table 5.1. A significant disagreement between the analytical (given by Eq. (2.23)) and numerical solutions of pressure is observed in Figure 5.10 for boundary configurations I and IV. The velocity results in Figure 5.9 are similar to the results in BP1. However, the shape of the curves is different, and the smallest differences between numerical and analytical velocity are observed near the middle of the domain Ω. Boundary configurations V and VI have a similar error distribution along the x_1 axis.

Finally, the L_1 and L_2 relative errors of velocity and pressure calculated in the entire domain are given in Table 5.4. As in BP1, the smallest errors are obtained with boundary configuration VI. The outflow boundary configuration V shows very close results to those for the outflow condition VI. Since the lowest errors are within hundredths of percent points, the results can be considered satisfactory. Contrary to BP1 results, the results in Table 5.3 indicate the convergence (in terms of pressure and velocity errors) of our proposed BCs V and VI.
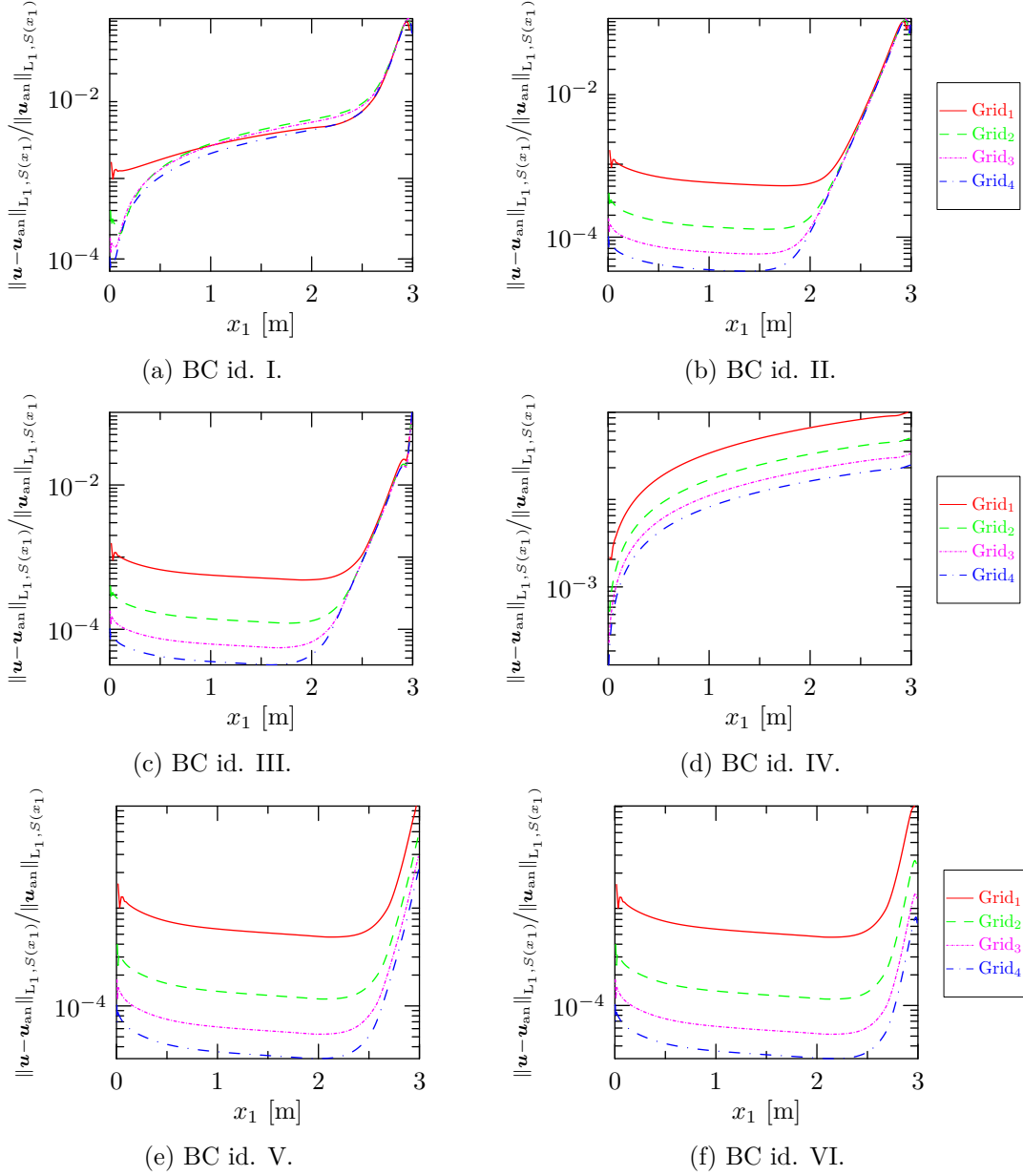
(a) BC id. I.

(b) BC id. II.

(c) BC id. III.

(d) BC id. IV.

(e) BC id. V.

(f) BC id. VI.

Figure 5.9: BP2: L_1 relative error plots $\|\boldsymbol{u}-\boldsymbol{u}_{\mathrm{an}}\|_{\mathrm{L}_1,S(x_1)}\big/\|\boldsymbol{u}_{\mathrm{an}}\|_{\mathrm{L}_1,S(x_1)}$ $[-]$ for different BC configurations defined in Table 5.1.
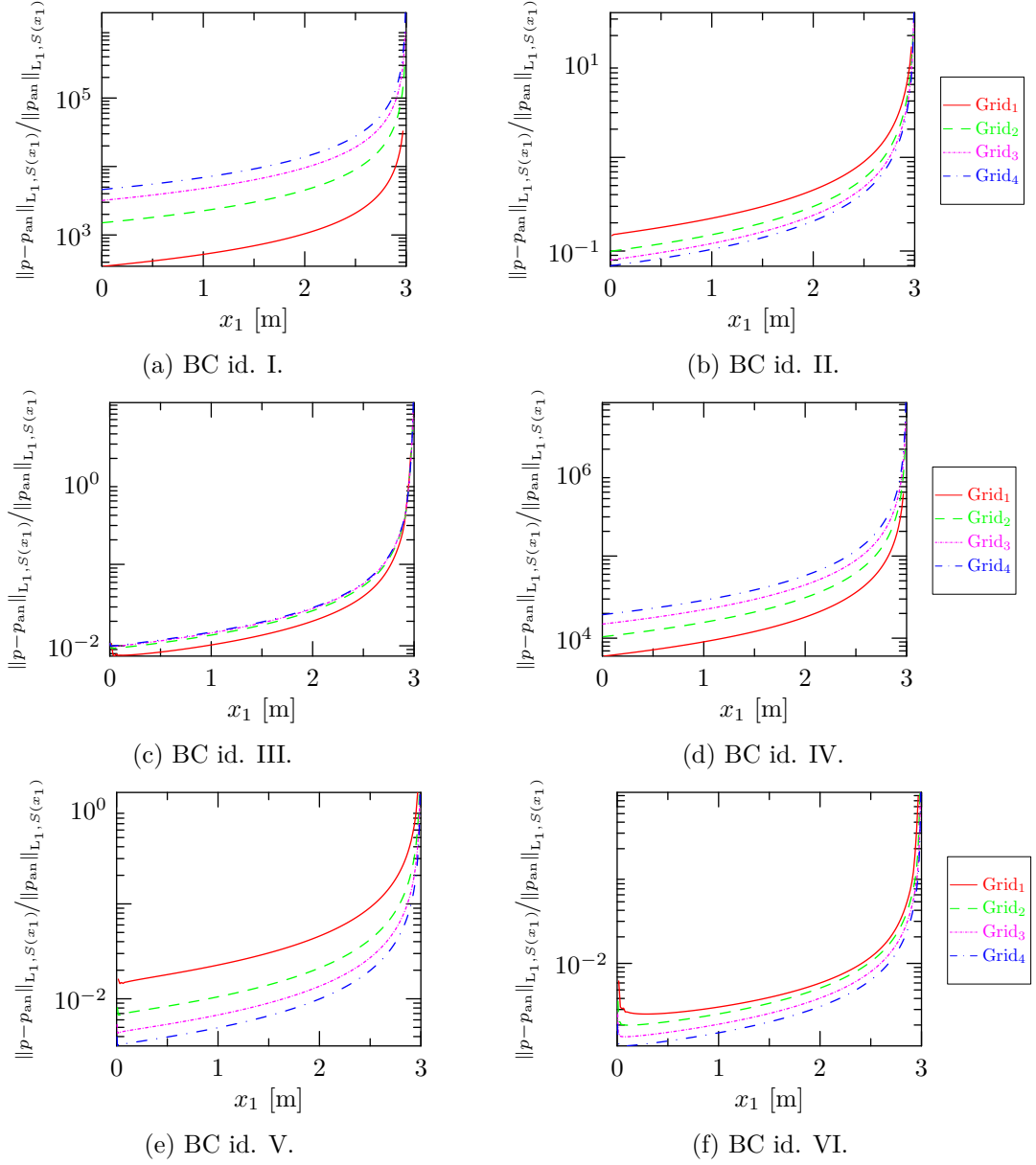
Figure 5.10: BP2: L_1 relative error plots $\|p-p_{\mathrm{an}}\|_{\mathrm{L}_1,S(x_1)}/\|p_{\mathrm{an}}\|_{\mathrm{L}_1,S(x_1)}$ $[-]$ for different BC configuration defined in Table 5.1.

BC id:	I	II	III	IV	V	VI
			$\|p - p_{an}\|_{L_1} / \|p_{an}\|_{L_1}$			
Grid$_1$	$6.91 \cdot 10^2$	$2.98 \cdot 10^{-1}$	$1.43 \cdot 10^{-2}$	$1.20 \cdot 10^4$	$3.01 \cdot 10^{-2}$	$\mathbf{4.45 \cdot 10^{-3}}$
Grid$_2$	$3.00 \cdot 10^3$	$2.00 \cdot 10^{-1}$	$1.86 \cdot 10^{-2}$	$2.07 \cdot 10^4$	$1.39 \cdot 10^{-2}$	$\mathbf{3.60 \cdot 10^{-3}}$
Grid$_3$	$6.37 \cdot 10^3$	$1.62 \cdot 10^{-1}$	$1.97 \cdot 10^{-2}$	$2.96 \cdot 10^4$	$8.98 \cdot 10^{-3}$	$\mathbf{2.74 \cdot 10^{-3}}$
Grid$_4$	$9.21 \cdot 10^3$	$1.40 \cdot 10^{-1}$	$2.02 \cdot 10^{-2}$	$3.86 \cdot 10^4$	$6.59 \cdot 10^{-3}$	$\mathbf{2.19 \cdot 10^{-3}}$
			$\|p - p_{an}\|_{L_2} / \|p_{an}\|_{L_2}$			
Grid$_1$	$6.01 \cdot 10^2$	$2.59 \cdot 10^{-1}$	$1.35 \cdot 10^{-2}$	$1.04 \cdot 10^4$	$2.62 \cdot 10^{-2}$	$\mathbf{4.53 \cdot 10^{-3}}$
Grid$_2$	$2.61 \cdot 10^3$	$1.74 \cdot 10^{-1}$	$1.68 \cdot 10^{-2}$	$1.80 \cdot 10^4$	$1.21 \cdot 10^{-2}$	$\mathbf{3.33 \cdot 10^{-3}}$
Grid$_3$	$5.53 \cdot 10^3$	$1.41 \cdot 10^{-1}$	$1.77 \cdot 10^{-2}$	$2.57 \cdot 10^4$	$7.81 \cdot 10^{-3}$	$\mathbf{2.50 \cdot 10^{-3}}$
Grid$_4$	$7.98 \cdot 10^3$	$1.22 \cdot 10^{-1}$	$1.81 \cdot 10^{-2}$	$3.34 \cdot 10^4$	$5.74 \cdot 10^{-3}$	$\mathbf{1.98 \cdot 10^{-3}}$
			$\|\boldsymbol{u} - \boldsymbol{u}_{an}\|_{L_1} / \|\boldsymbol{u}_{an}\|_{L_1}$			
Grid$_1$	$7.83 \cdot 10^{-3}$	$6.50 \cdot 10^{-3}$	$2.20 \cdot 10^{-3}$	$4.12 \cdot 10^{-2}$	$\mathbf{8.69 \cdot 10^{-4}}$	$9.23 \cdot 10^{-4}$
Grid$_2$	$8.78 \cdot 10^{-3}$	$6.21 \cdot 10^{-3}$	$1.93 \cdot 10^{-3}$	$2.12 \cdot 10^{-2}$	$2.90 \cdot 10^{-4}$	$\mathbf{2.41 \cdot 10^{-4}}$
Grid$_3$	$8.55 \cdot 10^{-3}$	$6.22 \cdot 10^{-3}$	$1.94 \cdot 10^{-3}$	$1.43 \cdot 10^{-2}$	$1.63 \cdot 10^{-4}$	$\mathbf{1.10 \cdot 10^{-4}}$
Grid$_4$	$7.92 \cdot 10^{-3}$	$6.25 \cdot 10^{-3}$	$1.96 \cdot 10^{-3}$	$1.08 \cdot 10^{-2}$	$1.11 \cdot 10^{-4}$	$\mathbf{6.30 \cdot 10^{-5}}$
			$\|\boldsymbol{u} - \boldsymbol{u}_{an}\|_{L_2} / \|\boldsymbol{u}_{an}\|_{L_2}$			
Grid$_1$	$1.10 \cdot 10^{-2}$	$1.16 \cdot 10^{-2}$	$3.81 \cdot 10^{-3}$	$4.25 \cdot 10^{-2}$	$\mathbf{9.53 \cdot 10^{-4}}$	$1.21 \cdot 10^{-3}$
Grid$_2$	$1.22 \cdot 10^{-2}$	$1.18 \cdot 10^{-2}$	$4.66 \cdot 10^{-3}$	$2.19 \cdot 10^{-2}$	$3.91 \cdot 10^{-4}$	$\mathbf{3.56 \cdot 10^{-4}}$
Grid$_3$	$1.21 \cdot 10^{-2}$	$1.20 \cdot 10^{-2}$	$5.19 \cdot 10^{-3}$	$1.48 \cdot 10^{-2}$	$2.46 \cdot 10^{-4}$	$\mathbf{1.71 \cdot 10^{-4}}$
Grid$_4$	$1.18 \cdot 10^{-2}$	$1.21 \cdot 10^{-2}$	$5.50 \cdot 10^{-3}$	$1.11 \cdot 10^{-2}$	$1.80 \cdot 10^{-4}$	$\mathbf{1.01 \cdot 10^{-4}}$

Table 5.4: BP2: L_1 and L_2 relative errors of pressure and velocity for different BC configurations (Table 5.1) and grid resolutions (Table 5.2). The values typeset in bold highlight the lowest error for the given grid resolution.

5.4   Chapter summary

In this chapter, the accuracy of seven different BCs was analyzed using two laminar flow problems.

First, two mesoscopic boundary conditions applied at the inflow were investigated. Based on the results, we hypothesize that the interface between the equilibrium BC and fullway bounce-back BC produces non-physical oscillations in the numerical solutions. Further investigation of these non-physical phenomena is required in a future study. However, these oscillations can be reduced by applying moment-based BCs at the inflow and at walls. Then, the outflow boundary conditions were investigated using two benchmark problems. All results indicate that the newly proposed interpolated boundary condition with decomposition and moment-based outflow boundary condition produces the results with the smallest error compared to the analytical solution.

The obtained results are important from several points of view. First, more accurate results are obtained using the proposed boundary conditions. Next, the proposed boundary conditions show convergence in both pressure and velocity compared to other boundary conditions. These findings are important for further investigation of LBM numerical simulations, especially for numerical simulations of almost all computational flow dynamics problems where the accuracy of boundary conditions can significantly affect the numerical solution.

Turbulent Boundary Layer Flow Above Rough Surfaces

<div style="text-align: right; font-size: 3em;">6</div>

Mathematical modeling of the turbulent fluid flow above rough surfaces belongs to the most challenging problems of computational fluid dynamics (CFD). Although the dynamic of wall-bounded flows in multi-scale processes has been investigated for many years, there are still open problems in the turbulence theory [104, 105]. A typical example of the boundary layer flow is the flow above a rough surface. The roughness of the surface affects the flow through the drag and sink of the fluid momentum. Next, the response of the surface to the flow, such as the particle entrainment, is also affected by the roughness [40]. Based on these observations, accurate and efficient numerical simulations of the boundary layer flow are essential for various applications, from kinetic energy loss [1], plant evaporation [177, 178], calculation of the friction drag of bodies in a flow [157], to wind erosion [161].

The crucial aspect of turbulent flow simulations is a high-resolution grid that can resolve turbulent structures of different size scales [85, 150]. To moderate the restrictions of DNS simulations, wall function methods, large eddy simulation methods, etc. have been developed [150]. Recent progress in LBM simulations showed that coupling of the LBM with the Wall-Adapting Local Eddy-viscosity model [77, 187] or a different subgrid Large Eddy simulation model [110, 119] produces satisfactory results of the turbulent fluid flow. In [64, 124, 146, 147, 163], the LBM was successfully used as a DNS solver for various problems, such as turbulent pipe flow or turbulent channel flow. Next, the active challenge in LBM-based DNS simulations is the comparison with experimental data [121]. In [50], DNS simulations using the CuLBM were performed and the results are summarized in this chapter.

In [50], the ability of the LBM to simulate turbulent fluid flow in the boundary layer region above rough surfaces is investigated using two benchmark problems. The first benchmark problem (BP1) studies fluid flow above the surface with regularly distributed protrusions. The results of LBM simulations are compared with the FDM results obtained using Extended Large-eddy Microscale Model (ELMM) [70]. The other benchmark problem (BP2) is inspired by the street-canyon flow experiment reported in [112]. LBM simulations are evaluated by comparing with simulations based on the FDM and with data sets from the wind tunnel experiment reported by [112].

The chapter is organized as follows. First, the numerical methods used for the simulations and processing of the results are introduced in Section 6.1. Next, the problem of the boundary layer flow above the surface with regularly distributed protrusions is solved in Section 6.2. The same problem is solved in Section 6.3 by the LBM with the grid refinement technique. The last benchmark problem of street-canyon flow is solved and discussed in Section 6.4. Finally, the last Section 6.5 summarizes the findings of this chapter.

6.1 Methodology

6.1.1 Numerical methods

Both the LBM and ELMM simulate the flow of incompressible fluid described by the Navier-Stokes equations (2.18). The considered fluid represents air with kinematic viscosity $\nu = 1/70000 \ \mathrm{m^2 \, s^{-2}}$. LBM simulations use the cumulant collision operator CuLBM to obtain better stability [35]. All relaxation rates except for the one related to the kinematic viscosity are set to 1. The fullway bounce-back BC is used for solid boundaries in the whole computational domain.

The setup of the ELMM code is described in [50] as:

ELMM uses the fourth order central differences in space and the fractional-step method with the explicit third order Runge-Kutta method in time. The pressure Poisson equation is solved directly using the fast Fourier transform. Solid obstacles' boundary conditions are treated using the immersed boundary method. The numerical scheme is described in [70]. ELMM simulations of the street canyon flow used the σ-model [144] for subgrid stresses for compatibility with older simulations in [112]. The subgrid fluxes are almost negligible. No subgrid model was used for the flow simulations above the surface with regularly spaced protrusions.

6.1.2 Time- and space-averaged quantities

The quantities are space- and time-averaged over the surface parallel to the (x_1, x_3)-plane. The space-averaged quantity φ over a surface parallel to (x_1, x_3)-plane is denoted by $\langle \varphi \rangle (x_2, t)$ and computed as

$$\langle \varphi \rangle (x_2, t) = \frac{1}{N_1} \frac{1}{N_3} \sum_{x_1=1}^{N_1-1} \sum_{x_3=1}^{N_3-1} \varphi(x_1, x_2, x_3, t). \tag{6.1}$$

The time-averaged quantity $\varphi(\boldsymbol{x}, t)$ is denoted by $\overline{\varphi}(\boldsymbol{x})$ and the integral over time is approximated for all $\boldsymbol{x} \in \hat{\Omega}$ as

$$\overline{\varphi}(\boldsymbol{x}) = \frac{1}{t_{avg}} \sum_{t=t_{ini}}^{t_{ini}+t_{avg}} \varphi(\boldsymbol{x}, t), \tag{6.2}$$

where $t_{ini} \in \hat{I}$ denotes the initial time step and $t_{avg}, t_{ini} + t_{avg} \in \hat{I}$, denotes the length of the integrated time interval. Since the initial condition can affect the results at the beginning of the simulation and to have the fully developed turbulent flow, the initial time for the averaging t_{ini} is chosen sufficiently large ($t_{ini} \geq 20$ s) in all cases.

6.2 Rough plate

6.2.1 Problem setup

First, the fluid flow above a rough plate is investigated. Two different configurations of the computational domain (marked by Ω_{1a} (BP1a) and Ω_{1b} (BP1b) and illustrated in Figures 6.1a, 6.1b) are considered in the first benchmark problem. The differences between BP1a and BP1b are summarized in Table 6.1.

The roughness of the bottom wall is defined by the regularly distributed protrusions of dimensions $1 \times 4 \times 4$ (in millimeters) in the x_1-, x_2-, and x_3-direction, respectively. The distribution of the protrusions is illustrated in Figure 6.1c. On the face perpendicular to the x_2 axis and with coordinate $x_2 = L_2$, the symmetric boundary condition is prescribed. Next, at the boundary faces perpendicular to the x_1 and x_3 axis, periodic boundary conditions are applied.

(a) Computational domain Ω_{1a}.

(b) Computational domain Ω_{1b}.
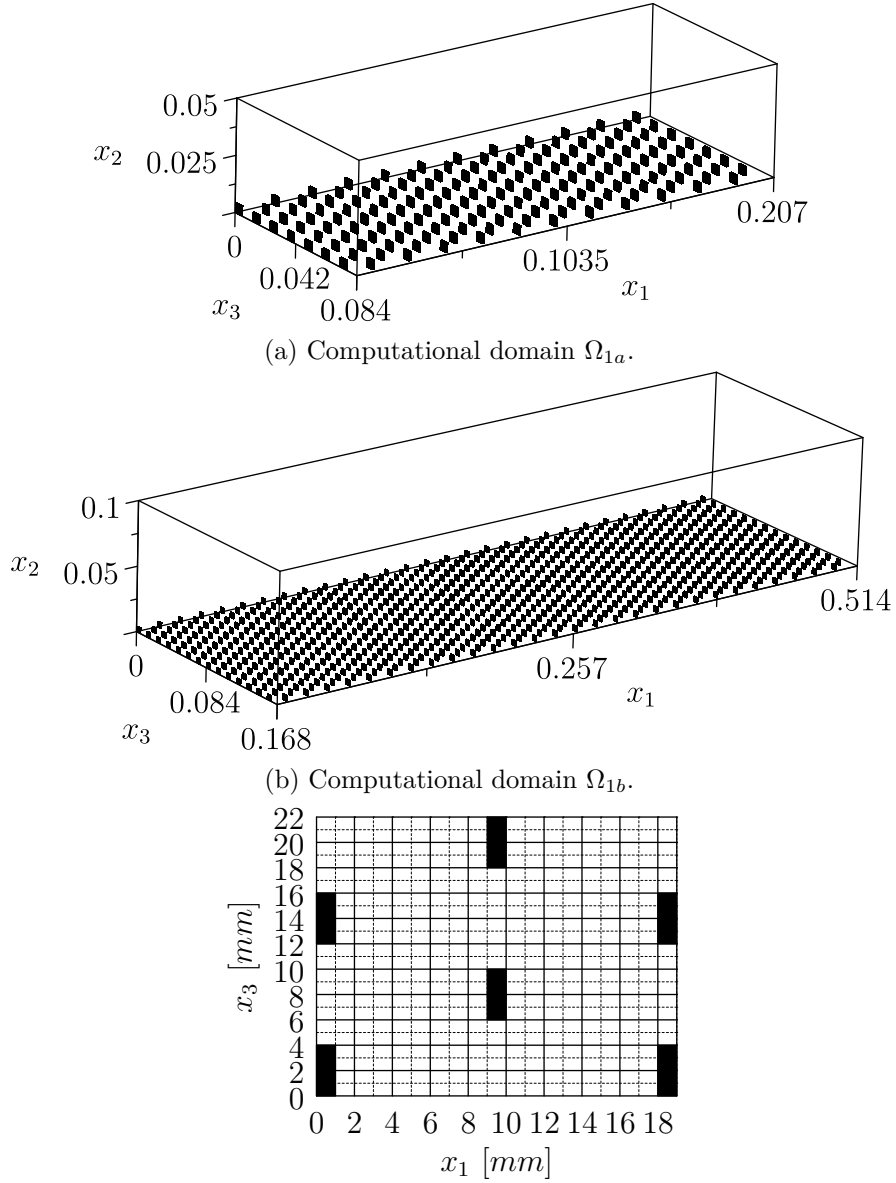
(c) Detail of the protrusions placed periodically in the (x_1, x_3)-plane at the bottom wall of Ω_{1a} and Ω_{1b}.

Figure 6.1: Geometry of the computational domains for the benchmark problems BP1a and BP1b.

Initially, the perturbed initial velocity field generated by the ELMM code was used in all LBM simulations.

The wall friction velocity u_τ defined by Eq. (2.43) and the friction Reynolds number Re_τ are defined by [50, 146]

$$u_\tau = \sqrt{gL_2}, \tag{6.3a}$$

$$Re_\tau = \frac{u_\tau L_2}{\nu}. \tag{6.3b}$$

The friction velocity is $u_\tau = 0.1 \text{ m s}^{-1}$ and the friction Reynolds number is $Re_\tau = 350$ for BP1a and $Re_\tau = 700$ for BP1b. The spaced averaged Kolmogorov scales $\langle \ell_K \rangle$ given in Table 6.1 indicate that the simulations resolve all turbulent scales. Thus, simulations can be considered as well-resolved DNS. Finally, time averaging was performed over a time interval of $t_{avg} = 20$ s.

Benchmark	BP1a	BP1b
Domain geometry	Ω_{1a}, Fig. 6.1a	Ω_{1b}, Fig. 6.1b
Dimensions [mm]	$L_1 = 207, L_2 = 50$ $L_3 = 84$	$L_1 = 414, L_2 = 100,$ $L_3 = 168$
LBM grid parameter δ_x [mm]	0.25	0.2
ELMM grid parameter δ_x [mm]	0.25	0.25
Volume force $\boldsymbol{g}$ [m s^{-2}]	$(0.2, 0, 0)^T$	$(0.1, 0, 0)^T$
LBM time step δt [s]	$4.375 \cdot 10^{-6}$	$2.8 \cdot 10^{-6}$
Kolmogorov length scale $\langle \ell_K \rangle$ [mm]	0.48	0.56
t_{ini} [s]	357	73

Table 6.1: Parameters for LBM simulations of benchmark problem BP1a and BP1b. The time steps of ELMM simulations were variable with Courant number CFL = 0.6.

6.2.2   Results and discussion

In Figures 6.2 and 6.3 space and time averaged results are presented for the benchmark problem BP1 and BP2, respectively. The results in Figure 6.2a show small differences in the velocity magnitude near the bottom wall. Good agreement is observed between the LBM and ELMM in the Reynolds stress tensor components in Figures 6.2b, 6.2c, 6.2d, and 6.2e. The results of the turbulent kinetic energy presented in Figure 6.2f are similar too and the biggest differences are observed near the top wall (coordinate $x_2 = L_2$). It can be addressed to the influence of the symmetric boundary condition.

Figure 6.3a shows small differences in the velocity magnitude. The differences in Figures 6.3b, 6.3c, 6.3d, and 6.3e that present the numerical results of the Reynolds stress tensor component are similar to the BP1a results. Finally, a satisfactory agreement between the LBM and ELMM results is observed in Figure 6.3f.

Furthermore, differences between the numerical results of the LBM and ELMM may result from differences in the discretization of the Navier-Stokes equations and LBM compressibility artifacts.
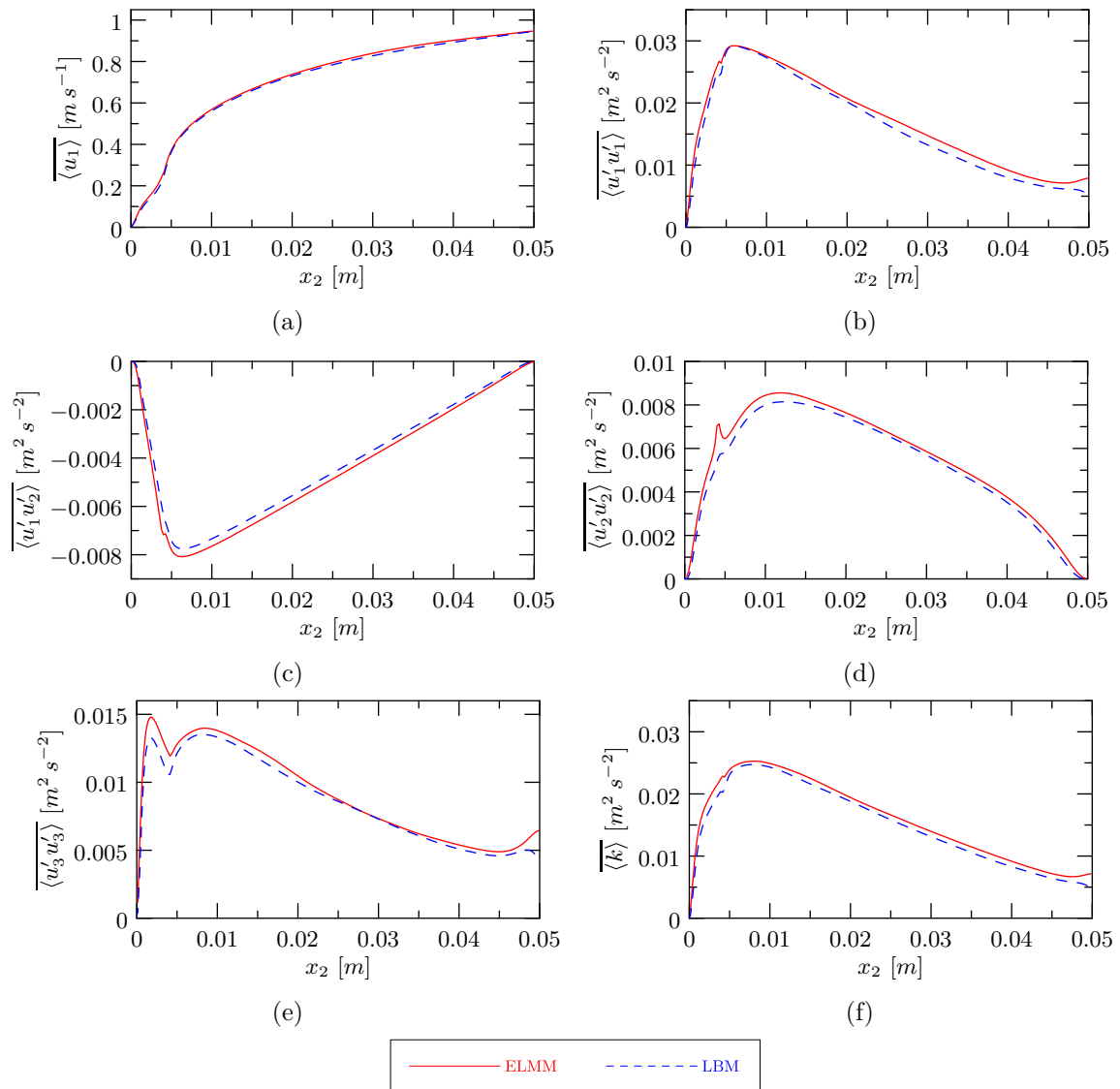
Figure 6.2: The results of BP1a. The time- and space-averaged horizontal velocity component $\overline{\langle u_1 \rangle}$, approximations of the Reynolds stress tensor components $\overline{\langle u_1' u_1' \rangle}$, $\overline{\langle u_1' u_2' \rangle}$, $\overline{\langle u_2' u_2' \rangle}$, $\overline{\langle u_3' u_3' \rangle}$, and turbulent kinetic energy $\overline{\langle k \rangle}$ are compared.

Figure 6.3: The results of BP2a. The time- and space-averaged horizontal velocity component $\overline{\langle u_1 \rangle}$, approximations of the Reynolds stress tensor components $\overline{\langle u_1' u_1' \rangle}$, $\overline{\langle u_1' u_2' \rangle}$, $\overline{\langle u_2' u_2' \rangle}$, $\overline{\langle u_3' u_3' \rangle}$, and turbulent kinetic energy $\overline{\langle k \rangle}$ are compared.
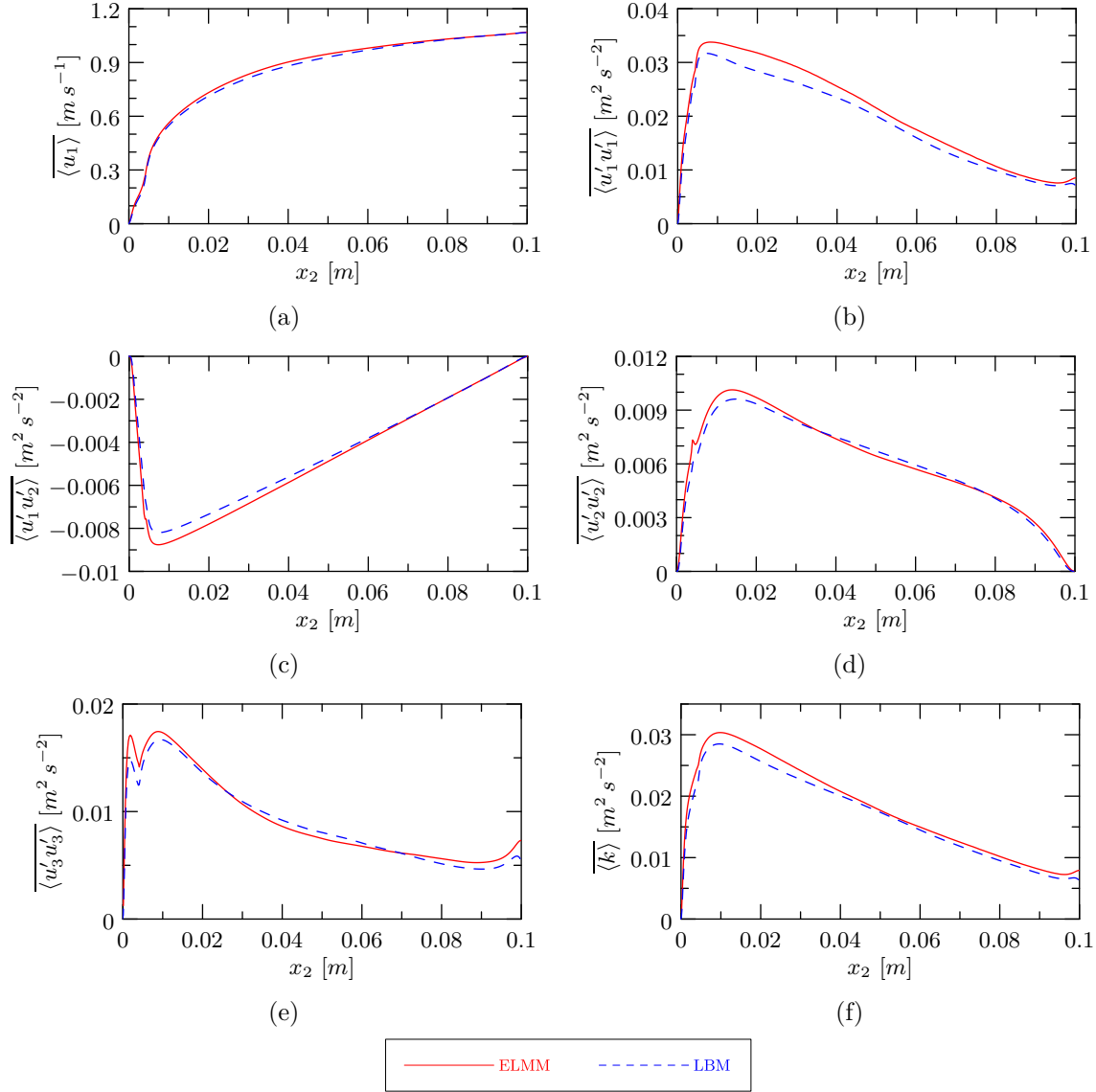
6.3   Rough plate with mesh refinement

The previous results were obtained using a regular grid with fine resolution. The restriction on resolution depends on the position in the computational domain. Near the rough wall, the grid must be fine enough to resolve all turbulence scales. However, the restrictions on the grid resolution decrease as the distance from the rough wall increases. Thus, the grid refinement technique described in Section 3.8 is tested using the benchmark problem BP1a. As in BP1a, the integration time is $t_{avg} = 20$ s and the initial time for the time integration is set to $t_{ini} = 20$ s.

The interpolation of variables between grids with different levels produces additional numerical errors, especially if the single-precision arithmetic is used. Thus, the well-conditioning technique introduced in Section 3.9 is used. Next, both interpolation strategies (i.e. linear vs. quadratic interpolation of velocity) are tested to see their influence on the numerical solution. Finally, two collision operators are used: CuLBM and CuLBM2.

The computational domain Ω_{1a} is discretized with a two- and three-level grid. All grids are uniform in the x_1- and x_3-direction. Thus, the interface between grids of different levels lies in the plane perpendicular to the x_2 axis. The block with the finest grid is located near the rough wall. The height of the grids in the x_2-direction and the resolution of the particular grid levels are given in Table 6.2.

Grid level ℓ	Number of grid levels G_N	Height of the grid block	Grid resolution δ_x^ℓ
0	2	45 mm	0.25 mm
	3	40 mm	0.5 mm
1	2	5 mm	0.125 mm
	3	5 mm	0.25 mm
2	2	–	–
	3	5 mm	0.125 mm

Table 6.2: Height and resolution of the grid blocks with level ℓ used in Section 6.3.

Finally, two interpolation strategies were introduced in Section 3.8 (**S.I** and **S.II**) and both are used in this section. The specific combination of interpolation strategies with the number of grid levels and the chosen collision operator is denoted as follows: *Interpolation_strategy-G_N-Collision_operator.*

6.3.1   Results and discussion

In Figures 6.4 and 6.5, the results of the benchmark problem BP1a with the grid refinement technique are presented for interpolation strategies **S.I** and **S.II**, respectively.

In Figure 6.4a, the results of the horizontal velocity component averaged in time and space u_1 for the interpolation strategy **S.I** are presented. The results of the LBM with grid refinement overestimate the original results of the ELMM and LBM with a uniform grid. There are only small
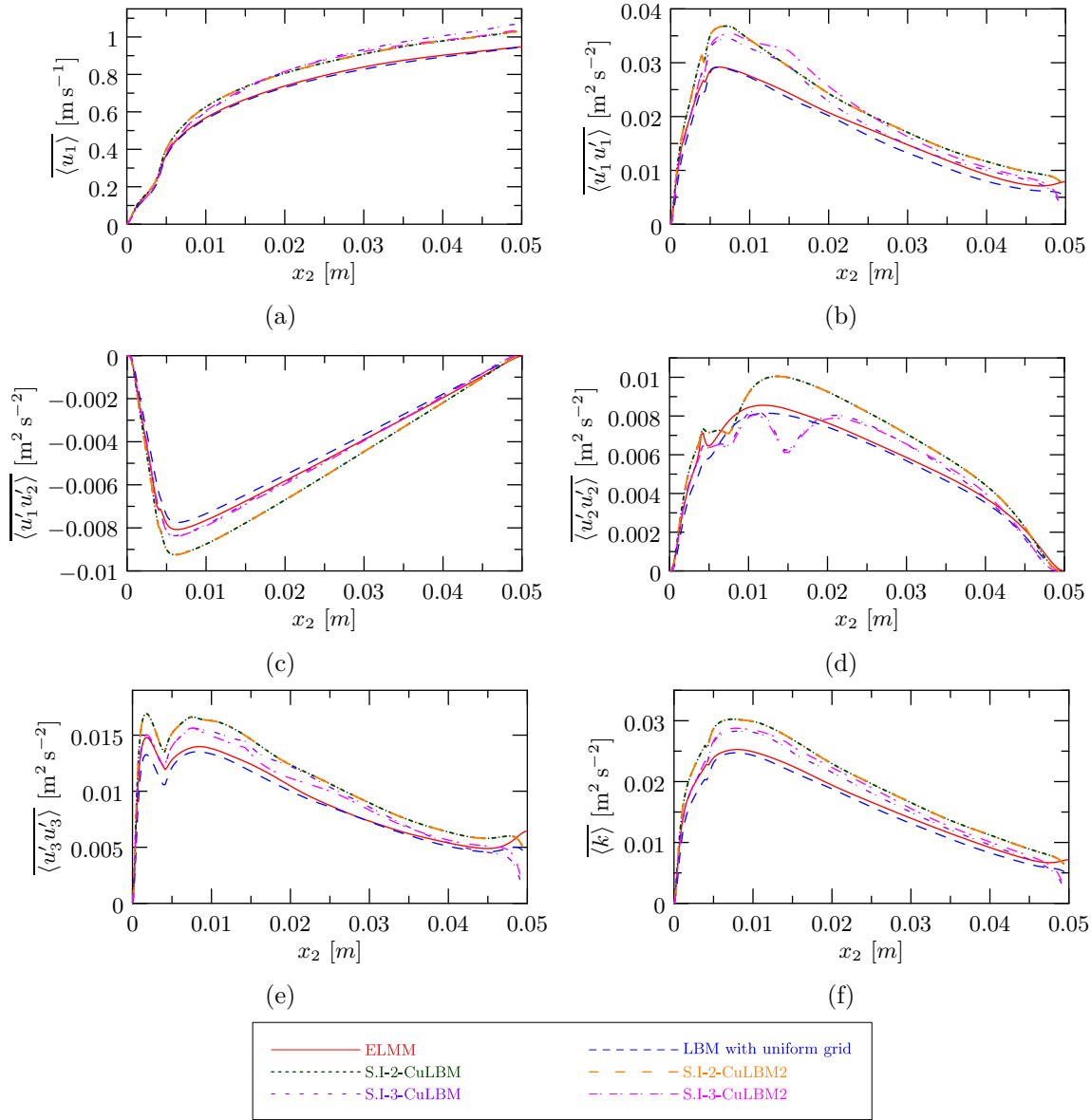
Figure 6.4: The results of BP1a with grid refinement. The parameters of grids are defined in Table 6.2. Interpolation strategy **S.I** with linear interpolation of velocity is used.

differences near the wall, but as the distance from the wall increases, the differences increase, too. The differences between the chosen number G_N and the collision operator are small. A similar trend is observed in Figures 6.4b, 6.4e, and 6.4f. In Figure 6.4c, the results of S.I-3-CuLBM and S.I-3-CuLBM2 are closer to the results of ELMM than S.I-2-CuLBM, S.I-2-CuLBM2, and LBM on a uniform grid. However, in Figure 6.4d, the results of S.I-3-CuLBM and S.I-3-CuLBM2 for $\overline{\langle u_2' u_2' \rangle}$ show a significant drop that is not observed in other results. The source of the differences can be the computational time. Another source of the differences can be the linear interpolation, which is not sufficiently accurate. This is confirmed by Figure 6.5.

In Figure 6.5a, good agreement between all results of the velocity component u_1 is observed, especially near the wall. The closest results to the ELMM simulations and LBM simulations with the uniform grid are obtained by the S.II-2-CULBM2 method. A similar trend is observed for the results in Figures 6.5c, 6.5e, and 6.5f. In Figure 6.5b, the results of the S.II-3-CuLBM
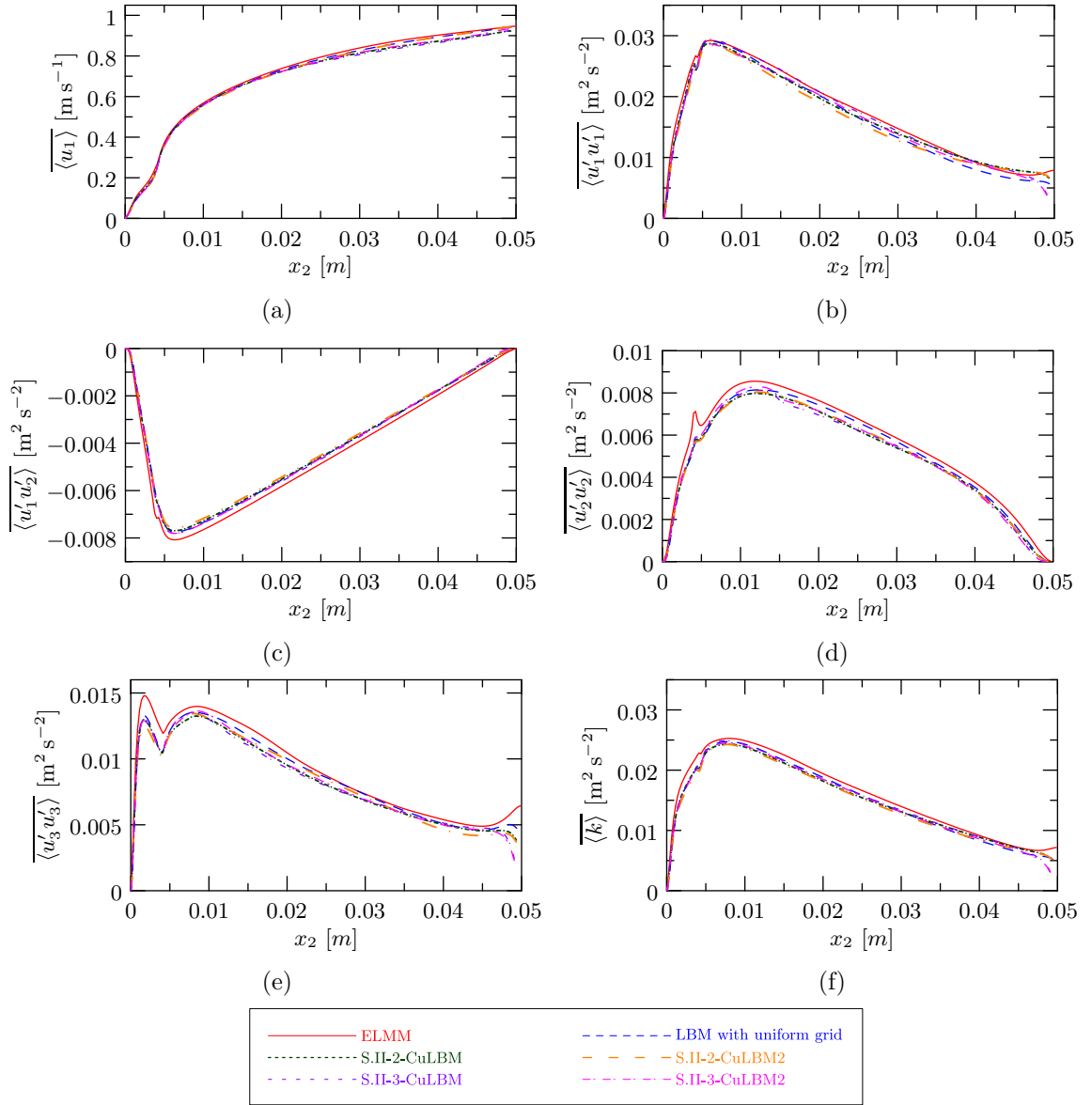
Figure 6.5: The results of BP1a with grid refinement. The parameters of grids are defined in Table 6.2. Interpolation strategy **S.II** with linear interpolation of velocity is used.

approximate the results of the ELMM best. In Figure 6.5d, the non-physical drop in LBM results with a three-level grid is observed as in Figure 6.4d, however, the drop is much smaller than in the results with linear interpolation. Since this drop occurs near the interface between grids with different levels, we hypothesize that it is caused by the interpolation errors.

Another aspect of the grid refinement technique is the computational time needed for the simulations. CuLBM on the uniform grid needed 2907 s to simulate 1 s. On the other hand, simulations with S.II-3-CuLBM needed 12267 s to perform 1 s simulation using the same hardware as the CuLBM on the uniform grid. In the future work, it is desirable to optimize the grid refinement implementation.

6.4   Street canyon flow

6.4.1   Problem setup

The second benchmark problem BP2 is based on the street-canyon flow experiment in a wind tunnel reported by [112]. LBM simulations are compared within this benchmark problem with experimental results and ELMM simulations. The experimental measurements were performed using the Particle Image Velocimetry (PIV) method and the CTA(Constant Temperature Anemometer) hot wire anemometry (HWA) technique [112]. The HWA only measures the velocity component u_1. PIV produces two-dimensional data in the plane perpendicular to the x_3 axis. As in BP1, the computational domain Ω_2 illustrated in Figure 6.6 represents a part of the wind tunnel. The dimensions in millimeters of the computational domain are $L_1 = 800$, $L_2 = 250$, and $L_3 = 250$.

On the bottom wall, buildings are placed periodically. The dimensions of the buildings (height and length) are $H = 50$ mm as illustrated in Figure 6.7. In the x_1-direction, the fluid is accelerated by the volume force $\boldsymbol{g} = (0.5, 0, 0)^T$ m s^{-2}. Thus, the periodic boundary conditions are used in this direction. In the x_2- and x_3-directions, the no-slip boundary conditions are used at the domain boundary $\partial\Omega_2$. The perturbed initial velocity field computed using the ELMM code was prescribed at the initial time.
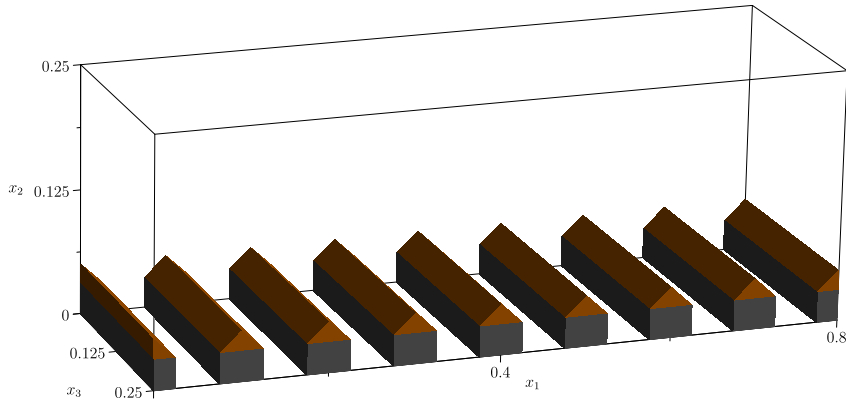
Figure 6.6: Illustration of the computational domain Ω_2 for the benchmark problem BP2.
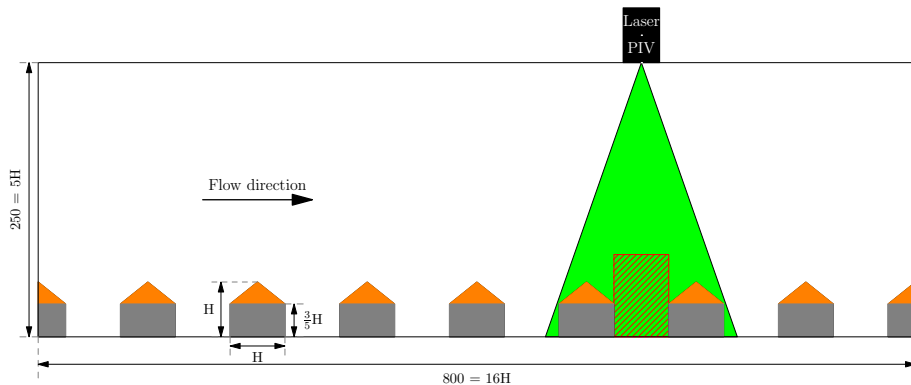

Figure 6.7: The cross section of the computational domain Ω_2. The dimensions are in mm. The green triangle represents the measurement area of the PIV method. The red hatched rectangle represents the test section for the computations of validation metrics.

The grid parameters for the LBM and ELMM simulations are $\delta_x = 0.625$ mm and

$\delta_x = 0.417$ mm, respectively. The spatially-averaged Kolmogorov length scale is $\langle \ell_K \rangle = 0.28$ mm. Both numerical methods do not resolve all turbulent scales. In [34], good agreement was observed between simulations with grid resolutions close to $2\langle \ell_K \rangle$ and an experiment of flow around buildings. These simulations therefore represent a coarse-resolution DNS. Fixed time step $\delta t = 2.59 \cdot 10^{-5}$ s was used in LBM simulations. The ELMMM time step was variable with Courant number CFL = 0.6.

Based on the measurement area, the simulated data are compared with the experiment in a rectangular section, as shown in Fig. 6.7. The dimensions of the rectangular section are $2H$ and $1.5H$ in the x_1- and x_2-directions, respectively. The BP2 results are presented in a non-dimensional form, where the scaling factor for the velocity is the time averaged reference velocity U_{ref} at $1.5H$ above the bottom wall. The data are integrated over a time interval of 10 s and spatial integration over 8 canyons is used for better convergence within the street canyon. Finally, to validate the LBM, several statistical metrics defined in the appendix A.2 are used. The parameters for the hit rate metric are given in [50].

6.4.2   Results and discussion

First, the contours of the simulated and experimental data are compared in Figure 6.8. Nice visual agreement is observed between the corresponding results, and only small differences occur. Figures 6.9 and 6.10 are composed of mean profiles scaled by the reference velocity U_{ref}. Excellent agreement is observed between the simulated and measured results of $\overline{\langle u_1 \rangle}/U_{ref}$. More significant differences occur in the $\overline{\langle u_2 \rangle}/U_{ref}$ results, especially in the canyon. Subsequently, the profiles of $\overline{\langle u_1' u_2' \rangle}/U_{ref}^2$ and $\frac{1}{2}\overline{\langle u_1' u_1' \rangle + \langle u_2' u_2' \rangle}/U_{ref}^2$ in Figures 6.10 show satisfactory agreement between the experimental and LBM results.

The statistical comparison presented in Table 6.3 shows that the ELMM better approximates the velocity component u_1 and the Reynolds stress tensor component $u_1' u_2'$. On the other hand, according to the metrics, the velocity component u_2 is better approximated by the LBM. However, the differences between the metrics considered are small. Thus, both numerical methods give acceptable results.

	Model	**FB**	**NMSE**	**L2**	**r**	**FAC2**	**q**
$\overline{u_1}/U_{ref}$	LBM	0.025478	0.003370	0.040390	0.998691	0.931538	0.840733
	ELMM	**0.017437**	**0.001254**	**0.014579**	**0.999540**	**0.958465**	**0.883987**
$\overline{u_2}/U_{ref}$	LBM	0.308255	**1.614179**	0.193975	**0.981573**	**0.854769**	**0.769121**
	ELMM	**0.247244**	2.177708	**0.017558**	0.977090	0.679175	0.492123
$\overline{u_1' u_2'}/U_{ref}^2$	LBM	0.062781	**0.013515**	0.088780	0.992628	0.827557	0.918934
	ELMM	**-0.057229**	0.016011	**0.001987**	**0.993779**	**0.871097**	**0.959610**

Table 6.3: Statistical comparison of $\overline{u_1}/U_{ref}$, $\overline{u_2}/U_{ref}$, and $\overline{u_1' u_2'}/U_{ref}^2$ between the experimental and numerical results using different estimation metrics defined in Appendix A.2. The bold values represent the best results between the ELMM and LBM.

Eventually, the scatter plots with the accepted intervals of the hit rate metric are used to classify the numerical results. The results in Figure 6.11a show a small underestimation of the LBM data for the velocity component u_1. On the other hand, the results in Figure 6.11b indicate that the LBM results overestimate the value of the u_2 velocity component. The results of

(a) Experimental data [112].

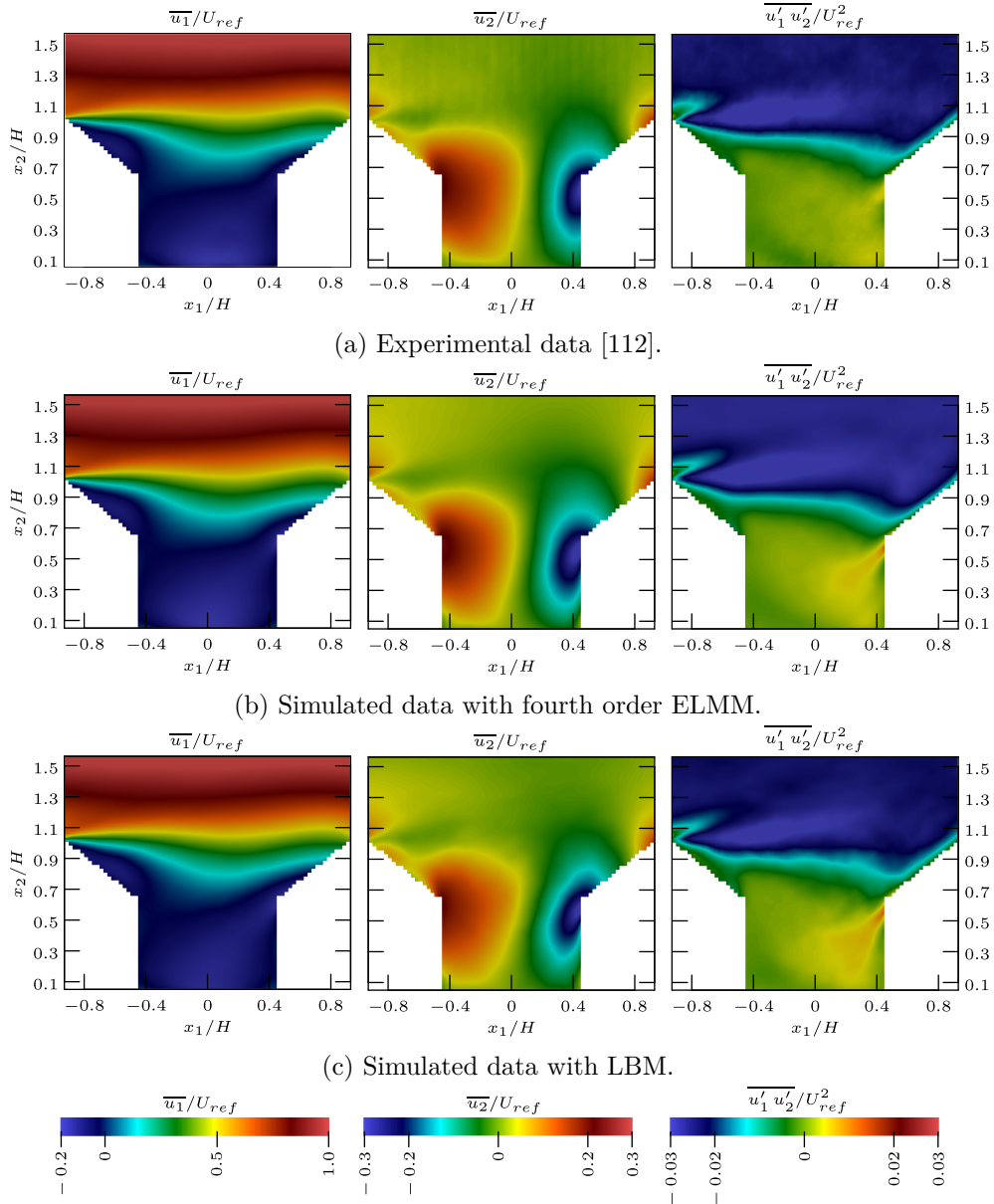(b) Simulated data with fourth order ELMM.

(c) Simulated data with LBM.

Figure 6.8: Results of $\overline{u_1}/U_{ref}$, $\overline{u_2}/U_{ref}$, and $\overline{u_1'u_2'}/U_{ref}^2$.

$\overline{u_1'u_2'}/U_{ref}^2$ and $\frac{1}{2}\overline{u_1'u_1' + u_2'u_2'}/U_{ref}^2$ in scatter plots 6.11c and 6.11d show good agreement between simulated and experimental data.
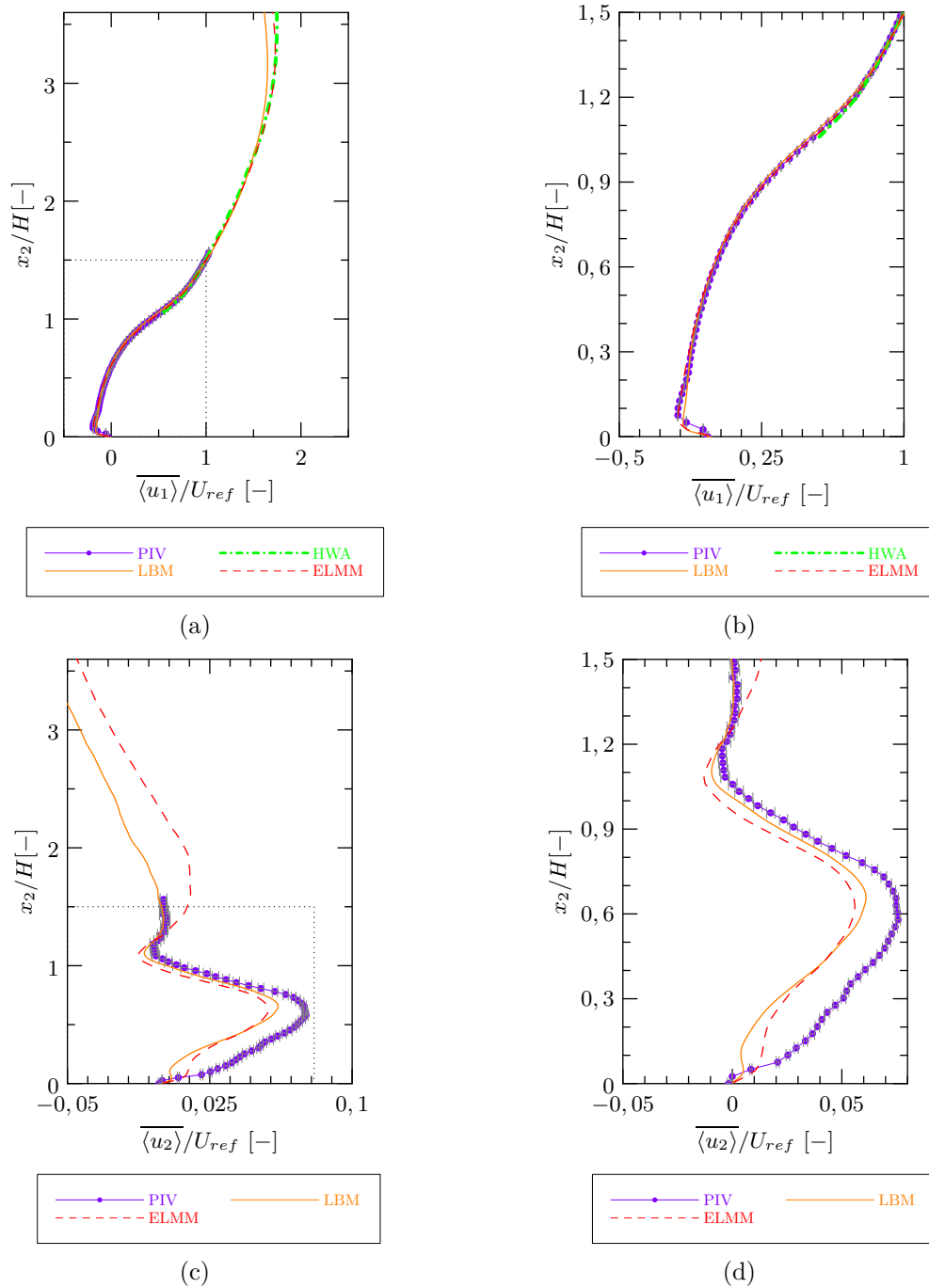
Figure 6.9: Results of numerical simulations and experiment for $\overline{\langle u_1 \rangle}/U_{ref}$ and $\overline{\langle u_2 \rangle}/U_{ref}$. The data in Figures 6.9b and 6.9d are zoomed in the rectangle defined by the dotted lines in the corresponding Figures 6.9a and 6.9c, respectively. The error of the PIV is illustrated by the solid vertical gray lines.
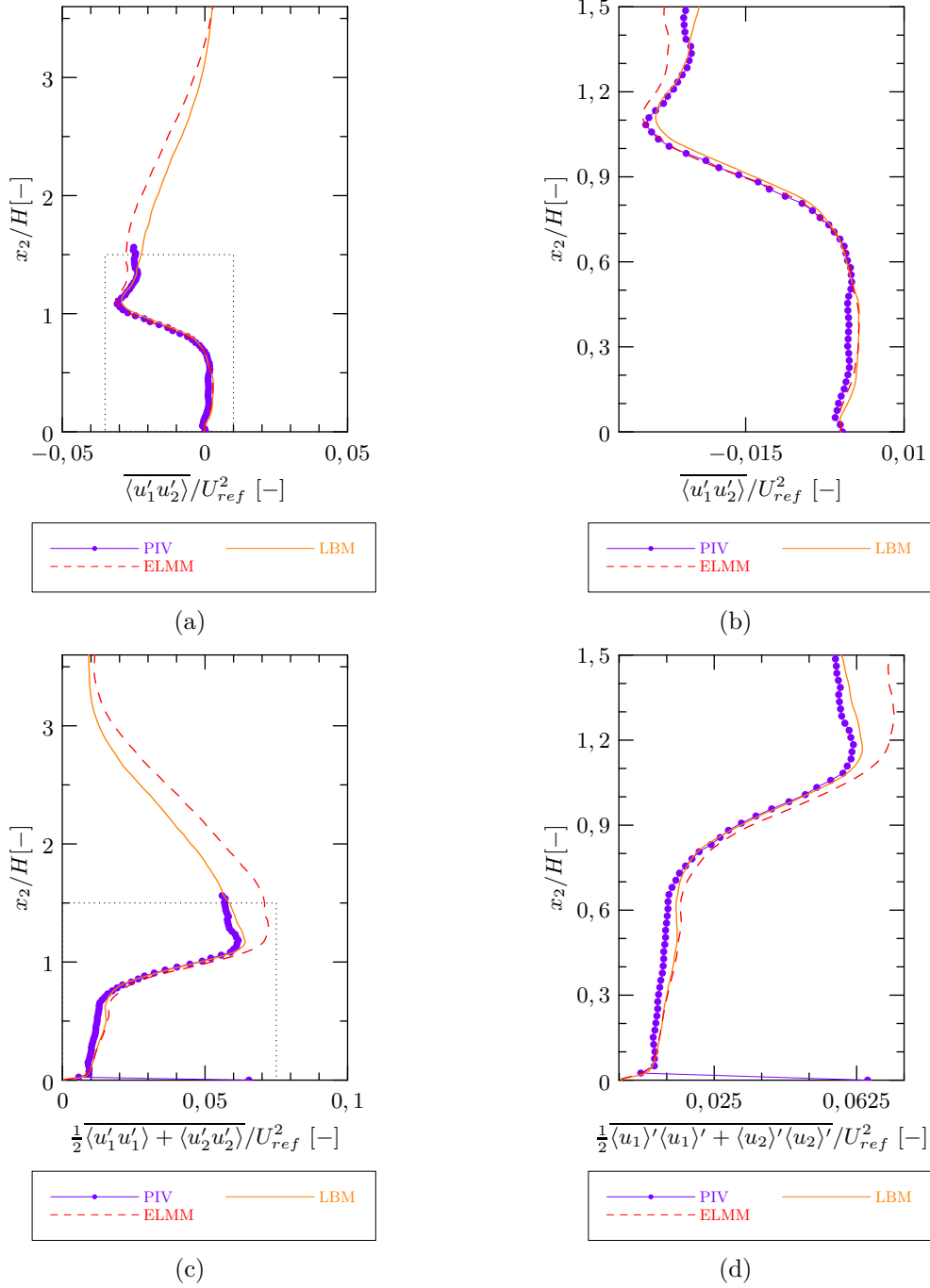
Figure 6.10:   Results of numerical simulations and experiment for $\overline{\langle u_1' u_2' \rangle}/U_{ref}^2$ and $\frac{1}{2}\overline{\langle u_1' u_1' \rangle + \langle u_2' u_2' \rangle}/U_{ref}^2$. The data in Figures 6.10b and 6.10d are zoomed in the rectangle defined by the dotted lines in the corresponding Figures 6.10a and 6.10c, respectively.

(a) $\overline{u_1}/U_{ref}$

(b) $\overline{u_2}/U_{ref}$

(c) $\overline{u_1'u_2'}/U_{ref}^2$

(d) $\frac{1}{2}\overline{u_1'u_1' + u_2'u_2'}/U_{ref}^2$

Figure 6.11: Scatter plot for experimental PIV data and simulated data using ELMM and LBM. Accepted intervals of the hit rate metric are illustrated by the dashed and dash-dotted lines.

6.5   Chapter summary

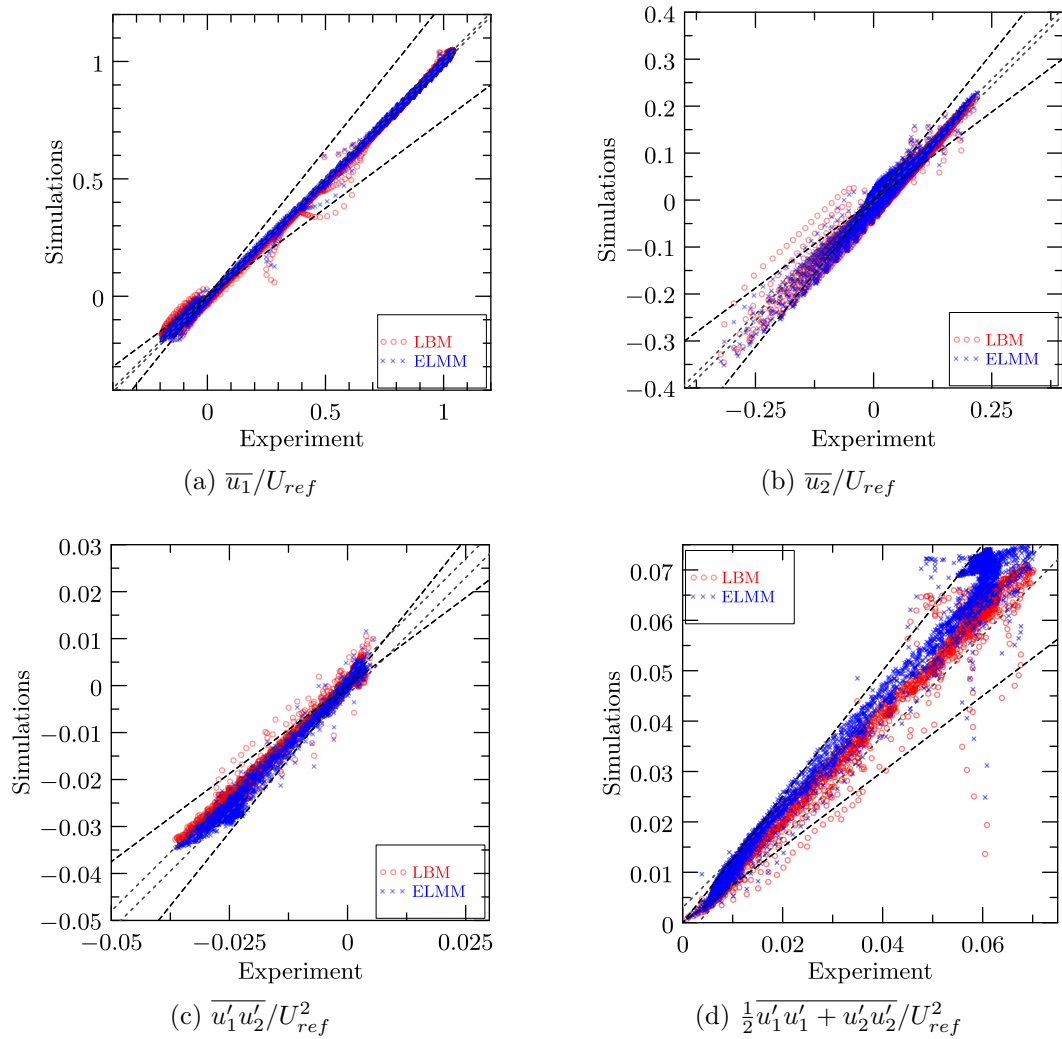Fluid flow simulations above rough surfaces were the main objective of this chapter. The LBM was validated against the experimental data and compared with the FDM within two benchmark problems.

The first results in the first benchmark problems showed a good agreement between LBM and FDM results. Next, the Kolmogorov length scale was fully resolved. The LBM can therefore be considered as a DNS solver for this type of problem.

Next, the results of the LBM with the grid refinement technique were presented. BP1a was used for the first step of the investigation. The results indicate that the linear interpolation of the velocity field significantly influences the numerical solution. Therefore, it is not recommended to use it in further studies. On the other hand, LBM results with quadratic interpolation of the velocity show better agreement with the ELMM results and the LBM results on a uniform grid. Only small differences were observed between used grids and collision operators. All setups with quadratic interpolation of velocity can be recommended for further simulations of the turbulent flow in the boundary layer above a rough plate.

The validation of the LBM against the experimental data was performed in the second benchmark problem. The results were compared using 2D contours, 1D graphs, and statistical metrics. Although all turbulent scales were not sufficiently resolved, satisfactory agreement was observed between numerical and experimental results.

Based on the results presented by both numerical methods, the LBM can be regarded as a reliable numerical method for turbulent fluid flow simulations in the boundary layer above the rough surface.

The planned future work is to optimize the grid refinement technique implementation to achieve comparable computation time to the LBM on a uniform grid.

Turbulent Fluid Flow Through Distributor Plate

7

Energy production is a problem that is being investigated extensively. Fluidized bed (FB) combustion [5, 193] belongs to the technology that is commonly used for energy generation. It is efficient in heat transfer and elimination of sulfur oxide production. Since the entire FB geometry is very complex, several processes are studied separately, for example using complex numerical CFD simulations [11, 12]. These simulations can help to optimize the cost and efficiency of the energy production. In addition, simpler experimental models are created to study bubbling processes in the combustion chamber. One of these simpler experimental devices is a plastic model of the fluidization chamber and a windbox located at the Faculty of Mechanical Engineering of the CTU in Prague.

The plastic model is used to study the bubbling processes of different materials in the combustion chamber of FB. The combustion chamber is separated from the windbox by the distributor plate. It evenly distributes the air in the combustion chamber and prevents the granular material from falling into the windbox.

The main aim of this chapter is to study the properties of distributor plates. First, the numerical results of the pressure drop on the distributor plate are compared with the results of the experiment for different air flow rates. Next, the flow field near the distributor plate is investigated using two numerical methods: the lattice Boltzmann method and the FVM implemented in ANSYS Fluent. The results presented here are summarized in [9].

The chapter is organized as follows. First, the experiment is described in Section 7.1.1. Next, the details of the numerical methods are summarized in Section 7.1.2. Section 7.2 is composed of results and their discussions. The last Section 7.3 summarizes the presented findings.

7.1 Methodology

7.1.1 Mathematical model and experiment

The experiment is performed in a plastic model of the fluidized bed boiler and all experimental data were measured and collected by J. Hrdlička and P. Skopec from FME CTU in Prague. The main part of the plastic model is a column with a rectangular cross section. The column is divided into two parts: windbox and fluidized chamber, as illustrated in Figure 7.1. The walls of the column are made of polymethyl methacrylate.

The windbox is separated from the fluidized chamber by the distributor plate. This 2 mm thick metal plate contains 201 holes with a diameter of 3 mm. One of the holes is blocked by the attachment flange; see Figure 7.2. The pressure drop on the distributor plate is measured using pressure gauges above and below the distributor plate. The inflow rate is measured by the
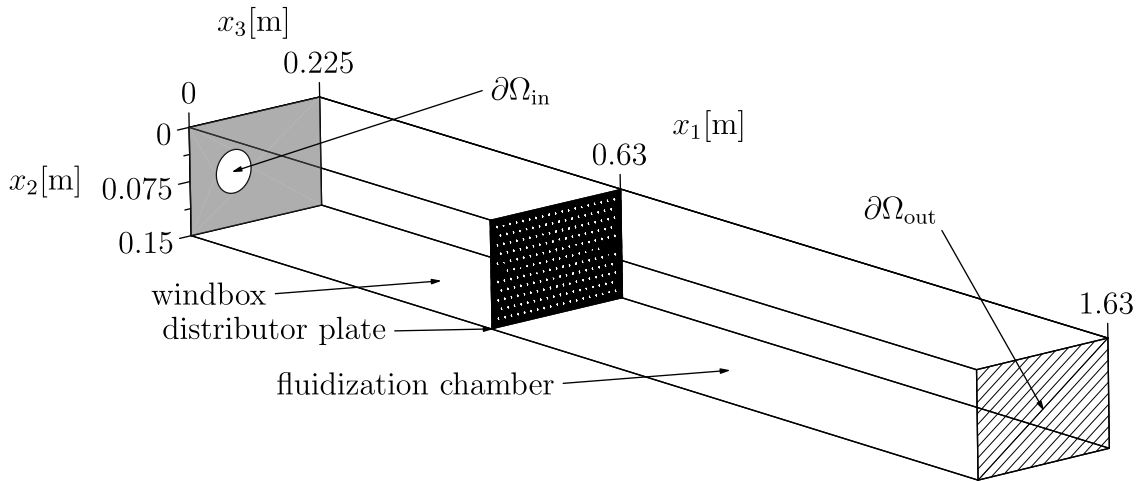
Figure 7.1: Schematic representation of the computational domain that represents a part of the plastic fluidization device. On the bottom wall ($x_1 = 0$ m), there is an inflow hole with a diameter of 60 mm labeled as $\partial\Omega_{\text{in}}$. The outflow boundary condition is prescribed at the top face $\partial\Omega_{\text{out}}$.

orifice plate flow meter. The fluid used in the experiment was air with density $\rho = 1.295$ kg m^{-3} and dynamic viscosity $\mu = 1.71 \cdot 10^{-5}$ kg m^{-1} s^{-1}. At $\partial\Omega_{\text{in}}$ and $\partial\Omega_{\text{out}}$, parabolic velocity profile and the constant pressure $p_{\text{out}} = 0$ kg m^{-1} s^{-2} are prescribed. The influence of the gravitational field is neglected. The final time is set to $T = 5$ s. At the initial time $t = 0$ s, zero velocity and pressure are established in the entire domain Ω.
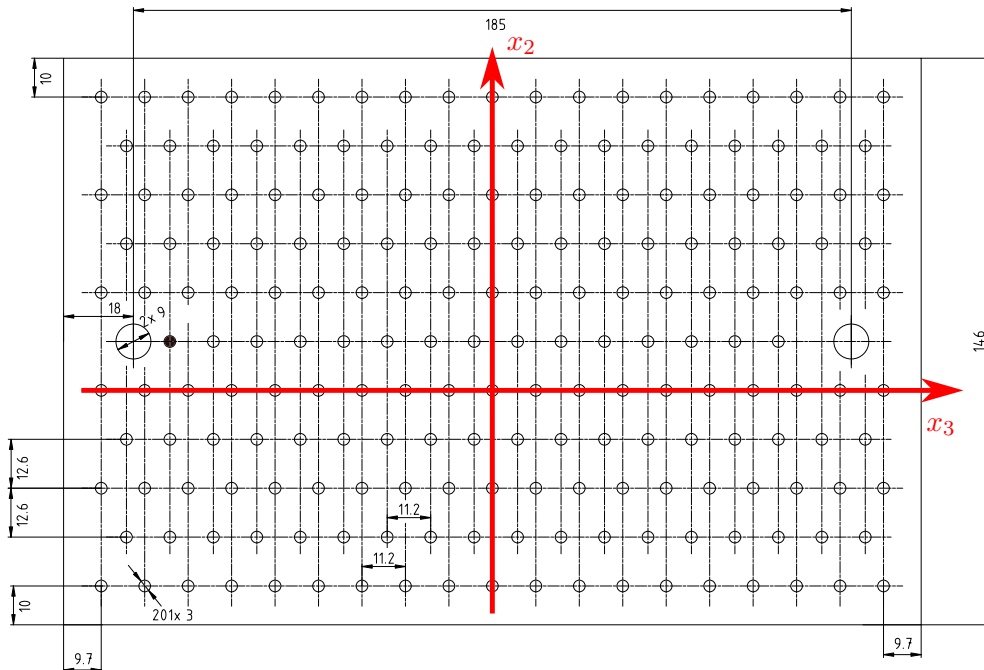

Figure 7.2: Geometry of the distributor plate. All dimensions are in millimeters. The circles represent the holes in the distributor with a diameter of 3 mm. One hole (black filled circle) is blocked by the attachment flange. The red arrows define the positions of the sections used in Figures 7.6, 7.7 and 7.9.

Air flow [m^3 h^{-1}]	3.7	4.3	17.4	29.1	38.9	47.6	56.5	65.6
U_∞ [m s^{-1}]	0.7	0.8	3.4	5.7	7.6	9.3	11.1	12.8
Re	3303	3839	15534	25980	34730	42497	50443	58568
Air flow [m^3 h^{-1}]	74.3	82.9	91.6	99.9	108.4	116.9	124.2	133.3
U_∞ [m s^{-1}]	14.5	16.2	17.9	19.6	21.3	22.9	24.4	26.2
Re	66335	74014	81781	89191	96780	104369	110887	119011
Air flow [m^3 h^{-1}]	140.8	–	–	–	–	–	–	–
U_∞ [m s^{-1}]	27.6	–	–	–	–	–	–	–
Re	125707	–	–	–	–	–	–	–

Table 7.1: Flow rates, maximal velocity, and Reynolds numbers used for the experiment.

The details of the experiment are described in [9] as:
The air flow was controlled by setting the rotation speed of the fan motor, which was given in the number of revolutions per second (Hz). During the experiment, the fan speed increased from 7 Hz to 37 Hz in 2 Hz steps. Between each two successive steps, the speed was kept constant for a period of 30 s. The pressure drop on the orifice plate and the pressure drop on the fluidized bed were recorded at 1s intervals. Both pressure drop measurements (at the orifice plate and at the distributor plate) suffered from intermittent but significant slumps of unknown origin, which were efficiently filtered out by a median filter with window size 5. The air flow rates and superficial velocities in the fluidization chamber were calculated from the filtered data and averaged over each 30 s period of constant fan speed.

Seventeen different flow rates given in Table 7.1 have been prescribed at the inflow. Table 7.1 is further composed of maximal velocities U_∞ [m s^{-1}] of the parabolic profile prescribed at the inflow and Reynolds numbers computed as $\mathrm{Re} = \frac{\rho\,R_{\partial\Omega_{\mathrm{in}}}\,U_\infty}{\mu}$, where $R_{\partial\Omega_{\mathrm{in}}} = 0.06$ m is the diameter of $\partial\Omega_{\mathrm{in}}$.

7.1.2 Numerical methods

To analyze the numerical results, simulated data are space and time averaged. The time averaging for any scalar quantity φ is defined by a discrete equivalent (defined below) of the formula

$$\overline{\varphi}(\boldsymbol{x}) = \frac{1}{T}\int\limits_0^T \varphi(\boldsymbol{x}, t)\mathrm{d}t, \tag{7.1}$$

where $\boldsymbol{x} \in \Omega$. Temporal averaging of a vector quantity is performed as temporal averaging of individual scalar components.

Next, the time-averaged distribution along the x_1 axis is obtained by spatial averaging $\overline{\varphi}(\boldsymbol{x})$ over the horizontal cross section $S(x_1)$ as

$$\langle\varphi\rangle(x_1) = \frac{1}{|S(x_1)|}\int\limits_{S(x_1)} \overline{\varphi}(\boldsymbol{x})\mathrm{d}x_2\mathrm{d}x_3, \tag{7.2}$$

where $|S(x_1)|$ represents the size of the cross section. Both numerical methods use the discrete equivalent of Eq. (7.2) which are defined later.

The pressure drop dp $[\mathrm{kg\,m^{-1}\,s^{-2}}]$ is the first quantity investigated. In the numerical simulations, it is computed as

$$dp = \frac{1}{L_{dp}} \int_{x_F}^{x_F+L_{dp}} \langle p \rangle(x_1) dx_1 - \frac{1}{L_{dp}} \int_{x_B}^{x_B+L_{dp}} \langle p \rangle(x_1) dx_1, \tag{7.3}$$

i.e., the pressure drop is computed from the space averaged pressure in front of ($x_F = 0.2$ m) and behind ($x_B = 0.8$ m) the distributor plate using intervals of length $L_{dp} = 0.2$ m. The limits in the integrals (given in meters) are chosen to minimize the influence of the pressure oscillations near the distributor plate.

Lattice Boltzmann method

The first numerical method used is the lattice Boltzmann method. Two collision operators are used: CuLBM and CuLBM2. Most simulations use a uniform reference lattice composed of $3260 \times 320 \times 452 \doteq 4.72 \cdot 10^8$ sites. The grid spacing parameter is $\delta_x = 0.5$ mm. At the inflow and outflow boundaries, the equilibrium boundary condition is used. At the walls, the full-way bounce-back boundary condition is applied. Thus, the offset vector (defined in Section 3.1) of the computational grid is $\boldsymbol{P} = \left(0, \frac{\delta_x}{2}, \frac{\delta_x}{2}\right)^T$. Diffusive scaling is used between the time step and the grid spacing parameters with non-dimensional kinematic viscosity $\widetilde{\nu} = 10^{-4}$. Finally, for the highest inflow rate, a finer grid with the gird spacing parameter $\delta_x = 0.33$ mm is used to show the effect of the grid resolution.

For the space averaging of LBM results, the formula in Eq. (7.1) is approximated by

$$\overline{\varphi}(\boldsymbol{x}) \approx \frac{1}{N_t} \sum_{\ell=1}^{N_t} \varphi(\boldsymbol{x}, \ell \delta_t), \tag{7.4}$$

where $\boldsymbol{x} \in \widehat{\Omega}$. Next, the formula in Eq. (7.2) is approximated by

$$\langle \varphi \rangle(x_1) \approx \frac{1}{|S(x_1) \cap \widehat{\Omega}|} \sum_{\boldsymbol{x} \in S(x_1) \cap \widehat{\Omega}} \overline{\varphi}(\boldsymbol{x}), \tag{7.5}$$

where $|S(x_1) \cap \widehat{\Omega}|$ represents the number of grid points in $S(x_1) \cap \widehat{\Omega}$. Finally, integrals in Eq. (7.3) are approximated by

$$\int_a^b \langle p \rangle(x_1) dx_1 \approx \sum_{x_1 \in \mathcal{A}} \langle p \rangle(x_1) \delta_x, \tag{7.6}$$

where $a, b \in (0, L_1), a < b, \mathcal{A} = \{i\delta_x \in \langle a, b \rangle \,|\, i \in \{1, 2, \cdots, N_1 - 2\}\}$.

The LBM simulations on the reference lattice were run on two nodes of Helios cluster located at the the Department of Mathematics FNSPE CTU in Prage with the following configuration: 4x NVIDIA TESLA V100 (Volta) w. 16GB HBM2 RAM, 2x16-core Intel XEON Gold 6130@2.1GHz CPU (hyper-threading disabled), 384 GB RAM, 360 GB local SSD storage. 4 NVIDIA TESLA V100 with 8 CPU cores were utilized on each node. Next, the simulations on the finest lattice were run on two nodes of the RCI cluster located at FEE CTU in Prague with configuration: 128 cores/256 threads 3.1GHz (2 x AMD EPYC 7763), 1TB RAM, 8 x Tesla A100 40GB with NVLink. 4 NVIDIA TESLA A100 with 8 CPU cores were utilized on each node.

Finite volume method

The second numerical method used is the finite volume method (FVM) implemented in the ANSYS 19.1 multiphysics software package. Fluid flow simulations were performed using the ANSYS Fluent. The governing equations for Fluent simulations are Eqs. (2.18). Fluent uses a pressure-based solver for viscous fluids with the $k - \epsilon$ turbulence model (with the default setting). The *mass-flow inlet* BC and the *pressure-outlet* BC are applied at the inflow and at the outflow boundary, respectively. At the walls, the no-slip boundary condition is considered. Finally, the initialization is performed using the *hybrid initialization method*. The complete setting of the Fluent solver is given in [9].

The advantage of the FVM is that it can use non-uniform unstructured mesh, which is locally refined around the distributor plate. The computational domain in Figure 7.1 is discretized using the unstructured mesh illustrated in Figure 7.3. The reference mesh is composed of 1 223 725 cells, 2 498 815 faces, and 230 271 nodes. The smallest diameter of the mesh cell inside the distributor holes is approximately. $\delta_x^{(FVM)} = 0.5$ mm. To observe the influence of the mesh resolution, especially in the distributor holes, finer unstructured meshes were used. The unstructured meshes are generated using ANSYS Meshing software with constraints on the mesh resolution of the distributor holes. The time step $\delta_t^{(FVM)} = 10^{-4}$ s was constant within all FVM simulations.
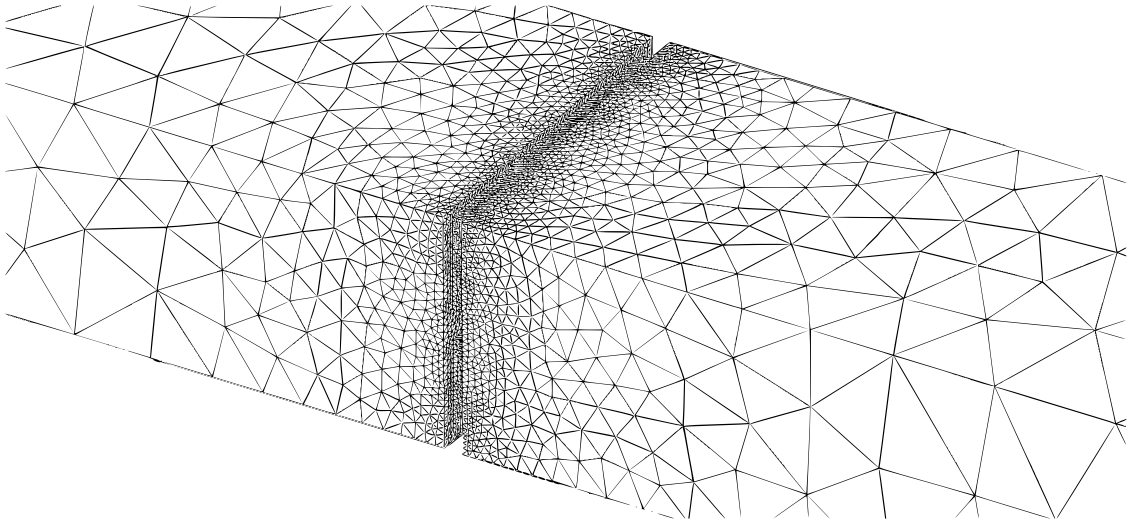

Figure 7.3: Schematic illustration of the non-uniform unstructured mesh with refinement on the distributor plate generated by ANSYS Meshing software.

ParaView software [4] is used to calculate spatial and temporal averages defined by Eqs. (7.1), (7.2), and (7.3) on the unstructured mesh.

The FVM simulations were run on a single node of Helios cluster located at the Department of Mathematics FNSPE CTU in Prage with the following configuration: node: 2x16-core AMD EPYC 7281@2.1GHz CPU (SMT mode disabled), 128 GB RAM, 360 GB local SSD storage. 16 cores were utilized for individual simulations. Since the academic ANSYS license is limited, it was not possible to use a higher number of processor cores.

7.2 Results and discussion

The pressure drop results (evaluated using Eq. (7.3)) of the experiment and the simulations are plotted in Figure 7.4. It can be seen in Figure 7.4 that the CuLBM method with the reference

mesh significantly overestimates the experimental pressure drop results for higher air flow rates. However, the ANSYS Fluent produces better results than the CuLBM method on the reference mesh. The best results are obtained by the CuLBM2 method for all air flow rates with the reference mesh. The discrepancy between the CuLBM and the experiment is probably caused by coarse resolution of the reference mesh. This is illustrated by simulations of ANSYS Fluent on a coarse mesh (labeled ANSYS Fluent ($\delta_x^{(FVM)} = 2$ mm) in Figure 7.4). The problem of the mesh resolution is further investigated in Figure 7.5 for the highest air flow rate. The results of LBM simulations on the reference mesh and the finer mesh indicate that the LBM results tend to the experimental results. Similar behavior is observed for the ANSYS Fluent simulations on meshes with different resolutions of distributor holes.
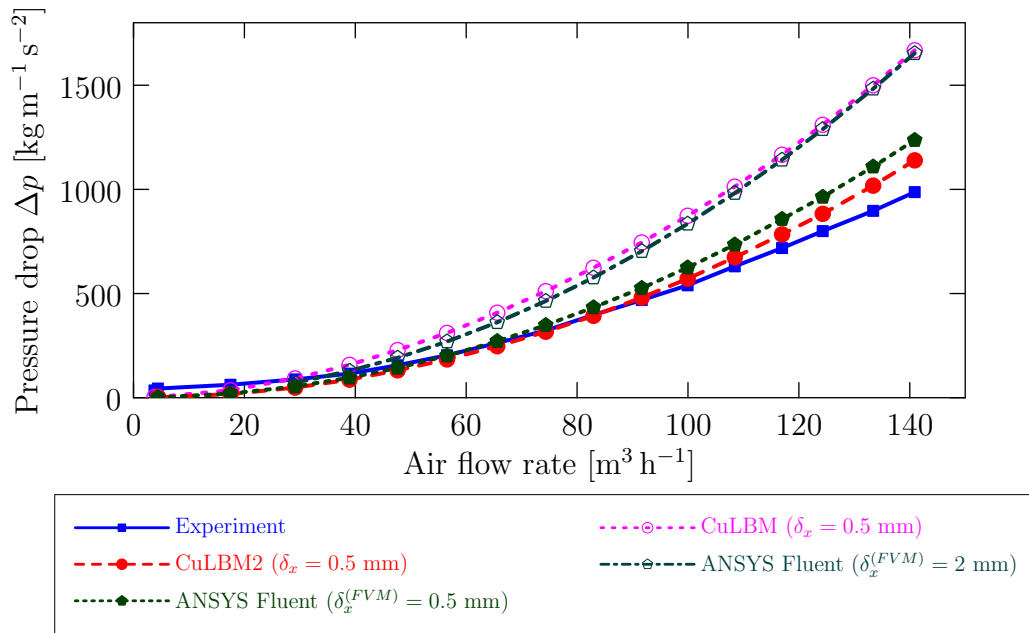

Figure 7.4: Results of the pressure drop dp simulations and experiment for different air flow rates.

The purpose of the distributor plate is to evenly distribute the air flow. To investigate uniformity, two sections are presented in the fluidization chamber at different elevations above the distributor plate in Figures 7.6, 7.7, and 7.9 for CuLBM, CuLBM2, and ANSYS Fluent, respectively. The velocity magnitudes in the cross sections obtained by the CuLBM are higher than the magnitudes obtained by ANSYS Fluent. This is in natural agreement, since the higher pressure drop in CuLBM simulations produces higher velocities. The CuLBM results in Figure 7.6 indicate that the flow field is non-uniform even 6 cm above the distributor plate. Similar results, but with a smaller magnitude, are obtained by the CuLBM2, as illustrated in Figure 7.7. On the other hand, the results obtained by ANSYS Fluent in Figure 7.9 show that the flow field is almost uniform 3 cm above the plate. Although the pressure drop simulated by the CuLBM2 is smaller than the pressure drop simulated by ANSYS Fluet, the velocity magnitudes behind the distributor plates simulated by the CuLBM2 are higher than those simulated by ANSYS Fluent. This disagreement can be addressed to the presence of the $k - \epsilon$ model turbulence model in ANSYS Fluent and to the coarsening of the volume mesh in the direction away from the distributor plate. Since the CuLBM2 uses a sufficiently fine uniform mesh in the whole computational domain, it can predict the turbulent field more accurately. This is demonstrated in Figures 7.8 and 7.10, where the instantaneous and time-averaged velocity field is presented in
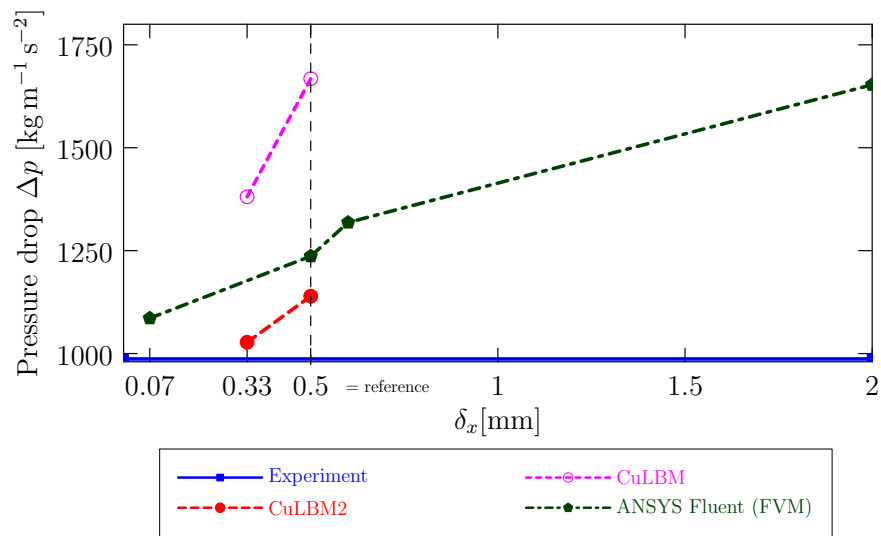
Figure 7.5: Dependence of the simulated pressure drop dp on the mesh resolution for the highest air flow rate 141 m^3 h^{-1}.

the vicinity of the distributor plate for CuLBM2 and ANSYS Fluent and air flow rate 100 m^3 h^{-1}, respectively. Figure 7.8 indicates that the velocity field in the windbox is approximated by the CuLBM2 more accurately than by ANSYS Fluent.

Figure 7.6: Time-averaged velocity magnitude distribution at different elevations over the distributor plate for the highest flow rate 141 m³h⁻¹. Slices through the center of the domain parallel to the x_3 and x_2 axes at positions indicated in Figure 7.2. CuLBM simulations on the reference lattice.
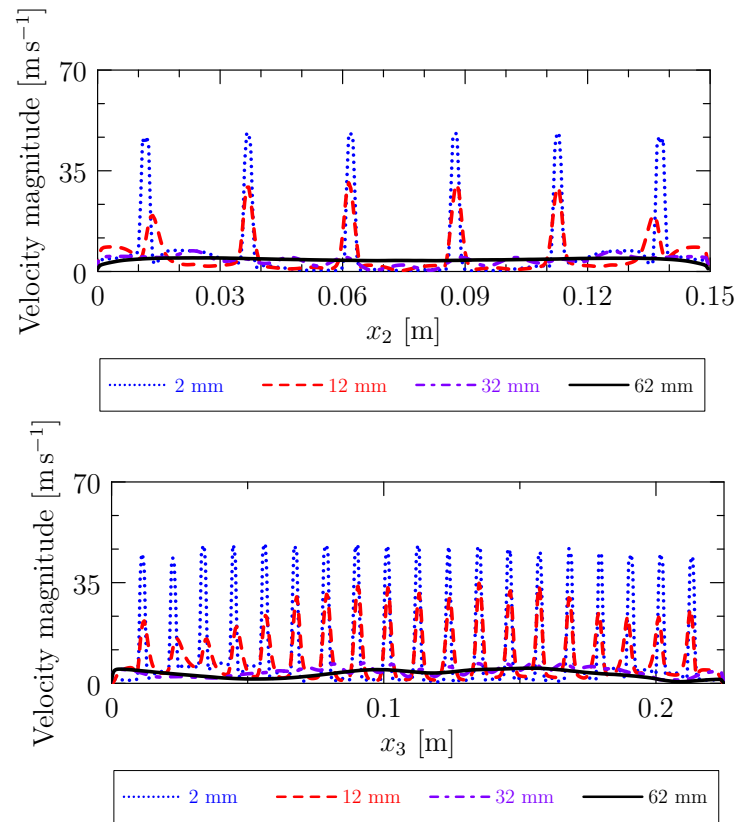
Figure 7.7: Time-averaged velocity magnitude distribution at different elevations over the distributor plate for the highest flow rate 141 m³h^{-1}. Slices through the center of the domain parallel to the x_3 and x_2 axes at positions indicated in Figure 7.2. CuLBM2 simulations on the reference lattice.

(a) Instantaneous velocity field.

(b) Time averaged velocity field.

Velocity magnitude $[\text{m s}^{-1}]$

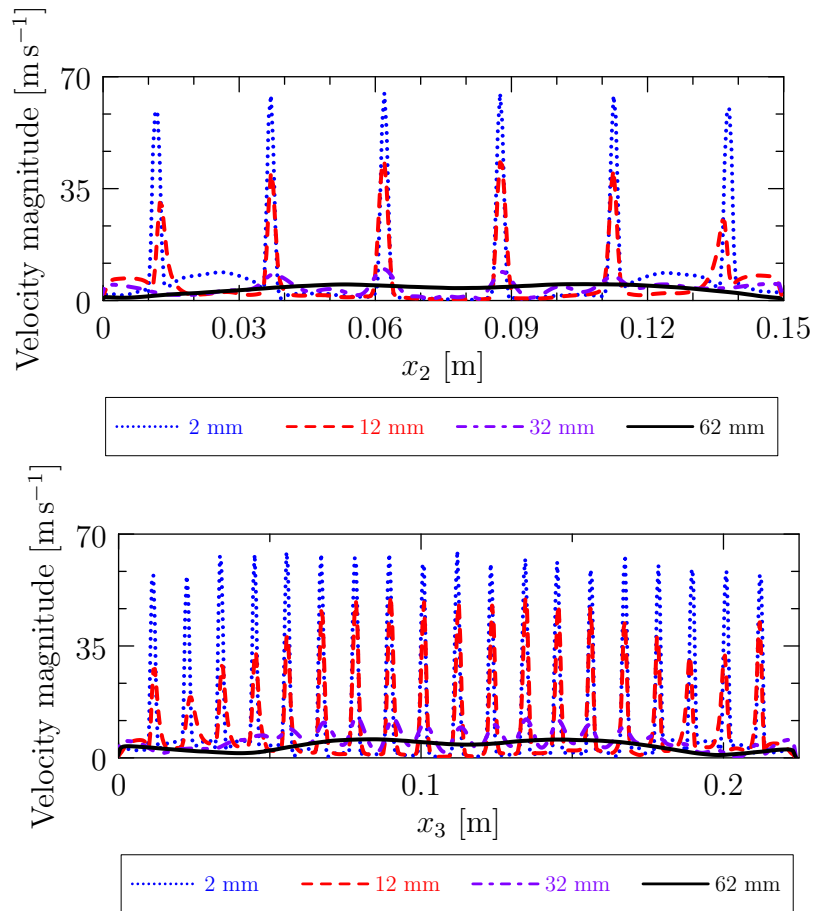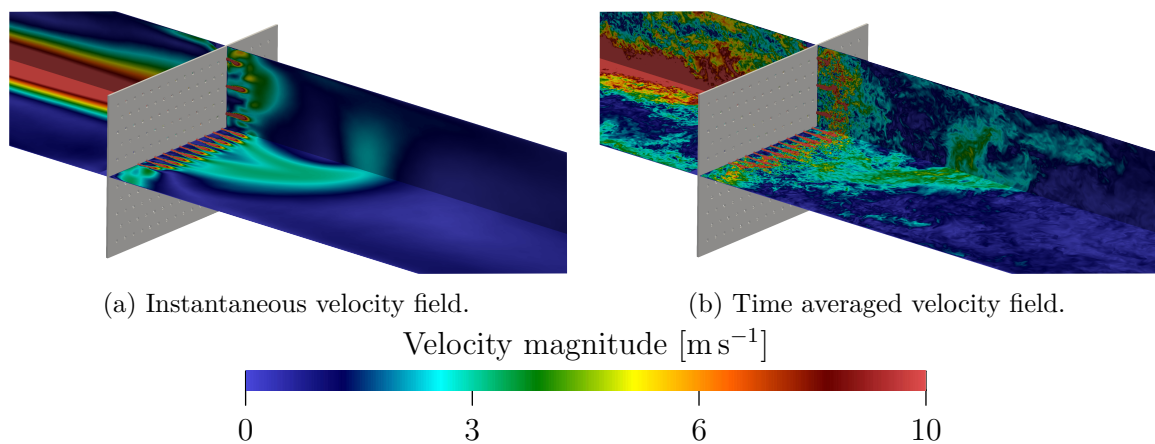Figure 7.8: Velocity fields obtained by the CuLBM2 simulations for the flow rate 100 m³ h^{-1}.
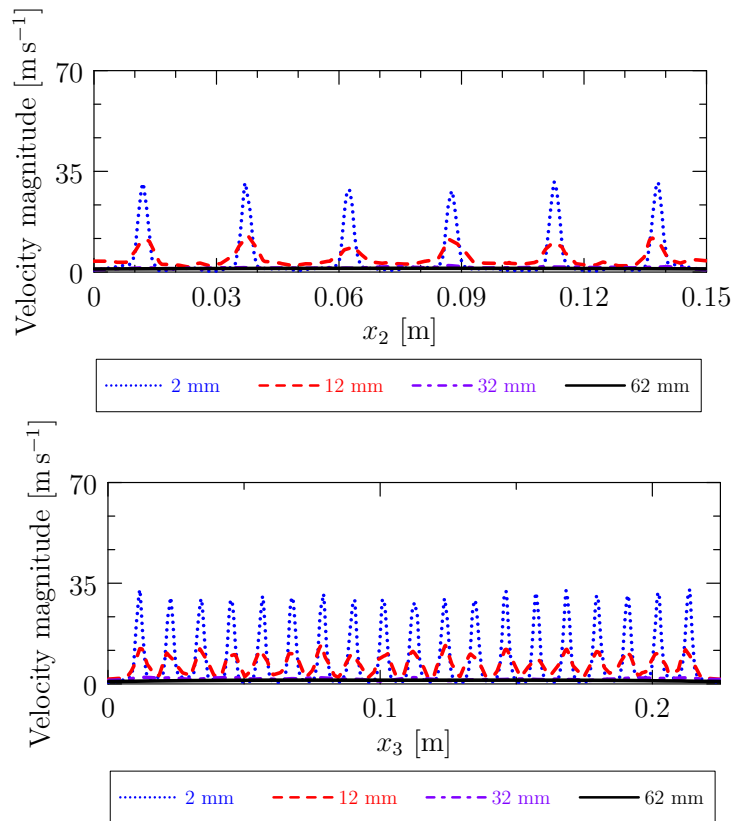
Figure 7.9: Time-averaged velocity magnitude distribution at different elevations over the distributor plate for the highest flow rate 141 m^{3}h^{-1}. Slices through the center of the domain parallel to the x_3 and x_2 axes at positions indicated in Figure 7.2. Fluent simulations on the reference lattice.

(a) Instantaneous velocity field.   (b) Time averaged velocity field.

Velocity magnitude [m s^{-1}]

0   3   6   10

Figure 7.10: Velocity fields obtained by the ANSYS Fluent simulations for the flow rate 100 m^3 h^{-1}.
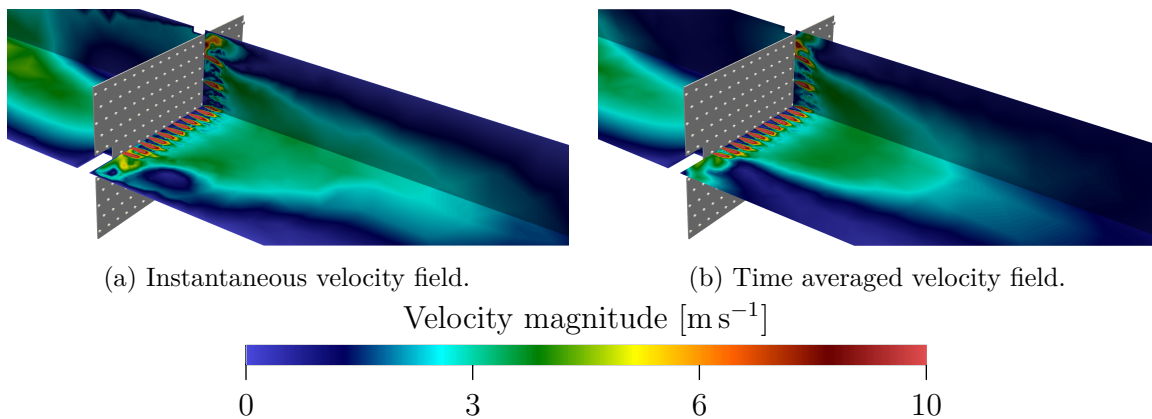
A comparison of the computational times is given in Table 7.2. The LBM simulations on the finest mesh were obtained within 2 days. The ANSYS Fluent simulations on the mesh with the same resolution of the distributor holes were obtained in a shorter time since the unstructured mesh with less degrees of freedom was used. Nevertheless, the ANSYS Fluent simulations on the finest mesh took more than 19 days.

Method	δ_x [mm]	Computational time	HW resources used
CuLBM2	0.5	23h 36min	8×NVIDIA V100
CuLBM2	0.33	38h 23min	8×NVIDIA A100
ANSYS Fluent	2	4h 27min	16 CPU cores
ANSYS Fluent	0.5	7h 22min	16 CPU cores
ANSYS Fluent	0.07	465h 24min	16 CPU cores

Table 7.2: Comparison of the computational cost between CuLBM2 and ANSYS Fluent on meshes with different spacing δ_x. The problem with the highest air flow rate 141 m^3 h^{-1} is used.

7.3 Chapter summary

The objective of this chapter was the investigation of the distributor properties in the fluidized bed reactor. Experimental measurements and two different numerical methods were used for the investigation. The first numerical method was the FVM implemented in the ANSYS Fluent software package. Next, the lattice Boltzmann method implemented in the in-house code with the support for parallel run on the system equipped with multiple GPUs is used. Two different collision operators were used for the lattice Boltzmann method: CuLBM and CuLBM2.

First, the pressure drop at the distributor plate was investigated. It was observed that the differences between numerical simulations and experimental measurement increase with increasing air flow rate. The biggest disagreements between simulated and experimental data was observed by the CuLBM method. However, the CuLBM2 produced the closest results to the experimental measurement. Furthermore, it was confirmed that more accurate results can be obtained with a finer mesh.

Next, the velocity distribution in the vicinity of the distributor plate was investigated. The ANSYS Fluent simulations used unstructured mesh with fine resolution around the distributor holes and coarse resolution of other parts of the computational domain. Therefore, the numerical results obtained using the CuLBM2 on the uniform mesh provided more detailed information about the velocity field, especially in the windbox. Next, simulations showed that the velocity is not evenly distributed right behind the distributor plate. CuLBM2 results showed that the velocity starts to be uniform 6 cm above the distributor plate. On the other hand, the ANSYS Fluent simulations predict the uniformity 3 cm above the distributor plate. We hypothesize that it can be addressed to the unstructured mesh and turbulence models used in ANSYS Fluent.

Additionally, the computational cost was compared. Although the CuLBM2 has higher memory demands than the FVM, the CuLBM2 computational time was substantially lower than the ANSYS Fluent computational time. The results obtained provided valuable insights for the further development of complex models for the simulations of the processes in the whole fluidized bed boilers.

Non-Newtonian Fluid Flow Simulations 8

In recent years, the interpretation and post-processing of clinical data have been enhanced with numerical simulations of CFD [13, 25, 62, 81, 135, 170, 173]. Typical examples of measurements that are accompanied with CFD are medical non-invasive measurements. 4D phase-contrast magnetic resonance imaging (PC-MRI) is an example of non-invasive measurements providing pieces of information about three-dimensional and three-directional in vivo blood flow [165]. This method has some limitations, e.g., low spatio-temporal resolution, signal-to-noise ratio, and partial volume effects. These limitations can be reduced by applying appropriate CFD models. Furthermore, in [71], the uncertainty in the PC-MRI measurement was observed in areas with high turbulent flow. Hence, CFD can be used to improve the accuracy of the measurement in these regions.

4D PC-MRI measurement is often used in clinical practice to assess blood flow in vessels. Blood is a typical non-Newtonian fluid. In vessels with diameter close to the dimensions of the blood components (erythrocytes, leucocytes, thrombocytes), the non-Newtonian properties of blood play a dominant role [176]. The non-Newtonian property mainly influences physical quantities such as wall shear stress or relative residence time [65, 66, 87, 95]. At high velocities and in large vessels, blood is only considered a Newtonian fluid [143]. Large vessels sometimes contain some pathological regions with constrictions that affect the flow. On the basis of the level of narrowing, non-Newtonian affects can be negligible [134, 139, 154]. To assess the influence of non-Newtonian properties on the blood flow, an artificial experiment with three types of narrowing was used in the presented study. The experiment uses PC-MRI fluid flow measurements in a phantom device composed of acrylic tubes that approximate arterial vessels with valves. The valves have different shapes representing different severity of stenosis. To investigate the effect of the non-Newtonian properties, three different fluids are used.

One of the key features of CFD is the computational time, which should be comparable to the time of a clinical examination. Therefore, efficient CFD methods are needed to complete the final assessment. One of such CFD methods is the lattice Boltzmann method as shown in Chapter 7. However, the addition of non-Newtonian affects to the numerical models increases computational costs. To see the necessity of non-Newtonian models, an in-depth investigation conducted in [52] is summarized in this chapter.

The chapter is organized as follows. First, experiments, mathematical models, and numerical methods are introduced in Sections 8.1.1, 8.1.2, and 8.1.3, respectively. Then, the methods used for the data processing are described in Section 8.1.7. The results with their discussion are given in Section 8.2. This chapter is concluded by Section 8.3.

8.1   Methods

8.1.1   Experimental method

The experiment uses an artificial model of human vessels called *phantom* and has been conducted by R. Galabov and J. Tintěra from Institute for Clinical and Experimental Medicine in Prague. As shown in Figure 8.1, the phantom is composed of a acrylic box with inserted acrylic tubes. The tubes are connected by rubber rings, as illustrated in Figure 8.2. This connection allows for insertion of the acrylic plate with an orifice. Three different orifices are used that mimic mild (MiS), moderate (MoS), and severe (SeS) stenosis, see Table 8.1. The complete setup of the experiment is described in detail in [71].
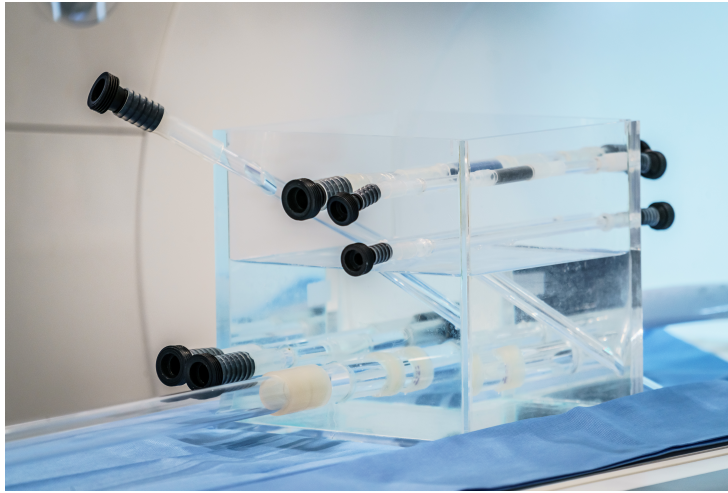
Figure 8.1: Phantom device for in vivo investigation of the fluid flow through stenotic vessels. Photo: J. Ryszawy.
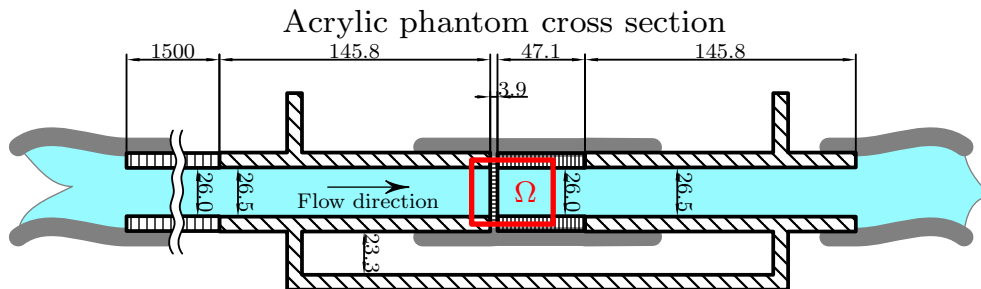
Figure 8.2: Geometry of the phantom with dimensions in millimeters. The red rectangle defines the position of the domain for the numerical simulations. The gray thick lines represent rubber holes. The blue regions illustrated the area of the fluid flow.

The fluid flow in the phantom was measured using Avanto Fit 1.5T MRI scanner by Siemens Healthineers, Erlangen, Germany. The flow was constantly induced by the aquarium pump inserted in the reservoir of fluid. To evaluate MRI measurement, three different fluids are considered: (1) clear water (typical Newtonian fluid), (2) glycerine water solution with xanthan gum ($\rho = 1088$ kg m^{-3}), and (3) sucrose water solution with xanthan gum ($\rho = 1151$ kg m^{-3}). Fluids (2) and (3) represent non-Newtonian fluids with properties closed to human blood and are referred to as GX and SX, respectively. The complete details of the GX and SX are given in [52]. Next, two different flow regimes are considered for each level of stenosis. Flow and velocity were

Mild stenosis (MiS)	Moderate stenosis (MoS)	Sever stenosis (SeS)
1 cm		

Table 8.1: Photos of the acrylic plates mimicking different level of the valvular stenosis in the experimental phantom device. Photo: R. Galabov.

measured using a mechanical flow meter and MRI. The results of the measurement are given in Table 8.2. For further details, the reader is referred to [52].

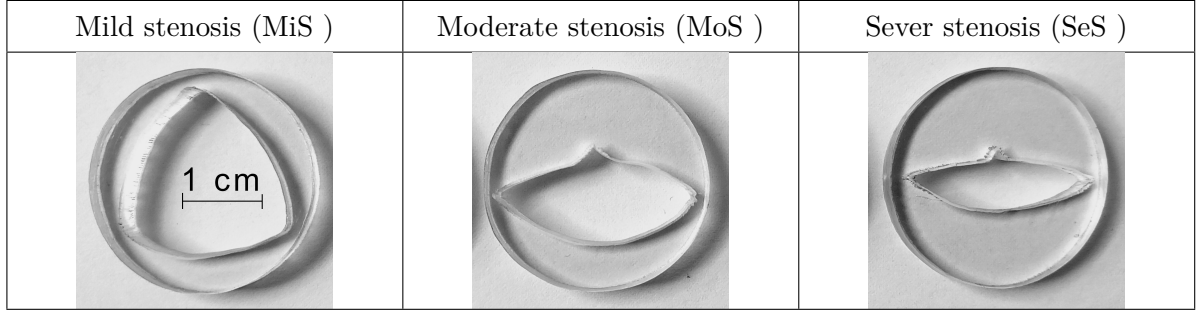| Vessel	Fluid	Flow [ml s^{-1}]		Velocity [cm s^{-1}]	
Flow regime		U_{low}	U_{high}	U_{low}	U_{high}
SeS	Water	107.1	283.21	25.45	80.58
	GX	104.6	244.33	37.35	95.22
	SX	97.63	255.95	36.35	83.47
MoS	Water	103.97	320.81	24.80	80.36
	GX	106.86	173.82	35.31	57.78
	SX	102.85	296.2	47.48	124.02
MiS	Water	105.78	211.34	25.31	54.81
	GX	107.12	260.95	36.95	93.01
	SX	98.32	165.7	38.09	62.64

Table 8.2: Input flow and maximal velocity condition measured using PC-MRI for different level of stenosis and different flow regime.

8.1.2   Mathematical model

The experimental setup is modeled in a cuboidal domain Ω illustrated in Figure 8.3. In Ω, there is a tube with the center $\boldsymbol{S_c} = \left(0, \frac{L_2}{2}, \frac{L_3}{2}\right)^T$, and radius of $r_{\text{in}} = 13.25$ mm and $r_{\text{out}} = 13$ mm before and behind the acrylic plate, respectively. It corresponds to the part of the phantom experiment defined by the red rectangle in Figure 8.2. The dimensions of the computational domain are $L_1 = 203.9$ mm, $L_2 = L_3 = 26.1$ mm. The governing equations for the fluid flow problem are incompressible Navier-Stokes equations. Mass conservation is expressed using Eq. (2.18a). For non-Newtonian fluids, the dynamic viscosity is not constant. Under the assumption of generalized

Newtonian fluids, see Chapter 2, and $\nabla \cdot \mu \approx 0$, the momentum conservation equation can be written as

$$\rho \frac{D\boldsymbol{u}}{Dt} = -\nabla p + 2\mu(\dot{\gamma})\nabla \cdot \mathbb{D}. \tag{8.1}$$

The generalized Newtonian viscosity μ depends on the shear rate $\dot{\gamma}$ defined by Eq. (2.24) and will be approximated using non-Newtonian models given in Section 2.3. Eq. (8.1) can be written as

$$\rho \frac{D\boldsymbol{u}}{Dt} = -\nabla p + 2\mu_\infty \nabla \cdot \mathbb{D} + \boldsymbol{G}, \tag{8.2}$$

where μ_∞ is the dynamic viscosity at an infinite shear rate and $\boldsymbol{G}$ $[\mathrm{kg\,m^{-2}\,s^{-2}}]$ reflects the non-Newtonian affects as

$$\boldsymbol{G} = 2(\mu(\dot{\gamma}) - \mu_\infty)\nabla \cdot \mathbb{D}. \tag{8.3}$$
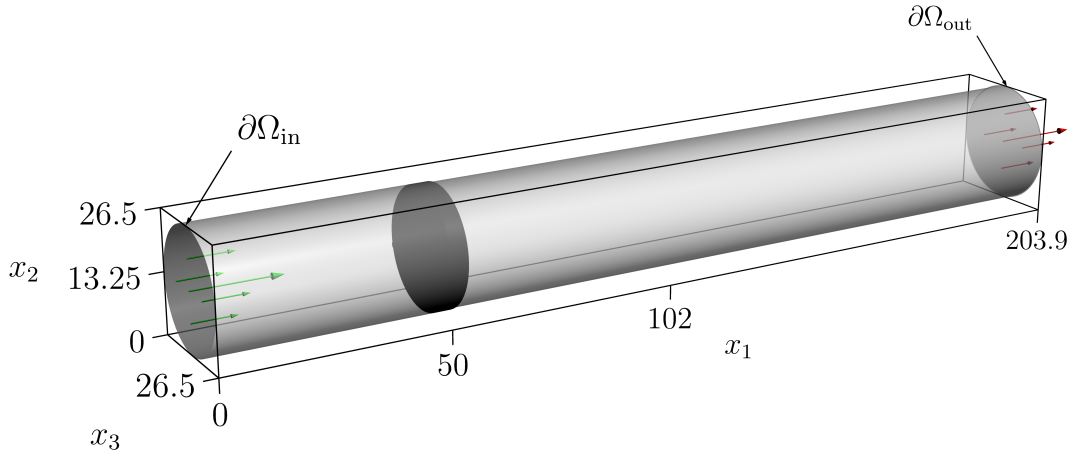
Figure 8.3: Schematic representation of the computational domain Ω with inserted acrylic plate. The dimensions are in millimeters and the flow is assumed in the cylinder defined by the gray wall only. The colored arrows illustrate the flow direction.

At the walls (represented by the gray color in Figure 8.3), the no-slip BC is prescribed. At the outflow, the free outflow BC is assumed. At the inflow, the velocity profile is prescribed as $\boldsymbol{u}_{\mathrm{in}} = (u_{1,\mathrm{in}}, 0, 0)^T$,

$$u_{1,\mathrm{in}}(x_2, x_3) = U\left(1 - \left(\frac{(x_2 - S_{c,2})^2 + (x_3 - S_{c,3})^2}{r_{\mathrm{in}}^2}\right)^{\frac{U_{\mathrm{avg}}}{U - U_{\mathrm{avg}}}}\right), \ \forall \boldsymbol{x} \in \partial\Omega_{\mathrm{in}}, \tag{8.4}$$

where U $[\mathrm{m\,s^{-1}}]$ is the maximal velocity. It is set to U_{high} or U_{low} (cf. Table 8.2), according to the measurement). The formula in Eq. (8.4) is inspired by the velocity profile measured by MRI. U_{avg} $[\mathrm{m\,s^{-1}}]$ is the average velocity calculated using the cross-sectional area and measured flux given in Table 8.2. Initially, $\boldsymbol{u}_{\mathrm{ini}}(\boldsymbol{x}) = (u_{1,\mathrm{in}}(x_2, x_3), 0, 0)^T$ and $p_{\mathrm{ini}}(\boldsymbol{x}) = 0$, $\forall \boldsymbol{x} \in \widehat{\Omega}$, and the final time for the simulations is $T = 10$ s.

Next, blood flow in human arteries is not constant in time. Thus, a more realistic inflow condition is considered. The time-dependent inflow velocity BC is defined by

$$\boldsymbol{u}_{\mathrm{ini}}(\boldsymbol{x}, t) = (h(t)u_{1,\mathrm{in}}(x_2, x_3), 0, 0)^T, \ \forall \boldsymbol{x} \in \partial\Omega_{\mathrm{in}}, \tag{8.5}$$

where $h(t)$ is the time-dependent function defined by [52]

$$h(t) = \max\left\{0, 11.8549504359 \sin\left(20\left(t - \lfloor t \rfloor\right)^2\right) \exp\left(-11\left(t - \lfloor t \rfloor\right)\right)\right\}. \tag{8.6}$$

The scaling function $h(t)$ is periodic with a period of 1 s, non-negative, and normalized to the interval $[0, 1]$, see Figure 8.4. The shape of the scaling function $h(t)$ is inspired by the measured

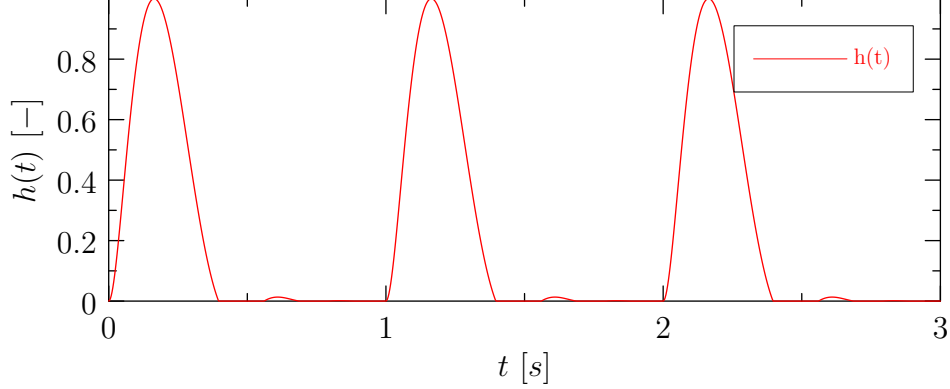Figure 8.4: Values of the scaling function $h(t)$ in time.

profile of human pulses in arterial vessels.

8.1.3 Numerical method

The CuLBM is used for all numerical simulations in this chapter. At the inflow and outflow boundary, the equilibrium BC is prescribed. The no-slip BC at the wall is approximated using the fullway bounce-back BC. At the initial time, all DDFs are set to the equilibrium computed from the initial velocity and density (pressure).

The computational grid with spacing parameter $\delta_x = 9.125874 \cdot 10^{-5}$ m was used for all simulations in this chapter. The fixed time step $\delta_t = 4 \cdot 10^{-6}$ s was considered. Due to the fullway bounce-back BCs used on the walls, the offset vector (defined in Section 3.1) is $\boldsymbol{P} = \left(0, \frac{\delta_x}{2}, \frac{\delta_x}{2}\right)^T$. The lattice $\widetilde{\Omega}$ was composed of $N_1 = 2249, N_2 = 288, N_3 = 288$ sites in the x_1-, x_2- and x_3-direction, respectively.

The term $\boldsymbol{G}$ is added to the force term of the LBM and discretized using the finite difference method. Both components of $\mathbb{D}$ and divergence of $\mathbb{D}$ are approximated using central or one-sided finite differences. Let $\varphi = u_i$, or $\varphi = \mathbb{D}_{ij}$, $i, j = 1, 2, 3$, then the following finite difference scheme is used:

$$\frac{\partial \varphi}{\partial x_j}(\boldsymbol{x}) \approx \frac{\varphi(\boldsymbol{x} + \delta_x \boldsymbol{e}_j) - \varphi(\boldsymbol{x} - \delta_x \boldsymbol{e}_j)}{2\delta_x}, \tag{8.7}$$

where $i, j \in \{1, 2, 3\}$, $\boldsymbol{x} \in \hat{\Omega}$. Eq. (8.7) is used for all $\boldsymbol{x}$ that satisfies $(\boldsymbol{x} - \delta_x \boldsymbol{e}_j) \notin \partial\hat{\Omega}$ and $(\boldsymbol{x} + \delta_x \boldsymbol{e}_j) \notin \partial\hat{\Omega}$, that is, both nodes in the direction $\pm\boldsymbol{e}_k$ do not belong to the boundary $\partial\hat{\Omega}$. If $(\boldsymbol{x} - \delta_x \boldsymbol{e}_j) \notin \partial\hat{\Omega}$ and $(\boldsymbol{x} + \delta_x \boldsymbol{e}_j) \in \partial\hat{\Omega}$ one-sided finite differences are used, that is,

$$\frac{\partial \varphi}{\partial x_j}(\boldsymbol{x}) \approx \frac{\varphi(\boldsymbol{x} + \delta_x \boldsymbol{e}_j) - \varphi(\boldsymbol{x})}{\delta_x}, \tag{8.8}$$

or

$$\frac{\partial \varphi}{\partial x_j}(\boldsymbol{x}) \approx \frac{\varphi(\boldsymbol{x}) - \varphi(\boldsymbol{x} - \delta_x \boldsymbol{e}_j)}{\delta_x} \tag{8.9}$$

if $(\boldsymbol{x} - \delta_x \boldsymbol{e}_j) \in \partial\hat{\Omega}$ and $(\boldsymbol{x} + \delta_x \boldsymbol{e}_j) \notin \partial\hat{\Omega}$.

In Chapter 5, the non-physical behavior was observed near the domain boundary. Thus, Eqs. (8.8) and (8.9) are used to minimize the influence of such non-physical effects on the approximation of the spatial derivatives of the velocity components.

All LBM simulations were run on HPC cluster HELIOS located at FNSPE, CTU in Prague and RCI cluster located at FEL, CTU in Prague. Both clusters contain nodes equipped with multiple GPU cards (NVIDIA V100 or NVIDIA A100).

8.1.4   Data processing

The simulated and experimental data are time-averaged before comparison. The quantity averaged in time $\varphi(\boldsymbol{x}, t)$ is denoted by $\overline{\varphi}(\boldsymbol{x})$ and the integral over time is approximated for all $\boldsymbol{x} \in \widetilde{\Omega}$ as

$$\overline{\varphi}(\boldsymbol{x}) = \frac{1}{N_{ti}} \sum_{k=0}^{N_{ti}-1} \phi\left(\boldsymbol{x}, t_{ini} + \frac{k}{\omega_t}\right), \tag{8.10}$$

where $t_{ini} \in \hat{I}$ denotes the initial time step, ω_t [s^{-1}] is the integration frequency, and N_{ti} is the number of data used for the integration. All presented results are integrated with frequency $\omega_t = \frac{1}{500}$. To minimize the influence of the initial condition, all data are averaged within the time interval $(5, 10)$ s. The averaging of the experimental data is described in [52].

Data are compared in cross-sectional areas $S(x_1)$ of the computational domain perpendicular to the axis x_1 defined by

$$S(x_1) = \left\{ \boldsymbol{x} \in \hat{\Omega} \,\middle|\, \|\boldsymbol{x} - \boldsymbol{S_c}\| \leq r, \ r = r(x_1) = \begin{cases} r_{\text{in}} & \text{for } x_1 < 0.05 \\ r_{\text{out}} & \text{otherwise} \end{cases} \right\}. \tag{8.11}$$

The corresponding projection of $S(x_1)$ on the lattice $\widetilde{\Omega}$ is labeled by $\widetilde{S}(x_1)$.

Furthermore, data are space-averaged over $\widetilde{S}(x_1)$. The space-averaged quantity φ in a cross section $\widetilde{S}(x_1)$ is denoted by $\langle \varphi \rangle(x_1, t)$ and defined by

$$\langle \varphi \rangle(x_1, t) = \frac{1}{\left|\widetilde{S}(x_1)\right|} \sum_{(x_2, x_3) \in \widetilde{S}(x_1)} \varphi(x_1, x_2, x_3, t), \tag{8.12}$$

where $\left|\widetilde{S}(x_1)\right|$ represents the number of lattice sites in $\widetilde{S}(x_1)$.

Based on the investigation in [71], the positive flux q^+ [m^3 s^{-1}] and the negative flux q^- [m^3 s^{-1}] are defined by

$$q^+(x_1) = \left\langle \overline{\max\left(\rho u_1, 0\right)} \right\rangle(x_1) \tag{8.13a}$$

$$q^-(x_1) = \left\langle \overline{\min\left(\rho u_1, 0\right)} \right\rangle(x_1). \tag{8.13b}$$

8.1.5   Comparison of viscosity models

As already mentioned, the inclusion of a non-Newtonian model to the numerical method increases the computational time. Therefore, the effect of the non-Newtonian model is investigated by comparing it with two Newtonian models. The first Newtonian model uses viscosity $\mu_0 = \lim_{\dot{\gamma} \to 0} \mu(\dot{\gamma})$, that is, dynamic viscosity at zero shear rate. The second Newtonian model uses the viscosity $\mu_\infty = \lim_{\dot{\gamma} \to +\infty} \mu(\dot{\gamma})$, i.e., the dynamic viscosity at an infinite shear rate. Newtonian models are further referred to as μ_∞-model and μ_0-model.

8.1.6   Selection of non-Newtonian model

In Section 2.3, there are five different constitutive models that approximate the dynamic viscosity dependence on the shear rate. All these models have parameters that must be adjusted to a given fluid. Based on the data sets for GX [22] and SX [23], the parameters are estimated using the `NonlinearFit` function in a symbolic and numeric software Maple 2015. The output of this function is the approximation of parameters and final residual. Based on the values of the residuals in Section 8.2.1, the non-Newtonian model is selected.

8.1.7   Presentation of results

First, the experimental and numerical results are visually compared using 2D cross-sectional areas of the domain Ω. 2D velocity magnitude distribution and profiles of spatio-temporal means of the positive q^+ and negative q^- flux along the x_1 axis are presented. The results in the cross sections of non-Newtonian fluids are then subjected to the following statistical analyses:

Histogram and Correlation analysis

A histogram analysis was performed based on the pixel-wise comparison of differences $\boldsymbol{Z}_{\mathrm{diff}}$ defined in the Appendix A.2. Next, correlation and linear fit analyses were performed. As these complete analyses are extensive, they are not presented here and can be found in [52].

Bland-Altman analysis

One of the well-known disadvantages of the correlation analysis is the dependence on the range of input data. Thus, the Bland-Altman analysis is used to overcome this disadvantage. The complete Bland-Altman analysis is described in the Appendix A.2. A typical output of the Bland-Altmann analysis are scatter plots, which can be found in [52]. To present the results of the Bland-Altman analysis in compressed format, violin plots of $\langle \boldsymbol{Z} \rangle_{\mathrm{diff}}$ are used. Each violin plot represents one set of slices related to one LBM-MRI pair. The violin plots contain the following information: the median value of the studied quantity (white dot); values of the first and third quartile (lower and upper limit of the gray rectangle); upper and lower adjacent values (upper and lower end of the solid vertical line); and density distribution of the values (colored region).

8.1.8   Averaging of pulsating flow

To detect the evolution of the pulsating flow, the period is repeated ten times, resulting in a simulation with the duration of 10 s. Within this study, the non-Newtonian numerical model is compared with Newtonian models only. To minimize the influence of the initial setup, the last five periods are averaged. To detect the flow evolution in particular phases of the profile (8.5), the one-second period is divided into 25 equally large subintervals. The flow is then averaged five times at these subintervals. Thus, the resulting sets for time integration are denoted I_i and defined by

$$I_i = \bigcup_{p \in \{5,6,7,8,9\}} \left(S\,(i-1) + p,\, S\,i + p \right), \tag{8.14}$$

where $S = 0.04$ s, $i \in \{1, 2, \cdots, 25\}$.

8.2   Results and discussion

In this section, the results of the numerical simulations and experimental measurement using MRI are presented and discussed. First, the non-Newtonian models are fitted to the reference

data, and the non-Newtonian model used for the simulations is selected. Next, the simulated and experimental data are compared using several criteria given in Section 8.1.7. Finally, the results of the pulsating flow are presented.

8.2.1   Approximation of non-Newtonian models

The parameters of non-Newtonian models given in Section 2.3 are estimated and the results for particular models are given in Tables 8.3 and 8.4. Based on these parameters, non-Newtonian models are plotted in Figures 8.5 and 8.6.

Based on the results, the Carreau-Yasuda non-Newtonian model produces the closest results to the reference data and is illustrated for both fluids in Figure 8.7. Moreover, data of the human blood viscosity [200] are shown in Figure 8.7 for the comparison with investigated non-Newtonian fluids. Thus, the Carreau-Yasuda model is used in the following numerical simulations and is referred to as μ_{CY}-model.

Non-Newtonian model	Parameters					residual
μ_{PL}	C_p	n				
	$1.905 \cdot 10^{-2}$	0.869				$7.394 \cdot 10^{-3}$
μ_{SP}	μ_0	$\dot{\gamma}_0$	n			
	$2.461 \cdot 10^{-2}$	0.115	0.874			$7.394 \cdot 10^{-3}$
μ_{CY}	μ_0	μ_∞	ϑ	a	n	
	$1.585 \cdot 10^{-2}$	$4.856 \cdot 10^{-3}$	$2.805 \cdot 10^{-2}$	2.341	$0.463\,(\star)$	$\mathbf{8.689 \cdot 10^{-4}}$
μ_{CR}	μ_0	μ_∞	k	n		
	$1.599 \cdot 10^{-2}$	$6.511 \cdot 10^{-3}$	$9.989 \cdot 10^{-3}$	1.383		$1.148 \cdot 10^{-3}$
μ_{CA}	k_0	k_1				
	$5.066 \cdot 10^{-2}$	$9.548 \cdot 10^{-2}$				$1.280 \cdot 10^{-2}$

Table 8.3: Parameters and residuals of non-Newtonian models approximated by the `NonlinearFit` function for non-Newtonian fluid GX. The residual in bold is the lowest residual between all non-Newtonian models. The value labeled by $(\star)$ was fixed according to [98]. All variables are given in SI units introduced in Section 2.3.

Non-Newtonian model	Parameters					residual
μ_{PL}	C_p	n				
	$2.043 \cdot 10^{-2}$	0.771				$4.030 \cdot 10^{-3}$
μ_{SP}	μ_0	$\dot{\gamma}_0$	n			
	$3.282 \cdot 10^{-2}$	0.155	0.758			$4.030 \cdot 10^{-3}$
μ_{CY}	μ_0	μ_∞	ϑ	a	n	
	$4.481 \cdot 10^{-2}$	$3.323 \cdot 10^{-3}$	1.193	0.486	$0.463\ (\star)$	$\mathbf{1.587 \cdot 10^{-3}}$
μ_{CR}	μ_0	μ_∞	k	n		
	$4.320 \cdot 10^{-2}$	$3.336 \cdot 10^{-3}$	1.335	0.524		$1.609 \cdot 10^{-3}$
μ_{CA}	k_0	k_1				
	$3.502 \cdot 10^{-2}$	$8.736 \cdot 10^{-2}$				$1.628 \cdot 10^{-2}$

Table 8.4: Parameters and residuals of non-Newtonian models approximated by the `NonlinearFit` function for non-Newtonian fluid SX. The residual in bold is the lowest residual between all non-Newtonian models. The value labeled by $(\star)$ was fixed according to [98]. All variables are given in SI units introduced in Section 2.3.

Figure 8.5: Illustration of the non-Newtonian models for fluid GX with parameters given in Table 8.3. The reference data are from [22].

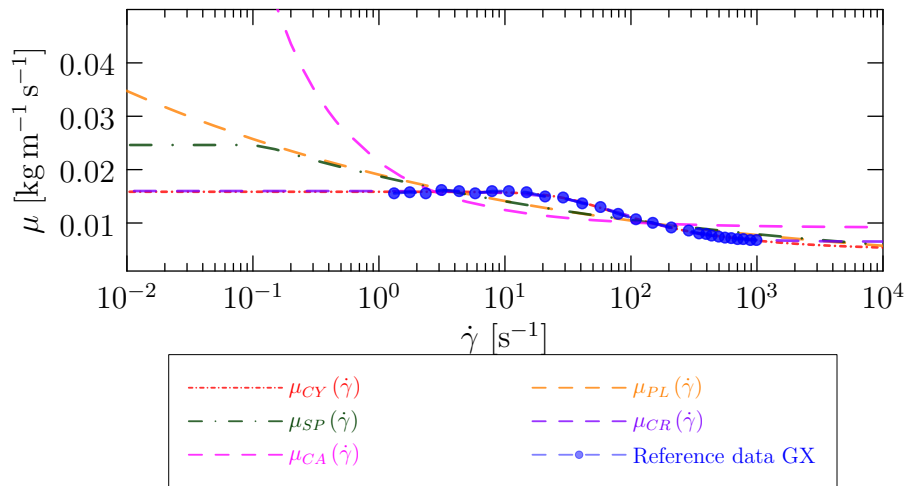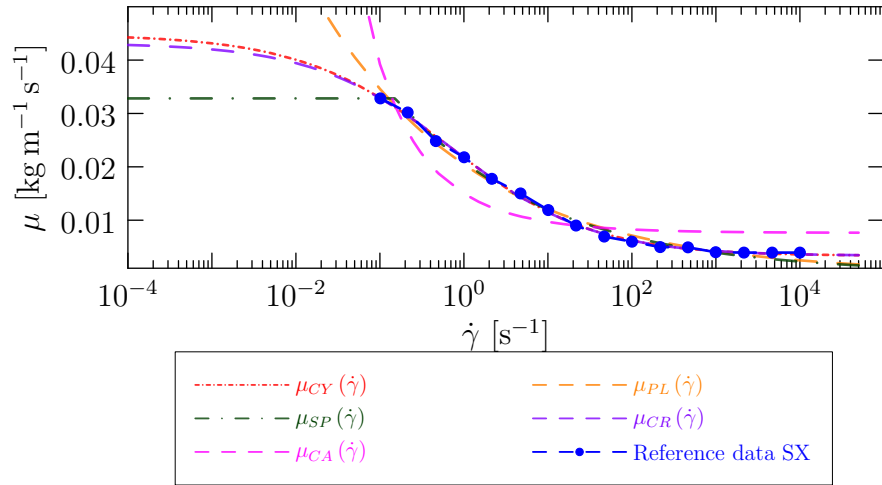Figure 8.6: Illustration of the non-Newtonian models for fluid SX with parameters given in Table 8.4. The reference data are from [23].
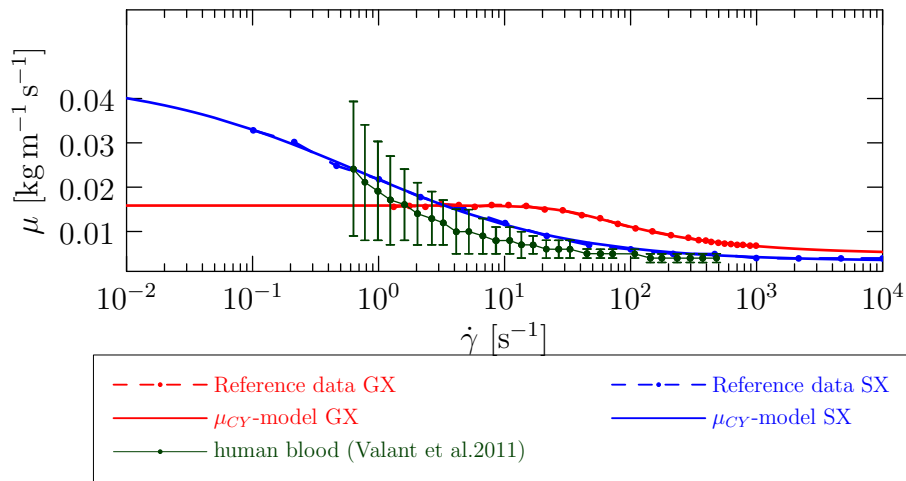

Figure 8.7: Comparison of $\mu_{\text{CY}}(\dot{\gamma})$ with estimated values given in Tables 8.3 and 8.4 with reference data [22] for GX and [23] for SX. Viscosity of human blood [200] is included for the comparison with investigated non-Newtonian fluids.
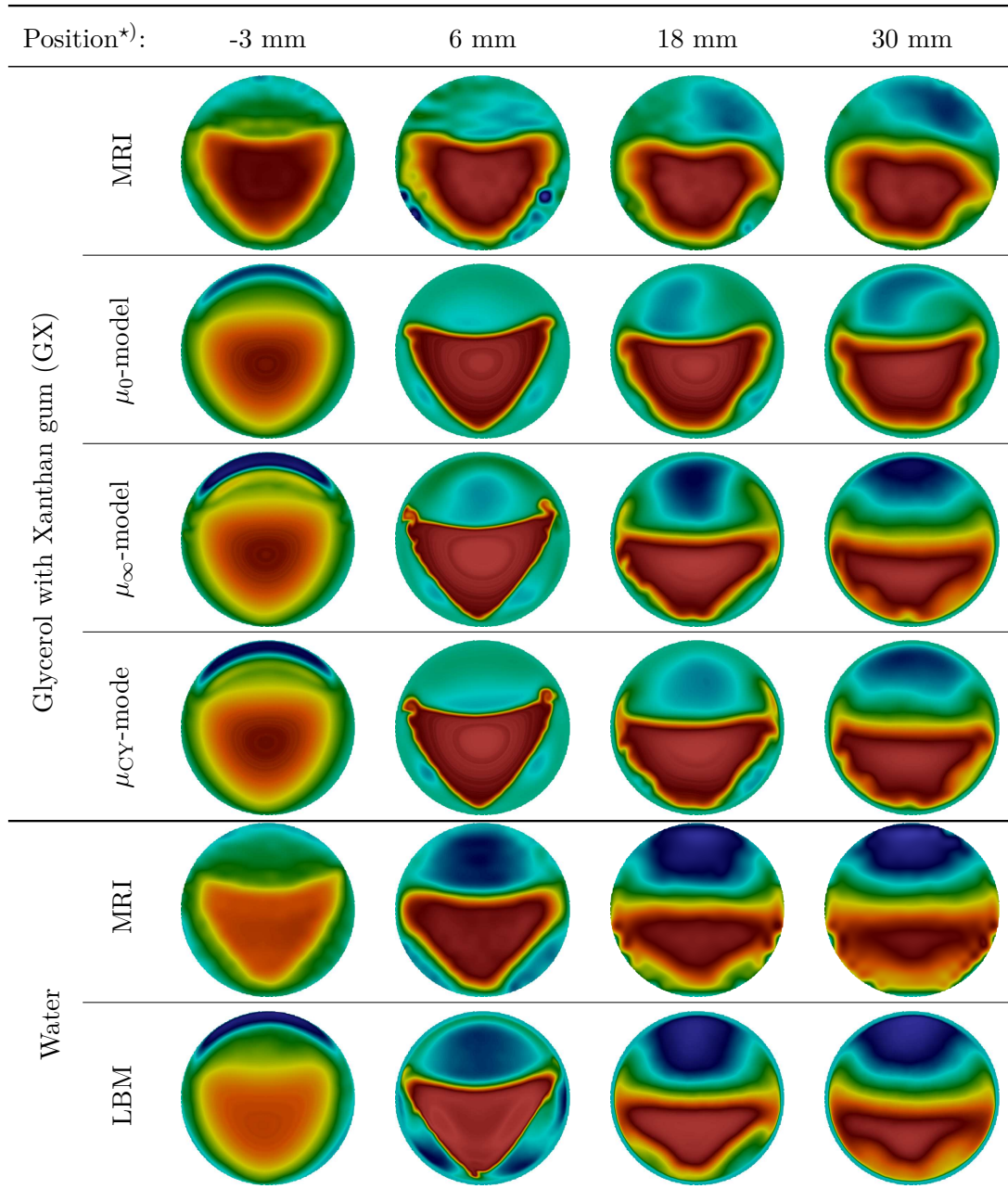
8.2.2 Visual comparison of 2D velocity distribution

Based on the good visual agreement between the LBM and MRI results in each cross-sectional area $S(x_1)$, the LBM can be considered a capable and accurate flow simulator for various geometries and fluid properties, see Table 8.5.

The numerical results for the valves MiS and MoS are in good visual agreement with the experimental data. The complete set of these results can be found in [52]. The results for the SeS valve show a consistent velocity profile in sections before stenosis. However, more significant differences occurred between the LBM and MRI results in the slices behind the stenosis. The measured velocity profile is rotated clockwise or counterclockwise between individual cross sections. We hypothesize that the source of rotation is the curved geometry of the holes behind the phantom, which is not currently considered in the numerical model and will be investigated in the future work. A sample of the discrepancy between the LBM and MRI results for valve SeS is presented in Table 8.6 for water and fluid SX, velocity regimes U_{high}. Since a statistical comparison of the results for the problems with valve SeS will be unwarranted, valve SeS is omitted in the next statistical investigation.

In Table 8.7, only negative velocity regions for SeS–SX–U_{high} and SeS–Water–U_{high} are illustrated for the cross sections 3 mm before the stenosis. The results in this figure show the areas of negative flow that are located mainly near the wall. This discrepancy between the numerical and experimental data is probably due to the MRI measurement being affected by poor resolution and noise caused by the acrylic walls. In addition, the total flux of the MRI measurement is not conserved between individual slices, as indicated in Figure 8.11, indicating another problem with the experiment.

In general, the numerical simulations suggest an underestimation of the negative fluxes q^- by MRI measurements, as reported in [71].

Position$^{\star)}$:	-3 mm	6 mm	18 mm	30 mm

Glycerol with Xanthan gum (GX)

MRI

μ_0-model

μ_∞-model

μ_{CY}-mode

Water

MRI

LBM

$^{\star)}$ position behind the stenosis

u_1 [cm s^{-1}]

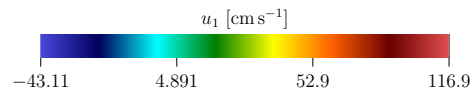-43.11 4.891 52.9 116.9

Table 8.5: Comparison of 2D velocity profiles for MoS–GX–U_{high} and MoS–Water–U_{high} with different positions behind the valve for all simulated and measured data.
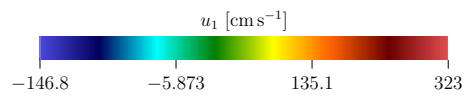
Table 8.6: Comparison of 2D velocity profiles for SeS–SX–U_{high} and SeS–Water–U_{high} with different positions behind the valve for all simulated and measured data.
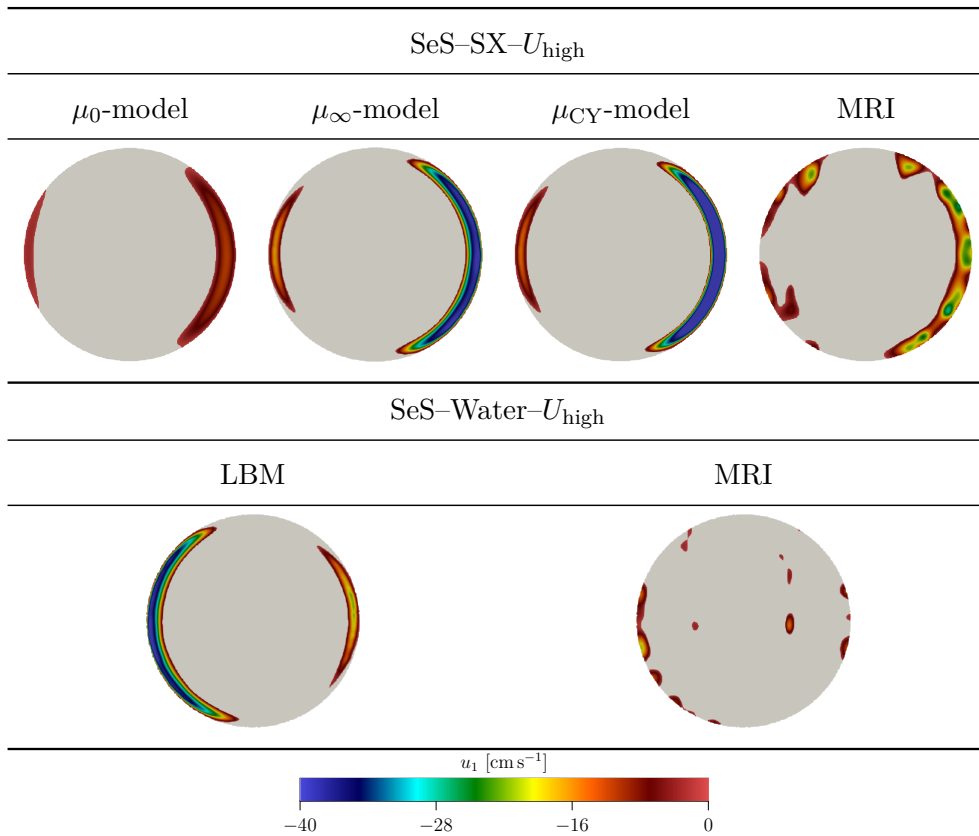
Table 8.7: Visualization of the negative flow regions for different viscosity models and fluids for stenosis SeS and velocity U_{high}. The slices are at position -3mm. The gray color represents the area with positive velocity.

8.2.3   Comparison of 1D flow profiles

To further illustrate the differences between the LBM viscosity models and MRI measurements, graphs with time- and space-averaged positive q^+ and negative q^- fluxes are presented for water and non-Newtonian fluids, see Figures 8.8, 8.9, and 8.10. A similar study was conducted for water in [71] and the discrepancy between the LBM and MRI was observed for high-velocity flow and valve SeS with severe stenosis. This contradiction is also observed in this study.

On the basis of the 2D velocity profiles and 1D flux plots, the most general non-Newtonian μ_{CY}-model matches the experimental data best. According to the level of stenosis, the fluid considered, and the velocity regime, one of the Newtonian models approaches the non-Newtonian model. Thus, no specific criterion can be derived for the selection of a Newtonian model. However, in most cases, the Newtonian μ_∞-model is the closest model to the μ_{CY}-model.

The possible source of disagreements between LBM and MRI results is the accuracy of the MRI measurement. In Figure 8.11 the total flow is plotted for all experimental data and each cross section. The experimental data, especially in Figure 8.11a, show that the total flow in MRI measurement is not conserved along the x_1 axis.
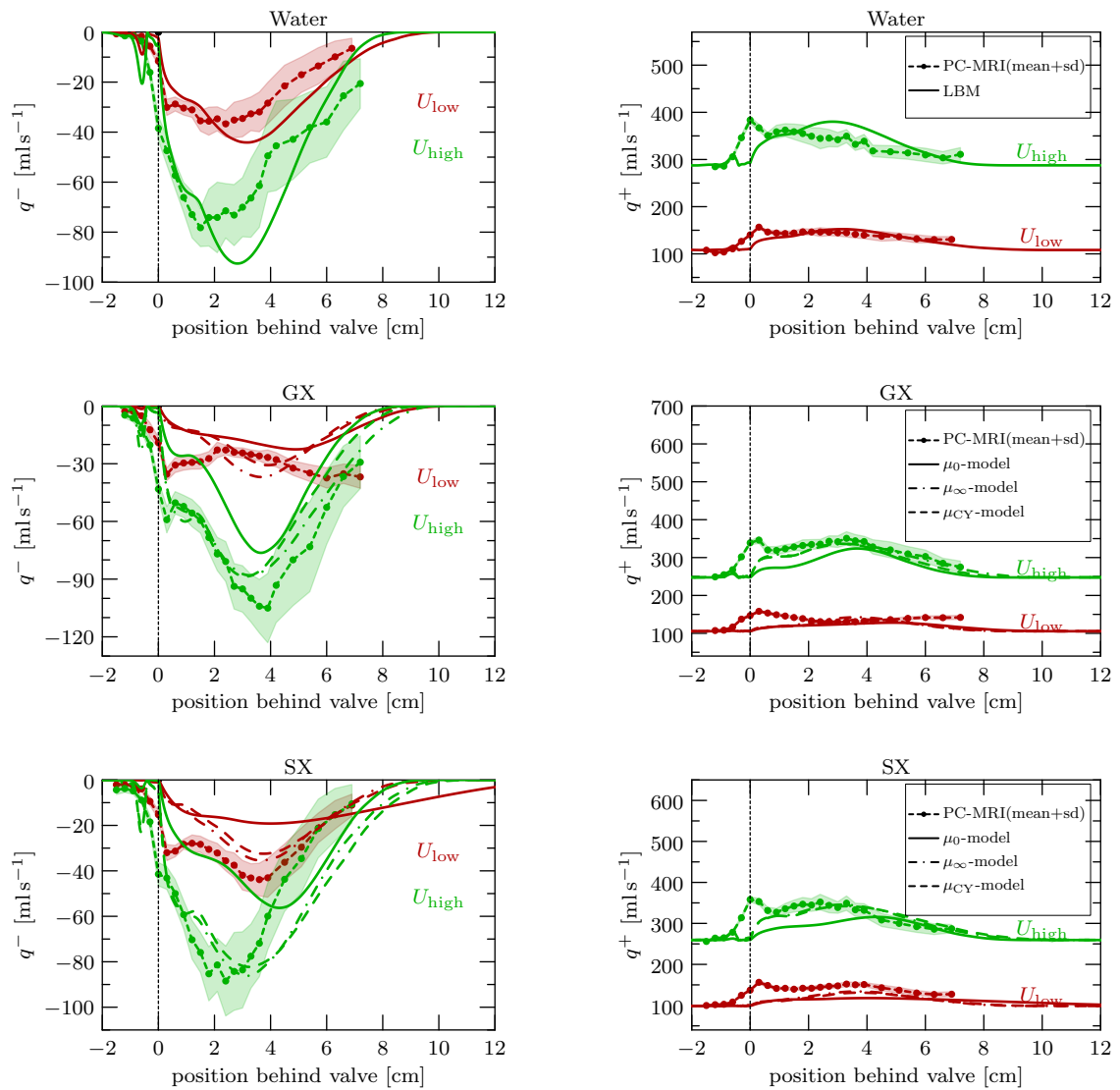
Figure 8.8: Positive (right) and negative (left) horizontal flux for narrowing SeS ⬭ and all considered models. The PC-MRI data consists of mean values (filled circles) and standard deviation intervals (sd) illustrated by the filled region.

Figure 8.9: Positive (right) and negative (left) horizontal flux for narrowing MoS ⬭ and all considered models. The PC-MRI data consists of mean values (filled circles) and standard deviation intervals (sd) illustrated by the filled region.

Figure 8.10: Positive (right) and negative (left) horizontal flux for narrowing MiS ⬭ and all considered models. The PC-MRI data consists of mean values (filled circles) and standard deviation intervals (sd) illustrated by the filled region.

(a) SeS

(b) MoS

(c) MiS

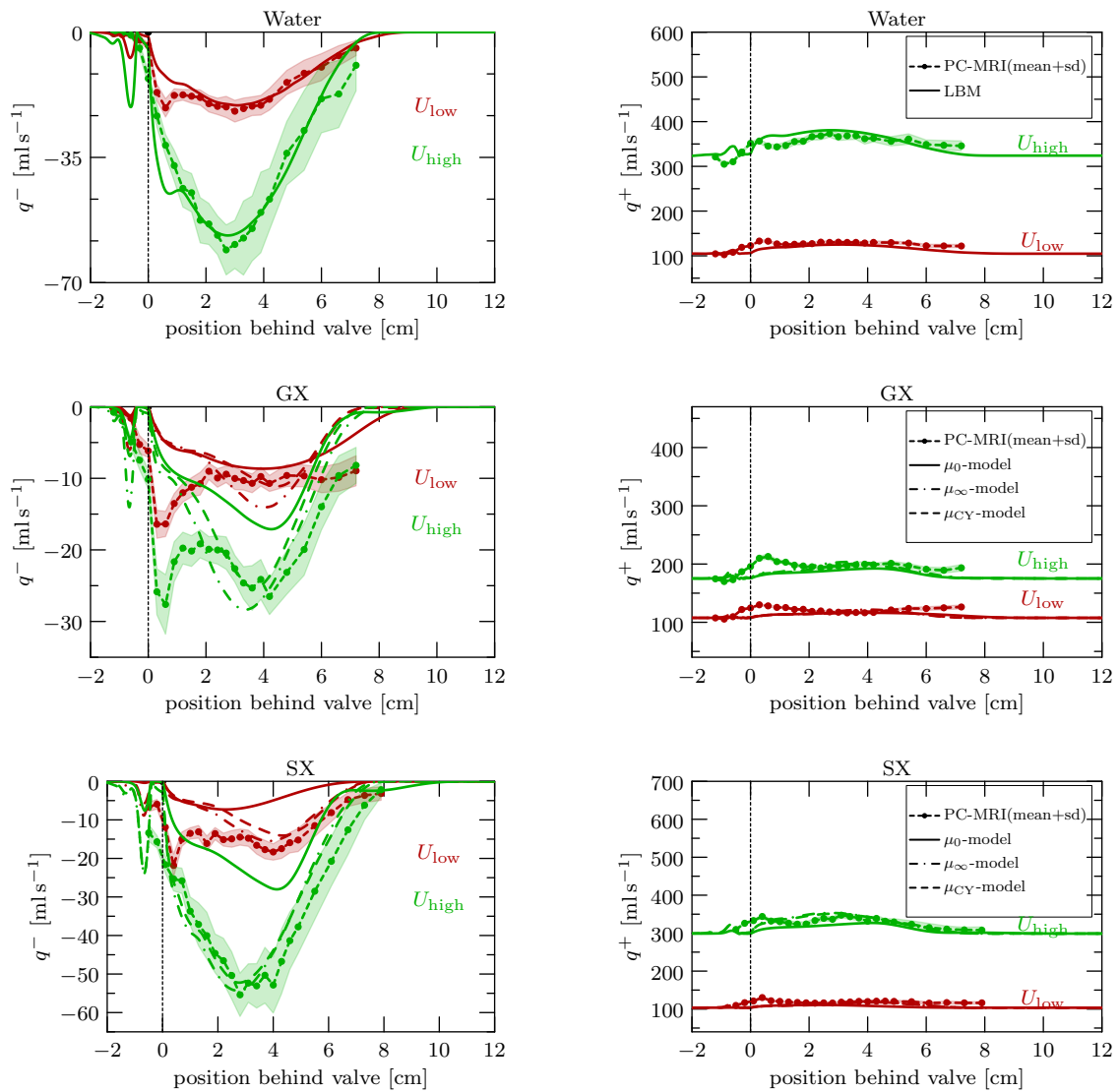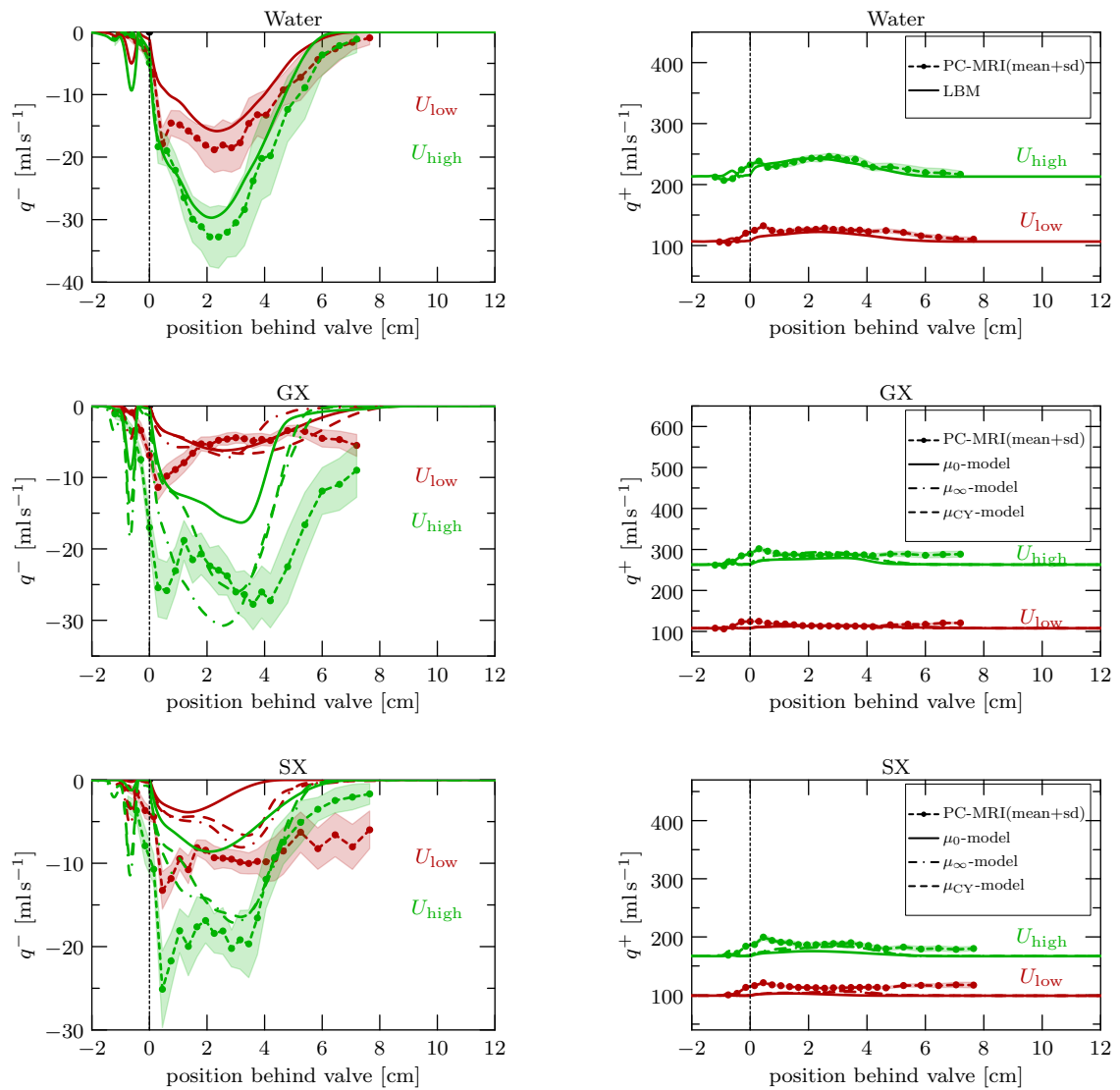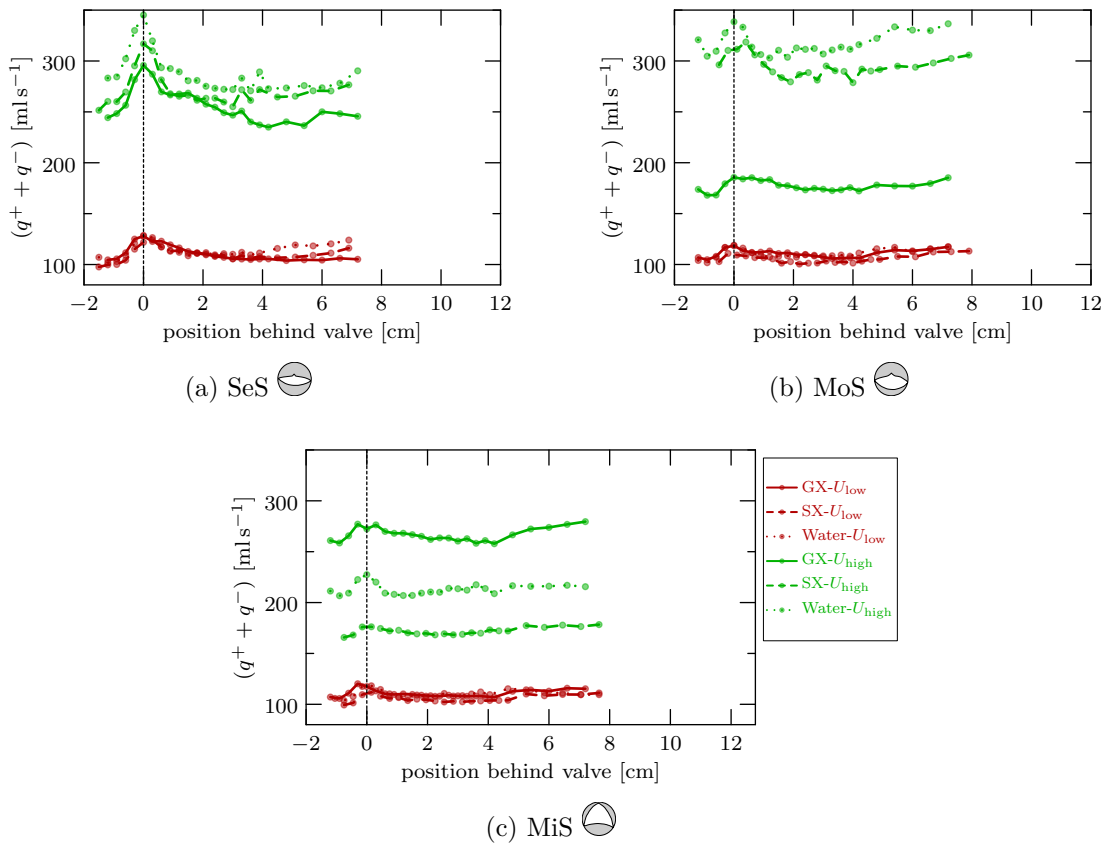Figure 8.11: Experimental data of total flow $(q^+ + q^-)$ in cross-sectional areas for all considered fluids and flow regimes.

8.2.4 Statistical comparison

The statistical results follow the results of the visual inspection. In this section, only examples of Bland-Altman statistical analysis are presented. The complete set of results can be found in [52]. Figure 8.12 is composed of violin plots of mean difference $\langle \boldsymbol{Z} \rangle_{\mathrm{diff}}$ between the measured and simulated data. The measurement in slices in the vicinity of the valve was affected by the limitation of the MRI measurement. Therefore, these slices were not used for the statistical assessment. As in the previous sections, the non-Newtonian μ_{CY}-model is the best fit to the simulated data, and the Newtonian μ_{∞}-model gives results closest to the non-Newtonian model in most cases.

The mean difference $\overline{\boldsymbol{Z}}_{\mathrm{diff}}$ in velocities shows the discrepancy between the time-averaged velocities in the individual cross sections. The mild negative difference indicates that the velocities simulated by the LBM are underestimated relative to the MRI data. The absolute and relative discrepancy between LBM and MRI data is illustrated in Figure 8.12.

In the cases MoS–GX–U_{low} and MiS–SX–U_{low}, the normalized median of the mean difference $\langle \boldsymbol{Z} \rangle_{\mathrm{diff}}$ is less than 10%, which is acceptable in clinical practice. In other cases, the normalized median is less than 5%.

The results summarized in [52] show that the limits of agreement are one order of magnitude greater than $\langle \boldsymbol{Z} \rangle_{\mathrm{diff}}$. The limits of agreement indicate the deviation of a single velocity measurement, and in all cases the relative deviation exceeds 25 %. The Bland-Altman plots show a relatively low discrepancy for velocities close to zero and velocities close to the maximal velocity, whereas it is elevated for intermediate velocities. We assume that this is due to the calculation of the differences of the velocity data, which are small for regions with low and maximal velocities and higher for regions with averaged velocities. Therefore, the small spatial mismatch of the profiles explains the higher absolute velocity difference in the mid-range velocities. Fortunately, it does not influence the mean differences obtained by the Bland-Altman analysis, which are the basis for the flow rate error. For this reason, the correlation coefficient is relatively low for slices where the velocities are high (slices in the vicinity of the valve).

8.2.5 Time dependent inflow velocity profile

For the sake of brevity, only results for the case SeS with velocity U_{low} are presented. The full set of results can be found in [52]. In contrast to previous results, no experimental data are available for this problem.

The results in Figure 8.13 illustrate the averaged negative fluxes in particular time intervals. In most time intervals, the μ_{∞}-model gives the same results as the μ_{CY}-model. The largest relative differences were observed at the beginning of the pulse, where the μ_{∞}-model responds faster to temporal velocity changes. However, these differences at the beginning of the time period are smaller compared to the differences in the later period.

Differences between the non-Newtonian model and Newtonian models normalized by the temporal maximum of the μ_{CY}-model results (using the L_2 norm) are demonstrated using Figure 8.14 consisting of colored bars for each time interval. Based on these results, the μ_{∞}-model provides results similar to the μ_{CY}-model.

The μ_{CY}-model behaves as the μ_0-model for low velocities at the beginning of the periodic profile and low shear rate, and thus the results of the μ_{CY}-model are closer to the results of the μ_0-model. On the other hand, the μ_{CY}-model approaches the μ_{∞}-model as the velocity magnitude and shear rate increase. At the end of the period, the differences between μ_{CY}- and both Newtonian are similar.
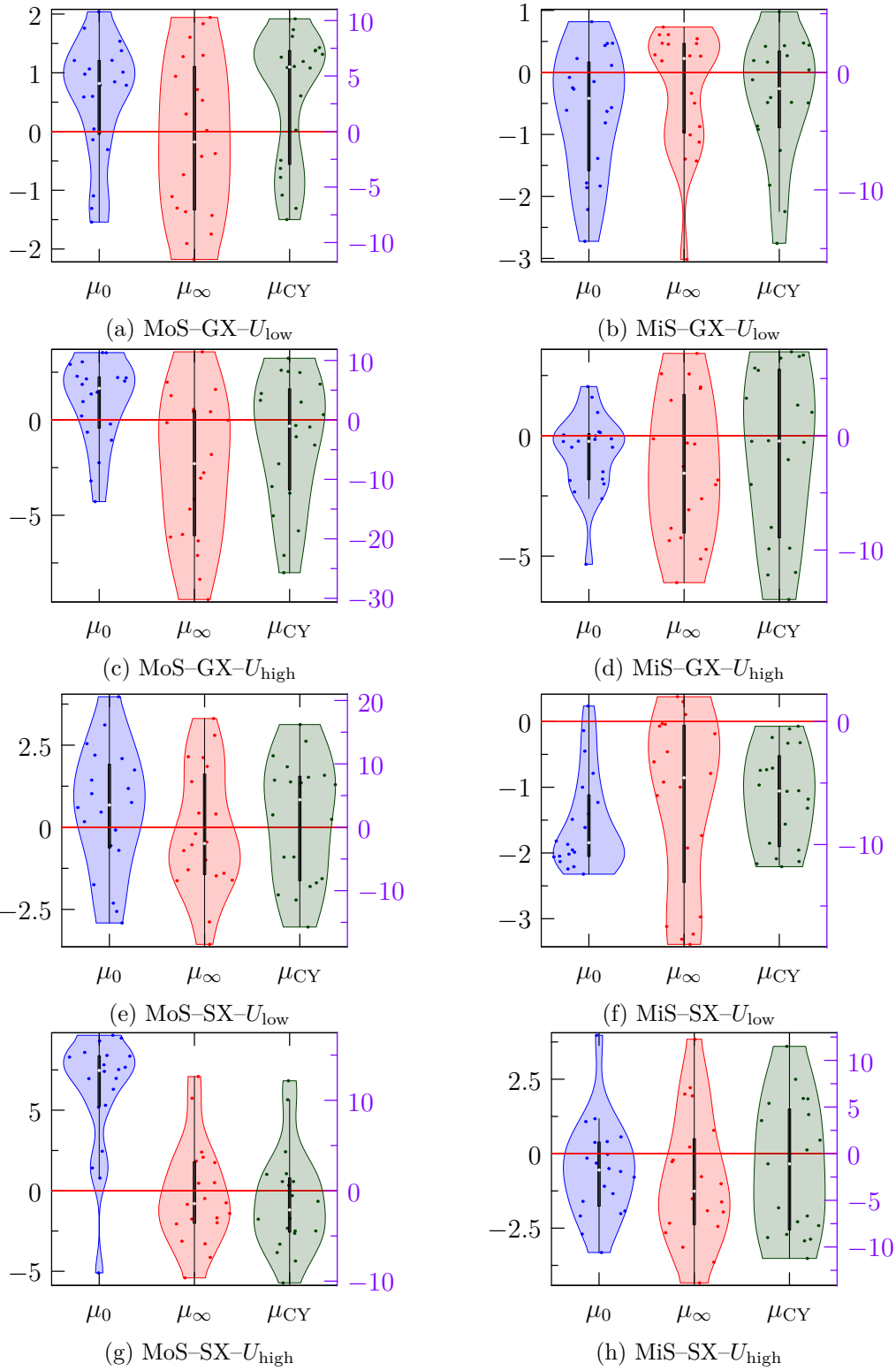
Figure 8.12: Violin plot analysis for $\langle \boldsymbol{Z} \rangle_{\mathrm{diff}}$ [cm s^{-1}] used in the Bland-Altman analysis. The red horizontal line represents the optimal value. The left vertical axis shows values in cm s^{-1}. The right purple vertical axis shows values divided by factor U_{avg} in %.
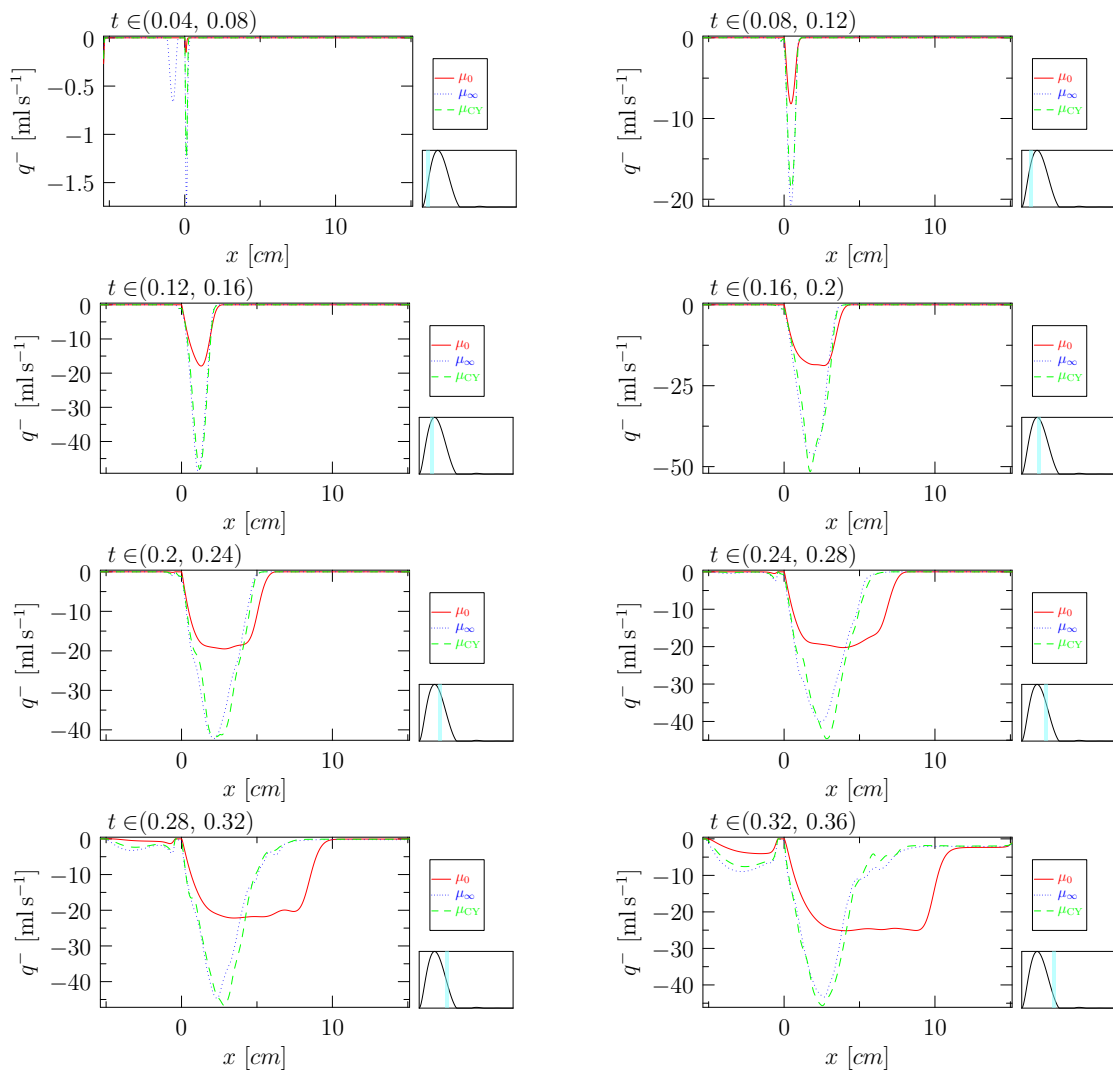
Figure 8.13: Space and time averaged negative flux for time dependent inflow velocity condition for SeS–SX–U_{low}. The phase of the inflow condition is represented by the light blue column in the small graph.
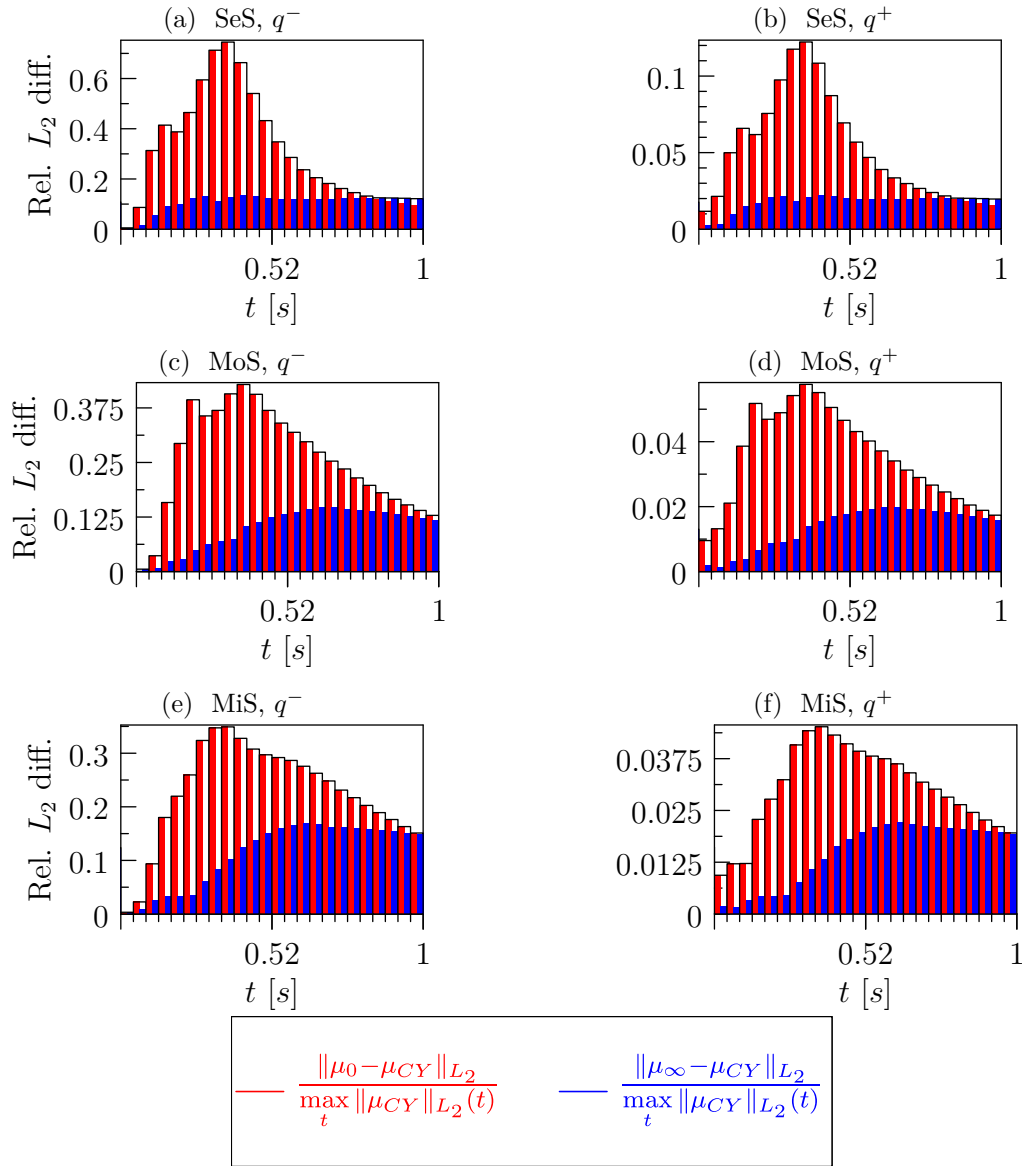
Figure 8.14: Space and time averaged relative L_2 differences between positive and negative fluxes for time dependent inflow velocity condition for SeS–SX–U_{low}. In each time interval (bounded by the black lines) the differences between non-Newtonian and two Newtonian models (with viscosity μ_0 and μ_∞) are drawn using bars with different color.

8.2.6   Computational performance of Newtonian and non-Newtonian model

Since the non-Newtonian model has mainly more complex implementation and higher memory requirements(i.e., more variables need to be stored and accessed in the global GPU memory), the applicability of a simpler Newtonian model is investigated. Table 8.8 demonstrates higher computational times of the μ_{CY}-model compared to the μ_∞-model. In addition, non-Newtonian models contain more parameters for adjustment to the particular fluid compared to the Newtonian model and have some limits of applications [134, 155].

Based on the results presented, the μ_∞-model (Newtonian) can be recommended as an appropriate, less computationally expensive model for the blood flow simulations in large arterial vessels.

LBM model	Computational time [min]
μ_∞-model	182
μ_{CY}-model	229

Table 8.8: Comparison of computational times for μ_∞-model and μ_{CY}-model. Both simulations used the setting SeS–GX–U_{high}. The simulated time was 1 s. The simulations were performed using four NVidia V100 GPU cards with 16GB of RAM memory on each GPU.

8.3   Chapter summary

This chapter was inspired by the fluid flow problem of the blood flow in large vessels. Three different valves, three experimental fluids, two different flow rates, and three variants of numerical models were used for the study. First, a good visual agreement was observed between experimental MRI measurement and LBM simulations. In all cases considered, the more general non-Newtonian model proved to be the most accurate. Newtonian models μ_∞ and μ_0 provided satisfactory results for all flow rates and fluid GX. Moreover, the μ_∞-model gave satisfactory results for all flow rates and the fluid SX, which has rheological properties closer to real blood than the fluid GX. Hence, the Newtonian μ_∞-model and non-Newtonian μ_{CY}-model are recommended for further simulations of non-Newtonian fluids. In addition, the Newtonian μ_∞-model is more computationally favorable. The obtained results further question the reliability of the MRI measurements near the narrowing.

The results of the pulsating flow problem showed that the Newtonian μ_∞-model is the closest to the non-Newtonian model considered in this study.

Based on the observations of this study, the less demanding Newtonian model is sufficient for further simulations of hemodynamics in large vessels.

Conclusion 9

The main objective of this work was the numerical lattice Boltzmann method (LBM) for incompressible fluid simulations. The study of this method follows on from previous Bachelor's degree project and Master's thesis [47, 48]. This thesis consists of two main parts: theoretical and practical.

The theoretical part starts with Chapter 2 consisting of the introduction to the theory used in this work, i.e., the theory of Navier-Stokes equations, boundary layer theory, theory of non-Newtonian fluids, and kinetic theory of fluids. It is followed by Chapter 3 composed of the introduction to the LBM. In this chapter, two boundary conditions and two interpolation strategies for the LBM with the grid refinement technique have been proposed.

The practical part is composed of five chapters. In the first of them, Chapter 4, the asymptotic analysis of the LBM with the cumulant collision operator has been conducted. The results of the asymptotic analysis showed that the LBM approximates the solution of the incompressible Navier-Stokes equations. Next, local approximations of velocity partial derivatives that are used by the interpolation of discrete density functions have been derived.

In the second chapter, Chapter 5, mesoscopic boundary conditions have been investigated using two benchmark problems. The obtained results show that our proposed boundary conditions provide numerical results with the smallest error compared to the other boundary conditions tested. It was further found that the non-physical artifacts occurring at the corners of the computational domain are minimized by the proposed boundary conditions. These observations are crucial for accurate simulations of problems inspired by the experiments.

The following three Chapters 6, 7, and 8 studied the applicability of the LBM to problems inspired by experiments. The first problem inspired by an experiment carried out in a wind tunnel with a rough surface has been studied. LBM simulations were compared with the finite difference method simulations and with the experimental results. Both comparisons showed that the LBM produces satisfactory results and can be regarded as a reliable method for direct numerical simulations of the turbulent fluid flow. Next, the LBM with the grid refinement technique has been tested. The results showed that the interpolation strategy significantly affects the numerical results. Thus, the quadratic interpolation of the velocity is recommended for the further use.

The second real-world application problem was inspired by the problem of biomass combustion in a fluidized bed reactor. The fluid flow in a part of the combustion chamber through the distributor (perforated plate) was investigated by simulations using the LBM and FVM. Particularly, the pressure drop at the distributor and velocity distribution behind the distributor were analyzed. The obtained results confirmed that the accuracy of the numerical results depends on the grid resolution. In the case of the LBM, the restrictions on the grid resolution were reduced by the use of the improved cumulant collision operator (CuLBM2). In addition, the

LBM provided more detailed results in less time than the FVM implemented in ANSYS Fluent software package, which used unstructured mesh for the computations. Furthermore, differences in the velocity distribution behind the distributor were observed between used numerical methods. The obtained results show the applicability of the LBM to these problems.

The last Chapter 8 is inspired by the collaboration with the Institute for Clinical and Experimental Medicine in Prague. It dealt with the numerical simulations of non-Newtonian fluids in geometries mimicking those of human vessels with stenosed valves. Numerical LBM model used three types of viscosity models, two Newtonian and one non-Newtonian. The results of all these models were compared with the experimental MRI measurement. Finally, two flow regimes, time-constant and periodically induced, were used. The results showed that the cheaper Newtonian model with constant kinematic viscosity can be used to obtain sufficiently accurate results. In addition, the numerical results showed imperfections in the MRI measurements, especially in regions of turbulent fluid flow. The results obtained are the first step toward accurate and efficient simulations of human arterial blood flow.

This work also involved the development of a computational code for numerical simulations using the LBM. It is implemented in C++ with the support of CUDA and MPI for parallel run on distributed nodes equipped with multiple GPUs. All simulations using the LBM used this in-house code.

Future work

Although we have accomplished many goals in this doctoral thesis, many unanswered questions remain for further research. For instance, the proposed boundary conditions need to be tested using turbulent fluid flow problems with more accurate approximations of the raw moments. Next, the implementation of the LBM with the grid-refinement technique will be optimized and tested using problems with more complex geometries. Consequently, the numerical pressure solution obtained by the LBM will be investigated. Finally, the LBM for the non-Newtonian fluid flow simulations will be further tested for possible future use in the clinical practice.

Appendices

Remarks from Probability and Statistics A

The lattice Boltzmann method is based on the kinetic theory, which uses a statistical description of the fluid. Thus, some terms from the probability theory are summarized in this chapter. In addition, some statistical methods, which are used to quantify the numerical results, are also included.

A.1 Continuous case

To describe the state of the phase space at time t, the probability density function $f_p\,[-]$ is used. It is a real positive function that can be used to calculate the probability $\mathcal{P}$ of finding a particle in the subset $\mathcal{A} \subset \mathbb{R}^3 \times \mathbb{R}^3$ of the phase space at time t as [94]

$$\mathcal{P}\left[\mathcal{A}\right] = \int_{\mathcal{A}} f_p\left(\boldsymbol{x}, \boldsymbol{\xi}, t\right) \mathrm{d}\boldsymbol{x}\mathrm{d}\boldsymbol{\xi}. \tag{A.1}$$

Since $f_p\left(\boldsymbol{x}, \boldsymbol{\xi}, t\right) \geq 0$ and $\mathcal{P} \leq 1$, the PDF satisfies $f_p \in [0,1]$.

Raw moment

Using the probability density function, the raw moment at point $(\boldsymbol{x}, t)$ of order $|\boldsymbol{\alpha}|$ can be defined by [86]

$$m_{\boldsymbol{\alpha}}\left(\boldsymbol{x}, t\right) = \int_{\mathbb{R}^3} \xi_1^{\alpha_1} \xi_2^{\alpha_2} \xi_3^{\alpha_3} f_p\left(\boldsymbol{x}, \boldsymbol{\xi}, t\right) \mathrm{d}\boldsymbol{\xi}, \tag{A.2}$$

where $\boldsymbol{\alpha} = (\alpha_1, \alpha_2, \alpha_3) \subset \mathbb{N}_0^3$ is the multi-index and $|\boldsymbol{\alpha}| = \alpha_1 + \alpha_2 + \alpha_3$.

The raw moments can be defined using the raw moment generating function that is defined by

$$M\left(\boldsymbol{\Xi}, \boldsymbol{x}, t\right) = \int_{\mathbb{R}^3} \exp\left(\boldsymbol{\Xi} \cdot \boldsymbol{\xi}\right) f_p\left(\boldsymbol{x}, \boldsymbol{\xi}, t\right) \mathrm{d}\boldsymbol{\xi}. \tag{A.3}$$

Then, the raw moment of order $|\boldsymbol{\alpha}|$ is calculated as

$$m_{\boldsymbol{\alpha}}\left(\boldsymbol{x}, t\right) = \left. \frac{\partial^{|\boldsymbol{\alpha}|}}{\partial \Xi_1^{\alpha_1} \partial \Xi_2^{\alpha_2} \partial \Xi_3^{\alpha_3}} M\left(\boldsymbol{\Xi}, \boldsymbol{x}, t\right) \right|_{\boldsymbol{\Xi}=\boldsymbol{0}}, \tag{A.4}$$

i.e., the raw moments are coefficients of the Taylor expansion at the point $\boldsymbol{\Xi} = \boldsymbol{0}$ of the moment generating function M.

Central moment

Another statistical moment is the central moment that expresses the deviation of the observed quantity from its mean value. Central moments are raw moments of the observed quantity shifted by the first moment, i.e., by the mean values. Thus, the central moment at point $(\boldsymbol{x}, t)$ of order $|\boldsymbol{\alpha}|$ can be defined by [86]

$$\kappa_{\boldsymbol{\alpha}}(\boldsymbol{x}, t) = \int_{\mathbb{R}^3} \left(\xi_1 - m_{(1,0,0)} \right)^{\alpha_1} \left(\xi_2 - m_{(0,1,0)} \right)^{\alpha_2} \left(\xi_3 - m_{(0,0,1)} \right)^{\alpha_3} f_p(\boldsymbol{x}, \boldsymbol{\xi}, t) \, \mathrm{d}\boldsymbol{\xi}. \tag{A.5}$$

Similarly, the central moment generating function can be defined by

$$\widetilde{M}(\boldsymbol{\Xi}, \boldsymbol{x}, t) = \int_{\mathbb{R}^3} \exp\left(\left(\boldsymbol{\xi} - \left(m_{(1,0,0)}, m_{(0,1,0)}, m_{(0,0,1)} \right)^T \right) \cdot \boldsymbol{\Xi} \right) f_p(\boldsymbol{x}, \boldsymbol{\xi}, t) \, \mathrm{d}\boldsymbol{\xi}. \tag{A.6}$$

The central moments can be calculated as

$$m_{\boldsymbol{\alpha}}(\boldsymbol{x}, t) = \frac{\partial^{|\boldsymbol{\alpha}|}}{\partial \Xi_1^{\alpha_1} \partial \Xi_2^{\alpha_2} \partial \Xi_3^{\alpha_3}} \widetilde{M}(\boldsymbol{\Xi}, \boldsymbol{x}, t) \bigg|_{\boldsymbol{\Xi}=\boldsymbol{0}}. \tag{A.7}$$

Cumulant

The alternative quantity to the moments is cumulant. Contrary to the moments, the cumulant cannot be defined using the mean value, but the cumulant generating function needs to be used. It is defined by [174]

$$K(\boldsymbol{\Xi}, \boldsymbol{x}, t) = \ln\left(M(\boldsymbol{\Xi}, \boldsymbol{x}, t) \right). \tag{A.8}$$

The cumulant at point $(\boldsymbol{x}, t)$ of order $|\boldsymbol{\alpha}|$ is defined by

$$c_{\boldsymbol{\alpha}} = \frac{\partial^{|\boldsymbol{\alpha}|}}{\partial \Xi_1^{\alpha_1} \partial \Xi_2^{\alpha_2} \partial \Xi_3^{\alpha_3}} K(\boldsymbol{\Xi}, \boldsymbol{x}, t) \bigg|_{\boldsymbol{\Xi}=\boldsymbol{0}}. \tag{A.9}$$

The zeroth-order cumulant is the logarithm of the mean value. The first- and second-order cumulants are proportional to the first- and second-order central moments, respectively. But the higher-order cumulants are not identical to the central moments. The advantage of cumulant is the logarithm. For the equilibrium density function, the generating function is polynomial. Thus, only few cumulants are non-zero contrary to the central moments.

A.2 Discrete case

To quantify the measured or simulated data, some statistical metrics described in this section are used.
Let $\boldsymbol{X} = (X_1, X_2, \cdots, X_n)$ and $\boldsymbol{Y} = (Y_1, Y_2, \cdots, Y_n)$ be two sets of simulated and experimental data, respectively. Then the following metrics and analysis techniques can be introduced.

Mean value

The mean value of data $\boldsymbol{X}$ is defined by [94]

$$\langle X \rangle = \frac{1}{n} \sum_{i=1}^{n} X_i \tag{A.10}$$

and represents the average value of the data set $\boldsymbol{X}$. The mean value is also called the *expected value* in statistics.

Standard deviation

The standard deviation of data $\boldsymbol{X}$ is defined by [174]

$$\sigma_X = \sqrt{\frac{1}{n-1}\sum_{i=1}^{n}(X_i - \langle X \rangle)^2} \tag{A.11}$$

and represents the degree of deviation of the data from the mean $\langle X \rangle$.

Mean absolute deviation

The mean absolute deviation of data $\boldsymbol{X}$ is defined by [94]

$$\varsigma_X = \frac{1}{n}\sum_{i=1}^{n}|X_i - \langle X \rangle|. \tag{A.12}$$

Correlation

The correlation expresses the measure of the linear relation between two data sets $\boldsymbol{X}$ and $\boldsymbol{Y}$. The most familiar measure of the data dependence is the Pearson linear correlation coefficient ϱ defined by [18]

$$\varrho_{X,Y} = \frac{\sum_{i=1}^{n}(X_i - \langle X \rangle)(Y_i - \langle Y \rangle)}{\sqrt{\sum_{i=1}^{n}(X_i - \langle X \rangle)^2 \sum_{i=1}^{n}(Y_i - \langle Y \rangle)^2}}. \tag{A.13}$$

It is clear that $|\varrho_{X,Y}| \le 1$. If $|\varrho_{X,Y}| \approx 1$, then the data are correlated, that is, dependent. On the other hand, if $|\varrho_{X,Y}| \approx 0$, then the data are independent.

Fractional bias

Fractional bias is a metric for the comparison of experimental $\boldsymbol{Y}$ and simulated $\boldsymbol{X}$ data defined by [195]

$$\mathbf{FB} = 2\frac{\langle Y \rangle - \langle X \rangle}{\langle Y \rangle + \langle X \rangle}. \tag{A.14}$$

The values of $\mathbf{FB}$ are in $(-2, 2)$ and the optimal value is 0.

Normalized mean square error

The normalized mean square error $\mathbf{NMSE}$ is defined by [149]

$$\mathbf{NMSE} = \frac{\left\langle (Y - X)^2 \right\rangle}{\langle Y \rangle \langle X \rangle}. \tag{A.15}$$

This statistic emphasizes the scatter in the entire data set and the optimal value is 0.

Relative L1 error

The relative error **L1** of the simulated data $\boldsymbol{X}$ with reference(experimental) data $\boldsymbol{Y}$ is defined by [16]

$$\mathbf{L1} = \frac{\sum\limits_{i=1}^{n} |Y_i - X_i|}{\sum\limits_{i=1}^{n} |Y_i|}.$$

The optimal value is 0.

Relative L2 error

The relative error **L2** of the simulated data $\boldsymbol{X}$ with reference (experimental) data $\boldsymbol{Y}$ is defined by [16]

$$\mathbf{L2} = \frac{\sqrt{\sum\limits_{i=1}^{n} (Y_i - X_i)^2}}{\sqrt{\sum\limits_{i=1}^{n} Y_i^2}}.$$

The optimal value is 0.

Factor 2 metric

This metric **FAC2** [45] represents the fraction of predictions within a factor of two of observations, that is,

$$\mathbf{FAC2} = \frac{1}{n} \sum_{i=1}^{n} q_i \text{ with } q_i = \begin{cases} 1 \text{ for } \frac{1}{2} \leq \frac{X_i}{Y_i} \leq 2 \\ 0 \text{ else.} \end{cases} \tag{A.16}$$

Hit rate metric

To validate the predicted mean velocity field, a hit rate metric **q**, defined by [179]

$$\mathbf{q} = \frac{1}{n} \sum_{i=1}^{n} q_i \text{ with } q_i = \begin{cases} 1 \text{ for } \left| \frac{X_i - Y_i}{Y_i} \right| \leq \sigma_Y \text{ or } |X_i - Y_i| \leq \varsigma_Y, \\ 0 \text{ else,} \end{cases} \tag{A.17}$$

is used, where $\boldsymbol{X}$ and $\boldsymbol{Y}$ represent simulated and experimental data, respectively.

Bland-Altman analysis

Another statistic used to assess the obtained data is the Bland-Altman analysis. It works with the difference $\boldsymbol{Z}_{\text{diff}} = \boldsymbol{X} - \boldsymbol{Y}$ and with the average $\boldsymbol{Z}_{\text{avg}} = \frac{1}{2}(\boldsymbol{X} + \boldsymbol{Y})$. The output of the Bland-Altman analysis is the scatter plot of $\boldsymbol{Z}_{\text{diff}}$ depending on $\boldsymbol{Z}_{\text{avg}}$ with mean difference $\langle Z_{\text{diff}} \rangle$ and limits of agreement computed according to [15].

The average $\boldsymbol{Z}_{\text{avg}}$ represents the best estimate of the true velocity value. Therefore, the differences $\boldsymbol{Z}_{\text{diff}}$ are assessed across the range of incident velocity values. Ideally, the plotted data are scattered in the neighborhood of zero velocity difference across the whole velocity range. The spread around zero is expressed by the standard deviation $\sigma_{Z_{\text{diff}}}$ of the set of differences $\boldsymbol{Z}_{\text{diff}}$ estimated by the student's t_s-test with the level of significance equal to 0.05 [94].

The inconsistency between the simulated and experimental data is demonstrated by the mean difference $\langle \boldsymbol{Z} \rangle_{\mathrm{diff}}$. The limits of agreement

$$\left(\langle \boldsymbol{Z} \rangle_{\mathrm{diff}} - t\left(1 - \frac{0.05}{2}, n - 1\right) \sigma_{Z_{\mathrm{diff}}}, \ \langle \boldsymbol{Z} \rangle_{\mathrm{diff}} + t\left(1 - \frac{0.05}{2}, n - 1\right) \sigma_{Z_{\mathrm{diff}}} \right)$$

bound 95 % of the data.

Ordering of DDFs B

To accurately define the transformation matrix of the collision operators, the ordering of the set $\mathcal{Q}$ is introduced. The ordering is defined by the function $\Psi : \{1, 2, \cdots, 27\} \rightarrow \mathcal{Q}$ as

$$\Psi(1) = (0, 0, 0),$$
$$\Psi(2) = (1, 0, 0),$$
$$\Psi(3) = (0, 1, 0),$$
$$\Psi(4) = (0, 0, 1),$$
$$\Psi(5) = (-1, 0, 0),$$
$$\Psi(6) = (0, -1, 0),$$
$$\Psi(7) = (0, 0, -1),$$
$$\Psi(8) = (0, 1, 1),$$
$$\Psi(9) = (0, 1, -1),$$
$$\Psi(10) = (0, -1, 1),$$
$$\Psi(11) = (0, -1, -1),$$
$$\Psi(12) = (1, 1, 0),$$
$$\Psi(13) = (1, -1, 0),$$
$$\Psi(14) = (-1, 1, 0),$$
$$\Psi(15) = (-1, -1, 0),$$
$$\Psi(16) = (1, 0, 1),$$
$$\Psi(17) = (1, 0, -1),$$
$$\Psi(18) = (-1, 0, 1),$$
$$\Psi(19) = (-1, 0, -1),$$
$$\Psi(20) = (1, 1, 1),$$
$$\Psi(21) = (1, 1, -1),$$
$$\Psi(22) = (1, -1, 1),$$
$$\Psi(23) = (1, -1, -1),$$
$$\Psi(24) = (-1, 1, 1),$$
$$\Psi(25) = (-1, 1, -1),$$
$$\Psi(26) = (-1, -1, 1),$$
$$\Psi(27) = (-1, -1, -1).$$

Coefficients for Second Order Interpolation of Velocity

<div style="text-align: right;">

C

</div>

Based on the interpolation defined in Eq. (3.60), the interpolation coefficients $a_{\{\cdot\}}, b_{\{\cdot\}}, c_{\{\cdot\}}$ need to be expressed using the velocity in the vertices of the unit cube and spatial second-order derivatives of the velocity in the center of the unit cube. For better readability, the second-order derivatives are labeled by

$$A_{12} = \frac{\partial}{\partial x_1}\left(\frac{\partial}{\partial x_1}u_2 + \frac{\partial}{\partial x_2}u_1\right), \tag{C.1a}$$

$$A_{13} = \frac{\partial}{\partial x_1}\left(\frac{\partial}{\partial x_1}u_3 + \frac{\partial}{\partial x_3}u_1\right), \tag{C.1b}$$

$$A_{11} = \frac{\partial^2}{\partial x_1^2}(u_1), \tag{C.1c}$$

$$B_{12} = \frac{\partial}{\partial x_2}\left(\frac{\partial}{\partial x_2}u_1 + \frac{\partial}{\partial x_1}u_2\right), \tag{C.1d}$$

$$B_{23} = \frac{\partial}{\partial x_2}\left(\frac{\partial}{\partial x_2}u_3 + \frac{\partial}{\partial x_3}u_2\right), \tag{C.1e}$$

$$B_{22} = \frac{\partial^2}{\partial x_2^2}(u_2), \tag{C.1f}$$

$$C_{13} = \frac{\partial}{\partial x_3}\left(\frac{\partial}{\partial x_3}u_1 + \frac{\partial}{\partial x_1}u_3\right), \tag{C.1g}$$

$$C_{23} = \frac{\partial}{\partial x_3}\left(\frac{\partial}{\partial x_3}u_2 + \frac{\partial}{\partial x_2}u_3\right), \tag{C.1h}$$

$$C_{33} = \frac{\partial^2}{\partial x_3^2}(u_3). \tag{C.1i}$$

Next, the vertices of the unit cube are labeled as

$$\boldsymbol{x}_1 = \left(-\frac{1}{2}, -\frac{1}{2}, -\frac{1}{2}\right)^T, \qquad\qquad \boldsymbol{x}_2 = \left(\frac{1}{2}, -\frac{1}{2}, -\frac{1}{2}\right)^T,$$

$$\boldsymbol{x}_3 = \left(\frac{1}{2}, -\frac{1}{2}, \frac{1}{2}\right)^T, \qquad\qquad \boldsymbol{x}_4 = \left(-\frac{1}{2}, -\frac{1}{2}, \frac{1}{2}\right)^T,$$

$$\boldsymbol{x}_5 = \left(-\frac{1}{2}, \frac{1}{2}, -\frac{1}{2}\right)^T, \qquad\qquad \boldsymbol{x}_6 = \left(\frac{1}{2}, \frac{1}{2}, -\frac{1}{2}\right)^T,$$

$$\boldsymbol{x}_7 = \left(\frac{1}{2}, \frac{1}{2}, \frac{1}{2}\right)^T, \qquad\qquad \boldsymbol{x}_8 = \left(-\frac{1}{2}, \frac{1}{2}, \frac{1}{2}\right)^T. \tag{C.2}$$

Using notation defined in Eqs. (C.1i), (C.2), the unknown interpolation coefficients can be expressed as

$$
\begin{aligned}
a_0 =& \frac{1}{16}\left[2u_1(\boldsymbol{x}_5) + 2u_1(\boldsymbol{x}_4) + 2u_1(\boldsymbol{x}_7) + 2u_1(\boldsymbol{x}_1) - u_3(\boldsymbol{x}_8) - 2A_{11} + u_3(\boldsymbol{x}_5) + u_3(\boldsymbol{x}_7)\right.\\
&+ 2u_1(\boldsymbol{x}_6) - 2C_{13} - u_3(\boldsymbol{x}_4) + u_3(\boldsymbol{x}_1) + u_2(\boldsymbol{x}_7) - 2B_{12} - u_3(\boldsymbol{x}_6) + u_3(\boldsymbol{x}_3) - u_3(\boldsymbol{x}_2)\\
&+ 2u_1(\boldsymbol{x}_3) - u_2(\boldsymbol{x}_2) - u_2(\boldsymbol{x}_8) - u_2(\boldsymbol{x}_5) + u_2(\boldsymbol{x}_4) + u_2(\boldsymbol{x}_1) + u_2(\boldsymbol{x}_6) - u_2(\boldsymbol{x}_3)\\
&\left.+ 2u_1(\boldsymbol{x}_8) + 2u_1(\boldsymbol{x}_2)\right],
\end{aligned}\tag{C.3a}
$$

$$a_1 = \frac{1}{4}\left[-u_1(\boldsymbol{x}_5) - u_1(\boldsymbol{x}_4) + u_1(\boldsymbol{x}_7) - u_1(\boldsymbol{x}_1) + u_1(\boldsymbol{x}_6) + u_1(\boldsymbol{x}_3) - u_1(\boldsymbol{x}_8) + u_1(\boldsymbol{x}_2)\right], \tag{C.3b}$$

$$a_2 = \frac{1}{4}\left[u_1(\boldsymbol{x}_5) - u_1(\boldsymbol{x}_4) + u_1(\boldsymbol{x}_7) - u_1(\boldsymbol{x}_1) + u_1(\boldsymbol{x}_6) - u_1(\boldsymbol{x}_3) + u_1(\boldsymbol{x}_8) - u_1(\boldsymbol{x}_2)\right], \tag{C.3c}$$

$$a_3 = \frac{1}{4}\left[-u_1(\boldsymbol{x}_6) - u_1(\boldsymbol{x}_5) + u_1(\boldsymbol{x}_4) + u_1(\boldsymbol{x}_7) - u_1(\boldsymbol{x}_1) + u_1(\boldsymbol{x}_3) + u_1(\boldsymbol{x}_8) - u_1(\boldsymbol{x}_2)\right] \tag{C.3d}$$

$$a_{12} = \frac{1}{2}\left[-u_1(\boldsymbol{x}_5) + u_1(\boldsymbol{x}_4) + u_1(\boldsymbol{x}_7) + u_1(\boldsymbol{x}_1) + u_1(\boldsymbol{x}_6) - u_1(\boldsymbol{x}_3) - u_1(\boldsymbol{x}_8) - u_1(\boldsymbol{x}_2)\right], \tag{C.3e}$$

$$a_{13} = \frac{1}{2}\left[u_1(\boldsymbol{x}_5) - u_1(\boldsymbol{x}_4) + u_1(\boldsymbol{x}_7) + u_1(\boldsymbol{x}_1) - u_1(\boldsymbol{x}_6) + u_1(\boldsymbol{x}_3) - u_1(\boldsymbol{x}_8) - u_1(\boldsymbol{x}_2)\right], \tag{C.3f}$$

$$a_{23} = \frac{1}{2}\left[-u_1(\boldsymbol{x}_5) - u_1(\boldsymbol{x}_4) + u_1(\boldsymbol{x}_7) + u_1(\boldsymbol{x}_1) - u_1(\boldsymbol{x}_6) - u_1(\boldsymbol{x}_3) + u_1(\boldsymbol{x}_8) + u_1(\boldsymbol{x}_2)\right], \tag{C.3g}$$

$$a_{11} = \frac{1}{2}\left[A_{11}\right], \tag{C.3h}$$

$$
\begin{aligned}
a_{22} =& \frac{1}{4}\left[-u_2(\boldsymbol{x}_7) + 2B_{12} + u_2(\boldsymbol{x}_2) + u_2(\boldsymbol{x}_8) + u_2(\boldsymbol{x}_5) - u_2(\boldsymbol{x}_4) - u_2(\boldsymbol{x}_1) - u_2(\boldsymbol{x}_6)\right.\\
&\left.+ u_2(\boldsymbol{x}_3)\right],
\end{aligned}\tag{C.3i}
$$

$$
\begin{aligned}
a_{33} =& \frac{1}{4}\left[u_3(\boldsymbol{x}_8) - u_3(\boldsymbol{x}_5) - u_3(\boldsymbol{x}_7) + 2C_{13} + u_3(\boldsymbol{x}_4) - u_3(\boldsymbol{x}_1) + u_3(\boldsymbol{x}_6) - u_3(\boldsymbol{x}_3)\right.\\
&\left.+ u_3(\boldsymbol{x}_2)\right],
\end{aligned}\tag{C.3j}
$$

$$a_{123} = \left[u_1(\boldsymbol{x}_5) + u_1(\boldsymbol{x}_4) + u_1(\boldsymbol{x}_7) - u_1(\boldsymbol{x}_1) - u_1(\boldsymbol{x}_6) - u_1(\boldsymbol{x}_3) - u_1(\boldsymbol{x}_8) + u_1(\boldsymbol{x}_2)\right]. \tag{C.3k}$$

$$b_0 = \frac{1}{16} \left[-u_1(\boldsymbol{x}_5) + u_1(\boldsymbol{x}_4) + u_1(\boldsymbol{x}_7) + u_1(\boldsymbol{x}_1) - 2B_{33} + u_3(\boldsymbol{x}_8) - u_3(\boldsymbol{x}_5) + u_3(\boldsymbol{x}_7) \right.$$
$$- 2C_{23} + u_1(\boldsymbol{x}_6) - u_3(\boldsymbol{x}_4) + u_3(\boldsymbol{x}_1) + 2u_2(\boldsymbol{x}_7) - u_3(\boldsymbol{x}_6) - u_3(\boldsymbol{x}_3) + u_3(\boldsymbol{x}_2)$$
$$- 2A_{12} - u_1(\boldsymbol{x}_3) + 2u_2(\boldsymbol{x}_2) + 2u_2(\boldsymbol{x}_8) + 2u_2(\boldsymbol{x}_5) + 2u_2(\boldsymbol{x}_4) + 2u_2(\boldsymbol{x}_1)$$
$$\left. + 2u_2(\boldsymbol{x}_6) + 2u_2(\boldsymbol{x}_3) - u_1(\boldsymbol{x}_8) - u_1(\boldsymbol{x}_2) \right], \tag{C.4a}$$

$$b_1 = \frac{1}{4} \left[-u_2(\boldsymbol{x}_5) + u_2(\boldsymbol{x}_6) + u_2(\boldsymbol{x}_7) - u_2(\boldsymbol{x}_8) - u_2(\boldsymbol{x}_4) + u_2(\boldsymbol{x}_3) + u_2(\boldsymbol{x}_2) - u_2(\boldsymbol{x}_1) \right], \tag{C.4b}$$

$$b_2 = \frac{1}{4} \left[-u_2(\boldsymbol{x}_4) + u_2(\boldsymbol{x}_5) + u_2(\boldsymbol{x}_6) + u_2(\boldsymbol{x}_7) + u_2(\boldsymbol{x}_8) - u_2(\boldsymbol{x}_3) - u_2(\boldsymbol{x}_2) - u_2(\boldsymbol{x}_1) \right], \tag{C.4c}$$

$$b_3 = \frac{1}{4} \left[u_2(\boldsymbol{x}_4) - u_2(\boldsymbol{x}_5) - u_2(\boldsymbol{x}_6) + u_2(\boldsymbol{x}_7) + u_2(\boldsymbol{x}_8) + u_2(\boldsymbol{x}_3) - u_2(\boldsymbol{x}_2) - u_2(\boldsymbol{x}_1) \right] \tag{C.4d}$$

$$b_{12} = \frac{1}{2} \left[u_2(\boldsymbol{x}_7) - u_2(\boldsymbol{x}_2) - u_2(\boldsymbol{x}_8) - u_2(\boldsymbol{x}_5) + u_2(\boldsymbol{x}_4) + u_2(\boldsymbol{x}_1) + u_2(\boldsymbol{x}_6) - u_2(\boldsymbol{x}_3) \right], \tag{C.4e}$$

$$b_{13} = \frac{1}{2} \left[u_2(\boldsymbol{x}_7) - u_2(\boldsymbol{x}_2) - u_2(\boldsymbol{x}_8) + u_2(\boldsymbol{x}_5) - u_2(\boldsymbol{x}_4) + u_2(\boldsymbol{x}_1) - u_2(\boldsymbol{x}_6) + u_2(\boldsymbol{x}_3) \right], \tag{C.4f}$$

$$b_{23} = \frac{1}{2} \left[-u_2(\boldsymbol{x}_5) - u_2(\boldsymbol{x}_6) + u_2(\boldsymbol{x}_7) + u_2(\boldsymbol{x}_8) - u_2(\boldsymbol{x}_4) - u_2(\boldsymbol{x}_3) + u_2(\boldsymbol{x}_2) + u_2(\boldsymbol{x}_1) \right], \tag{C.4g}$$

$$b_{11} = \frac{1}{4} \left[u_1(\boldsymbol{x}_5) - u_1(\boldsymbol{x}_4) - u_1(\boldsymbol{x}_7) - u_1(\boldsymbol{x}_1) - u_1(\boldsymbol{x}_6) + 2A_{12} + u_1(\boldsymbol{x}_3) + u_1(\boldsymbol{x}_8) \right.$$
$$\left. + u_1(\boldsymbol{x}_2) \right], \tag{C.4h}$$

$$b_{22} = \frac{1}{2} \left[B_{33} \right], \tag{C.4i}$$

$$b_{33} = \frac{1}{4} \left[u_3(\boldsymbol{x}_5) + u_3(\boldsymbol{x}_3) + u_3(\boldsymbol{x}_4) + u_3(\boldsymbol{x}_6) - u_3(\boldsymbol{x}_8) - u_3(\boldsymbol{x}_7) - u_3(\boldsymbol{x}_1) - u_3(\boldsymbol{x}_2) \right.$$
$$\left. + 2C_{23} \right], \tag{C.4j}$$

$$b_{123} = \left[u_2(\boldsymbol{x}_7) + u_2(\boldsymbol{x}_2) - u_2(\boldsymbol{x}_8) + u_2(\boldsymbol{x}_5) + u_2(\boldsymbol{x}_4) - u_2(\boldsymbol{x}_1) - u_2(\boldsymbol{x}_6) - u_2(\boldsymbol{x}_3) \right]. \tag{C.4k}$$

$$c_0 = \frac{1}{16} \left[u_1(\boldsymbol{x}_5) - u_1(\boldsymbol{x}_4) - 2C_{33} + u_1(\boldsymbol{x}_7) + u_1(\boldsymbol{x}_1) + 2u_3(\boldsymbol{x}_8) + 2u_3(\boldsymbol{x}_5) + 2u_3(\boldsymbol{x}_7) \right.$$
$$- 2B_{23} - u_1(\boldsymbol{x}_6) + 2u_3(\boldsymbol{x}_4) + 2u_3(\boldsymbol{x}_1) + u_2(\boldsymbol{x}_7) - 2A_{13} + 2u_3(\boldsymbol{x}_6) + 2u_3(\boldsymbol{x}_3)$$
$$+ 2u_3(\boldsymbol{x}_2) + u_1(\boldsymbol{x}_3) + u_2(\boldsymbol{x}_2) + u_2(\boldsymbol{x}_8) - u_2(\boldsymbol{x}_5) - u_2(\boldsymbol{x}_4) + u_2(\boldsymbol{x}_1) - u_2(\boldsymbol{x}_6)$$
$$\left. - u_2(\boldsymbol{x}_3) - u_1(\boldsymbol{x}_8) - u_1(\boldsymbol{x}_2) \right], \tag{C.5a}$$

$$c_1 = \frac{1}{4} \left[-u_3(\boldsymbol{x}_5) + u_3(\boldsymbol{x}_3) - u_3(\boldsymbol{x}_4) + u_3(\boldsymbol{x}_6) - u_3(\boldsymbol{x}_8) + u_3(\boldsymbol{x}_7) - u_3(\boldsymbol{x}_1) + u_3(\boldsymbol{x}_2) \right], \tag{C.5b}$$

$$c_2 = \frac{1}{4} \left[u_3(\boldsymbol{x}_5) - u_3(\boldsymbol{x}_3) - u_3(\boldsymbol{x}_4) + u_3(\boldsymbol{x}_6) + u_3(\boldsymbol{x}_8) + u_3(\boldsymbol{x}_7) - u_3(\boldsymbol{x}_1) - u_3(\boldsymbol{x}_2) \right], \tag{C.5c}$$

$$c_3 = \frac{1}{4} \left[-u_3(\boldsymbol{x}_5) + u_3(\boldsymbol{x}_3) + u_3(\boldsymbol{x}_4) - u_3(\boldsymbol{x}_6) + u_3(\boldsymbol{x}_8) + u_3(\boldsymbol{x}_7) - u_3(\boldsymbol{x}_1) - u_3(\boldsymbol{x}_2) \right] \tag{C.5d}$$

$$c_{12} = \frac{1}{2} \left[-u_3(\boldsymbol{x}_8) - u_3(\boldsymbol{x}_5) + u_3(\boldsymbol{x}_7) + u_3(\boldsymbol{x}_4) + u_3(\boldsymbol{x}_1) + u_3(\boldsymbol{x}_6) - u_3(\boldsymbol{x}_3) - u_3(\boldsymbol{x}_2) \right], \tag{C.5e}$$

$$c_{13} = \frac{1}{2} \left[-u_3(\boldsymbol{x}_8) + u_3(\boldsymbol{x}_5) + u_3(\boldsymbol{x}_7) - u_3(\boldsymbol{x}_4) + u_3(\boldsymbol{x}_1) - u_3(\boldsymbol{x}_6) + u_3(\boldsymbol{x}_3) - u_3(\boldsymbol{x}_2) \right], \tag{C.5f}$$

$$c_{23} = \frac{1}{2} \left[-u_3(\boldsymbol{x}_5) - u_3(\boldsymbol{x}_3) - u_3(\boldsymbol{x}_4) - u_3(\boldsymbol{x}_6) + u_3(\boldsymbol{x}_8) + u_3(\boldsymbol{x}_7) + u_3(\boldsymbol{x}_1) + u_3(\boldsymbol{x}_2) \right], \tag{C.5g}$$

$$c_{11} = \frac{1}{4} \left[-u_1(\boldsymbol{x}_5) + u_1(\boldsymbol{x}_4) - u_1(\boldsymbol{x}_7) - u_1(\boldsymbol{x}_1) + u_1(\boldsymbol{x}_6) + 2A_{13} - u_1(\boldsymbol{x}_3) + u_1(\boldsymbol{x}_8) \right.$$
$$\left. + u_1(\boldsymbol{x}_2) \right], \tag{C.5h}$$

$$c_{22} = \frac{1}{4} \left[u_2(\boldsymbol{x}_5) + 2B_{23} + u_2(\boldsymbol{x}_6) - u_2(\boldsymbol{x}_7) - u_2(\boldsymbol{x}_8) + u_2(\boldsymbol{x}_4) + u_2(\boldsymbol{x}_3) - u_2(\boldsymbol{x}_2) \right.$$
$$\left. - u_2(\boldsymbol{x}_1) \right], \tag{C.5i}$$

$$c_{33} = \frac{1}{2} \left[C_{33} \right], \tag{C.5j}$$

$$c_{123} = \left[-u_3(\boldsymbol{x}_8) + u_3(\boldsymbol{x}_5) + u_3(\boldsymbol{x}_7) + u_3(\boldsymbol{x}_4) - u_3(\boldsymbol{x}_1) - u_3(\boldsymbol{x}_6) - u_3(\boldsymbol{x}_3) + u_3(\boldsymbol{x}_2) \right]. \tag{C.5k}$$

Bibliography

[1] Al-Abadi, A, Kim, Y., Ertunç, Ö., and Delgado, A. "Turbulence impact on wind turbines: experimental investigations on a wind turbine model". In: *Journal of Physics: Conference Series*. Vol. 753. 3. IOP Publishing. 2016, p. 032046. DOI: 10.1088/1742-6596/753/3/032046.

[2] Ansumali, S. and Karlin, I. V. "Kinetic boundary conditions in the lattice Boltzmann method". In: *Physical Review E* 66.2 (2002), p. 026311. DOI: 10.1103/PhysRevE.66.026311.

[3] *ANSYS software package*. https://www.ansys.com. Accessed: 2022-11-09.

[4] Ayachit, U. *The paraview guide. A Parallel Visualization Application*. Kitware, Incorporated, 2015. ISBN: 978-1930934306.

[5] Basu, P. *Combustion and Gasification in Fluidized Beds*. CRC Press, 2006. ISBN: 0849333962. DOI: 10.1201/9781420005158.

[6] Batchelor, G. K. *An introduction to fluid dynamics*. Cambridge university press, 2000. ISBN: 9780511800955. DOI: 10.1017/CBO9780511800955.

[7] Bazarin, R. L. M., Philippi, P. C., Randles, A, and Hegele Jr, L. A. "Moments-based method for boundary conditions in the lattice Boltzmann framework: A comparative analysis for the lid driven cavity flow". In: *Computers & Fluids* 230 (2021), p. 105142. DOI: 10.1016/j.compfluid.2021.105142.

[8] Bellomo, N. and Arlotti, L. *Lecture notes on the mathematical theory of the Boltzmann equation*. Vol. 33. World scientific, 1995. ISBN: 9810221665. DOI: 10.1142/2658.

[9] Beneš, M., Eichler, P., Fučík, R., Hrdlička, J., Klinkovský, J., Kolář, M., Smejkal, T., Skopec, P., Solovský, J., Strachota, P., Straka, R., and Žák, A. "Experimental and numerical investigation of air flow through the distributor plate in a laboratory-scale model of a bubbling fluidized bed boiler". In: *Japan Journal of Industrial and Applied Mathematics* 39 (2022), pp. 1–16. DOI: 10.1007/s13160-022-00518-x.

[10] Beneš, M., Eichler, P., Klinkovský, J., Kolář, M., Solovský, J., Strachota, P., and Žák, A. "Numerical simulation of fluidization for application in oxyfuel combustion". In: *Discrete & Continuous Dynamical Systems-S* 14.3 (2021), p. 769. DOI: 10.3934/dcdss.2020232.

[11] Beneš, M., Eichler, P., Klinkovský, J., Kolář, M., Solovský, J., Strachota, P., and Žák, A. "Modeling and Simulation of Bed Dynamics in Oxyfuel Fluidized Bed Boilers". In: *Numerical Mathematics and Advanced Applications ENUMATH 2019*. Vol. 139. Lecture Notes in Computational Science and Engineering. Springer International Publishing, 2021, pp. 919–927. ISBN: 978-3-030-55873-4. DOI: 10.1007/978-3-030-55874-1_91.

[12] Beneš, M., Eichler, P., Klinkovský, J., Kolář, M., Solovský, J., Strachota, P., and Žák, A. "Numerical Simulation of Fluidization for Applications in Oxyfuel Combustion". In: *Discrete and Continuous Dynamical Systems - S* 14.3 (2021), pp. 769–783. DOI: `10.3934/dcdss.2020232`.

[13] Bertoglio, C., Moireau, P., and Gerbeau, J.-F. "Sequential parameter estimation for fluid–structure problems: Application to hemodynamics". In: *International Journal for Numerical Methods in Biomedical Engineering* 28.4 (2012), pp. 434–455. DOI: `10.1002/cnm.1476`.

[14] Bhamagar, P., Gross, E., and Krook, M. "A model for collision processes in gases". In: *Physical Review* 94.3 (1954), p. 511.

[15] Bland, J. M. and Altman, D. G. "Statistical methods for assessing agreement between two methods of clinical measurement". In: *The Lancet* 327.8476 (1986), pp. 307–310. DOI: `10.1016/S0140-6736(86)90837-8`.

[16] Blank, J., Řezáčová, K., Exner, P., and Havlíček, M. *Lineární operátory v kvantové fyzice.* 1st ed. Karolinum, 1993. ISBN: 80-7066-586-6.

[17] Böhmer, K. "Asymptotic Expansions for the Discretization Error In Poisson's Equation on General Domains". In: *Multivariate Approximation Theory: Proceedings of the Conference held at the Mathematical Research Institute at Oberwolfach Black Forest, February 4–10, 1979.* Birkhäuser Basel, 1979, pp. 30–45. ISBN: 978-3-0348-6289-9. DOI: `10.1007/978-3-0348-6289-9_2`.

[18] Bolstad, W. M. and Curran, J. M. *Introduction to Bayesian statistics.* 3rd ed. John Wiley & Sons, 2016. ISBN: 978-1-118-59322-6. DOI: `10.1002/9780470181188`.

[19] Born, M. and Wolf, E. *Principles of optics: electromagnetic theory of propagation, interference and diffraction of light.* 6th ed. Elsevier, 2013. ISBN: 0-08-026482-4.

[20] Boyd, J., Buick, J. M., and Green, S. "Analysis of the Casson and Carreau-Yasuda non-Newtonian blood models in steady and oscillatory flows using the lattice Boltzmann method". In: *Physics of Fluids* 19.9 (2007), p. 093103. DOI: `10.1063/1.2772250`.

[21] Brenner, S. C., Scott, L. R., and Scott, L. R. *The mathematical theory of finite element methods.* 3rd ed. Springer New York, NY, 2008. ISBN: 978-1-4419-2611-1. DOI: `10.1007/978-0-387-75934-0`.

[22] Brookshier, K. A. and Tarbell, J. "Evaluation of Transparent Blood Analogue Fluids—Aqueous Xanthan Gum Glycerin". In: *Biorheology* 30 (Mar. 1993), pp. 107–16. DOI: `10.3233/BIR-1993-30202`.

[23] Campo-Deaño, L., Dullens, R., Aarts, D., Pinho, F., and Oliveira, M. "Viscoelasticity of blood and viscoelastic blood analogues for use in polydymethylsiloxane in vitro models of the circulatory system". In: *Biomicrofluidics* 7 (May 2013), p. 034102. DOI: `10.1063/1.4804649`.

[24] Canuto, C., Hussaini, M. Y., Quarteroni, A., Thomas Jr, A, et al. *Spectral methods in fluid dynamics.* 1st ed. Springer Berlin, Heidelberg, 2012. ISBN: 978-3-540-52205-8. DOI: `10.1007/978-3-642-84108-8`.

[25] Chabiniok, R., Hron, J., Jarolímová, A., Málek, J., Rajagopal, K. R., Rajagopal, K., Švihlová, H., and Tůma, K. "Three-dimensional flows of incompressible Navier-Stokes fluids in tubes containing a sinus, with varying slip conditions at the wall". In: *International Journal of Engineering Science* 180 (2022), p. 103749. DOI: `10.1016/j.ijengsci.2022.103749`.

[26]   Chabiniok, R., Škardová, K., Galabov, R., Eichler, P., Gusseva, M., Janoušek, J., Fučík, R., Tintěra, J., Oberhuber, T., and Hussain, T. "Translational Cardiovascular Modeling: Tetralogy of Fallot and Modeling of Diseases". In: *Modeling Biomaterials*. Springer, 2021, pp. 241–276. DOI: `https://doi.org/10.1007/978-3-030-88084-2_6`.

[27]   Chai, Z.-H. and Zhao, T.-S. "A pseudopotential-based multiple-relaxation-time lattice Boltzmann model for multicomponent/multiphase flows". In: *Acta Mechanica Sinica* 28.4 (2012), pp. 983–992. DOI: `10.1007/s10409-012-0123-6`.

[28]   Chai, Z. and Shi, B. "A novel lattice Boltzmann model for the Poisson equation". In: *Applied mathematical modelling* 32.10 (2008), pp. 2050–2058. DOI: `10.1016/j.apm.2007.06.033`.

[29]   Chapman, S. and Cowling, T. G. "The Mathematical Theory of Non-Uniform gases". In: (1952).

[30]   Chen, H., Filippova, O., Hoch, J., Molvig, K., Shock, R., Teixeira, C., and Zhang, R. "Grid refinement in lattice Boltzmann methods based on volumetric formulation". In: *Physica A: Statistical Mechanics and its Applications* 362.1 (2006), pp. 158–167. DOI: `10.1016/j.physa.2005.09.036`.

[31]   Chen, S. and Doolen, G. D. "Lattice Boltzmann method for fluid flows". In: *Annual Review of Fluid Mechanics* 30.1 (1998), pp. 329–364. DOI: `10.1146/annurev.fluid.30.1.329`.

[32]   Chen, S., Martinez, D., and Mei, R. "On boundary conditions in lattice Boltzmann methods". In: *Physics of fluids* 8.9 (1996), pp. 2527–2536. DOI: `10.1063/1.869035`.

[33]   Chikatamarla, S. S. and Karlin, I. V. "Entropic lattice Boltzmann method for turbulent flow simulations: Boundary conditions". In: *Physica A: Statistical Mechanics and its Applications* 392.9 (2013), pp. 1925–1930. DOI: `10.1016/j.physa.2012.12.034`.

[34]   Coceal, O, Thomas, T., Castro, I., and Belcher, S. "Mean flow and turbulence statistics over groups of urban-like cubical obstacles". In: *Boundary-Layer Meteorology* 121.3 (2006), pp. 491–519. DOI: `10.1007/s10546-006-9076-2`.

[35]   Coreixas, C., Chopard, B., and Latt, J. "Comprehensive comparison of collision models in the lattice Boltzmann framework: Theoretical investigations". In: *Physical Review E* 100.3 (2019), p. 033305. DOI: `10.1103/PhysRevE.100.033305`.

[36]   Corless, R. M. and Nicolas, F. *A Graduate Introduction to Numerical Methods: From the Viewpoint of Backward Error Analysis*. 1st ed. Springer New York, NY, 2013. ISBN: 978-1-4614-8452-3. DOI: `10.1007/978-1-4614-8453-0`.

[37]   Csébfalvi, B. "Beyond Trilinear Interpolation: Higher Quality for Free". In: *ACM Transactions on Graphics (TOG)* 38.4 (2019). DOI: `10.1145/3306346.3323032`.

[38]   De Rosis, A. "A central moments-based lattice Boltzmann scheme for shallow water equations". In: *Computer Methods in Applied Mechanics and Engineering* 319 (2017), pp. 379–392. DOI: `10.1016/j.cma.2017.03.001`.

[39]   De Rosis, A. and Enan, E. "A three-dimensional phase-field lattice Boltzmann method for incompressible two-components flows". In: *Physics of Fluids* 33.4 (2021), p. 043315. DOI: `doi.org/10.1063/5.0046875`.

[40]   Dey, S. and Ali, S. Z. "Advances in modeling of bed particle entrainment sheared by turbulent flow". In: *Physics of Fluids* 30.6 (2018), p. 061301. DOI: `10.1063/1.5030458`.

[41]   d'Humières, D. "Generalized lattice-Boltzmann equations". In: *Rarefied gas dynamics* (1992).

[42] d'Humières, D. "Multiple–relaxation–time lattice Boltzmann models in three dimensions". In: *Philosophical Transactions of the Royal Society of London. Series A: Mathematical, Physical and Engineering Sciences* 360.1792 (2002), pp. 437–451. DOI: `10.1098/rsta.2001.0955`.

[43] Dubois, F. "Equivalent partial differential equations of a lattice Boltzmann scheme". In: *Computers & Mathematics with Applications* 55.7 (2008), pp. 1441–1449. DOI: `10.1016/j.camwa.2007.08.003`.

[44] Dupuis, A. and Chopard, B. "Theory and applications of an alternative lattice Boltzmann grid refinement algorithm". In: *Physical Review E* 67.6 (2003), p. 066707. DOI: `10.1103/PhysRevE.67.066707`.

[45] Efthimiou, G. C., Andronopoulos, S, and Bartzis, J. G. "Prediction of dosage-based parameters from the puff dispersion of airborne materials in urban environments using the CFD-RANS methodology". In: *Meteorology and Atmospheric Physics* 130.1 (2018), pp. 107–124. DOI: `10.1007/s00703-017-0506-0`.

[46] Eichler, P. "Asymptotic analysis of cumulant lattice Boltzmann method". In: *Technical Report MMG 1-22* (2022).

[47] Eichler, P. "Mathematical modeling of elastic body interaction with incompressible fluid". Masters's thesis. FNSPE, CTU in Prague, 2018.

[48] Eichler, P. "Mathematical modelling of subsonic flow around obstacles using Lattice–Boltzmann method on GPU". Bachelor's degree project. FNSPE, CTU in Prague, 2016.

[49] Eichler, P., Fučík, R., and Straka, R. "Computational study of immersed boundary-lattice Boltzmann method for fluid-structure interaction". In: *Discrete & Continuous Dynamical Systems-S* 14.3 (2021), pp. 819–833. DOI: `10.3934/dcdss.2020349`.

[50] Eichler, P., Fuka, V., and Fučík, R. "Cumulant lattice Boltzmann simulations of turbulent flow above rough surfaces". In: *Computers & Mathematics with Applications* 92 (2021), pp. 37–47. DOI: `10.1016/j.camwa.2021.03.016`.

[51] Eichler, P., Fučík, R., and Strachota, P. "Investigation of mesoscopic boundary conditions for lattice Boltzmann method in laminar flow problems". In: *Under review in Computers & Mathematics with Applications* (2022).

[52] Eichler, P., Galabov, R., Fučík, R., Škardová, K., Oberhuber, T., Pauš, P., Tintěra, J., and Chabiniok, R. "Non-Newtonian turbulent flow through aortic phantom: Experimental and computational study using magnetic resonance imaging and lattice Boltzmann method". In: *Under review in Computers & Mathematics with Applications* (2022).

[53] Eitel-Amor, G., Meinke, M., and Schröder, W. "A lattice-Boltzmann method with hierarchically refined meshes". In: *Computers & Fluids* 75 (2013), pp. 127–139. DOI: `10.1016/j.compfluid.2013.01.013`.

[54] Fakhari, A., Geier, M., and Lee, T. "A mass-conserving lattice Boltzmann method with dynamic grid refinement for immiscible two-phase flows". In: *Journal of Computational Physics* 315 (2016), pp. 434–457. DOI: `10.1016/j.jcp.2016.03.058`.

[55] Fakhari, A. and Lee, T. "Finite-difference lattice Boltzmann method with a block-structured adaptive-mesh-refinement technique". In: *Physical Review E* 89.3 (2014), p. 033310. DOI: `10.1103/PhysRevE.89.033310`.

[56] Fakhari, A. and Rahimian, M. H. "Phase-field modeling by the method of lattice Boltzmann equations". In: *Physical Review E* 81 (3 2010), p. 036707. DOI: `10.1103/PhysRevE.81.036707`.

[57] Feichtinger, C., Donath, S., Köstler, H., Götz, J., and Rüde, U. "WaLBerla: HPC software design for computational engineering simulations". In: *Journal of Computational Science* 2.2 (2011), pp. 105–112. DOI: 10.1016/j.jocs.2011.01.004.

[58] Feiger, B., Vardhan, M., Gounley, J., Mortensen, M., Nair, P., Chaudhury, R., Frakes, D., and Randles, A. "Suitability of lattice Boltzmann inlet and outlet boundary conditions for simulating flow in image-derived vasculature". In: *International journal for numerical methods in biomedical engineering* 35.6 (2019), e3198. DOI: 10.1002/cnm.3198.

[59] Feng, Y., Boivin, P., Jacob, J., and Sagaut, P. "Hybrid recursive regularized lattice Boltzmann simulation of humid air with application to meteorological flows". In: *Physical Review E* 100.2 (2019), p. 023304. DOI: 10.1103/PhysRevE.100.023304.

[60] Feng, Y., Guo, S, Jacob, J., and Sagaut, P. "Solid wall and open boundary conditions in hybrid recursive regularized lattice Boltzmann method for compressible flows". In: *Physics of Fluids* 31.12 (2019), p. 126103. DOI: 10.1063/1.5129138.

[61] Filippova, O. and Hänel, D. "Grid refinement for lattice-BGK models". In: *Journal of computational Physics* 147.1 (1998), pp. 219–228. DOI: 10.1006/jcph.1998.6089.

[62] Formaggia, L., Quarteroni, A., and Veneziani, A. *Cardiovascular Mathematics. Modeling and simulation of the circulatory system*. Vol. 1. Springer Milano, 2010. ISBN: 978-88-470-5805-7. DOI: 10.1007/978-88-470-1152-6.

[63] Frapolli, N., Chikatamarla, S. S., and Karlin, I. V. "Entropic lattice Boltzmann model for gas dynamics: Theory, boundary conditions, and implementation". In: *Physical Review E* 93.6 (2016), p. 063302. DOI: 10.1103/PhysRevE.93.063302.

[64] Freitas, R. K., Henze, A., Meinke, M., and Schröder, W. "Analysis of Lattice-Boltzmann methods for internal flows". In: *Computers & Fluids* 47.1 (2011), pp. 115–121. DOI: 10.1016/j.compfluid.2011.02.019.

[65] Frolov, S. V., Sindeev, S. V., Liepsch, D, and Balasso, A. "Experimental and CFD flow studies in an intracranial aneurysm model with Newtonian and non-Newtonian fluids". In: *Technology and Health Care* 24.3 (2016), pp. 317–333. DOI: 0.3233/THC-161132.

[66] Frolov, S. V., Sindeev, S. V., Liepsch, D, Balasso, A, Arnold, P, Kirschke, J. S., Prothmann, S, and Potlov, A. Y. "Newtonian and non-Newtonian blood flow at a 90°-bifurcation of the cerebral artery: A comparative study of fluid viscosity models". In: *Journal of Mechanics in Medicine and Biology* 18.05 (2018), p. 1850043. DOI: 10.1142/S0219519418500434.

[67] Fučík, R., Eichler, P., Klinkovský, J., Straka, R., and Oberhuber, T. "Lattice Boltzmann Method Analysis Tool (LBMAT)". In: *Numerical Algorithms* (2022), pp. 1–17. DOI: 10.1007/s11075-022-01476-8.

[68] Fučík, R., Eichler, P., Straka, R., Pauš, P., Klinkovský, J., and Oberhuber, T. "On optimal node spacing for immersed boundary–lattice Boltzmann method in 2D and 3D". In: *Computers & Mathematics with Applications* 77.4 (2019), pp. 1144–1162. DOI: 10.1016/j.camwa.2018.10.045.

[69] Fučík, R. and Straka, R. "Equivalent finite difference and partial differential equations for the lattice Boltzmann method". In: *Computers & Mathematics with Applications* 90 (2021), pp. 96–103. DOI: 10.1016/j.camwa.2021.03.014.

[70] Fuka, V. "PoisFFT–A free parallel fast Poisson solver". In: *Applied Mathematics and Computation* 267 (2015), pp. 356–364. DOI: 10.1016/j.amc.2015.03.011.

[71]   Fučík, R., Galabov, R., Pauš, P., Eichler, P., Klinkovský, J., Straka, R., Tintěra, J., and
        Chabiniok, R. "Investigation of phase-contrast magnetic resonance imaging underestima-
        tion of turbulent flow through the aortic valve phantom: Experimental and computational
        study using lattice Boltzmann method". In: *Magnetic Resonance Materials in Physics,
        Biology and Medicine* 33 (2020), 649—662. DOI: 10.1007/s10334-020-00837-5.

[72]   Gebäck, T. and Heintz, A. "A lattice Boltzmann method for the advection-diffusion
        equation with Neumann boundary conditions". In: *Communications in Computational
        Physics* 15.2 (2014), pp. 487–505. DOI: 10.4208/cicp.161112.230713a.

[73]   Geier, M., Fakhari, A., and Lee, T. "Conservative phase-field lattice Boltzmann model
        for interface tracking equation". In: *Physical Review E* 91 (6 2015), p. 063309. DOI:
        10.1103/PhysRevE.91.063309.

[74]   Geier, M., Greiner, A., and Korvink, J. G. "A factorized central moment lattice Boltzmann
        method". In: *The European Physical Journal Special Topics* 171.1 (2009), pp. 55–61. DOI:
        10.1140/epjst/e2009-01011-1.

[75]   Geier, M., Greiner, A., and Korvink, J. G. "Bubble functions for the lattice Boltzmann
        method and their application to grid refinement". In: *The European Physical Journal
        Special Topics* 171.1 (2009), pp. 173–179. DOI: 10.1140/epjst/e2009-01026-6.

[76]   Geier, M., Greiner, A., and Korvink, J. G. "Cascaded digital lattice Boltzmann automata
        for high Reynolds number flow". In: *Physical Review E* 73.6 (2006), p. 066705. DOI:
        10.1103/PhysRevE.73.066705.

[77]   Geier, M., Lenz, S., Schönherr, M., and Krafczyk, M. "Under-resolved and large eddy
        simulations of a decaying Taylor–Green vortex with the cumulant lattice Boltzmann
        method". In: *Theoretical and Computational Fluid Dynamics* 35.2 (2021), pp. 169–208.
        DOI: 10.1007/s00162-020-00555-7.

[78]   Geier, M., Pasquali, A., and Schönherr, M. "Parametrization of the cumulant lattice
        Boltzmann method for fourth order accurate diffusion part I: Derivation and validation".
        In: *Journal of Computational Physics* 348 (2017), pp. 862–888. DOI: 10.1016/j.jcp.
        2017.05.040.

[79]   Geier, M. and Schönherr, M. "Esoteric twist: An efficient in-place streaming algorithmus
        for the lattice Boltzmann method on massively parallel hardware". In: *Computation* 5.2
        (2017), p. 19. DOI: 10.3390/computation5020019.

[80]   Geier, M., Schönherr, M., Pasquali, A., and Krafczyk, M. "The cumulant lattice Boltzmann
        equation in three dimensions: Theory and validation". In: *Computers & Mathematics with
        Applications* 70.4 (2015), pp. 507–547. DOI: 10.1016/j.camwa.2015.05.001.

[81]   Gerbeau, J.-F., Vidrascu, M., and Frey, P. "Fluid–structure interaction in blood flows
        on geometries based on medical imaging". In: *Computers & Structures* 83.2-3 (2005),
        pp. 155–165. DOI: 10.1016/j.compstruc.2004.03.083.

[82]   Ginzburg, I. "Truncation errors, exact and heuristic stability analysis of two-relaxation-
        times lattice Boltzmann schemes for anisotropic advection-diffusion equation". In: *Com-
        munications in Computational Physics* 11.5 (2012), pp. 1439–1502. DOI: 10.4208/cicp.
        211210.280611a.

[83]   Ginzburg, I., Verhaeghe, F., and d'Humieres, D. "Study of simple hydrodynamic solu-
        tions with the two-relaxation-times lattice Boltzmann scheme". In: *Communications in
        computational physics* 3.3 (2008), pp. 519–581.

[84] Ginzburg, I., Verhaeghe, F., and d'Humieres, D. "Two-relaxation-time lattice Boltzmann scheme: About parametrization, velocity, pressure and mixed boundary conditions". In: *Communications in computational physics* 3.2 (2008), pp. 427–478.

[85] Green, S. I. *Fluid vortices*. Vol. 30. Springer Science & Business Media, 2012. ISBN: 978-94-010-4111-9. DOI: `10.1007/978-94-011-0249-0`.

[86] Grimmett, G. and Stirzaker, D. *Probability and random processes*. 4th ed. Oxford University Press, 2020. ISBN: 978-0-19-884760-1.

[87] Guerciotti, B. and Vergara, C. "Computational comparison between Newtonian and non-Newtonian blood rheologies in stenotic vessels". In: *Biomedical Technology*. Springer, 2018, pp. 169–183. ISBN: 978-3-319-59548-1. DOI: `10.1007/978-3-319-59548-1_10`.

[88] Guo, Z. and Shu, C. *Lattice Boltzmann method and its application in engineering*. Vol. 3. World Scientific, 2013. ISBN: 9814508292. DOI: `10.1142/8806`.

[89] Guzik, S. M., Weisgraber, T. H., Colella, P., and Alder, B. J. "Interpolation methods and the accuracy of lattice-Boltzmann mesh refinement". In: *Journal of Computational Physics* 259 (2014), pp. 461–487. DOI: `10.1016/j.jcp.2013.11.037`.

[90] Hairer, E., Norsett, S. P., and Wanner, G. "Solving Ordinary Differential Equations I: Nonstiff Problems". In: *Siam Review* 32.3 (1990), pp. 485–530. DOI: `10.1137/1032091`.

[91] Hauswirth, S. C., Bowers, C. A., Fowler, C. P., Schultz, P. B., Hauswirth, A. D., Weigand, T., and Miller, C. T. "Modeling cross model non-Newtonian fluid flow in porous media". In: *Journal of Contaminant Hydrology* 235 (2020), p. 103708. DOI: `10.1016/j.jconhyd.2020.103708`.

[92] He, X., Shan, X., and Doolen, G. D. "Discrete Boltzmann equation model for nonideal gases". In: *Physical Review E* 57.1 (1998), R13–R16. DOI: `10.1103/PhysRevE.57.R13`.

[93] Hecht, M. and Harting, J. "Erratum: Implementation of on-site velocity boundary conditions for D3Q19 lattice Boltzmann simulations". In: *Journal of Statistical Mechanics: Theory and Experiment* 2013.02 (2013), E02001. DOI: `10.1088/1742-5468/2013/02/E02001`.

[94] Heumann, C., Schomaker, M., et al. *Introduction to statistics and data analysis. With Exercises, Solutions and Applications in R*. Springer Cham, 2016. ISBN: 978-3-319-83456-6. DOI: `10.1007/978-3-319-46162-5`.

[95] Hippelheuser, J. E., Lauric, A., Cohen, A. D., and Malek, A. M. "Realistic non-Newtonian viscosity modelling highlights hemodynamic differences between intracranial aneurysms with and without surface blebs". In: *Journal of biomechanics* 47.15 (2014), pp. 3695–3703. DOI: `10.1016/j.jbiomech.2014.09.027`.

[96] Holdych, D. J., Noble, D. R., Georgiadis, J. G., and Buckius, R. O. "Truncation error analysis of lattice Boltzmann methods". In: *Journal of Computational Physics* 193.2 (2004), pp. 595–619. DOI: `10.1016/j.jcp.2003.08.012`.

[97] Holman, D. M., Brionnaud, R. M., and Abiza, Z. "Solution to industry benchmark problems with the lattice-Boltzmann code XFlow". In: *Proceeding in the European Congress on Computational Methods in Applied Sciences and Engineering (ECCOMAS)*. 2012.

[98] Hong, H., Song, J. M., and Yeom, E. "Variations in pulsatile flow around stenosed microchannel depending on viscosity". In: *PLoS one* 14.1 (2019), e0210993. DOI: `10.1371/journal.pone.0210993`.

[99]   Hu, K., Meng, J., Zhang, H., Gu, X.-J., Emerson, D. R., and Zhang, Y. "A comparative study of boundary conditions for lattice Boltzmann simulations of high Reynolds number flows". In: *Computers & Fluids* 156 (2017), pp. 1–8. DOI: `10.1016/j.compfluid.2017.06.008`.

[100] Huang, H., Sukop, M. C., and Lu, X. *Multiphase lattice Boltzmann methods: Theory and application.* John Wiley & Sons, 2015. ISBN: 978-1-118-97133-8. DOI: `10.1002/9781118971451`.

[101] Huang, R. and Wu, H. "A modified multiple-relaxation-time lattice Boltzmann model for convection–diffusion equation". In: *Journal of Computational Physics* 274 (2014), pp. 50–63. DOI: `10.1016/j.jcp.2014.05.041`.

[102] Irgens, F. *Rheology and non-Newtonian fluids.* 1st ed. Vol. 190. Springer Cham, 2014. ISBN: 978-3-319-01052-6. DOI: `10.1007/978-3-319-01053-3`.

[103] Izquierdo, S. and Fueyo, N. "Characteristic nonreflecting boundary conditions for open boundaries in lattice Boltzmann methods". In: *Physical Review E* 78.4 (2008), p. 046707. DOI: `10.1103/PhysRevE.78.046707`.

[104] Jiménez, J. "Cascades in wall-bounded turbulence". In: *Annual Review of Fluid Mechanics* 44 (2012), pp. 27–45. DOI: `10.1146/annurev-fluid-120710-101039`.

[105] Jiménez, J. "Turbulent flows over rough walls". In: *Annual Review of Fluid Mechanics* 36 (2004), pp. 173–196. DOI: `10.1146/annurev.fluid.36.050802.122103`.

[106] Junk, M., Klar, A., and Luo, L.-S. "Asymptotic analysis of the lattice Boltzmann equation". In: *Journal of Computational Physics* 210.2 (2005), pp. 676–704. DOI: `10.1016/j.jcp.2005.05.003`.

[107] Junk, M. and Yang, Z. "Analysis of lattice Boltzmann boundary conditions". In: *Proceedings in Applied Mathematics and Mechanics.* Vol. 3. 1. Wiley Online Library. 2003, pp. 76–79. DOI: `10.1002/pamm.200310320`.

[108] Junk, M. and Yang, Z. "Asymptotic analysis of finite difference methods". In: *Applied mathematics and computation* 158.1 (2004), pp. 267–301. DOI: `10.1016/j.amc.2003.08.097`.

[109] Junk, M. and Yang, Z. "Outflow boundary conditions for the lattice Boltzmann method". In: *Progress in Computational Fluid Dynamics, an International Journal* 8.1-4 (2008), pp. 38–48. DOI: `10.1504/PCFD.2008.018077`.

[110] Kang, S. K. and Hassan, Y. A. "The effect of lattice models within the lattice Boltzmann method in the simulation of wall-bounded turbulent flows". In: *Journal of Computational Physics* 232.1 (2013), pp. 100–117. DOI: `10.1016/j.jcp.2012.07.023`.

[111] Karlin, I. V., Bösch, F., and Chikatamarla, S. "Gibbs' principle for the lattice-kinetic theory of fluid dynamics". In: *Physical Review E* 90.3 (2014), p. 031302. DOI: `10.1103/PhysRevE.90.031302`.

[112] Kellnerová, R., Fuka, V., Uruba, V., Jurčáková, K., Nosek, Š., Chaloupecká, H., and Jaňour, Z. "On street-canyon flow dynamics: Advanced validation of LES by time-resolved PIV". In: *Atmosphere* 9.5 (2018), p. 161. DOI: `10.3390/atmos9050161`.

[113] Kennedy, P. and Zheng, R. *Flow analysis of injection Molds.* 2nd ed. Carl Hanser Verlag GmbH Co KG, 2013. DOI: `10.3139/9781569905227.fm`.

[114] Kolmogorov, A. N. "The local structure of turbulence in incompressible viscous fluid for very large Reynolds numbers". In: *Cr Acad. Sci. URSS* 30 (1941), pp. 301–305.

[115] Krastins, I., Kao, A., Pericleous, K., and Reis, T. "Moment-based boundary conditions for straight on-grid boundaries in three-dimensional lattice Boltzmann simulations". In: *International Journal for Numerical Methods in Fluids* 92.12 (2020), pp. 1948–1974. DOI: 10.1002/fld.4856.

[116] Krause, M. J., Kummerländer, A., Avis, S. J., Kusumaatmaja, H., Dapelo, D., Klemens, F., Gaedtke, M., Hafen, N., Mink, A., Trunk, R., et al. "OpenLB—Open source lattice Boltzmann code". In: *Computers & Mathematics with Applications* 81 (2021), pp. 258–288. DOI: 10.1016/j.camwa.2020.04.033.

[117] Kremer, G. M. *An introduction to the Boltzmann equation and transport processes in gases*. 1st ed. Springer Berlin, Heidelberg, 2010. ISBN: 978-3-642-11695-7. DOI: 10.1007/978-3-642-11696-4.

[118] Krüger, T., Kusumaatmaja, H., Kuzmin, A., Shardt, O., Silva, G., and Viggen, E. M. *The lattice Boltzmann method. Principles and Practice*. 1st ed. Springer Cham, 2017. ISBN: 978-3-319-83103-9. DOI: 10.1007/978-3-319-44649-3.

[119] Kumar, P., Kutscher, K., Mößner, M., Radespiel, R., Krafczyk, M., and Geier, M. "Validation of a vrans-model for turbulent flow over a porous flat plate by cumulant lattice Boltzmann dns/les and experiments". In: *Journal of Porous Media* 21.5 (2018), pp. 471–482. DOI: 10.1615/JPorMedia.v21.i5.60.

[120] Kummerländera, A., Dornd, M., Franka, M., and Krausea, M. J. *Implicit Propagation of Directly Addressed Grids in Lattice Boltzmann Methods*. 2021. DOI: 10.13140/RG.2.2.35085.87523.

[121] Kutscher, K., Geier, M., and Krafczyk, M. "Multiscale simulation of turbulent flow interacting with porous media based on a massively parallel implementation of the cumulant lattice Boltzmann method". In: *Computers & Fluids* 193 (2019), p. 103733. DOI: 10.1016/j.compfluid.2018.02.009.

[122] Lagrava, D., Malaspinas, O., Latt, J., and Chopard, B. "Advances in multi-domain lattice Boltzmann grid refinement". In: *Journal of Computational Physics* 231.14 (2012), pp. 4808–4822. DOI: 10.1016/j.jcp.2012.03.015.

[123] Lallemand, P. and Luo, L.-S. "Theory of the lattice Boltzmann method: Dispersion, dissipation, isotropy, Galilean invariance, and stability". In: *Physical review E* 61.6 (2000), pp. 6546–6562. DOI: 10.1103/PhysRevE.61.6546.

[124] Lammers, P., Beronov, K. N., Volkert, R., Brenner, G., and Durst, F. "Lattice BGK direct numerical simulation of fully developed turbulence in incompressible plane channel flow". In: *Computers & Fluids* 35.10 (2006), pp. 1137–1153. DOI: 10.1016/j.compfluid.2005.10.002.

[125] Latt, J., Chopard, B., Malaspinas, O., Deville, M., and Michler, A. "Straight velocity boundaries in the lattice Boltzmann method". In: *Physical Review E* 77.5 (2008), p. 056703. DOI: 10.1103/PhysRevE.77.056703.

[126] Latt, J., Malaspinas, O., Kontaxakis, D., Parmigiani, A., Lagrava, D., Brogi, F., Belgacem, M. B., Thorimbert, Y., Leclaire, S., Li, S., et al. "Palabos: parallel lattice Boltzmann solver". In: *Computers & Mathematics with Applications* 81 (2021), pp. 334–350. DOI: 10.1016/j.camwa.2020.03.022.

[127] Lebowitz, J., Frisch, H., and Helfand, E. "Nonequilibrium distribution functions in a fluid". In: *The Physics of Fluids* 3.3 (1960), pp. 325–338. DOI: 10.1063/1.1706037.

[128] LeVeque, R. J. *Finite difference methods for ordinary and partial differential equations. steady-state and time-dependent problems.* Society for Industrial and Applied Mathematics, 2007. ISBN: 978-0-898716-29-0. DOI: 10.1137/1.9780898717839.

[129] Li, Q., Zhou, P., and Yan, H. J. "Revised Chapman-Enskog analysis for a class of forcing schemes in the lattice Boltzmann method". In: *Physical Review E* 94.4 (2016), p. 043313. DOI: 10.1103/PhysRevE.94.043313.

[130] Li, Y., Choi, J.-I., Choic, Y., and Kim, J. "A simple and efficient outflow boundary condition for the incompressible Navier–Stokes equations". In: *Engineering Applications of Computational Fluid Mechanics* 11.1 (2017), pp. 69–85. DOI: 10.1080/19942060.2016.1247296.

[131] Liboff, R. L. *Kinetic Theory. Classical, Quantum, and Relativistic Descriptions.* 3rd ed. Springer Science+Business Media New York, 2003. ISBN: 978-1-4419-3052-1. DOI: 10.1007/b97467.

[132] Lin, X., Wu, J., and Zhang, T. "A mesh-free radial basis function–based semi-Lagrangian lattice Boltzmann method for incompressible flows". In: *International Journal for Numerical Methods in Fluids* 91.4 (2019), pp. 198–211. DOI: 10.1002/fld.4749.

[133] Liu, H., Zhou, J. G., and Burrows, R. "Lattice Boltzmann simulations of the transient shallow water flows". In: *Advances in Water Resources* 33.4 (2010), pp. 387–396. DOI: 10.1016/j.advwatres.2010.01.005.

[134] Liu, H., Lan, L., Abrigo, J., Ip, H. L., Soo, Y., Zheng, D., Wong, K. S., Wang, D., Shi, L., Leung, T. W., et al. "Comparison of Newtonian and Non-newtonian Fluid Models in Blood Flow Simulation in Patients With Intracranial Arterial Stenosis". In: *Frontiers in Physiology* 12 (2021), p. 718540. DOI: 10.3389/fphys.2021.718540.

[135] Marlevi, D., Mariscal-Harana, J., Burris, N. S., Sotelo, J., Ruijsink, B., Hadjicharalambous, M., Asner, L., Sammut, E., Chabiniok, R., Uribe, S., et al. "Altered Aortic Hemodynamics and Relative Pressure in Patients with Dilated Cardiomyopathy". In: *Journal of cardiovascular translational research* 15 (2022), pp. 1–16. DOI: 10.1007/s12265-021-10181-1.

[136] Marson, F., Thorimbert, Y., Chopard, B., Ginzburg, I., and Latt, J. "Enhanced single-node lattice Boltzmann boundary condition for fluid flows". In: *Physical Review E* 103.5 (2021), p. 053308. DOI: 10.1103/PhysRevE.103.053308.

[137] McNamara, G. R. and Zanetti, G. "Use of the Boltzmann equation to simulate lattice-gas automata". In: *Physical review letters* 61.20 (1988), pp. 2332–2335. DOI: 10.1103/PhysRevLett.61.2332.

[138] Mei, R., Luo, L.-S., Lallemand, P., and d'Humières, D. "Consistent initial conditions for lattice Boltzmann simulations". In: *Computers & Fluids* 35.8-9 (2006), pp. 855–862. DOI: 10.1016/j.compfluid.2005.08.008.

[139] Mezali, F., Benmamar, S., Naima, K., Ameur, H., and Rafik, O. "Evaluation of stent effect and thrombosis generation with different blood rheology on an intracranial aneurysm by the Lattice Boltzmann method". In: *Computer Methods and Programs in Biomedicine* 219 (2022), p. 106757. DOI: 10.1016/j.cmpb.2022.106757.

[140] Mikyška, J. *Asymptotické metody.* Praha : Česká technika, 2008. ISBN: 978-80-01-04061-4.

[141] Mohamad, A. A. *Lattice boltzmann method. Fundamentals and Engineering Applications with Computer Codes.* 1st ed. Vol. 70. Springer London, 2011. ISBN: 978-1-4471-6099-1. DOI: 10.1007/978-0-85729-455-5.

[142] Mohrhard, M., Thäter, G., Bludau, J., Horvat, B., and Krause, M. J. "Auto-vectorization friendly parallel lattice Boltzmann streaming scheme for direct addressing". In: *Computers & Fluids* 181 (2019), pp. 1–7. DOI: 10.1016/j.compfluid.2019.01.001.

[143] Nichols, W., O'Rourke, M., and Vlachopoulos, C. *McDonald's Blood Flow in Arteries. Theoretical, Experimental and Clinical Principles.* CRC Press, 2011. ISBN: 978-0-340-98501-4. DOI: 10.1201/b13568.

[144] Nicoud, F., Toda, H. B., Cabrit, O., Bose, S., and Lee, J. "Using singular values to build a subgrid-scale model for large eddy simulations". In: *Physics of fluids* 23.8 (2011), p. 085106. DOI: 10.1063/1.3623274.

[145] Obrecht, C., Kuznik, F., Tourancheau, B., and Roux, J.-J. "Multi-GPU implementation of the lattice Boltzmann method". In: *Computers & Mathematics with Applications* 65.2 (2013), pp. 252–261. DOI: 10.1016/j.camwa.2011.02.020.

[146] Pasquali, A., Geier, M., and Krafczyk, M. "Near-wall treatment for the simulation of turbulent flow by the cumulant lattice Boltzmann method". In: *Computers & Mathematics with Applications* 79.1 (2020), pp. 195–212. DOI: 10.1016/j.camwa.2017.11.022.

[147] Peng, C., Geneva, N., Guo, Z., and Wang, L.-P. "Direct numerical simulation of turbulent pipe flow using the lattice Boltzmann method". In: *Journal of Computational Physics* 357 (2018), pp. 16–42. DOI: 10.1016/j.jcp.2017.11.040.

[148] Peskin, C. S. "The immersed boundary method". In: *Acta numerica* 11 (2002), pp. 479–517. DOI: 10.1017/S0962492902000077.

[149] Poli, A. A. and Cirillo, M. C. "On the use of the normalized mean square error in evaluating dispersion model performance". In: *Atmospheric Environment. Part A. General Topics* 27.15 (1993), pp. 2427–2434. DOI: 10.1016/0960-1686(93)90410-Z.

[150] Pope, S. B. *Turbulent flows.* 2000. DOI: 10.1017/CBO9780511840531.

[151] Pozrikidis, C. *A practical guide to boundary element methods with the software library BEMLIB.* CRC Press, 2002. ISBN: 9780429139628. DOI: 10.1201/9781420035254.

[152] Premnath, K. N. and Abraham, J. "Three-dimensional multi-relaxation time (MRT) lattice-Boltzmann models for multiphase flow". In: *Journal of Computational Physics* 224.2 (2007), pp. 539–559. DOI: 10.1016/j.jcp.2006.10.023.

[153] Premnath, K. N. and Banerjee, S. "On the three-dimensional central moment lattice Boltzmann method". In: *Journal of Statistical Physics* 143.4 (2011), pp. 747–794. DOI: 10.1007/s10955-011-0208-9.

[154] Rahman, M. M., Hossain, M. A., Mamun, K., and Akhter, M. N. "Comparative study of Newtonian and Non-Newtonian blood flow through a stenosed carotid artery". In: *AIP Conference Proceedings.* Vol. 1980. 1. AIP Publishing LLC. 2018, p. 040017. DOI: 10.1063/1.5044327.

[155] Sankar, D. S. and Hemalatha, K. "A non-Newtonian fluid flow model for blood flow through a catheterized artery—steady flow". In: *Applied mathematical modelling* 31.9 (2007), pp. 1847–1864. DOI: 10.1016/j.apm.2006.06.009.

[156] Sbragaglia, M. and Succi, S. "A note on the lattice Boltzmann method beyond the Chapman-Enskog limits". In: *Europhysics Letters* 73.3 (2005), p. 370. DOI: 10.1209/epl/i2005-10404-8.

[157] Schlichting, H. and Gersten, K. *Boundary-Layer Theory.* 9th ed. Springer-Verlag Berlin Heidelberg 2017, 2017. ISBN: 978-3-662-52917-1. DOI: 10.1007/978-3-662-52919-5.

[158] Schornbaum, F. and Rude, U. "Massively parallel algorithms for the lattice Boltzmann method on nonuniform grids". In: *SIAM Journal on Scientific Computing* 38.2 (2016), pp. C96–C126. DOI: 10.1137/15M1035240.

[159] Schupbach, W. T. "Central Moment Lattice Boltzmann Method Based on Modified Fokker-Planck Guided Collision for Flow Simulations". PhD thesis. University of Colorado at Denver, 2020.

[160] Scopus database. https://www.scopus.com. Accessed: 2022-11-09. 2022.

[161] "Integrated Wind-Erosion Modelling". In: *Physics and Modelling of Wind Erosion.* Ed. by Shao, Y. Vol. 37. Springer Netherlands, 2008, pp. 303–360. ISBN: 978-1-4020-8894-0. DOI: 10.1007/978-1-4020-8895-7_9.

[162] Sharma, K. V., Straka, R., and Tavares, F. W. "New cascaded thermal lattice Boltzmann method for simulations of advection-diffusion and convective heat transfer". In: *International Journal of Thermal Sciences* 118 (2017), pp. 259–277. DOI: 10.1016/j.ijthermalsci.2017.04.020.

[163] Spasov, M, Rempfer, D, and Mokhasi, P. "Simulation of a turbulent channel flow with an entropic lattice Boltzmann method". In: *International journal for numerical methods in fluids* 60.11 (2009), pp. 1241–1258. DOI: 10.1002/fld.1946.

[164] Spriggs, T. W. "A four-constant model for viscoelastic fluids". In: *Chemical Engineering Science* 20.11 (1965), pp. 931–940. DOI: 10.1016/0009-2509(65)80091-4.

[165] Stankovic, Z., Allen, B. D., Garcia, J., Jarvis, K. B., and Markl, M. "4D flow imaging with MRI". In: *Cardiovascular diagnosis and therapy* 4.2 (2014), pp. 173–192. DOI: 10.3978/j.issn.2223-3652.2014.01.02.

[166] Strzelczyk, D. and Matyka, M. "How Nodes Layout, Refinement and Velocity Discretization Influence Convergence of the Meshless Lattice Boltzmann Method". In: *Journal of Computational Physics* (2022). DOI: 10.2139/ssrn.4070398.

[167] Succi, S. *The Lattice Boltzmann Equation. For Complex States of Flowing Matter.* Oxford University Press, 2018. ISBN: 9780199592357. DOI: 10.1093/oso/9780199592357.001.0001.

[168] Sukop, M. C. and Thorne, D. T. "Lattice Boltzmann Modeling Lattice Boltzmann Modeling. An Introduction for Geoscientists and Engineers". In: (2006). DOI: 10.1007/978-3-540-27982-2.

[169] Švec, O. and Skoček, J. "Simple Navier's slip boundary condition for the non-Newtonian Lattice Boltzmann fluid dynamics solver". In: *Journal of Non-Newtonian Fluid Mechanics* 199 (2013), pp. 61–69. DOI: 10.1016/j.jnnfm.2013.06.003.

[170] Švihlová, H, Hron, J, Málek, J, Rajagopal, K., and Rajagopal, K. "Determination of pressure data from velocity data with a view towards its application in cardiovascular mechanics. Part 2. A study of aortic valve stenosis". In: *International Journal of Engineering Science* 114 (2017), pp. 1–15. DOI: 10.1016/j.ijengsci.2017.01.002.

[171] Tao, S., He, Q., Chen, B., Yang, X., and Huang, S. "One-point second-order curved boundary condition for lattice Boltzmann simulation of suspended particles". In: *Computers & Mathematics with Applications* 76.7 (2018), pp. 1593–1607. DOI: 10.1016/j.camwa.2018.07.013.

[172] Tartar, L. *An Introduction to Navier-Stokes Equation and Oceanography.* 1st ed. Springer Berlin, Heidelberg, 2006. ISBN: 978-3-540-35743-8. DOI: 10.1007/3-540-36545-1.

[173] Taylor, C. A. and Figueroa, C. "Patient-specific modeling of cardiovascular mechanics". In: *Annual review of biomedical engineering* 11 (2009), pp. 109–134. DOI: 10.1146/annurev.bioeng.10.061807.160521.

[174] Terrell, G. R. *Mathematical Statistics. A Unified Introduction.* 1st ed. Springer Texts in Statistics. Springer New York, NY, 1999. ISBN: 978-1-4419-3141-2. DOI: 10.1007/b98961.

[175] Tesch, K. "Generalised Herschel model applied to blood flow modelling". In: *Task Quarterly* 16.3-4 (2012), pp. 253–262.

[176] Thurston, G. B. "Viscoelasticity of human blood". In: *Biophysical journal* 12.9 (1972), pp. 1205–1217. DOI: 10.1016/S0006-3495(72)86156-3.

[177] Trautz, A. C., Illangasekare, T. H., Howington, S., and Cihan, A. "Sensitivity of a Continuum-Scale Porous Media Heat and Mass Transfer Model to the Spatial-Discretization Length-Scale of Applied Atmospheric Forcing Data". In: *Water Resources Research* 55.4 (2019), pp. 3520–3540. DOI: 10.1029/2018WR023923.

[178] Trautz, A. C., Illangasekare, T. H., and Rodriguez-Iturbe, I. "Role of co-occurring competition and facilitation in plant spacing hydrodynamics in water-limited environments". In: *Proceedings of the National Academy of Sciences* 114.35 (2017), pp. 9379–9384. DOI: 10.1073/pnas.1706046114.

[179] VDI Guideline 3783 Part 9. *Environmental meteorology—Prognostic micro-scale wind field models—Evaluation for flow around buildings and obstacles.* 2005.

[180] Venturi, S., Di Francesco, S., Geier, M., and Manciola, P. "A new collision operator for lattice Boltzmann shallow water model: A convergence and stability study". In: *Advances in Water Resources* 135 (2020), p. 103474. DOI: 10.1016/j.advwatres.2019.103474.

[181] Verschaeve, J. C. and Müller, B. "A curved no-slip boundary condition for the lattice Boltzmann method". In: *Journal of Computational Physics* 229.19 (2010), pp. 6781–6803. DOI: 10.1016/j.jcp.2010.05.022.

[182] Versteeg, H. K. and Malalasekera, W. *An introduction to computational fluid dynamics. the finite volume method.* 2nd ed. Pearson education, 2007. ISBN: 978-0-13-127498-3.

[183] Vienne, L., Marié, S., and Grasso, F. "Lattice Boltzmann method for miscible gases: A forcing-term approach". In: *Physical Review E* 100.2 (2019), p. 023309. DOI: 10.1103/PhysRevE.100.023309.

[184] Vladimirov, V. S. *Methods of the theory of generalized functions.* 1st ed. CRC Press, 2002. ISBN: 9780367395940.

[185] Walsh, S. D. C. and Saar, M. O. "Interpolated lattice Boltzmann boundary conditions for surface reaction kinetics". In: *Physical Review E* 82.6 (2010), p. 066703. DOI: 10.1103/PhysRevE.82.066703.

[186] Wang, L., Tao, S., Meng, X., Zhang, K., and Lu, G. "Discrete effects on boundary conditions of the lattice Boltzmann method for fluid flows with curved no-slip walls". In: *Physical Review E* 101.6 (2020), p. 063307. DOI: 10.1103/PhysRevE.101.063307.

[187] Weickert, M., Teike, G., Schmidt, O., and Sommerfeld, M. "Investigation of the LES WALE turbulence model within the lattice Boltzmann framework". In: *Computers & Mathematics with Applications* 59.7 (2010), pp. 2200–2214. DOI: 10.1016/j.camwa.2009.08.060.

[188] Weiland, C. *Mechanics of Flow Similarities.* 1st ed. Springer Cham, 2020. ISBN: 978-3-030-42929-4. DOI: 10.1007/978-3-030-42930-0.

[189]   Weiß, J.-P. *Numerical analysis of lattice Boltzmann methods for the heat equation on a bounded interval.* KIT Scientific Publishing Germany, 2006. ISBN: 9783866440692.

[190]   Werner, L., Rettinger, C., and Rüde, U. "Coupling fully resolved light particles with the lattice Boltzmann method on adaptively refined grids". In: *International Journal for Numerical Methods in Fluids* 93.11 (2021), pp. 3280–3303. DOI: 10.1002/fld.5034.

[191]   White, F. M. and Majdalani, J. *Viscous fluid flow.* 3rd ed. McGraw-Hill New York, 2006. ISBN: 0-07-240231-8.

[192]   Yang, L., Shu, C., Chen, Z., Hou, G., and Wang, Y. "An improved multiphase lattice Boltzmann flux solver for the simulation of incompressible flow with large density ratio and complex interface". In: *Physics of Fluids* 33.3 (2021), p. 033306. DOI: doi.org/10.1063/5.0038617.

[193]   Yang, W.-C., ed. *Handbook of Fluidization and Fluid-Particle Systems.* 1st ed. CRC Press, 2003. ISBN: 9780429223341. DOI: 10.1201/9780203912744.

[194]   Yu, D., Mei, R., and Shyy, W. "A multi-block lattice Boltzmann method for viscous fluid flows". In: *International journal for numerical methods in fluids* 39.2 (2002), pp. 99–120. DOI: 10.1002/fld.280.

[195]   Yu, S., Eder, B., Dennis, R., Chu, S.-H., and Schwartz, S. E. "New unbiased symmetric metrics for evaluation of air quality models". In: *Atmospheric Science Letters* 7.1 (2006), pp. 26–34. DOI: 10.1002/asl.125.

[196]   Yu, Z. and Fan, L.-S. "An interaction potential based lattice Boltzmann method with adaptive mesh refinement (AMR) for two-phase flow simulation". In: *Journal of Computational Physics* 228.17 (2009), pp. 6456–6478. DOI: 10.1016/j.jcp.2009.05.034.

[197]   Zhao, W. and Yong, W.-A. "Maxwell iteration for the lattice Boltzmann method with diffusive scaling". In: *Physical Review E* 95.3 (2017), p. 033311. DOI: 10.1103/PhysRevE.95.033311.

[198]   Zhao-Li, G., Chu-Guang, Z., and Bao-Chang, S. "Non-equilibrium extrapolation method for velocity and pressure boundary conditions in the lattice Boltzmann method". In: *Chinese Physics* 11.4 (2002), p. 366. DOI: 10.1088/1009-1963/11/4/310.

[199]   Zou, Q. and He, X. "On pressure and velocity boundary conditions for the lattice Boltzmann BGK model". In: *Physics of fluids* 9.6 (1997), pp. 1591–1598. DOI: 10.1063/1.869307.

[200]   Zupančič Valant, A., Žiberna, L., Papaharilaou, Y., Anayiotos, A., and Georgiou, G. C. "The influence of temperature on rheological properties of blood mixtures with different volume expanders—implications in numerical arterial hemodynamics simulations". In: *Rheologica acta* 50.4 (2011), pp. 389–402. DOI: 10.1007/s00397-010-0518-x.